Development and Application of Novel Optoelectronic Materials for Photodetectors and Solar Cells

Erjin Zheng

A dissertation

submitted in partial fulfillment of the

requirements for the degree of

Doctor of Philosophy

University of Washington

2020

Reading Committee:

Qiuming Yu, Chair

Samson A. Jenekhe

Vincent C. Holmberg

Program Authorized to Offer Degree:

Chemical Engineering

University of Washington

Abstract

Development and Application of Novel Optoelectronic Materials for Photodetectors and Solar Cells

Erjin Zheng

Chair of the Supervisory Committee:

Qiuming Yu

Chemical Engineering

Modern society has shown increasing demands of optoelectronic devices with lightweight, flexible, and scalable features. Novel materials such as conducting polymer and perovskite are developed to replace the traditional group III-V inorganic materials and counter the new challenges.

Ultraviolet (UV) photodetectors play a critical role in scientific, commercial, civil, and military areas. Perovskite materials with tunable bandgap have been successfully applied to fabricate high-performance solar cells. However, their potential for UV detection has not been demonstrated yet. In this work, pinhole-free methylammonium lead trichloride ($CH_3NH_3PbCl_3$) perovskite thin films were fabricated via a two-step spin coating and solvent-vapor-assisted thermal annealing method under low temperature for the first time. Prototypical UV photodetectors based on $CH_3NH_3PbCl_3$ perovskite thin films were fabricated and showed strong photoresponse

in the 300-400 nm region. All the results demonstrated that low-temperature solution-processed $CH_3NH_3PbCl_3$ perovskite thin films offer great potential for making flexible, lightweight visible-blind UV-A photodetectors. Narrowband UV photodetectors are highly desired in multiple areas. Photodetectors based on organic-inorganic nanocomposite offer high sensitivity, widely adjustable response range, lightweight, and low-temperature solution processibility. However, the broad absorption range of organic and inorganic semiconductor materials make it difficult to achieve a narrowband detection feature. Nanocomposite thin films containing the conjugated polymer poly[(9,9-dioctylfluorenyl-2,7-diyl)-alt-co-(bithiophene)] (F8T2) blended with ZnO nanoparticles (NPs) were applied as the active layers of the photodetectors. Narrowband UV photodetectors with high gain and low driving voltage were demonstrated by adopting a symmetric device structure, controlling the active layer composition and microstructure, and manipulating the light penetration depth in the active layer. Our method offers a pathway to design and fabricate narrowband UV photodetectors.

Hybrid organic-inorganic perovskite has shown its potential as high-performance solar cell active layer. However, its instability, including intrinsic and operational instability, strongly hinders its real-life applications. Two types of methylammonium (MA)-free, formamidinium (FA)-based perovskite, $Rb_{0.05}Cs_{0.1}FA_{0.85}PbI_3$ and $Cs_{0.15}FA_{0.85}PbI_3$, was fabricated and the effect of Rb^+ on the device performance and long-term stability were investigated. By simply mixing the precursor solution before spin coating, the defect states in both types of perovskite were significantly reduced and device stabilities against the electric field were improved. The modified precursor solution provided devices with $Rb_{0.05}Cs_{0.1}FA_{0.85}PbI_3$ and $Cs_{0.15}FA_{0.85}PbI_3$ active layer that retained 68% and 92% of their initial PCE, respectively, over 30 days under N_2 protection.

The work sheds a light on the solution of the operational instability of perovskite solar cells and paves the pathway for their industrialization.

To further improve the optoelectronic device performance based on poly(3,4-ethylenedioxythiophene):polystyrene sulfonate (PEDOT:PSS) conducting polymer, a hydroxymethyl (-MeOH) and chloromethyl (-MeCl) function group was introduced to the oxyethylene ring of EDOT monomer. Oxidative chemical polymerization was applied to synthesize PEDOT:PSS and functionalized PEDOT:PSS. The polymerization mechanism of PEDOT:PSS and effects of functional group on the polymerization were revealed. The study sheds light on the polymerization of PEDOT with functional groups and provides a guideline for the synthesis of functionalized PEDOT conducting polymers with polyelectrolyte counterions using oxidative chemical polymerization.

TABLE OF CONTENTS

LIST OF FIGURES

LIST OF SCHEMES

LIST OF TABLES

ACKNOWLEDGEMENTS

I would like to express my great appreciation to my Ph.D. advisor, Professor Qiuming Yu, for all her guidance, encouragement, understanding, and especially patient considering my poor writing skill throughout my five years' study at the University of Washington. I still remember the first day I met her in Shanghai six years ago when I was an undergraduate student. I have learned tremendous knowledge, not only about the research subjects, but also the scientific vision and leadership from her during my study. All of which have made me a better person.

I would like to thank Professor Samson A. Jenekhe, Vincent C. Holmberg, and Lin Y. Lih for sharing their precious time serving as my committee members and providing valuable comments and suggestions on my research. I would also like to thank Professor John C. Berg for whom I have served as the TA twice. His passion for teaching and generosity to students have affected me a lot.

Additionally, I would like to thank the previous and current members in Professor Qiuming Yu research group, including Professor Ping Wu, Dr. Beau Richardson, Dr. Fang Sun, Dr. David Galvan, Dr. Monica Esopi, Dr. Chao Hou, Gabriella Tosado, Emerson Chen, Xiaoyu Zhang, Yi-Yu Lin, Vidit Parekh, Zhiyin Niu, Hao Dong, Suyash Bhagwat, Zonglun Li, Zizhao Xu, Chen Cai, E-lin Liu, and Shukun Zhong, for their wholeheartedly support and the fun we had together. I would also like to thank Dr. Mark Ziffer in Professor David S. Ginger group, Dr. Jingda Wu, Dr. Peifeng Jing, and Chen Zou in Professor Lin Y. Lih group, Dr. Xiaojie Lin, Dr. Roger Hung, Dr. Priyesh Jain, Dr. Peng Zhang, and Kan Wu in Professor Shaoyi Jiang group, and Dr. Lijian Zuo and Dr. Weifei Fu in Professor Alex Jen group for shearing their valuable knowledge and support alongside my study.

Finally, I would like to greatly thank my family and friends for their constant support. To my parents, they have been my strongest backing to allow me to become whomever I want. To my dear wife Yishu, I am extremely lucky to have you along my side to inspire and support me through the hard times, and I am looking forward to the future of our lives.

Chapter 1 INTRODUCTION

1.1 Overview

Optoelectronic devices have become essential components in our lives in communications, computing, entertainment, lighting, energy generation, and medical practice.[1, 2] Such devices have the function to convert optical signal to electrical signal (e.g. photodetectors and solar cells) or convert electric signal to optical signal (e.g. LEDs and lasers). Conventional optoelectronic devices apply inorganic semiconductor materials, the most commonly, III-V inorganic semiconductor compounds and their alloys such as solar cells as illustrated in **Figure 1-1**a.[1] Optoelectronic devices based on inorganic materials are generally robust and have a long lifetime. However, modern optoelectronics such as wearable sensors and printable solar cells requires the materials to be flexible, solution-processable, and cheap (Figure 1-1b).[3, 4] The high energy-consuming fabrication and low flexibility of traditional inorganic materials make them less promising candidates for modern optoelectronics. Besides, the state-of-the-art solar cells are also required to be upgraded with improved power conversion efficiency and reduced price to counter the fossil fuels induced environmental problems, such as pollution and global warming. With the advances of material science and chemistry, materials such as conducting polymers and hybrid organometal perovskites are developed to meet the needs of modern optoelectronic devices.

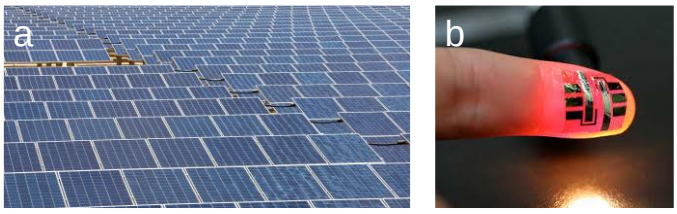

Figure 1-1 (a) Conventional rigid solar cell devices. (b) Modern conformable infrared photodetector device.

1.2 Solar Cells

1.2.1 Background

All of the energy consumed in the world over one year is approximately 14 TW. Fossil fuels, like coal, natural gas, and oil, supply 76% of the consumed energy to the world.[5] However, the fossil fuel reserve is finite, and it is estimated that only a few hundred years' supply is available at our current rate of consumption and the consumption rate is predicted to increase by 28% between 2015 and 2040. In addition, the released carbon dioxide from burning fossil fuels leads to global warming. It is predicted by the United Nations Intergovernmental Panel on Climate Change that the warming of Earth over the next 50 years could have devastating effects on sea levels, agriculture, climate, and economic development. Renewable energy refers to various energies that are supplied from nature at a rate which is faster than the world consumption, such as solar energy, wind power, hydropower, tide power, and geothermal energy. Among which, solar energy is almost infinite compared with our life span and has low geographical location dependence. Converting solar energy at only 10% efficiency using 1% of Earth's land area would supply us with twice our current energy needs worldwide. If all the supply of energy power is achieved through solar power generation, concerns such as the exhaustion of fossil fuels, global warming by carbon dioxide can be avoided.

1.2.2 Basic Principles and Parameters of Solar Cells

A solar cell refers to the device that absorbs and converts solar energy into electrical energy. The solar spectrum changes regarding the location and different time of the day. The benchtop solar cells are tested using solar simulator that simulates sunlight with an incident light intensity of 1000 W/m2 under the air mass 1.5 global (AM 1.5G) spectrum (**Figure 1-2**a), corresponding to

the standard solar spectrum hitting the earth's surface with the zenith angle of 48° at sea level. The semiconductor materials serving as the active materials that absorb light are the core part of the solar cell. When photons are absorbed by the semiconductor, the photovoltaic effect occurs: the light energy excites electrons from the low energy valance band (VB) across the bandgap (Eg) to the high energy conduction band (CB) with electron vacancies (holes) left (Figure 1-2b). The excited electrons could relax back to the VB, recombine with holes and give off photo energy or heat energy. In a solar cell, there is a built-in potential between the hole transporting layer (HTL, e.g. poly(3,4-ethylenedioxythiophene):polystyrene sulfonate (PEDOT:PSS)) and the electron transporting layer (ETL, e.g. Phenyl-C61-butyric acid methyl ester ($PC_{61}BM$)), which results in a built-in electric field in the active material. The electric field separates the electrons and holes, directs the holes to the HTL and electrons to the ETL, delivers them to the electrode and further external circuit to perform electrical work (Figure 1-2b and c).

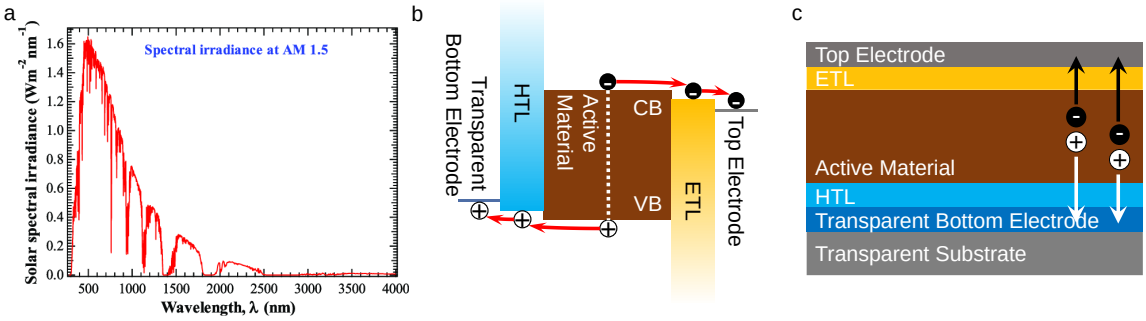

Figure 1-2 (a) Solar spectral irradiance at air mass 1.5 (AM 1.5) collected from American Society for Testing and Materials (ASTM), standard: ASTM G-173-03. (c) Energy level and basic working mechanism of a single junction solar cell device. (b) Illustration of a single junction solar cell device with the active layer sandwiched between ETL and HTL.

Solar cell performance is defined but not limited by some basic parameters, including short-circuit current (J_{SC}), open-circuit voltage (V_{OC}), fill factor (FF), and the combination of the

three, power conversion efficiency (PCE). The PCE is expressed by an energy ratio of the maximum electric output power from the solar cell and the light energy from the sun as described by the following Eq 1-1.[6]

$$PCE = \frac{P_{max}}{P_{in}} = \frac{V_{MP} \times j_{MP}}{P_{in}} = \frac{V_{OC} \times J_{SC} \times FF}{P_{in}} \qquad (1\text{-}1)$$

P_{max} is the maximum output power of the solar cell, which is equal to the product of V_{MP} and J_{MP} as illustrated in **Figure 1-3**a. P_{in} is the photo energy introduced in the solar cell device. V_{OC} is the maximum photovoltage available from a solar cell with infinite resistance or open circuit. J_{SC} is the current measured with zero resistance or short circuit. *FF* is the area defined by the product of V_{MP} and J_{MP} divided by that defined by the product of V_{OC} and J_{SC}.

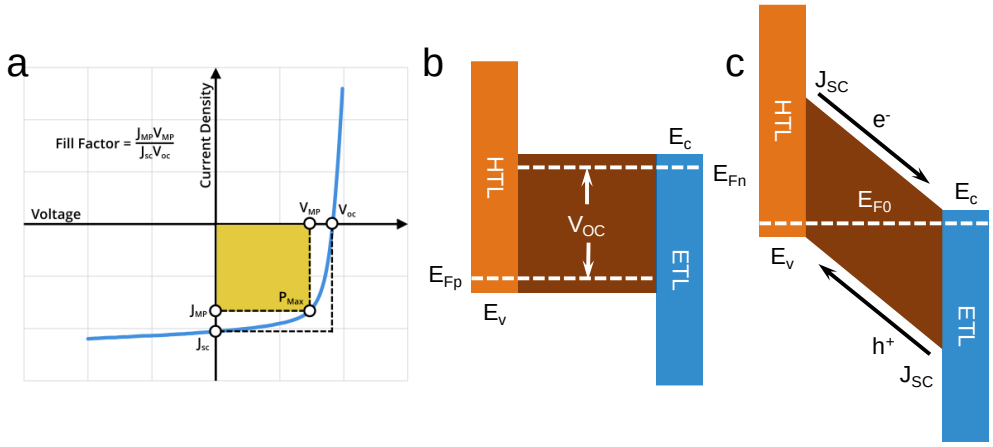

Figure 1-3 (a) Typical current-voltage characteristics (J-V) curve of the solar cell device. Energy level diagram of a solar cell under illumination at (b) open-circuit condition and (c) short-circuit condition.

V_{OC} of a solar cell is generated by a complicated process. Light produces a splitting of the electrons and holes quasi-Fermi level E_{Fn} and E_{Fp}, respectively, as illustrated in Figure 1-3b. The difference between these two levels is the maximum V_{OC} of the semiconductor layer. However, the energy can only be used after the charge separation. It is required to contact each quasi-Fermi

level independently by ETL and HTL. Consequently, the limit of V_{OC} depends on the selective contacts and how the selectivity is obtained.[6, 7] There are several factors that could affect the V_{OC} of a solar cell. From the perspective of semiconductor materials of active layers, defects existing in imperfect crystals can generate sub-bandgap states, narrowing down the quasi-Fermi level splitting range and thus reducing the V_{OC}. Interface-wise, unwell aligned ETL or HTL with the active layer would also lead to narrowed quasi-Fermi level splitting and reduce the V_{OC}. J_{SC} of a solar cell refers to the density of the charge carrier passing through the electrodes under short-circuit condition (Fig. 1-3c). It is directly related to the number of absorbed photons, which is defined by the bandgap of the semiconductors applied in the photoabsorption active layers. Generally, semiconductors with narrow band gaps can produce higher J_{SC}'s due to their wide light absorption range. The J_{SC} of a solar cell could be limited by the defect states in semiconductor materials, which serve as the electron-hole recombination centers. Imperfect interface energy level alignment can also hinder the flow of electrons and holes, and reduce J_{SC}. In addition, unbalanced charge carrier extraction rates can also affect J_{SC} because accumulated charge carriers at one side of the device can build up an internal electric field, attracting the opposite charge carriers but repulsing the same type of charge carriers. FF is probably one of the most complicated parameters in a solar cell. A high FF reflects good semiconductor quality, well-aligned carrier transport layers, and balanced electron and hole extraction rates. A low FF could be attributed to one flaw or the product of multiple flaws.

1.3 Photodetectors

1.3.1 Background

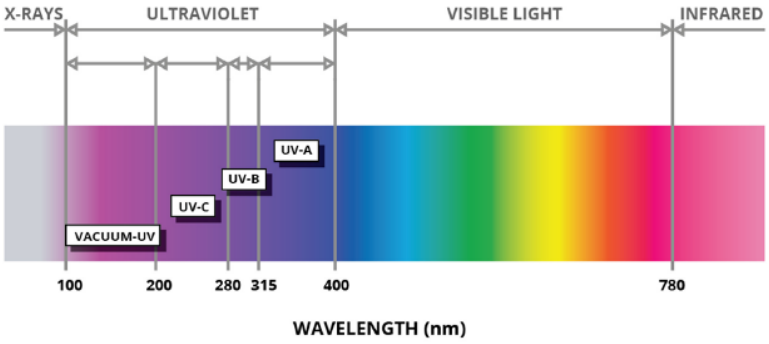

Figure 1-4 Electromagnetic spectrum.

The photodetector also refers to the device that converts the optical signal to the electrical signal. Different from the energy-generating solar cells, it can sometimes consume energy to amplify the photogenerated electrical signal intensity. The photodetector can be designed for different target spectrum region from x-ray to infrared (**Figure 1-4**). UV photodetectors have a broad application in scientific, commercial, civil, and military areas, such as chemical and biological sensing, smoke and fire detection, missile warning, combustion monitoring, and ozone sensing.[8, 9] GaN, SiC, and diamond serve as the state of art materials for UV photodetectors and have achieved responsivities in the 100-200 mA/W range with a superior UV radiation harness.[10-12] However, the fabrication of these photodetectors requires expensive processes and flexible devices cannot be achieved due to the rigid nature of these inorganic materials. Therefore, organic and organic-inorganic hybrid materials, such as polymer:fullerene, polymer:nanoparticles (NPs), and perovskite, are developed and offer a simple fabrication process and integration of cheap and flexible photodetectors.

1.3.2 Figure of Merits of Photodetectors

Photodetector performance can be evaluated by three basic figure of merits.[13] The external quantum efficiency (EQE) is defined as the number of charge carriers collected per photon in out circuit and is given in the Eq 1-2.

$$EQE = \frac{(J_L - J_D)/e}{I_{in}/h\nu} \qquad (1\text{-}2)$$

Where J_L is the photocurrent density under the illumination of different wavelength light, J_D is the dark current density, e is the elementary electron charge, I_{in} is the incident light intensity, h is the Plank constant and ν is the photon frequency. The responsivity (R) describes how efficiently the detector responds to the optical signal, which is calculated from the EQE and is given in Eq 3.

$$R = \frac{EQE \times e}{h\nu}\ (A/W) \qquad (1\text{-}3)$$

The specific detectivity, as the most important figure of merit of the photodetector, reflects the ability of the device to detect radiation energy and therefore can be applied to compare across devices. The specific detectivity is calculated by the following Eq 4.

$$D^* = \frac{R\sqrt{A}}{i_{noise}}\ (Jones\ or\ \sqrt{Hz}\ cm\ W^{-1}) \qquad (1\text{-}4)$$

Where A is the active area of the device and i_{noise} is the noise current spectral density (A $Hz^{-1/2}$). The i_{noise} is calculated from the fast Fourier transform of measured dark current versus time.

Beyond the three basic figure of merits, linear dynamic range (LDR) and bandwidth of the response window are also important parameters of the photodetector devices. LDR is the range of incident power intensity over which the current output changes linearly, which needs to be maximized. -3 dB cutoff refers to the input light modulation frequency at which the output signal

is -3 dB lower than the signal obtained under continuous-wave illumination and it needs to be maximized. Rise/decay time is the time duration from 10% to 90% or from 90% to 10% of the maximum output current. For high-speed detection such as missile detection, the rise time needs to be minimized. The full width at half maximum (FWHM) resonance width is applied to differ broadband and narrowband photodetectors.

1.3.3 Classification of Photodetectors

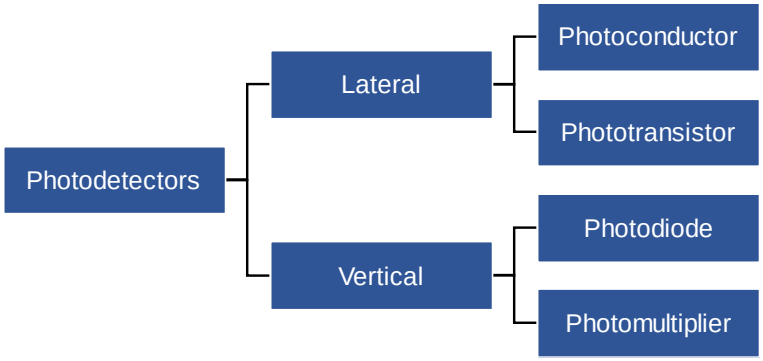

Figure 1-5 Classification of photodetectors based on device structure and working mechanism.

The photodetectors can be classified into two categories based on their device structure: lateral and vertical type (**Figure 1-5**).[14, 15] Lateral photodetectors refer to phototransistor and photoconductor. The phototransistor is consisted of substrate, photoactive layer, and source and drain metal electrode on the photoactive layer (**Figure 1-6**a). The photoconductor has a similar device structure to the phototransistor but has an extra dielectric layer and gate metal electrode underneath the photoactive layer (Figure 1-6b). In the photoconductor device, photo energy generates charge carriers in the active layer and current flows through the metal source and drain electrodes under applied external bias to achieve multiple carrier recirculation. In the photoconductor device, the charge carrier flow in the channel is controlled not only by the photogenerated charge carriers and applied source-drain voltage, but also the magnitude of the

applied gate voltage. For both devices, an incident photon triggers multiple charge carriers flow through the device, and the signal is amplified. Even though both devices can provide high sensitivity for weak light due to their photocurrent amplification feature, their response times are limited by the large electrode spacing and high bias.

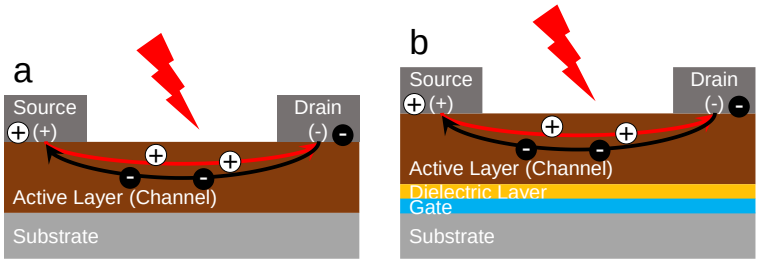

Figure 1-6 Device structure and working mechanism illustration of (a) phototransistor and (b) photoconductor, (c) photodiode, and (d) photomultiplier.

Vertical photodetectors can also be sub-divided into two categories: photodiode and photomultiplier.[15] Photodiode and photomultiplier have the same device structure, with transparent substrate, transparent electrode, charge carrier extraction layer, photoactive layer, charge carrier extraction layer, and metal electrode stacked onto each other as shown in **Figure 1-7**a and c. The working mechanism of photodiodes is similar to the solar cells: the photo energy excites electrons from VB to the CB and leaves holes in the VB. The photogenerated charge carriers then diffuse under the internal electric field generated by the ETL and HTL without external bias, to the out circuit and give electrical signal (Figure 1-7a and b). On the contrary, the photoconductors work under a reverse external bias to improve the electrical signal intensity under the illumination. Electronic trap states are intentionally introduced into the active layer. Fullerenes (e.g. PC61BM) and NPs (e.g. ZnO NPs) with high energy level barriers to the active material are popular options to create trap state. The electronic property of the active layer can also be modified directly during the synthesis or fabrication processes to create trap states without a secondary additive. The ETL

and HTL are also required to have the function to block holes and electrons, respectively, to prevent leakage current when the device is under reverse bias. Taking electron traps as an example, photo energy generates electrons and holes in the active layer, holes diffuse to the bottom negatively biased electrode with the help of both internal and external bias while electrons are trapped in the trap states in the active layer. The trapped electrons bend down the energy level of the active layer, therefore allow multiple holes to be injected from the positively charged top electrode across the ETL/HBL and active layer to the bottom electrode. An incident photon generates one electrode and hole pair and allows multiple holes flow through the device; therefore, the photomultiplication is achieved and the signal intensity is highly amplified. Each layer between the electrode has a thickness at nm scale in the vertical devices, which enables a small electrode spacing and a short carrier transit length. Therefore, the response speed of the vertical device is generally faster than the lateral device.

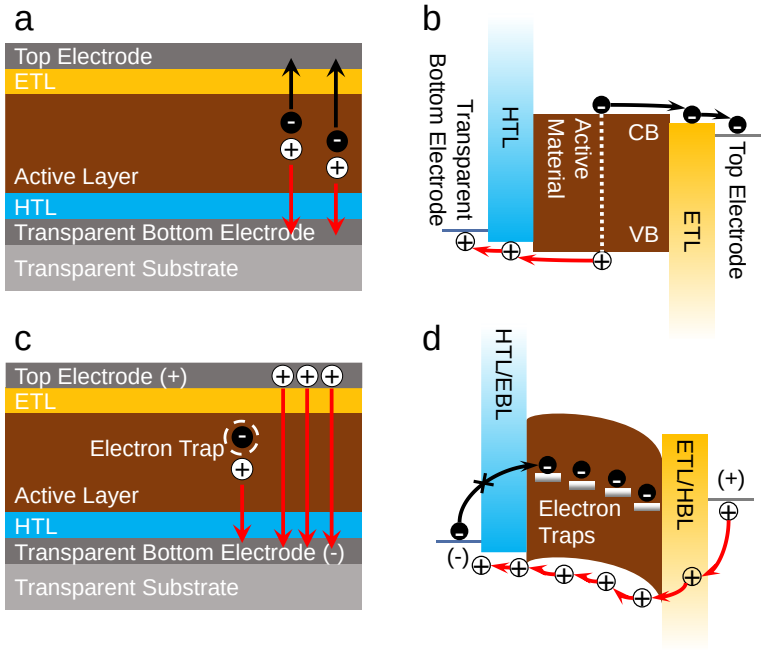

Figure 1-7 Device structure and working mechanism illustration of (a, b) photodiode and (c, d) photomultiplier.

1.3.4 Narrowband Photodetector

Photodetectors can be classified into another two categories based on the bandwidth of the response window: broadband and narrowband photodetectors. Broadband photodetector requires flat EQE, and therefore responsivity and specific detectivity spectra across the required wavelength range. On the contrary, narrowband photodetectors require small FWHM value (<100 nm) in the wavelength range of the response window. Narrowband photodetectors are essential part of imaging system, telecommunications, machine vision, biological sensing, and environmental surveillance.[16-19] The state-of-art narrowband photodetectors apply GaN,[20] Si,[21] and InGaAs,[22] as the active materials, and combine with a set of interference filters to narrow down the response window to a small target range for UV, visible, and near-infrared detection. However, the filter not only increases the complicity and cost of the photodetector and limits the pixel density in imaging system, but also hinders its integration into modern flexible electronics. Filter-free narrowband photodetectors based on organic or organic-inorganic hybrid materials serve as one of the promising candidates to meet the needs of modern electronics. Several filter-free strategies have been developed, including (1) enhancing light absorption of given wavelength through plasmonic effect;[23] (2) applying wide bandgap materials to limit adsorption range;[24] (3) manipulating the EQE through charge collection narrowing (CCN).[13] However, the plasmonic method is limited to a specific wavelength range and cannot be widely tunable, and the wide bandgap method does not apply to the visible and near-infrared detection. CCN provides widely tunable detection range based on the material absorption, therefore is one of the most successful methods to achieve narrowband photodetector. Despite its widely tunable feature, the CCN relies on the recombination loss of thick active layer by which only a small fraction of photons with the wavelength close to the material absorption cutoff are absorbed, and photogenerated charge

carriers need to travel through the thick active layer, results in a low EQE. Combing photomultiplication with CCN method would effectively solve the sensitivity issue when applying CCN method. The up-to-date state of art performance of the narrowband UV photodetectors based on organic and organic-inorganic semiconductor materials are summarized in **Table 1-1**.

Table 1-1 State of art performance of narrowband UV photodetectors based on polymer:fullerene, polymer:NPs, and perovskite active layer in different structures and working modes.

Materials	Bias (V)	Response Range (nm)	FWHM (nm)	EQE (%)	R (A/W)	D* (Jones)	Ref
C_{60}Cournarin30 /Alq_3[a]	10	375-475	~100	64			25
P3HT:$PC_{71}BM$[b]	-10	325-475	<100	5000	347.5	1.32×10^{14}	26
P3HT:$PC_{61}BM$[b]	-19	300-500	~100	~40000			27
P3HT:$PC_{71}BM$[b]	-19	300-500	~100	~126000	40.56	2.6×10^{13}	28
P3HT:$PC_{71}BM$[b]	-19	375-475	~100	16700	51.7		29
F8T2:$PC_{71}BM$[b]	-40	325-450	~50	5600	15.9		30
P3HT:$PC_{61}BM$[b]	60	300-400	27	7160	~0.3	4.08×10^{11} @10 V	31
PFP:NSN PVK/NSN[a]	-9	200-375 225-350	<100 <100		>0.06 >0.125		32
NPB:OXD-7[a]	0	300-400	~50		0.0226	10^{12}	33
C8-BTBT:PS[d]	-1.5	300-375	~50		3.1×10^{5}		34
P3HT: DC-IDT2T[b]	-20	350-500	~100	28000	~90	9×10^{13}	35
PVK:2CzPN[a]	-10	300-400	~50			5.31×10^{10}	36
PFTBT:PVK[a]	0.7	300-350	<50		0.22	1.78×10^{12}	37
PVK:ZnO[b]	-9	300-400	~50	245300	721	3.4×10^{15}	38
mCP:TiO_2[b]	-10	240-400	~80	8.5×10^{4}	240	3.72×10^{14}	40

Materials	Bias (V)	Response Range (nm)	FWHM (nm)	EQE (%)	R (A/W)	D* (Jones)	Ref
PDTP-DFBT:ZnO[b]	-4.5	300-400	~50	~1000	1.43	1.11×10^{10}	41
PVK:ZnO[b]	-10	300-375	~50	1093		2.58×10^{12}	42
PTAA:ZnO[a]	-1	410-450	12	0.66	0.23	2.6×10^{11}	43
F8T2:ZnO[b]	-15	335-410	19	2170	6.39	8.8×10^{11}	44
F8T2:ZnO[b]	3	340-390	16	782	2.32	8.45×10^{12}	45
$MAPbCl_3$ Single Crystal[a]	-1	420-440	<20	0.2-1.6			46
$MAPbCl_3$ Microcrystalline Film[c]		390-425	<30				47
$MAPbCl_3$ Thin Film[a]		400-500	66				48
$MAPbCl_3$ Thin Film[a]	0	300-400	<100	16	0.047	6.87×10^{10}	24
$MAPbCl_3$ Single Crystal[a]	0	300-400 nm	<100 nm	42.9	0.134	6×10^{12}	49

[a] Vertical structure, photodiode; [b] Vertical structure, photomultiplier; [c] Lateral structure, phototransistor; [d] Lateral structure, photoconductor

1.4 Perovskite Materials

1.4.1 Background

The basic technologies necessary to achieve the solar energy converting goal already exist to a certain extent. However, a large barrier about the price still exists. Even with a lower levelized cost of electricity, the capital costs of the solar cell system ($2000/kW) is still higher than that of gas/oil power plant ($1000/kW).[50, 51] Therefore, reducing the cost of the present silicon solar cell is very important. Hybrid organic-inorganic perovskite is one of the hottest materials that continually attracting worldwide attention, especially in the community of optoelectronic devices.

The attractive optical and electronic properties include direct bandgap,[52] high absorption coefficient,[53] long and balanced charge carrier diffusion length,[54] high charge carrier mobility,[55] and low charge carrier recombination rate.[56] Applications have been developed based on their outstanding optoelectronic properties, such as photodetectors,[24, 57] light emitting diodes,[58] lasers,[59] and solar cells.[60, 61] The certified power conversion efficiency (PCE) of the single junction perovskite solar cells rockets up to 25.2% within 15 years' research.[62] In addition, perovskite materials can be fabrication with their precursor inks under low temperature, which opens the possibility of roll-to-roll, low-cost manufacturing.

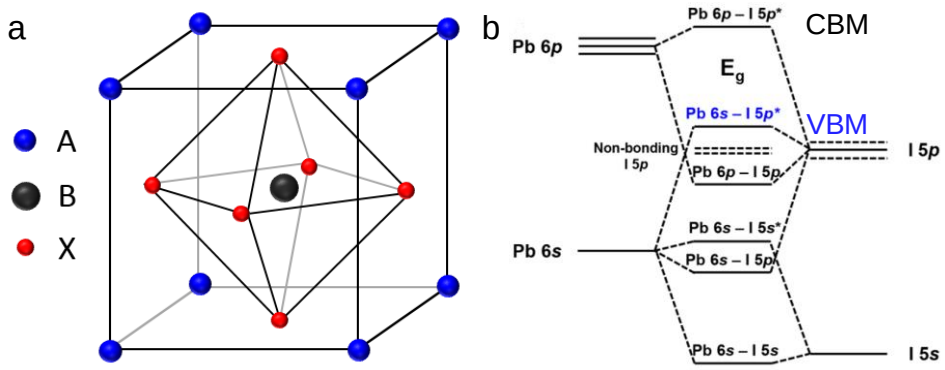

Figure 1-8 (a) Typical perovskite ABX_3 structure. (b) Molecular orbital diagram for the interaction between Pb, B site, and I, X site, atoms.[63]

Hybrid organic-inorganic perovskite materials generally have the ABX_3 three-dimensional structure (**Figure 1-8**a), where the A site cation refers to organic or inorganic monovalent cation (e.g., methylammonium ($CH_3NH_3^+$ or MA), formamidinium ($CH(NH_2)_2^+$ or FA), Cs^+, and Rb^+), B site refers to divalent group IV A metal (e.g., Pb^{2+} and Sn^{2+}), and X refers to halide anion (I^-, Br^-, and Cl^-). The forming of the valence band maximum (VBM) and the conduction band minimum (CBM) has been investigated using first-principle calculation.[63, 64] The VBM consists of Pb 6s-I 5p* antibonding states and the CBM is a hybrid of Pb 6p-I 5p orbital with less antibonding

and more nonbonding (Figure 1-8b). The bandgap of perovskite materials can be easily tuned by replacing the B site metal and X site halide atom. The bandgap can be increased by replacing X site atom I with Br or Cl and decreased by replacing B site atom Pb with Sn. The A site cation does not directly affect the bandgap but influences the extent of metal-halide orbital overlap. Partially replace the large A site cation, such as FA, with small A site cation, such as Rb and Cs, induces octahedral tilting and increased bandgap. The adjustable bandgap has enabled the development of all perovskite tandem solar cell.[65]

1.4.2 Instability and Solutions of Perovskite Materials

While perovskite solar cells yield high PCEs, the stability of perovskites, including intrinsic phase stability, and external humidity, oxygen, temperature stabilities, has always been an issue that potentially hinders their industrialization.[66] The phase stability of perovskite materials can be generally predicted by the Goldschmidt Tolerance Factor (t_f).[67] The t_f of a three-dimensional ABX_3 perovskite is given by Eq 1-5.

$$t_f = \frac{r_A + r_X}{\sqrt{2}(r_B + r_X)} \qquad (1\text{-}5)$$

Where r_A, r_B, and r_X refer to the ionic radii of the monovalent cation, divalent group IV A metal, and halide anion, respectively. Ideal α-phase perovskites usually have t_f in between 0.9 to 1. When the t_f is close to or below 0.8, perovskite materials tend to form δ-phase photoinactive orthorhombic perovskite structure and when close to or higher than 1.0 form hexagonal non-perovskite structure. The common pure ABX_3 perovskites, such as $FAPbI_3$, $MAPbI_3$, and $CsPbI_3$ have the t_f of 0.987, 0.909, and 0.807, which are at the boundaries or out of the α-phase perovskite region. Therefore, mixed cation, mixed metal, and mixed halide perovskites have been developed to keep their t_f in the α-phase region.[68]

$MAPbI_3$ perovskite is a widely studied material and used in solar cells. When exposed to oxygen, the photoexcited electrons in $MAPbI_3$ reacts with molecular oxygen to form superoxide (O_2^-). Subsequently, the decomposition of perovskite is initiated by the reaction between superoxide and methylammonium cation, thus leading to the formation of PbI_2, iodine, and water molecule.[69] When exposed to moisture, $MAPbI_3$ perovskite forms hydrated perovskite phase, such as $MAPbI_3 \cdot H_2O$ and $(MA)_4PbI_6 \cdot 2H_2O$ and finally decomposes to PbI_2.[70, 71] In addition, the MA cation in the $MAPbI_3$ perovskite decompose to CH_3 and NH_3 at the temperature as low as 80 °C and has been experimentally confirmed.[72] Therefore, MA needs to be avoided when selecting perovskite materials for solar cell devices with long term intrinsic and external stability. FA as another organic cation has been applied as a replacement for MA to fabricate MA-free perovskite solar cells. $FAPbI_3$ has improved thermal stability over $MAPbI_3$ due to both the intrinsic chemical stability of FA cation and the hydrogen bonding between the hydrogen atoms in NH_3 group in FA cation and I anion.[73] However, $FAPbI_3$ also suffers from phase instability – it stays in photoactive α-phase at high temperature (130-150 °C) while transfers to the photoinactive δ-phase under room temperature in a few days.[74] To solve the moisture and phase instability problem, Cs^+ and Rb^+ cations are introduced into the $FAPbI_3$ to form $Cs_xFA_{1-x}PbI_3$,[75-81] $Rb_yFA_{1-y}PbI_3$,[82, 83] and $Rb_xCs_yFA_{1-x-y}PbI_3$ with improved phase and moisture stability.[84] Therefore, they are one of the most promising candidates in perovskite with high intrinsic and external stability.

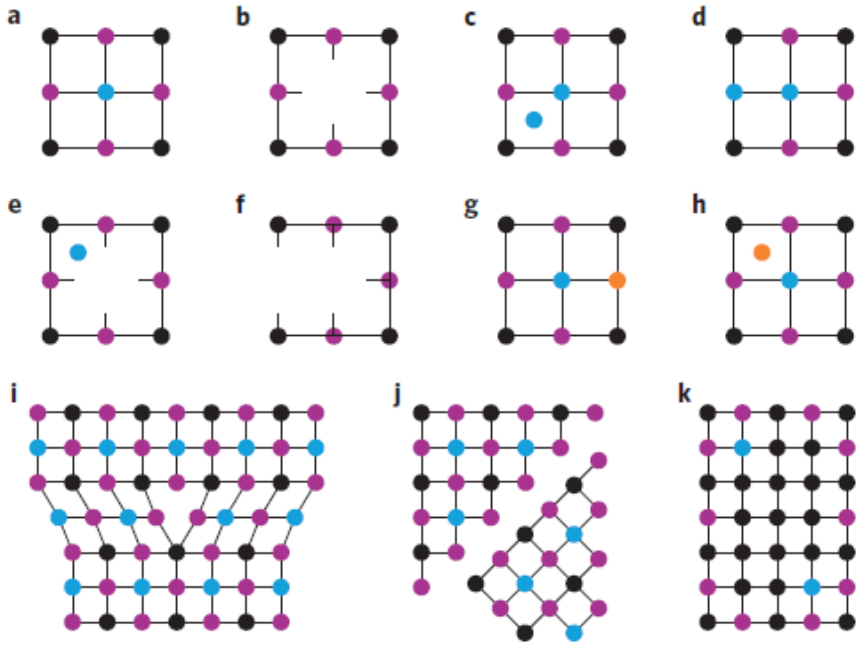

Figure 1-9 Possible defects in solution-processed perovskite crystal lattice (blue, black, and purple dots represent the A, B, and X site, respectively): (a) perfect lattice, (b) vacancy, (c) interstitial, (d) anti-site substitution, (e) Frenkel defect (interstitial and vacancy created from the same ion), (f) Schottky defect (anion and cation vacancies occurring together), (g) substitutional impurity, (h) interstitial impurity, (i) edge dislocation, (j) grain boundary, and (k) precipitate.[85]

The nature of perovskite materials is relatively soft ionic solids. As illustrated in **Figure 1-9**, different types of defects can be formed in perovskite materials. These defects strongly hinder the perovskite solar cell performance, mainly in two processes: charge carrier recombination and transport.[85] Non-radiative defect-mediated carrier recombination is of fundamental importance to the V_{OC}. Under illumination and open-circuit condition, electrons are photoexcited from the valence band into the conduction band, splitting the electron and hole quasi-Fermi levels, which is determined by the charge density at which the recombination rate equals the generation rate. When the defect state is localized within the semiconductor bandgap, it is likely that an approaching electron or hole will become captured or trapped by it, recombine non-radiatively,

and emit photons. Non-radiative recombination has a shorter lifetime than radiative decay, thus reduce the steady-state charge density level, the gap between the quasi-Fermi level, and V_{OC} of the device. Charge transport is also affected by defects. Under short-circuit condition, photoexcited charge carriers in the solar cell accelerate through the perovskite active layer under electric field until they interact with defects. Defects in perovskite are charged considering its ionic nature. Therefore, the charge carrier will be trapped in the defects through coulombic interaction, results in lower J_{SC}. In addition, defects in perovskite materials are reported to serves as the channel of the ion migration and mediate the operational degradation of the perovskite materials. To pave the path for the commercialization of perovskite solar cells, the intrinsic and operational stability issues need to be solved.

1.4.3 Single Junction Perovskite Solar Cells Structure Classification

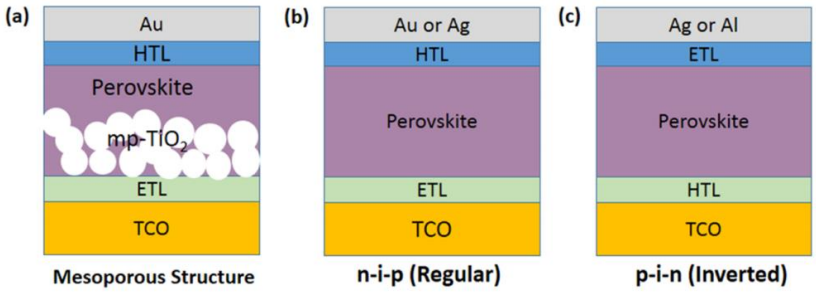

Figure 1-10 Perovskite solar cell devices in (a) mesoporous conventional, (b) planar conventional, and (c) planar inverted structure.[86]

To meet the requirements of flexible, solution-processable, and even printable solar cells, all the layers in the solar cells are required to be thin and can be processed under low temperature by solutions. Thin film types solar cells, including perovskite solar cells, are developed accordingly with the thickness of each layer less than 1 μm. Generally, perovskite solar cells are in either mesoporous structure or planar structure **(Fig. 1-10**a- c). The mesoporous structure refers

to the device with a mesoporous on the top of the ETL. In planar structure device, however, any pinhole in the perovskite layer thin film results in a shunt-path between the ETL and HTL resulting in low FF. In contrast, the mesoporous layer avoids direct contact between the ETL and HTL, which makes the mesoporous structure device more forgiving of thin film imperfection. Consequently, the processing window of the planar structure device becomes narrower than the mesoporous device. However, the planar device structure is more industrially preferable considering the complex fabrication process of the mesoporous layer. The perovskite solar cells can also be divided into another two categories, conventional and inverted structure. Conventional structure refers to the device with the transparent bottom electrode as the anode, ETL on the transparent electrode, HTL on the active layer thin film, and the top electrode serves as the cathode. In the inverted structure, the structure is simply inverted as illustrated in Fig. 1-10c. In the conventional structure, the ETL is usually made by metal oxide such as TiO_2 and SnO_2, which requires processing temperature as high as 300 °C and are not printable. In contrast, multiple low-temperature solution-processable and printable polymer materials, such as PEDOT:PSS, can be applied as the HTL in the inverted structure device. This thesis work mainly focuses on the thin film solar cell in the planar and inverted device structure.

1.5 Conducting Polymers

1.5.1 Background

Conducting polymers are organic materials that have similar optoelectronic properties to the inorganic conductor or semiconductor materials. While does not like the inorganic materials that require high energy-consuming process and sometimes consist rare elements, conducting polymers consist earth-abundant elements can be synthesized using simple, versatile, and cheap

approaches.[87] The conducting polymers have been applied to serve as different components in the optoelectronic devices, including charge carrier transport layer,[88] active layer,[45] and electrode.[89]

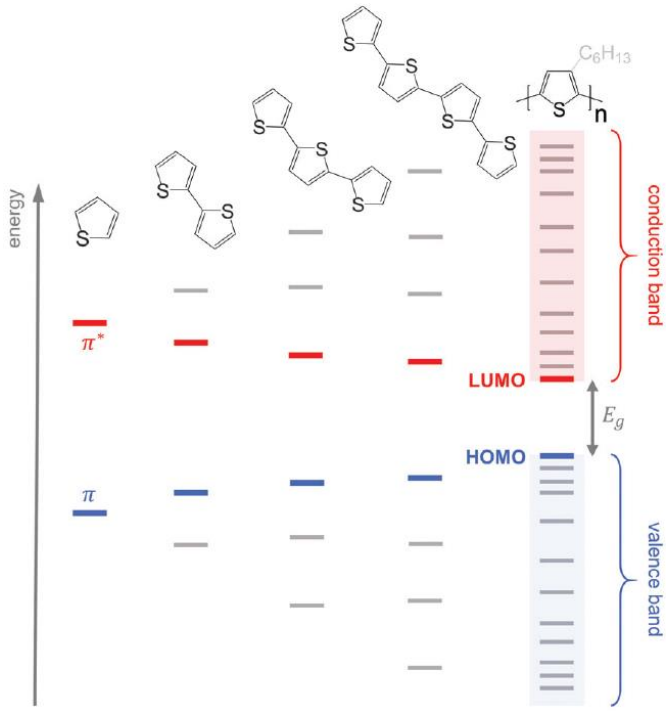

Figure 1-11 Evolution of HOMO, LUMO, and bandgap with an increasing number of thiophene repeat units.[90]

The optoelectronic properties of the conducting polymer come from their chemical structure and are well explained by the molecular orbital theory.[91] Take the conjugated thiophene as an example in **Figure 1-11**, a single thiophene molecule has two molecular orbitals: bonding molecular orbital (π) and antibonding molecular orbital (π*). Chemical coupling of the conjugated thiophene monomers into long polymer chains leads to orbital interaction and energy level splitting of the π and π* orbitals. The valences band was generated from the π orbitals and bordered by the highest occupied molecular orbital (HOMO). On the other hand, the π* orbitals form the conduction band, bordered by the lowest unoccupied molecular orbital (LUMO). The bandgap is correspondingly defined between the HOMO and LUMO. The optoelectronic properties of

conducting polymers can, therefore, be easily tuned by changing their chemical structures, including backbone, side chain, conjugating length, and doping level.

1.5.2 Conducting Polymer poly[(9,9-dioctylfluorenyl-2,7-diyl)-alt-co-(bithiophene)] (F8T2)

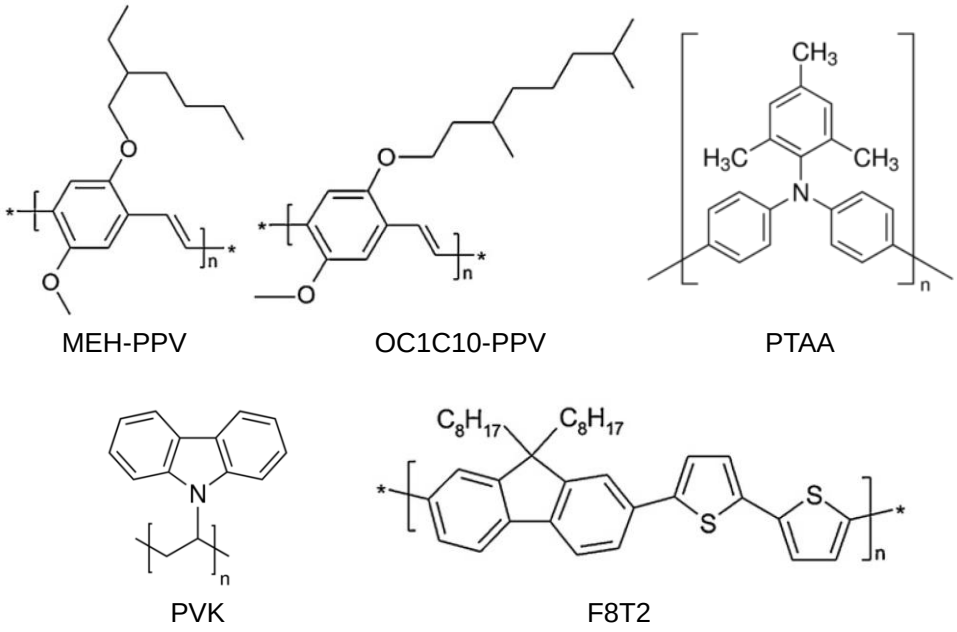

Figure 1-12 Chemical structure of common p-type wide bandgap conducting polymers

Wide bandgap conducting polymers are applied to build organic or organic-inorganic hybrid narrowband UV photodetectors to minimize the visible photoresponse. **Figure 1-12** and **Table 1-2** shows the chemical structure and electronic properties, respectively, of the commonly used p-type wide bandgap conducting polymers. Hole mobility is one of the most important parameters when selecting photodetector active layer, especially photomultiplication type photodetector. Because the holes need to be injected from the positively charged electrode, pass through the entire active layer, and reach the negatively charged electrode. Low hole mobility will significantly reduce the hole transport efficiency and therefore the sensitivity of the photodetector device. Polymer poly[(9,9-dioctylfluorenyl-2,7-diyl)-alt-co-(bithiophene)] (F8T2) has the

mobility of 0.01-0.02 cm^{-2}/v s, which is the highest among all the five conducting polymers listed in Table 1-2. F8T2 has been implemented in thin film transistors, and it was shown that the alignment, whether the polymer backbones are parallel or perpendicular to the lateral charge flow, significantly impacts hole mobility, which can be 6.5 times larger for parallel-oriented films.[92] F8T2 has also been blended with $PC_{61}BM$ and used in photodiode type photodetector with a ITO/F8T2:PC61BM/Au structure that showed good rectification and photocurrent density around 2 mA cm-2 under 460 nm illumination and a -1 V.[93] However, its potential on photomultiplication type photodetector has not been demonstrated yet considering its high hole mobility.

Table 1-2 Electronic properties of common wide-bandgap conducting polymers

Wide Bandgap Conducting Polymers	**Hole mobility (cm^{-2}/v s)**	**LUMO (eV)**	**HOMO (eV)**	**Eg (eV)**
MEH-PPV	1×10^{-4}-1×10^{-3}	-2.9	-5.3	2.4
OC1C10-PPV	1×10^{-6}	-3	-5.26	2.26
PTAA	1×10^{-4}-1×10^{-3}	-2	-5	3
PVK	1×10^{-5}	-2.2	-5.6	3.4
F8T2	0.01-0.02	-3.1	-5.5	2.4

1.5.3 Conducting Polymer Poly(3,4-ethylenedioxythiophene):polystyrene sulfonate (PEDOT:PSS)

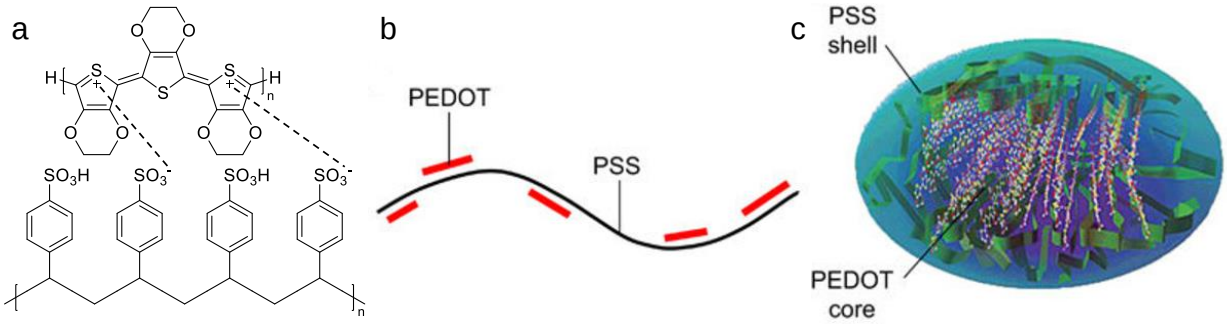

Figure 1-13 (a) Chemical structure, (b) secondary structure, (c) and trinary structure of PEDOT:PSS conducting polymer.[94]

Poly(3,4-ethylenedioxythiophene) (PEDOT) was developed and found to be an insoluble polymer by scientists at the Bayer AG research laboratories.[95] Later on, polystyrene sulfonate (PSS) was applied to serves as the charge-balancing dopant during the PEDOT polymerization process to yield water-dispersible Poly(3,4-ethylenedioxythiophene):polystyrene sulfonate (PEDOT:PSS).[96] As illustrated in Figure 1-13a, PEDOT:PSS consists of the positively charged hydrophobic conducting PEDOT and negatively charged hydrophilic PSS counterion. The secondary structure of PEDOT:PSS (Figure 1-13b) shows short PEDOT chains with 6-18 monomers are attached on long PSS chain with over 400 monomers. When dispersed in water, the hydrophobic PEDOT core is embedded in the hydrophilic PSS shell to make the entire polymer water dispersible (Figure 1-13c).[94]

PEDOT:PSS is broadly applied in optoelectronic devices because of its outstanding properties, such as high conductivity (over 4600 S/cm after post-treatment) and high transparency (>90% with 50 nm thickness). However, PEDOT:PSS based perovskite solar cells usually suffer from low V_{OC} and J_{SC}, therefore PCE, compared with metal oxide cells, and even p-type polymer

PTAA (**Figure 1-14**).[97] The reasons lay in the energy level mismatch, and lack of interfacial interaction with perovskite. Researchers have attempted to tune the work function of PEDOT:PSS by adding organic base or control the ratio between PEDOT and PSS,[98, 99] improve the conductivity while maintain the energy level alignment by adding polyethylene oxide,[100] improve the interfacial interaction by copolymerizing PEDOT with dopamine.[101, 102] These methods could solve individual problems well but cannot solve all the three stated problems simultaneously. Adding functional group onto the PEDOT could be a potential method to solve the three problems simultaneously and improve the perovskite solar cell performance.

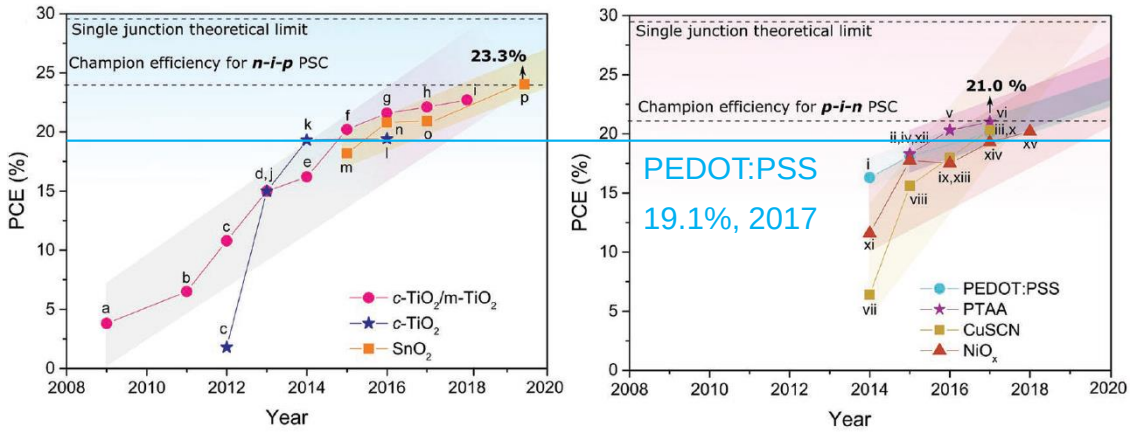

Figure 1-14 State of art performance of perovskite solar cells based on different device structures and charge extraction layers.[97]

1.6 Objectives and Goals

The goal of the work is to develop novel thin film type optoelectronic devices, including photodetectors and solar cells, by synthesizing or applying conducting polymer and perovskite materials. The objectives of this work include:

1. Apply wide bandgap materials: conducting polymer F8T2 and $CH_3NH_3PbCl_3$ perovskite to fabricate narrowband UV photodetector with high sensitivity under low driving voltage.
2. Synthesize and characterize solar cells based on MA-free perovskite materials, understand, and solve the instability issue.
3. Develop functionalized PEDOT:PSS conducting polymer as hole transport materials for further improvement of the optoelectronic device performance.

Chapter 2 SOLUTION-PROCESSED VISIBLE-BLIND UV-A PHOTODETECTORS BASED ON CH3NH3PbCl3 PEROVSKITE THIN FILMS

2.1 Introduction

Hybrid organic-inorganic perovskites have recently gained tremendous attention as they have enabled bright, widely tunable light-emitting diodes,[103, 104] photodetector with high detectivity,[57] as well as solar cells that have reached certified power conversion efficiency (PCE) to 22.1%.[62] The attractive optical and electronic properties of hybrid organic-inorganic perovskites include high light absorption coefficients,[53] direct band gaps,[52] long and balanced carrier diffusion lengths,[54] and high carrier mobilities.[55] The low temperature solution processibility enables low-cost, large-area fabrication to make flexible, lightweight devices.[105] The spectral response and the valence and conduction band positions of perovskites can be tuned via the choice of group IVa cation (Pb^{2+}, Sn^{2+}) and halide anion (I^-, Br^-, Cl^-).[106-110] The band gap of methylammonium lead-tin triiodide ($CH_3NH_3Sn_xPb_{1-x}I_3$) has been demonstrated to vary from 1.55 to 1.17 eV by varying x from 0 to 0.5 and 0.75, and then to 1.30 eV when x is further increased to 1.[106] The band gap of $CH_3NH_3PbX_3$ is increased from 1.55 eV for $CH_3NH_3PbI_3$ to 2.39 eV for $CH_3NH_3PbBr_3$ and to 3.17 eV for $CH_3NH_3PbCl_3$[107, 108] due to the stronger covalent interaction between halide anion and Pb^{2+} cation as the halide anion changes from I^- to Br^- and Cl^-.[109, 110]

Hybrid organic-inorganic perovskites have been applied to make photodetectors with the prototypes that are roughly divided into two sub-categories: vertically stacked photodiode-type detectors,[57, 111-116] and laterally structured phototransistor-type detectors.[117-124] While these

photodetectors utilized different polycrystalline thin film or nanowire perovskites as the light absorbing layer, all of them have demonstrated the detection of photons up to visible or near infrared wavelengths. The detection of ultraviolet (UV) light has a wide range of applications, such as chemical, environmental and biological analysis and monitoring, flame and radiation detection, astronomical studies, and optical communications. Development of UV photodetectors has drawn extensive attention.[8, 125] UV light is typically divided into four spectral regions from 400 to 10 nm: UV-A (400 to 320 nm), UV-B (320 to 280 nm), UV-C (280 to 200 nm), and far UV (200 to 10 nm).[8, 125] As visible light covers the range of wavelengths from 400 to 700 nm, UV photodetectors that have higher sensitivity to the radiation below 400 nm than above 400 nm are called 'visible-blind'. Methylammonium lead chloride ($CH_3NH_3PbCl_3$) as a wide-bandgap perovskite shows a high optical absorption coefficient in UV-A range (320 to 400 nm) while transparent to visible light,[107, 108] which makes it a promising candidate for visible-blind UV-A photodetectors.

Recently, a few UV photodetectors based on $CH_3NH_3PbCl_3$ perovskite have been reported. Maculan *et al*. applied inverse temperature crystallization method to grow bulk $CH_3NH_3PbCl_3$ single crystals and built the UV photodetectors by polishing the single crystals to the thickness of 350 μm, and coating 20 nm Pt on one side as the transparent anode and 25 nm Ti and 100 nm Au on the other side as the cathode. The device exhibits a responsivity of 46.9 mA/W and detectivity of 1.2×10^{10} Jones when illuminated by a 365 nm wavelength light with the intensity of 1 W/cm^2 and under a 15 V bias.[126] Fang *et al*. sandwiched a $CH_3NH_3PbCl_3$ single crystal about 1 mm thick, made by precipitating supersaturated precursor solution, between Ga and a thermally evaporated 20 nm Au electrode to build a photodetector device. The device exhibited narrow spectral response with a full-width at half-maximum (FWHM) of < 20 nm centered at around 420 nm. The narrow spectral band was achieved by surface-charge recombination-induced suppression of charge

collection for short-wavelength excitation. The external quantum efficiency (EQE) was low (0.2% ~ 1.6%) because of the low transparency of the 25 nm Au electrode and no other device performance data was reported.[46] Wang *et al.* reported phototransistor-type UV photodetectors by making $CH_3NH_3PbCl_3$ polycrystalline thin films on 50 nm thick, patterned Au electrodes with 5 μm gaps. The $CH_3NH_3PbCl_3$ polycrystalline thin films were fabricated by thermal evaporation of lead chloride ($PbCl_2$) thin layer followed by spin coating of methylammonium chloride (CH_3NH_3Cl) and annealing. The devices showed a responsivity of 7.56 A/W to 360 nm wavelength light with the intensity of 0.1 mW/cm^2 and under a 4 V bias.[127] Adinolfi *et al.* utilized a modified inverse temperature crystallization method to grow $CH_3NH_3PbCl_3$ single crystals that can cover the 5 μm gap between patterned ITO electrodes on glass to realize laterally structured phototransistor-type UV photodetectors. The devices demonstrated a very high responsivity of 18 A/W and detectivity of 10^{12} Jones under 385 nm wavelength light with 4 nW intensity under a 5 V bias.[128] As aforementioned, many studies have been reported on vertically stacked photodiode-type detectors based on solution-processed perovskite polycrystalline thin films in the visible light range,[57, 111-116] and demonstrated attractive device performance such as ultrahigh gain ~489 and high responsivity ~242 A/W,[111] high detectivity ~10^{14} Jones,[57] and low dark current density ~10^{-9} A/cm^2 under a -1 V reverse bias.[112] There is no report on UV photodetectors with the vertically stacked photodiode-type architecture using solution-processed $CH_3NH_3PbCl_3$ polycrystalline thin films, which could be partly due to the difficulty involved when fabricating high quality $CH_3NH_3PbCl_3$ polycrystalline thin films.[107, 108]

Here, we reported a two-step solution process, low-temperature solvent-vapor-assisted thermal annealing method to fabricate uniform, pinhole-free $CH_3NH_3PbCl_3$ thin films and its implication in UV photodetectors with a simple photodiode device structure of

ITO/$CH_3NH_3PbCl_3$/Poly (triaryl amine) (PTAA)/Al. The fabricated films exhibited high crystallinity with a cubic phase and a sharp absorption cutoff at the frontage of UV-A range (400 nm). The possible traps were investigated via the analysis of photoluminescence (PL) spectra of perovskite films prepared with different $PbCl_2$ precursor concentrations. Prototypical devices in photodiode structure based on trap-reduced $CH_3NH_3PbCl_3$ thin films were fabricated and showed a photoresponse in the 300-400 nm region and a high UV-visible rejection ratio up to 500. All the results demonstrated that low-temperature solution-processed $CH_3NH_3PbCl_3$ thin films could be a promising candidate for making flexible, lightweight visible-blind UV-A photodetectors.

2.2 Experimental Section

2.2.1 Methylammonium Chloride (CH_3NH_3Cl) Synthesis

CH_3NH_3Cl was synthesized by a modified procedure based on methods reported previously.[126] Specifically, 22 mL of methylamine (33 wt % in absolute ethanol, Sigma Aldrich) were charged with 100 mL ethanol (anhydrous, ≥ 99.5%, Sigma Aldrich) in a 250 mL round bottom flask. The solution was stirred in an ice bath under nitrogen protection. 12 mL of hydrochloride acid (37 wt % in water, Sigma Aldrich) were then added dropwise to the methylamine solution over 30 min. The resulting mixture was stirred under 0 °C for 2 h. The white precipitate was recovered by rotary evaporation at 40 °C, then dissolved in ethanol followed by sedimentation in diethyl ether (anhydrous, Fisher Scientific) by stirring the solution for 30 min. The mixture was then washed three times with diethyl ether. The precipitated solid was collected and dried under 50 °C in a vacuum oven for 24 h.

2.2.2 $CH_3NH_3PbCl_3$ Film Fabrication

2.2.2.1 Two-step spin coating

To fabricate $CH_3NH_3PbCl_3$ thin films, lead chloride ($PbCl_2$, 99.999%, Sigma Aldrich) and synthesized CH_3NH_3Cl were dissolved in dimethyl sulfoxide (DMSO, anhydrous, ≥99.9%, Sigma Aldrich) and 2-propanol (anhydrous, 99.5%, Sigma Aldrich) to form 350 mg/mL and 20 mg/mL solutions, respectively, under 70 °C in a nitrogen filled glovebox. CH_3NH_3Cl solution was filtered through a 0.2 μm PTFE filter before use. Substrates (plain glass or ITO coated glass with sheet resistance = 10 Ω sq^{-1}, Colorado Concept Coatings LLC) were first cut into 15 mm × 15 mm pieces, then cleaned sequentially by sonication in soapy millipore deionized water, millipore deionized water, acetone, and isopropanol each for 15 min and then treated with oxygen plasma for 10 min and transferred into glovebox. A drop of 70 μL $PbCl_2$ solution was first spin coated onto a substrate at 6000 rpm for 30 s and annealed at 70 °C for 10 min. A drop of 70 μL of CH_3NH_3Cl solution was then quickly spin coated onto the $PbCl_2$ film at 4000 rpm for 30 s and annealed at 70 °C for 30 min. For thermal-only annealing, the substrates were transferred onto a hotplate at 100 °C and annealed for 1 h. For solvent-assisted thermal annealing, the substrates were transferred onto a hotplate at 100 °C and covered by a glass petri dish. A drop of 10 μL DMSO was added onto the hotplate inside petri dish and annealed for 1 h. $CH_3NH_3PbCl_3$ thin films were also made with the $PbCl_2$ concentrations of 250, 300, and 450 mg/mL to vary the ratio of $PbCl_2$ to CH_3NH_3Cl.

2.2.2.2 One-step spin coating

Equal mole CH_3NH_3Cl and $PbCl_2$ were dissolved in DMSO-DMF (1:1 by volume) to get a 1 M $CH_3NH_3PbCl_3$ precursor solution. The precursor was stirred for 12 h at 70 °C and filtered by a 0.2 μm PTFE filter. 100 μL of precursor was added onto a 15 mm × 15 mm substrate and spin coated at 4000 rpm for 60 s. For thermal annealing, substrates were heated on a hotplate at 70 °C

for 60 min. For DMSO-vapor-assisted thermal annealing, substrates were first heated on a hotplate at 70 °C for 60 min. Then the substrates were covered with a glass petri dish on the hotplate, 10 μL of DMSO was added from the edge of the petri dish and heated at 70 °C for 60 min.

2.2.2.3 Nano-pinning

Precursor solution was prepared as described above. 100 μL of precursor solution was added onto a 15 mm × 15 mm substrate. Nano-pinning method was performed as reported previously with slight modification. [54] Two spin speeds were applied to perform nano-pinning: 500 rpm for 10 s and then 3000 rpm for 90 s. When 70 s passed, 100 μL of toluene or chloroform was added on the substrate in less than 2 s. For thermal annealing, substrates were heated on a hotplate at 70 °C for 10 min. For DMSO-vapor-assisted thermal annealing, substrates were first heated on a hotplate at 70 °C for 10 min. Then the substrates were covered with a glass petri dish on the hotplate, 10 μL of DMSO was added from the edge of the petri dish and heated at 70 °C for 60 min.

2.2.3 Film Characterization

Scanning electron microscopy (SEM) measurements were carried out on an FEI Sirion SEM to investigate the surface morphology of the thin films. Two-dimensional X-ray diffraction (XRD) measurements were performed on a Bruker GADDS D8 Discover diffractometer using Cu Kα radiation ($\lambda = 1.5419$ Å) to study the crystalline structures of the precursor and perovskite films. Data was processed using the EVA package provided by Bruker Axs. UV-Vis absorption and photoluminescence (PL) spectra of perovskite thin films were collected via a Varian Cary 5000 UV-Vis-NIR spectrophotometer and a Horiba Fluorolog 3 Spectrofluorometer, respectively. Film thicknesses were measured using a KLA Tencor Alpha-Step 500 Profiler.

2.2.4 Device Fabrication

The $CH_3NH_3PbCl_3$ films on ITO coated glass substrates were fabricated as described above. After the substrates were cooled down to room temperature, a drop of 70 μL of 10 mg/mL Poly (triaryl amine) (PTAA, MW = 15-25 KDa, Solaris Chem Inc.) toluene solution was spin coated onto a $CH_3NH_3PbCl_3$ thin film at 3000 rpm for 30 s, followed by annealing at 100 °C for 10 min. Devices were finished by thermal deposition of 100 nm aluminum layer at the rate of 0.2 nm/s in a background vacuum less than 2×10^{-6} Torr. The resulting devices have a structure of ITO/$CH_3NH_3PbCl_3$/PTAA/Al. The working area of devices for monochromatic illumination and EQE measurements is 0.057 cm^2, and for the illumination by solar simulator is 0.1 cm^2.

2.2.5 Device Characterization

The devices were characterized under dynamic vacuum in a custom built vacuum chamber fitted with electrical leads. White light from a 75 W xenon arc lamp (Newport Co., Oriel PhotoMax) was filtered by a grating monochromator (Acton Research Co., SpectraPro-2150i) to achieve a bandpass of ~3 nm (FWHM) for the incident CW probe light. The current density-voltage (J-V) characteristics under dark and 360 nm illumination with the intensity of 0.267 mW/cm^2 were recorded using a Keithley 2400 with a scan step of 10 mV from +1 V to -1 V and current values were averaged from 10 points under each bias with a delay time of 10 ms. The external quantum efficiency (EQE) was recorded with a wavelength step of 2 nm/s and current values were averaged from 20 points with a delay time of 10 ms. The J-V characteristics were also measured by a Keithley 2400 under AM 1.5 G of simulated solar light with an illuminated intensity of 100 mW/cm^2 calibrated by employing a standard Si photodiode detector equipped with KG-5 filter. The devices were scanned from +1 V to -1 V with voltage step and time interval of 4 mV and 10 ms, respectively.

2.3 Results and Discussion

2.3.1 Fabrication, Characterization, and Optimization of $CH_3NH_3PbCl_3$ Thin Films

Perovskites thin films have been typically made via one-step or two-step solution processes. One-step solution process was firstly applied to fabricate perovskite thin films by spin coating a solution containing all precursors followed by thermal annealing. While non-continuous perovskite films were frequently observed using lead iodide (PbI_2) and methyl ammonium halide (CH_3NH_3X) blend solutions, which might be related to the interaction of perovskite with a substrate surface,[129, 130] it may also be due to the low viscosity of the perovskite solution and the quick crystallization of the mixed precursor upon drying the spun films.[131] Nano-pinning method were then developed based on the one-step spin coating technique by introducing toluene or chloroform during spin coating to wash out "good" solvent such as DMSO. The $CH_3NH_3PbBr_3$ thin films made with the nano-pinning method exhibited flat and uniform morphologies.[132] Two-step solution spin coating method, also known as an interdiffusion method, has been further developed to form continuous, compact iodine perovskite films for solar cell applications.[105] By spin coating precursor stacking layers of PbI_2 and methylammonium iodide (CH_3NH_3I), methylammonium cations diffuse into the PbI_2 layer to form perovskites during thermal annealing. Later on, it was reported that a solvent-vapor-assisted thermal annealing can effectively increase the perovskite grain size and crystallinity, resulting in a significant improvement in material electronic properties and a great enhancement in photovoltaic device performance.[133, 134]

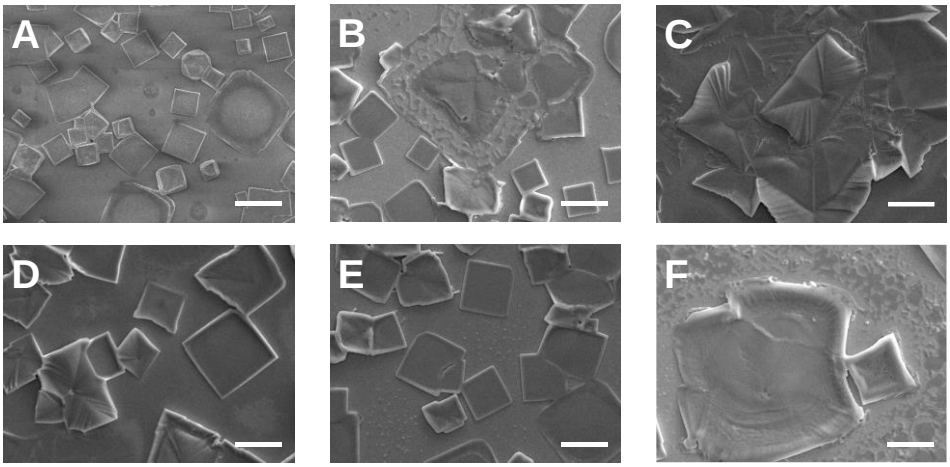

Figure 2-1 SEM images of $CH_3NH_3PbCl_3$ thin film fabricated via (A) one-step spin coating with thermal annealing, (B) one-step spin coating with DMSO-vapor-assisted thermal annealing, (C) nano-pinning with chloroform followed by thermal annealing, (D) nano-pinning with toluene followed by thermal annealing, (E) nano-pinning with chloroform followed by DMSO-vapor-assisted thermal annealing and (F) nano-pinning with toluene followed by DMSO-vapor-assisted thermal annealing. Scale bar: 10 μm.

We fabricated $CH_3NH_3PbCl_3$ thin films using both one-step and two-step solution process methods. We used different one-step solution process methods, including one-step spin coating followed by thermal annealing and solvent-vapor-assisted thermal annealing, and one-step spin coating with nano-pinning followed by thermal annealing and solvent-vapor-assisted annealing. All films exhibited rough, nonuniform surfaces with many large size cuboids as shown in **Figure 2-1**. We further applied the two-step solution process method followed by thermal annealing and solvent-vapor-assisted thermal annealing under different temperatures to fabricate $CH_3NH_3PbCl_3$ thin films as illustrated in **Figure 2-2**. A $PbCl_2$ DMSO solution with the concentration of 350 mg/mL was spin coated onto cleaned ITO-coated glass substrates followed by thermal annealing at 70 °C for 10 min. Three tiny dull peaks at 19.6°, 22.86°, and 23.34° exhibited in the XRD pattern

of the $PbCl_2$ thin film (**Figure 2-3**) match the standard orthorhombic $PbCl_2$ pattern (PDF#74-1803). The weak crystallinity could be attributed to the strong coordination between Pb in $PbCl_2$ and O in DMSO.[135]

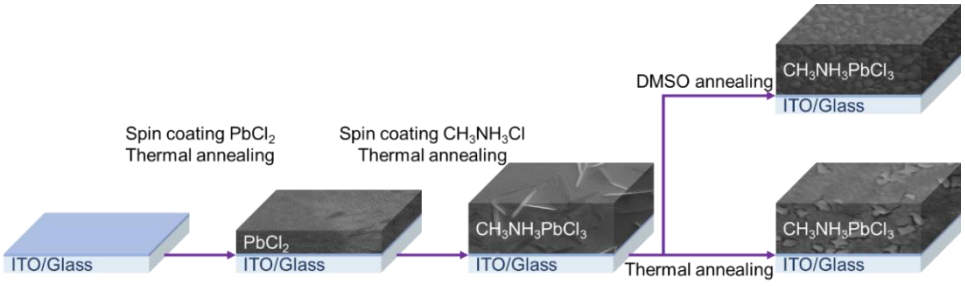

Figure 2-2 Schematic illustration of two-step solution process method for making $CH_3NH_3PbCl_3$ thin films.

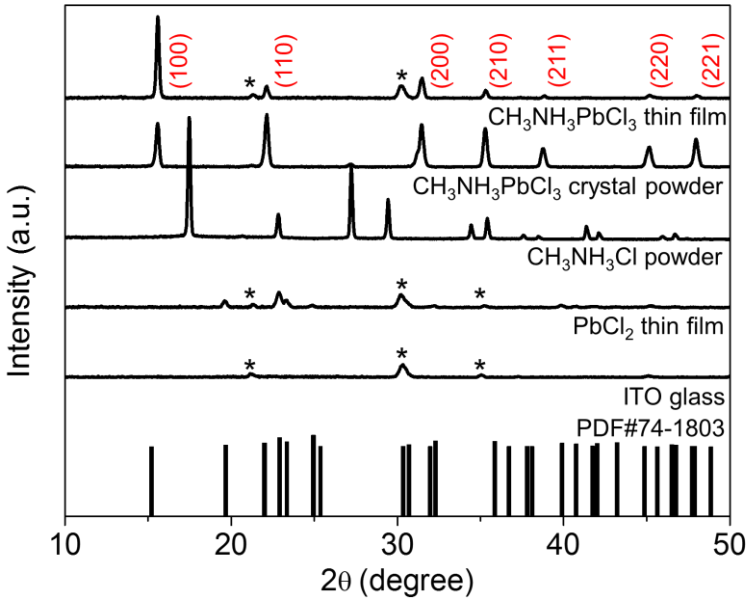

Figure 2-3 XRD patterns of $CH_3NH_3PbCl_3$ thin film on ITO glass, $CH_3NH_3PbCl_3$ crystal powder on glass, CH_3NH_3Cl powder on glass, $PbCl_2$ thin film on ITO glass, ITO glass, and the standard XRD pattern of orthorhombic $PbCl_2$.

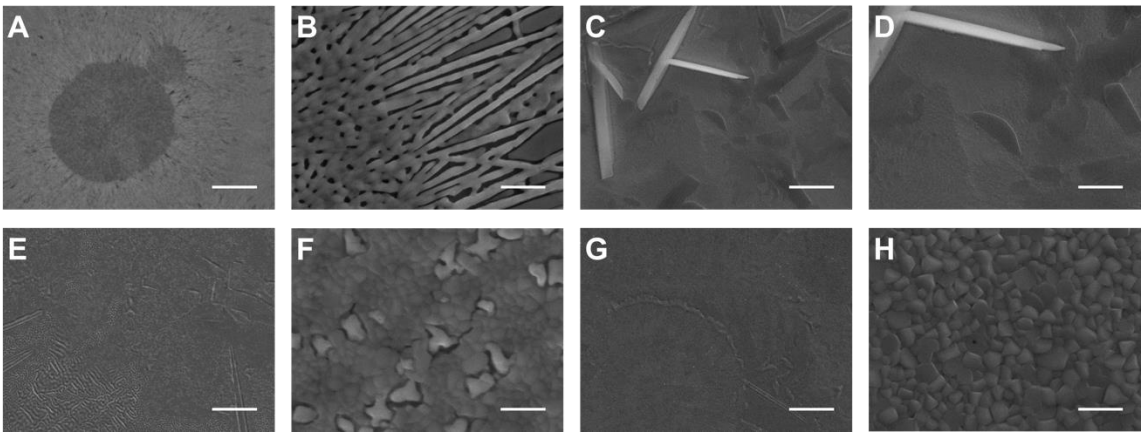

Figure 2-4 (A, B) Top-view SEM images of the $PbCl_2$ thin film annealed at 70 °C for 10 min. (C, D) Top-view SEM images of the $CH_3NH_3PbCl_3$ thin film annealed at 70 °C for 30 min after spin coating CH_3NH_3Cl. (E-H) Top-view SEM images of the final $CH_3NH_3PbCl_3$ thin films after further annealed (E, F) at 100 °C for 1 h and (G, H) DMSO-vapor-assisted thermal annealing at 100 °C for 1 h. Scale bars are 10 μm for A, C, E and G, 5 μm for D and 500 nm for B, F, and H.

SEM images of the $PbCl_2$ film (**Figures 2-4**A and B) show densely packed short and long lines with bright contrast and regions with dark contrast. Note that the $PbCl_2$ thin film made in this work exhibited sharper and higher XRD peaks than those of the $PbCl_2$ film fabricated via thermal evaporation.[127] The relatively better crystallinity of our $PbCl_2$ thin films might be the reason that a "harsh" annealing condition was required to fabricate $CH_3NH_3PbCl_3$ thin films as described below compared to the annealing condition (60 °C for 30 min) reported previously.[127] The purity of the synthesized CH_3NH_3Cl powder was verified by the XRD pattern shown in Figure 2-3, which is consistent with literature XRD patterns.[136] A CH_3NH_3Cl 2-propanol solution with the concentration of 20 mg/mL was then coated onto the $PbCl_2$ layers and annealed at 70 °C for 30 min to facilitate interdiffusion. As shown in Figures 2-4C and D, the morphology of the film after the interdiffusion annealing (70 °C for 30 min) showed needle-like, bright ridges. The bright ridges could be attributed to CH_3NH_3Cl, which has a low solubility in 2-propanol and is easily

precipitated during the spin coating process. When DMSO-vapor-assisted thermal annealing was introduced at 70 °C for 1 h after the interdiffusion annealing, the needle-like ridges became less bright and sharp (**Figures 2-5**A and B). Such changes indicated the improved conductivity of the ridges, the facilitated interdiffusion, and the more complete conversion from CH_3NH_3Cl to $CH_3NH_3PbCl_3$ during this additional DMSO-vapor-assisted thermal annealing. We further increased the temperature of the additional annealing to 100 °C after the interdiffusion annealing for 1h. The low magnification SEM image of this thermally annealed film (Figure 2-4E) showed that the continuous film was embedded with many white spots surrounded by cracks. The high magnification SEM image (Figure 2-4F) clearly showed that the white spots appeared as isolated grains with irregular grain boundaries and gaps, and relatively bright contrast compared to the adjacent grains. The rest of the film was packed with dense, smooth grains with blurry grain boundaries in the size of ~50-200 nm. Another film was annealed at 100 °C with DMSO vapor for 1 h after the interdiffusion annealing. The $CH_3NH_3PbCl_3$ thin film prepared via the DMSO-vapor-assisted thermal annealing exhibited densely packed ~100-400 nm grains with smooth and uniform morphology and clear grain boundaries as shown in both low and high magnification SEM images (Figures 2-4G and H). The quality of $CH_3NH_3PbCl_3$ thin films was found to be sensitive to the temperature of both the $PbCl_2$ annealing and the interdiffusion annealing when the final DMSO-vapor-assisted thermal annealing condition was kept the same as shown in Figures 2-5C-F. The higher annealing temperature for $PbCl_2$ resulted in better crystallinity of the $PbCl_2$ film (**Figures 2-6**A and B), causing a worse morphology of the $CH_3NH_3PbCl_3$ film with broken polycrystalline domains (Figures 2-5E and F). The best $CH_3NH_3PbCl_3$ thin film was prepared with the $PbCl_2$ annealing at 70 °C for 10 min, the interdiffusion annealing at 70 °C for 30 min, and the DMSO-

vapor-assisted thermal annealing at 100 °C for 1 h as shown in Figures 3.3G and H. This condition was used to prepare $CH_3NH_3PbCl_3$ thin films in the rest of this study.

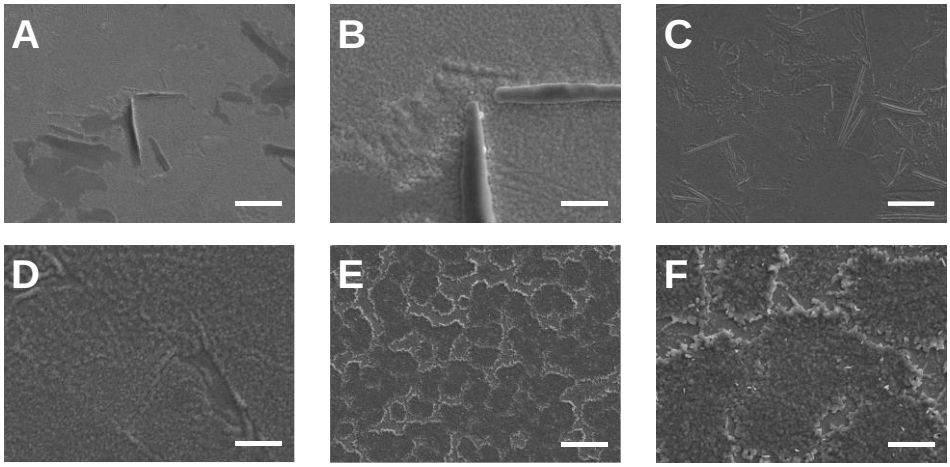

Figure 2-5 SEM images of $CH_3NH_3PbCl_3$ thin films made by two-step spin coating under different annealing conditions for each layer. $PbCl_2$ layer was annealed at X °C for 10 min. After spin coating CH_3NH_3Cl, the substrates were annealed at Y °C for 30 min. For DMSO-vapor-assisted thermal annealing, the substrates were annealed at Z °C for 1 h. The values of X, Y, and Z were (A, B) 70, 70 and 70; (C, D) 70, 100 and 100; and (E, F) 100, 100 and 100. Scale bars are 20 μm for A, C, E, and 5 μm for B, D, F.

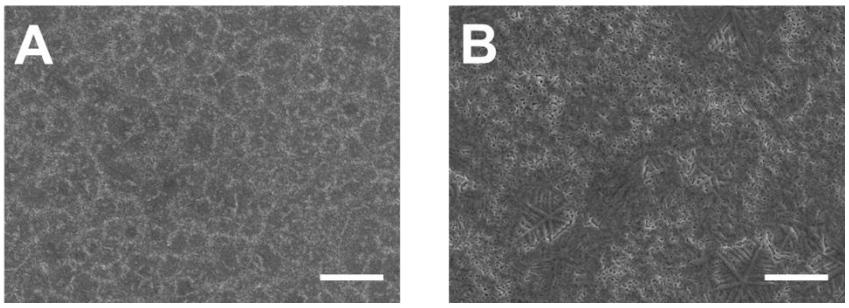

Figure 2-6 SEM images of $PbCl_2$ thin film annealed at 100 °C for 10 min. Scale bars are 20 μm and 5 μm for A and B, respectively.

The XRD pattern of the $CH_3NH_3PbCl_3$ thin film made by DMSO-vapor-assisted thermal annealing (Figure 2-3) showed high purity revealed by the absence of peaks originating from the CH_3NH_3Cl and $PbCl_2$ phases. We also synthesized bulk $CH_3NH_3PbCl_3$ single crystals (6 × 6 × 2 mm, **Figure 2-7**) using a modified inverse temperature crystallization method.[126, 137] The XRD pattern of the powder of synthesized single crystals is also shown in Figure 2-3. All the peaks in the XRD pattern of $CH_3NH_3PbCl_3$ thin film can be found in that of the powder of single crystals. Unlike that each peak (100, 110, 200, 210, 211, 220, and 221) has the similar intensities in the single crystalline powder XRD pattern, only the peaks at 15.58° (100) and 31.5° (200) dominate in the thin film XRD pattern, indicating that the grains are orientated with the 100 facets parallel to the substrate surface. This agrees well with the flat morphology shown in the SEM images (Figures 3.3G and H). Strong (100) and (200) peaks were also observed in the XRD pattern of the $CH_3NH_3PbCl_3$ thin films fabricated by the interdiffusion method even though the $PbCl_2$ layer was thermally deposited.[127] The $CH_3NH_3PbCl_3$ thin film with 100 orientated grains could benefit carrier transport and improve vertically structured device performance.

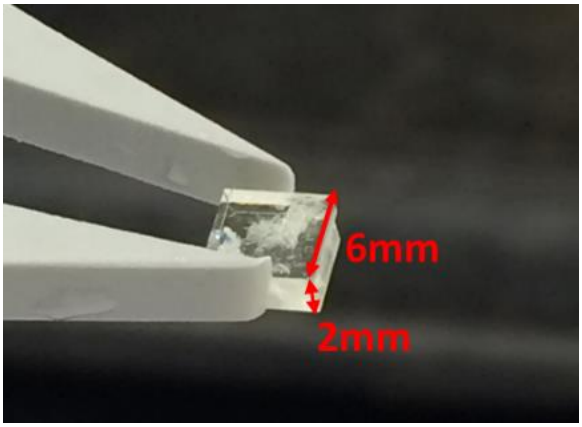

Figure 2-7 Photograph of $CH_3NH_3PbCl_3$ bulk crystal grown via modified inverse temperature crystallization method.

The different morphologies resulted from two annealing processes suggest that thermal annealing under the saturated DMSO vapor environment could facilitate the breaking and reforming of the Pb-Cl bond mediated via DMSO and eventually form the $CH_3NH_3PbCl_3$ thin films with 100 facets dominated larger grains with clear boundaries.[134] Under the super saturation condition, created by adding a DMSO drop too close to the substrate, the thin film went through a more complete recrystallization process resulting in 100-500 nm cubic crystals with identical 100 facets (**Figure 2-8**).

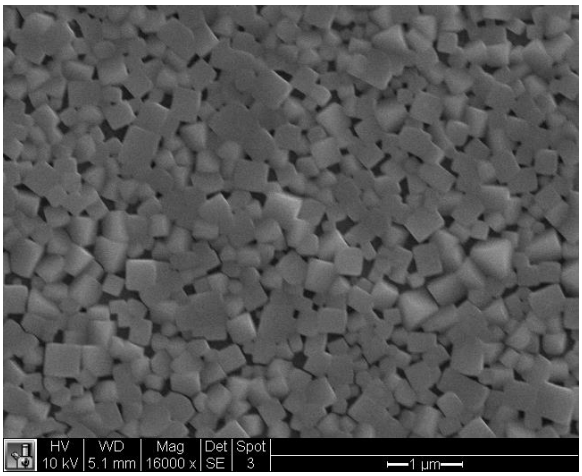

Figure 2-8 SEM image of the $CH_3NH_3PbCl_3$ thin film fabricated with DMSO-vapor-assisted thermal annealing method when the DMSO droplet was too close to the sample.

Molar ratio of two precursors used in the two-step spin coating method is a critical parameter that affects, not only the thickness, but most importantly, the optical and electronic properties of the resulting perovskite thin films, and thus device performance.[138] Therefore, we varied the molar ratio of $PbCl_2$ to CH_3NH_3Cl by changing the concentration of $PbCl_2$ (250, 300, 350 and 400 mg/mL) while maintaining the same CH_3NH_3Cl concentration (20 mg/mL), corresponding to the molar ratios of $PbCl_2$ to CH_3NH_3Cl as 3.03, 3.64, 4.25, and 4.86, respectively. $CH_3NH_3PbCl_3$ perovskite thin films were prepared with these molar ratios using DMSO-vapor-

assisted thermal annealing. The average film thicknesses are 97.2, 142.6, 169.3 and 207.4 nm for the $PbCl_2$ concentrations of 250, 300, 350 and 400 mg/mL, respectively. Absorption and steady-state photoluminescence (PL) spectra were acquired from freshly fabricated $CH_3NH_3PbCl_3$ films. As shown in **Figure 2-9**, all the four films exhibit a clear absorption cutoff around 405 nm with both excitonic peak and an extended absorption edge representing the continuum of valence-to-conduction band electronic excitations, similar to the reported polycrystalline $CH_3NH_3PbCl_3$ thin films absorption spectra.[107, 108, 127] The optical band gaps were estimated from the Tauc plots for four films and all are around 3.06 eV (Figure 2-9), close to the previously reported optical band gap of 2.97 eV[107] and ultraviolet photoemission spectroscopy (UPS) determined band gap of 3.17 eV.[108] The strong excitonic peak at band edge was attributed to the more pronounced ionic character in Cl-based perovskites, which leads to a higher exciton binding energy.[108, 127] No excitonic peak was displayed in the $CH_3NH_3PbCl_3$ single crystals and the absorption cutoff was around 430 nm, resulting in an optical band gap of 2.88 eV.[126] As reported previously, lower trap densities, due to higher dimensional structurally coherent units that are tight in the single crystal compared to their polycrystalline counterparts, result in the narrower band gap and the elimination of excitonic peak.[139, 140]

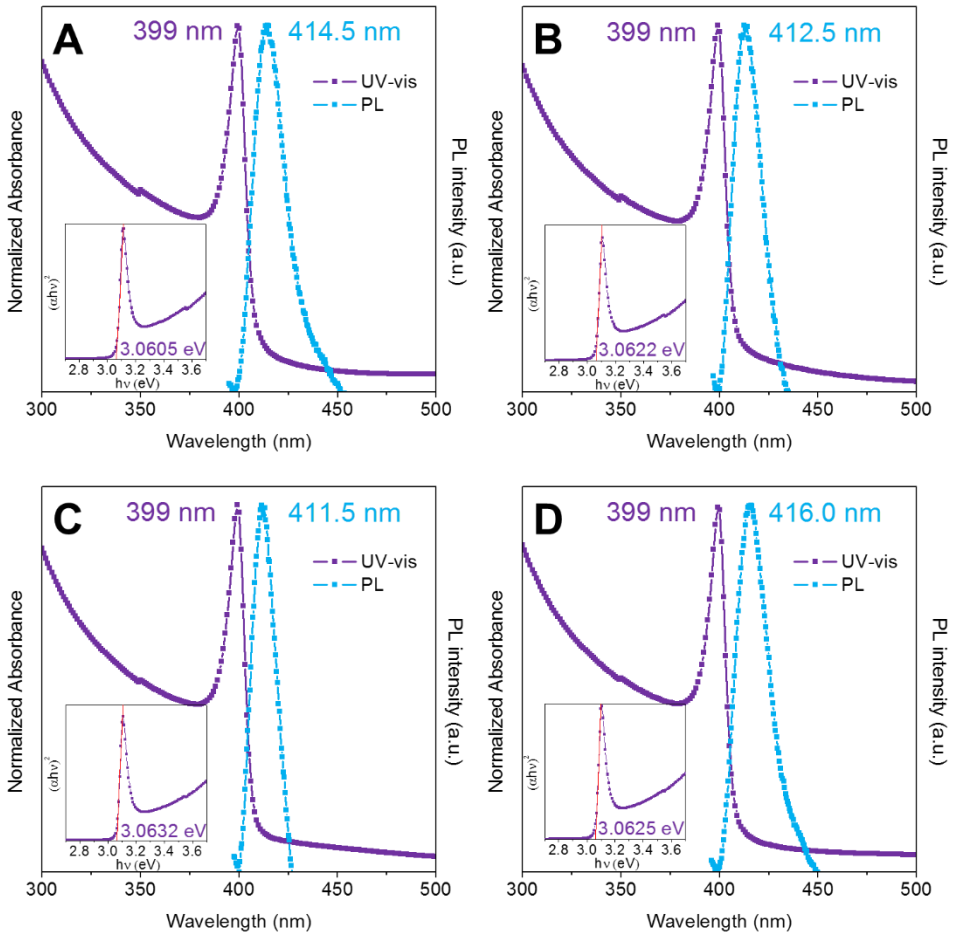

Figure 2-9 Steady-state photoluminescence and absorption spectra of $CH_3NH_3PbCl_3$ thin films fabricated with the $PbCl_2$ DMSO solutions with the concentrations of (A) 250 mg/mL, (B) 300 mg/mL, (C) 350 mg/mL, and (D) 400 mg/mL. The excitation light wavelength is 350 nm. Inset: The optical band gap calculated using the Tauc method.

The steady-state PL spectra of the four $CH_3NH_3PbCl_3$ thin films, however, show the shift of emission peaks and different tail lengths. The PL peak blue-shifted from 414.5 nm to 412.5 nm to 411.5 nm when the $PbCl_2$ concentration was increased from 250 mg/mL to 300 mg/mL to 350 mg/mL. Further increasing the $PbCl_2$ concentration to 400 mg/mL red-shifted the PL peak to 416 nm. A clear PL tail extension to 450 nm is shown in Figure 2-9A for the $CH_3NH_3PbCl_3$ thin film made with 250 mg/mL $PbCl_2$ concentration. With the increase of $PbCl_2$ concentration to 300

mg/mL, the tail was shortened to 430 nm and almost eliminated the tail for the film made with 350 mg/mL $PbCl_2$. The tail extended back to 450 nm when the $PbCl_2$ concentration was increased to 400 mg/mL. Both PL peak shift and tail length change follow the same trend with the concentration of $PbCl_2$. The $CH_3NH_3PbCl_3$ thin film made with the $PbCl_2$ concentration of 350 mg/mL exhibits the shortest wavelength of PL peak and almost no tail following the PL peak, indicating that the film has much less trap states than films made with other $PbCl_2$ concentrations. The formation of trap states in $CH_3NH_3PbI_3$ has been investigated computationally[141-144] and experimentally.[111, 145, 146] Elemental defects derived from Frenkel defects, such as Pb, I, and CH_3NH_3 vacancies, form shallow levels near band edges, which play the role of unintentional doping sources.[141] By investigating the trap states that could be formed by all possible intrinsic point defects in $CH_3NH_3PbI_3$, it was found that Pb vacancies can pull up the valence band and Pb interstitials can pull down the conduction band, which would finally result in a narrower band gap.[142-144] Experimental results showed hole traps at the surface of $CH_3NH_3PbI_3$ thin films and excitonic traps below the optical gaps in these materials, which are likely caused by electron-phonon coupling, especially at surfaces/interfaces of crystalline perovskites.[145] The electron paramagnetic resonance (EPR) studies also showed that in perovskites organic cations that deprotonate from their oxidized state, Pb^{2+} cations as Pb^{3+} centers trap holes while Pb^{2+} cation clusters trap electrons.[146] Pb^{2+} cations were purposely created at the top surface of perovskite films in making vertically stacked photodiode-type photodetectors to achieve high gain through trap-induced photomultiplication.[111] With $PbCl_2$ concentrations 250, 300, or 400 mg/mL, the $CH_3NH_3PbCl_3$ thin films could have more trap states formed either at surfaces, grain boundaries, or inside grains, leading to red-shift of PL peaks and extended tails. The PL results showed that the $CH_3NH_3PbCl_3$ perovskite thin films

fabricated with 350 mg/mL $PbCl_2$ and 20 mg/mL CH_3NH_3Cl had less trap states, providing a control material system to make UV photodetectors.

2.3.2 UV Photodetector Based on $CH_3NH_3PbCl_3$ Thin Films

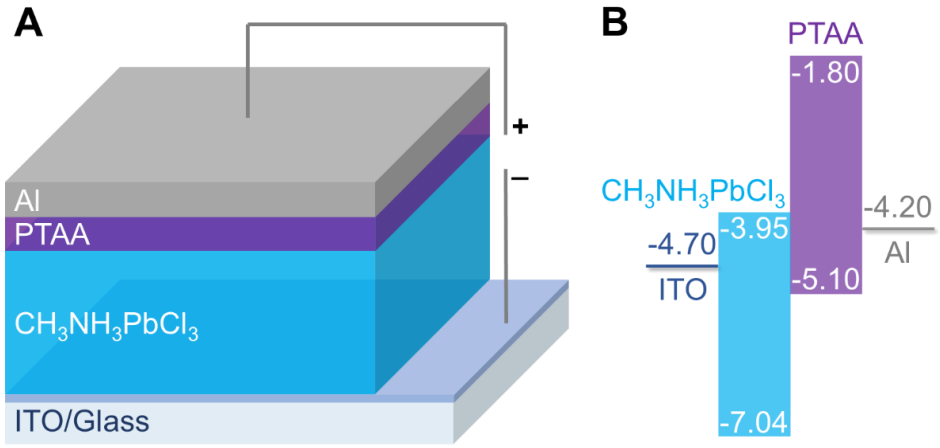

Figure 2-10 (A) Device structure and (B) energy diagram of prototypical visible-blind UV-A photodetector. Energy levels of CH3NH3PbCl3 were obtained from polycrystalline thin film.[107]

Motivated by the excellent optical properties of trap-reduced $CH_3NH_3PbCl_3$ thin films, we fabricated prototypical visible-blind UV-A photodetectors with the structure of ITO/$CH_3NH_3PbCl_3$/PTAA/Al (**Figure 2-10**A), where ITO serves as cathode, $CH_3NH_3PbCl_3$ thin film (~170 nm) works as the active layer, a visible-blind organic semiconductor PTAA (~35 nm formed by spin coating 10 mg/mL PTAA in toluene) with the band gap of 3.3 eV functions as hole transport/electron blocking layer, and Al (100 nm) serves as anode. The energy diagram of the device is shown in Figure 2-10B. The valence and conduction energy levels of $CH_3NH_3PbCl_3$ displayed in Figure 2-10B were adopted from the previous studies determined from $CH_3NH_3PbCl_3$ polycrystalline thin films since polycrystalline thin films were used in our devices and our optical band gap is close to the values reported.[107] Because of the large energy barrier of 2.34 eV between the work function of ITO (-4.70 eV) and the valence band (VB) edge of $CH_3NH_3PbCl_3$ (-7.04 eV),

holes would be difficult to inject from ITO cathode to $CH_3NH_3PbCl_3$ under reverse bias. A hole blocking layer can be eliminated. By inserting a PTAA layer between Al anode and $CH_3NH_3PbCl_3$ active layer, it can effectively prevent the electron injection from Al anode to PTAA due to the large energy barrier of 2.40 eV between the work function of Al (-4.20 eV) and the lowest unoccupied molecular orbital (LUMO) of PTAA (-1.80 eV). Therefore, a low dark current was expected. As shown in **Figure 2-11**, the device exhibited a dark current density as low as 1.60×10^{-5} mA/cm^2 under -1 V reverse bias. The dark current density under the same reverse bias is typically in the range of 1×10^{-3} to 2×10^{-6} mA/cm^2 for the previously reported photodiode-type photodetectors based on $CH_3NH_3PbI_3$ with hole/electron blocking layers on each side of the active layer or even double hole or electron blocking layers.[57, 111-114] The low dark current exhibited by our device indicated the good coverage of PTAA, which effectively reduced the electron injection from Al into the high carry mobility perovskite layer under reverse bias. It also demonstrated the high quality of our $CH_3NH_3PbCl_3$ thin films since poor quality films could induce dark current leakage due to the much lower barrier (0.40 eV) for hole injection from ITO to PTAA under reverse bias. The J-V characteristics measured under the illumination of 360 nm monochromatic light with the intensity of 0.267 mW/cm^2 is also shown in Fig. 2-11, exhibiting a photovoltaic feature with the open circuit voltage (V_{OC}) of 0.92 V. The light current density is 1.41×10^{-2} mA/cm^2 under zero bias, which is about five orders of magnitude higher than the dark current density under the same bias and leads to a photocurrent to dark current ratio, or ON-OFF ratio, to be ~9840 under 0 V bias.

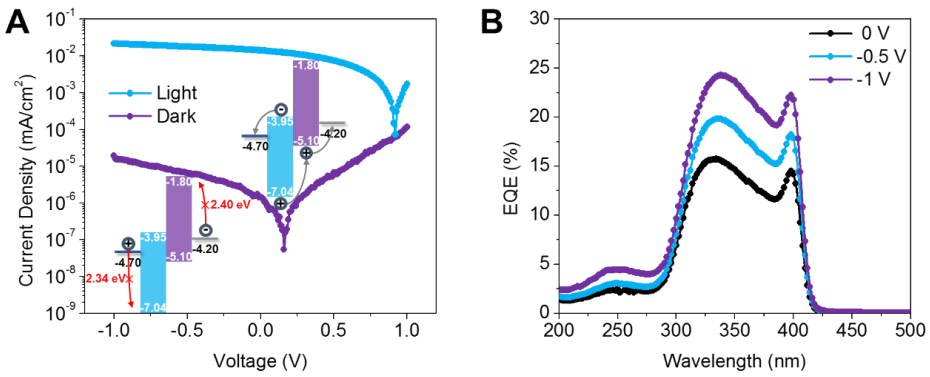

Figure 2-11 (A) Current density-voltage (J-V) characteristics of a prototypical visible-blind UV-A photodetector measured in dark and under 360 nm monochromatic illumination with the intensity of 0.267 mW/cm^2. (B) External quantum efficiency (EQE) of the device versus wavelength under different applied reverse biases.

The external quantum efficiency (EQE) spectra of the device under different applied reverse biases are shown in Figure 2-11B. The device has a significant photoresponse from 300 to 400 nm with a sharp cutoff at 410 nm. The EQE spectra showed two maxima corresponding to the wavelength of 334 and 398 nm and a dip around 380 nm under 0 V bias. When reverse bias was increased from 0 to -1 V, the first EQE maximum at 334 nm redshifted 4 nm while the wavelength for the second maximum and the dip had no change. The EQE values reached 16% and 15% at 334 and 398 nm, respectively, with no bias, and increased to 24% and 22% under -1 V bias at 338 and 398 nm, respectively, which were much higher than the reported maximum EQEs between 0.2 to 1.6% for narrowband photodetectors based on $CH_3NH_3Pb(Cl\text{-}Br)_3$ and $CH_3NH_3Pb(Br\text{-}I)_3$ single crystals.[46] A reverse bias can facilitate the extraction of carrier generated in the perovskite layer resulting in a higher EQE, which also indicates the carrier extraction is not essentially lossless. For most of the high performance diode type photodetectors based on $CH_3NH_3PbI_3$ polycrystalline thin films, EQE can reach 80% with or without the help of a low reverse bias,[57, 112-115] and one

even reached almost 1 × 10^5% due to photomultiplication via controlling surface traps of $CH_3NH_3PbI_3$ polycrystalline thin films.[111]

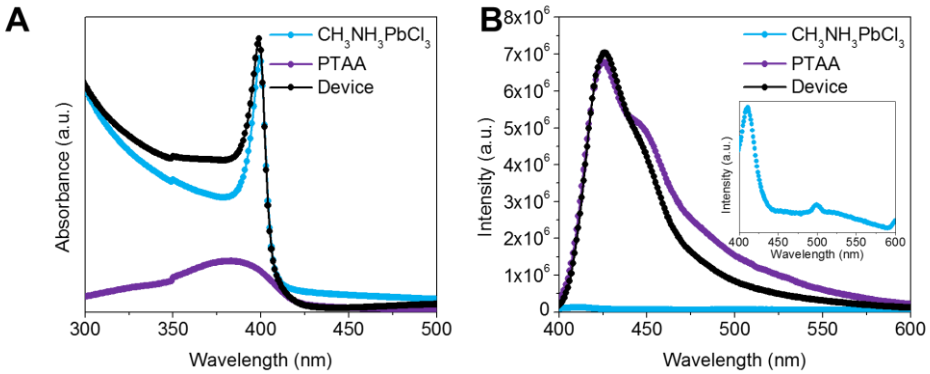

Figure 2-12 (A) Absorption and (B) steady-state PL spectra of $CH_3NH_3PbCl_3$ thin film (~170 nm) on glass, PTAA (~35 nm) on glass, and PTAA (~35 nm) on $CH_3NH_3PbCl_3$ thin film (~170 nm) on glass (i.e., glass/ $CH_3NH_3PbCl_3$/PTAA). The excitation light wavelength is 360 nm.

We investigated the optical properties of single layer $CH_3NH_3PbCl_3$ (~170 nm) and PTAA (~35 nm) and the thin film of PTAA (~35 nm) on $CH_3NH_3PbCl_3$ (~170 nm) as in the devices without two electrodes. The absorption spectra (**Figure 2-12**A) showed that both $CH_3NH_3PbCl_3$ and PTAA single films had a sharp optical cut-off at ~410 nm. After coating the PTAA layer on the $CH_3NH_3PbCl_3$ thin film, strong excitonic peak still appeared at the same position as pure $CH_3NH_3PbCl_3$ thin film, and the dip on the left of the excitonic peak was partially filled due to the absorption of PTAA. The absorption spectrum of the film of PTAA on $CH_3NH_3PbCl_3$ is consistent with the photoresponse range of EQE spectra and can help to understand the peaks (~334 and 398 nm) and dip (~380 nm) on EQE spectra. EQE can be expressed by Eq 3-1[147]

$$EQE(\lambda) = \eta_{abs}(\lambda)\eta_{gen}\eta_{coll} \qquad (3\text{-}1)$$

where η_{abs} is the light absorbance, η_{gen} is the charge carrier generation quantum yield, and η_{coll} is the photo-generated charge carrier collection efficiency. Assuming charge carrier generation

quantum yield (η_{gen}) and photo-generated charge carrier collection efficiency (η_{coll}) are the same for different wavelength light in our devices, EQE is only a function of light absorbance (η_{abs}). The peaks and dip of the EQE spectra (Figure 2-11B) align well with the absorption spectrum of the thin film of PTAA on $CH_3NH_3PbCl_3$ (Figure 2-12A), indicating that the shape of the EQE spectra mainly determined by the absorbance of the active layer.

Figure 2-12B shows the steady-state PL spectra of the single layer of $CH_3NH_3PbCl_3$ and PTAA and the thin film of PTAA on $CH_3NH_3PbCl_3$ with 360 nm excitation impinged from the sample side. While $CH_3NH_3PbCl_3$ thin film has the similar emission wavelength as that of PTAA thin film, its PL intensity is much weaker even though the $CH_3NH_3PbCl_3$ thin film is almost four times thicker. The PL spectrum of the film of PTAA on $CH_3NH_3PbCl_3$ is dominated by the emission of the thin PTAA with a slightly quenching above 450 nm compared to the PL spectrum of the pure PTAA layer. We also impinged the excitation light from the glass side (**Figure 2-13**). The PL intensity of the film of PTAA on $CH_3H_3PbCl_3$ is significantly lower than that of the pure PTAA layer. This is because the thicker $CH_3NH_3PbCl_3$ layer absorbed most of the light but emitted much less light. Therefore, the low EQE in this work could be attributed to the intrinsic poor optoelectronic properties of $CH_3NH_3PbCl_3$ compared to $CH_3NH_3PbI_3$ due to the stronger Pb-Cl interaction. In addition, the large energy offsets at each interface in the device could hinder the carry transport and collection, resulting in lower EQE.

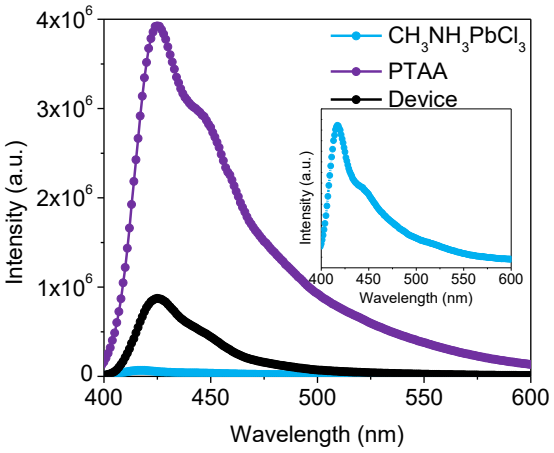

Figure 2-13 Steady-state photoluminescence spectra of $CH_3NH_3PbCl_3$ thin film, pure PTAA thin film, and the film of PTAA on $CH_3NH_3PbCl_3$ excited from glass side with 360 nm wavelength light.

We further evaluated the device performance by calculating the responsivity (R), the UV-visible rejection ratio, and the specific detectivity (D*). The responsivity, R, was calculated from EQE according to Eq 3-2

$$R = \frac{EQE \times e}{h\nu} \qquad (3\text{-}2)$$

where *e* is the electron charge, *h* is the Planck constant, *ν* is the frequency of incident light. The responsivity of the prototypical device reached a maximum of 0.047 A/W and 0.071 A/W at 398 nm under 0 V and -1 V bias, respectively, as shown in **Figure 2-14**A. The maximum responsivity of our prototypical device under -1 V bias is almost one fold higher than that (46.9 mA/W) of the photodetector with a $CH_3NH_3PbCl_3$ single crystal sandwiched between a transparent Pt electrode and a Ti/Au back electrode,[126] while it is still significantly lower than the responsivity of 7.56 A/W[46] and 18 A/W[127] of laterally structured phototransistor-type detectors utilizing single crystals. The UV-visible rejection ratio was calculated by $R_{UV}/R_{500\ nm}$ and shown in Fig. 2-14B. Under 0 and -0.5 V biases, UV-visible rejection ratios are similar between 300-400 nm with 508 and 556

at 338 and 398 nm, respectively, which is, to the best of our knowledge, the highest among all the reported UV photodetectors based on $CH_3NH_3PbCl_3$ perovskite.[46, 126-128]

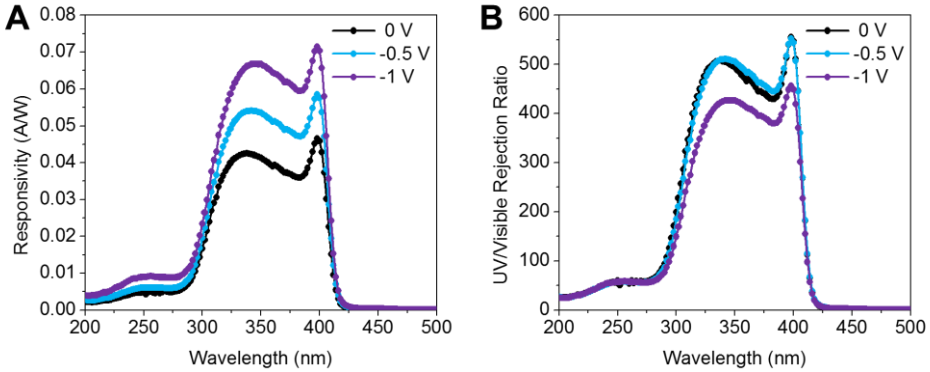

Figure 2-14 (A) Responsivity and (B) UV-visible rejection ratio $R_{UV}/R_{500\ nm}$ of the device versus wavelength under different reverse biases.

The specific detectivity is given by

$$D^* = \frac{R(A\triangle f)^{\frac{1}{2}}}{i_n} \qquad (3\text{-}3)$$

where R is the responsivity, A is the device area, $\triangle f$ is the bandwidth and i_n is the noise current. Assuming that shot noise from the dark current is a major contribution in the total noise current of the photodetector, the specific detectivity was then calculated as

$$D^* = \frac{R}{\sqrt{2eJ_d}} \qquad (3\text{-}4)$$

where J_d is the dark current density. Despite the device exhibiting a higher responsivity under -1 V bias, specific detectivity reached a maximum of 6.87×10^{10} Jones at 398 nm under 0 V bias and reduced to 4.07×10^{10} and 2.87×10^{10} Jones under -0.5 V and -1 V bias, respectively, due to the increased dark current at a higher reverse bias (**Figure 2-15**). It also indicates that our prototypical $CH_3NH_3PbCl_3$ visible-blind UV-A photodetectors exhibit the best performance when they are self-

powered and work at 0 V bias. The detectivity of our device is significantly higher than that of the 350 μm thick single crystal device sandwiched between Pt and Ti/Au electrodes, which is 1.2 × 10^{10} Jones,[126] while lower than 10^{12} Jones that was achieved by the lateral structured photodetector based on $CH_3H_3PbCl_3$ homogeneous single crystal.[128]

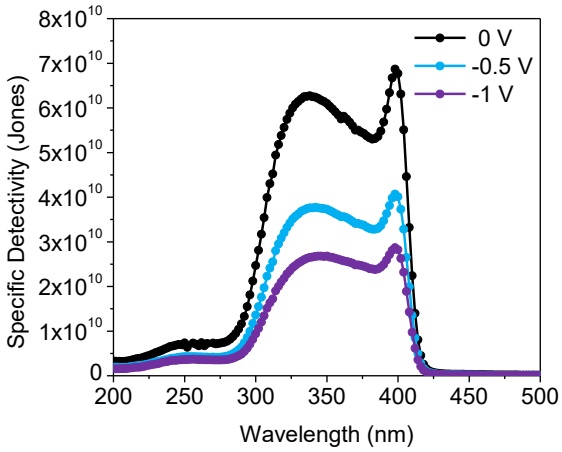

Figure 2-15 Specific detectivity of the device versus wavelength under different reverse biases.

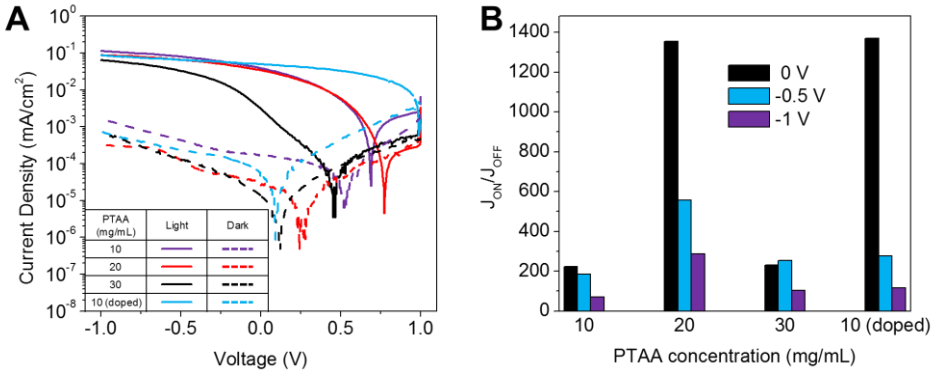

Figure 2-16 (A) J-V characteristics of the devices with the PTAA layer made by 10, 20 and 30 mg/mL PTAA solutions and a 10 mg/mL PTAA solution doped with 1% F4-TCNQ, respectively, under dark and illuminated by a solar simulator with 100 mW/cm^2 intensity. (B) I_{ON}/I_{OFF} ratios of the devices with different PTAA layers.

One of the applications of visible-blind UV-A photodetecotrs is to detect UV-A response when exposed to sunlight. To evaluate the device performance under sunlight and further investigate the effects of PTAA thickness and dopant in PTAA on device performance, we fabricated more devices and tested them using solar simulator. All the devices had $CH_3NH_3PbCl_3$ thin films prepared in the same conditions but the PTAA layers were formed with the concentrations of 10, 20, and 30 mg/mL in order to change the thickness of PTAA layer. F4-TCNQ, which has been reported to have the ability to enhance the solar cell performance by reducing device series resistance,[148] was introduced as a dopant for PTAA. **Figure 2-16**A shows the J-V curves of the devices tested in dark and under the illumination by solar simulator. With the increase of PTAA layer thickness by spin coating of 10, 20, and 30 mg/mL PTAA solutions, the dark current was reduced from 1.72×10^{-4} to 2.53×10^{-5} and 1.30×10^{-5} mA/cm^2, respectively, under 0 V bias, but reached almost the same under -1 V bias. Similarly, the light current density was decreased under 0 V bias as the PTAA layer was formed by spin coating 30 mg/mL PTAA solution, but reached similar level under -1 V bias. Dopant in PTAA not only decreased dark current density under reverse biases but also increased light current density and V_{OC}, which is consistent with the report for photovoltaic devices.[148] The increased dark current density of the device fabricated with 10 mg/mL PTAA compared to that in Figure 2-11A could be due to the increased device area from 0.057 cm^2 to 0.1 cm^2 and faster voltage scan speed. We used the ratio of current density measured under the illumination of solar simulator to that in dark, J_{ON}/J_{OFF}, to evaluate the performance of our visible-blind UV-A photodetectors. Figure 2-16B shows the ratio of J_{ON}/J_{OFF} under 0, -0.5 and -1 V biases for the devices made with different PTAA concentrations and with dopant. Device fabricated with F4-TCNQ doped PTAA owned the highest ON-OFF ratio of 1371 at 0 V bias because of its increased light current density and slightly decreased dark current density compared

to the device containing the 10 mg/mL PTAA layer without dopant. Following the highest ratio, the device containing the 20 mg/mL PTAA layer showed the second highest ON-OFF ratio of 1354, as both light and dark current densities were decreased. The devices with the 10 and 30 mg/mL PTAA layers suffered from high dark current density and low light current density, respectively, and thus exhibited relatively low ON-OFF ratios. When the reverse bias was increased to -0.5 V and further -1 V, the ON-OFF ratios of all the four devices decreased due to the significantly increased dark current density and slightly increased light current density.

The environmental instability of perovskite thin films has long been a challenge for the applications in photovoltaic devices.[149] In this study, we also attempted to expose the $CH_3NH_3PbCl_3$ perovskite thin film photodetector devices in ambient air and found that bubbles appeared under the Al electrodes (**Figure 2-17**). This phenomenon indicates the degradation of the devices under ambient air and encapsulation is needed in order to conduct the detection in ambient conditions.

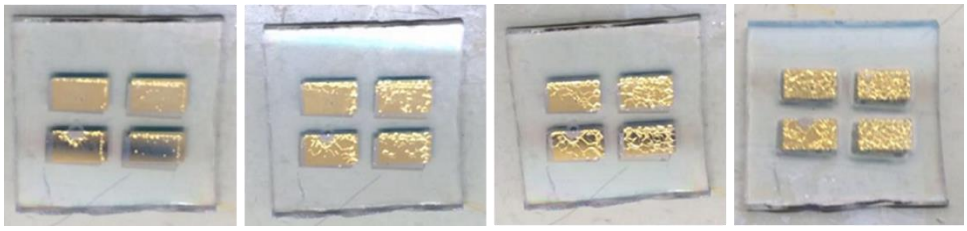

Figure 2-17 Photograph of devices exposed in ambient air (From left to right: 0 min, 1 min, 2 min, 3min)

2.4 Conclusion

In summary, we applied a two-step spin coating and solvent-vapor-assisted low-temperature thermal annealing method to successfully fabricate $CH_3NH_3PbCl_3$ perovskite thin films that exhibited a cubic crystalline structure and pinhole-free morphology. We demonstrated

that charge traps in the fabricated $CH_3NH_3PbCl_3$ perovskite thin films could be reduced by carefully adjusting the $PbCl_2$ precursor concentration while keeping the same CH_3NH_3Cl precursor concentration. We further fabricated prototypical UV photodetectors with the structure of ITO/$CH_3NH_3PbCl_3$/PTAA/Al. The devices showed a low dark current density 1.60×10^{-5} mA/cm^2 under -1 V reverse bias, strong photoresponose in 300-400 nm region, and a high UV-visible rejection ratio up to 500 under 0 or -0.5 V bias. The low-temperature solution-processed $CH_3NH_3PbCl_3$ thin films offer a great potential for making flexible, lightweight visible-blind UV-A photodetectors and other optoelectronic devices.

Chapter 3 NARROWBAND ULTRAVIOLET PHOTODETECTORS BASED ON NANOCOMPOSITE THIN FILMS WITH HIGH GAIN AND LOW DRIVING VOLTAGE

3.1 Introduction

Narrowband ultraviolet (UV) photodetectors are highly desired in multiple areas such as UV radiation dosimetry, combustion control, and nuclear radiation monitoring.[20] For nuclear radiation monitoring, for example, a scintillator is typically used to convert high energy radiation such as X-ray and/or Gamma-ray into UV light, which needs to be specifically detected by a UV photodetector attached to the scintillator.[150] To date, most of the commercial narrowband UV photodetectors are either based on photomultiplier tubes (PMTs),[150, 151] or use a broadband inorganic p-n junction combined with a band-pass optical filter.[152] The fragile vacuum tube and the requirement of extremely high driving voltages make PMT-based UV photodetectors unsuitable for field applications, while inorganic p-n junctions and band-pass optical filters require complex and expensive processing. In contrast, photodetectors based on the photodiode architecture with active layers composed of organic or organic-inorganic hybrid materials offer the benefits of being lightweight, mechanically flexible, and solution processable. The photoresponse range can be adjusted by selecting conjugated semiconductor polymers or inorganic nanoparticles (NPs) with different band gaps, and the desired high detection sensitivity can be achieved by manipulating the active layer composition and the device structure.[13, 26, 27, 29, 30, 35, 38, 40-44, 153-157] Therefore, they are promising candidates for next generation photodetectors. However, the fabrication of filterless narrowband photodetectors using organic or organic-inorganic hybrid

materials presents a great challenge, because of the inherently broad absorption range of these materials.

Narrowband photodetectors in the red or near-infrared (NIR) region have been reported with bulk heterojunction (BHJ) active layers based on the charge collection narrowing (CCN) mechanism.[13] Charge collection efficiency depends on the position-dependent exciton generation within the active layer, as determined by the penetration depth of different wavelength light in the active layer. When the active layer thickness is increased from the nanometer range to micrometers, only long-wavelength light can penetrate through the entire active layer. This light is then reflected off the top electrode and establishes an interference pattern throughout the active layer that enables bulk exciton generation, which can generate a photoresponse. Light within the absorption range is absorbed quickly, and therefore only generates excitons in the lower portion of the active layer, creating a space charge region that inhibits photoresponse. Thus, only light at the long-wavelength edge of the active layer absorption peak can generate photoresponse, so the photoresponse is narrowed to this wavelength. Because of the thick active layer, the charge carriers must travel a long distance to be collected at the corresponding electrode, which increases the likelihood that they will recombine before being collected. These thick devices produce a relatively low external quantum efficiency (EQE).[13] It is desirable to maximize the EQE produced by photodetectors, so photomultiplication can be utilized, where multiple charges can be collected per incident photon and it is therefore possible to achieve EQE > 100%. Photomultiplication cannot be accomplished by BHJ active layers. Therefore, the weight ratio of fullerene is significantly reduced to < 5% in the active layers so that it will form isolated electron traps. An accumulation of trapped electrons can bend the active layer energy bands at the top interface, enabling hole injection from the cathode.[29] For thick active layer devices, strong reverse biases, up to -60 V, have to be applied to

achieve photomultiplication and narrowband detection simultaneously.[153] Narrow band gap NPs, such as CdTe and PbS NPs, were also mixed with polymers to form thick active layers and photomultiplication-type red or NIR narrowband photodetectors were demonstrated.[154, 155] Recently, our group also demonstrated the narrowband photoresponse in the UV range utilizing the CNN mechanism by employing thick active layers composed of wide bandgap poly[bis(4-phenyl)(2,4,6-trimethylphenyl)amine] (PTAA) and ZnO NPs.[43]

Photomultiplication-type UV photodetectors with polymer-nanoparticle nanocomposite active layers have also been reported, where wide band gap NPs, such as ZnO and TiO_2 NPs, served as electron traps to induce hole injection from the top cathode.[38, 40-43] However, none of them showed narrowband characteristics and relative high reverse biases were needed to achieve photomultiplication effect. In these devices, trapped electrons in the NPs close to the top cathode come from two sources: migrated from trapped electrons in the NPs in the lower portion of the active layer, due to the direct absorption of UV light by NPs; or, transferred from photogenerated electrons in polymer after the absorption of visible light. High reverse biases are required to force the migration of UV-generated electrons from the NPs in the lower portion to those in the upper portion of the active layer. Photoresponse induced by the polymer absorption of visible light diminishes the UV-selectivity of the devices. Even though we demonstrated narrowband UV photodetectors with photomultiplication, it still requires high applied reverse biases and exhibits an additional weak photoresponse in the visible range.[44] Therefore, to make narrowband UV photodetectors exhibiting UV-selective photomultiplication while operating under low biases, creative new device structures and active layer material selection are necessary.

Here, we present such an approach by mixing wide band gap ZnO NPs with the wide band gap polymer poly[(9,9-dioctylfluorenyl-2,7-diyl)-alt-co-(bithiophene)] (F8T2) to form the active

layer, which is sandwiched between two hole transport layers of poly(3,4-ethylenedioxythiophene):polystyrene sulfonate (PEDOT:PSS) and MoO_3 with the similar highest occupied molecular orbital (HOMO) or valence band (VB) levels of 5.2 and 5.3 eV, respectively, and two electrodes of indium tin oxide (ITO) and Ag, each with a work function of 4.7 eV (**Figure 3-1**a and b). This structure favors hole transport. The addition of ZnO NPs in the active layer provides electron traps that induce the band bending required for hole injection and thus photomultiplication.[38] The absorption ranges of ZnO NPs and F8T2 thin films have almost no overlap and a narrow EQE peak will be located at the absorption cutoff of ZnO NPs, in the dip of the absorption spectra produced by the F8T2:ZnO blend thin film (Figure 3-1c). We report the first visible-blind UV-specific photodetector with an extremely narrow photoresponse, having a high EQE value of 782% under a low forward bias of 3 V with a full-width at half-maximum (FWHM) of 16 nm, corresponding to a high specific detectivity of 8.45×10^{12} Jones. We further investigated and discussed the impacts of the weight ratio of F8T2:ZnO NPs and device structure on the UV-selectivity and device performance. As this design principle is generalizable to many material systems, it could be applied to make low driving voltage, photomultiplication-type narrowband photodetectors in other spectral windows.

3.2 Experimental Section

3.2.1 Materials

Indium tin oxide (ITO) coated glass (sheet resistance = 10 Ω sq^{-1}) was purchased from Colorado Concept Coating LLC. Poly(3,4-ethylenedioxythiophene):polystyrene sulfonate (PEDOT:PSS, CLEVIOS P VP AI 4083) was purchased from Heraeus. MoO_3 powder (99.9995%) was purchased from Alfa Aesar. Bathocuproine (BCP) powder (99.99%) was purchased from Sigma-Aldrich. Ag and Al evaporation pellets (99.999%) were purchased from R.D. Mathis.

Poly[(9,9-dioctylfluorenyl-2,7-diyl)-alt-co-(bithiophene)] (F8T2, M_W = 30k, PDI = 4.5) was purchased from American Dye Source, Inc. $ZnAc_2 \cdot 2H_2O$ (ACS reagent, ≥ 98%) was purchased from Sigma-Aldrich. MeOH (Certified ACS) and KOH (Certified ACS) were purchased from Fisher Scientific. 1,2-dichlorobenzene (DCB, anhydrous, 99%) was purchased from Sigma-Aldrich. All the materials were used as received without further purification.

3.2.2 ZnO NPs Synthesis

ZnO NPs were prepared by hydrolysis method with some modifications.[158] $ZnAc_2 \cdot 2H_2O$ (2.36 g) was dissolved in MeOH (100 mL) at 60 °C in a three-neck round bottom flask and followed by adding KOH solution (1.256 g in 52 mL MeOH) within 5 min. A PID controller with a thermocouple was applied to control the solution temperature. After stirring under 60 °C for 1.5 h, when the reaction solution transitioned to turbid from transparent, the reaction mixture was stirred for one more hour. The ZnO NPs were collected by centrifuge at 10000 rpm for 10 min and washed with MeOH for three times. The ZnO NPs were then transferred into the N_2 filled glovebox and dispersed in DCB to form a transparent dispersion (200 mg/mL). The dispersion remains transparent while under the protection of N_2 and stored in a refrigerator at 4 °C. The average particle size was about 10 nm as determined by dynamic light scattering (DLS, Malvern Zetasizer Nano) measurements on different batches.

3.2.3 Thin Film Fabrication

Glass substrates were cut into 1.5 cm × 1.5 cm pieces, then cleaned by sonication in soapy deionized (DI) water, DI water, acetone, and isopropanol for 15 min each sequentially and finally treated with 100 W oxygen plasma for 10 min. F8T2 solution (40 mg/mL) was prepared in DCB by stirring at 70 °C overnight. The solution was cooled to room temperature and then mixed with ZnO NPs in DCB (200 mg/mL) in different volumes to form an active layer precursor with

F8T2:ZnO NPs weight ratios of 1:6 or 1:3. The mixed precursor was stirred at room temperature for 1 h and spin coated onto a cleaned glass substrate at 1000 rpm for 30 s. The composite thin films were annealed on a hotplate at 80 °C for 10 min. The pure F8T2 and ZnO NPs films were prepared by spin coating F8T2 (40 mg/mL) and ZnO NPs (200 mg/mL) precursor solutions, respectively, at 1000 rpm for 30 s. Both films were annealed at 80 °C for 10 min.

3.2.4 Thin Film Characterization

Energy-dispersive X-ray spectroscopy (EDS) measurements were carried out on an FEI Sirion SEM with the active layer coated on a Si/PEDOT:PSS substrate to avoid charge effects. Glow-discharge optical emission spectroscopy (GDOES) was performed on a Horiba GD-Profiler 2 with RF excitation of an argon plasma. The active layers for GDOES measurements were coated on ITO/PEDOT:PSS substrates. Ellipsometry measurements were performed on a Woollam M-2000 spectroscopic ellipsometer. UV-Vis absorption and photoluminescence (PL) spectra of the F8T2, ZnO, and F8T2:ZnO NPs thin films were collected using a Varian Cary 5000 UV-Vis-NIR spectrophotometer and a Horiba Fluorolog 3 spectrophotometer respectively. Film thickness were measured by a KL Tencor Alpha-Step 500 Profiler.

3.2.5 TMM and FDTD Simulations

Three-dimensional Finite-Difference Time-Domain (3D-FDTD, Lumerical FDTD Solutions) and Transfer Matrix Method (TMM)[159] simulations were performed to obtain the electric field distribution and exciton generation rate, respectively, following the methods reported in the previuos publication.[10, 15, 19] In this work, the exciton generation rate was calculated for incident light at 320, 360, 450, and 510 nm.

3.2.6 Device Fabrication

ITO coated glass substrates with the size of 1.5 cm × 1.5 cm were cleaned following the same cleaning procedure as glass substrates. PEDOT:PSS was spin coated onto the cleaned ITO coated glass substrate at 3000 rpm for 60 s, followed by annealing at 120 °C for 30 min in the ambient air condition. The substrates were then transferred into an N_2 filled glovebox. The active layers were fabricated as described in the thin film fabrication section. A 10 nm layer of MoO_3 or BCP was deposited by thermal evaporation at the rate of 0.02 nm s^{-1}. The devices were finished by the deposition of a 100 nm Ag or Al layer at the rate of 0.2 nm s^{-1} with a mask to a final device size of 0.1 cm^2. Both thermal evaporation processes were performed in a background vacuum less than 2×10^{-6} Torr.

3.2.7 Device Characterization

White light from a 150 W Xenon arc lamp (Newport Co., Oriel) was filtered using a grating monochromator (Oriel Cornerstone 130) for the incident continuous-wave probe light. The device characterization was carried out in ambient conditions. The wavelength dependent light intensity was measured using a power meter (Model 1918-R, Newport Co.) and a detector (DET-L-SIUV-R-C, Newport Co.). The dark and UV illuminated current density-voltage (*J*-*V*) characteristics were recorded using a Keithley 2635B system from -3 V to 3 V with a scan step of 0.05 V and current values were averaged from 20 points under each bias with a delay time of 20 ms. The EQE was recorded with a wavelength step of 2 nm s^{-1} and light current values were averaged from 10 points with a delay time of 10 ms. Response time was measured with a mechanical chopper (Stanford Research Systems Inc.) and recorded by a digital storage oscilloscope (TBS 1052B, Tektronix).

3.3 Results and Discussion

3.3.1 Device Structure and Current Density-Voltage (J-V) Characteristics

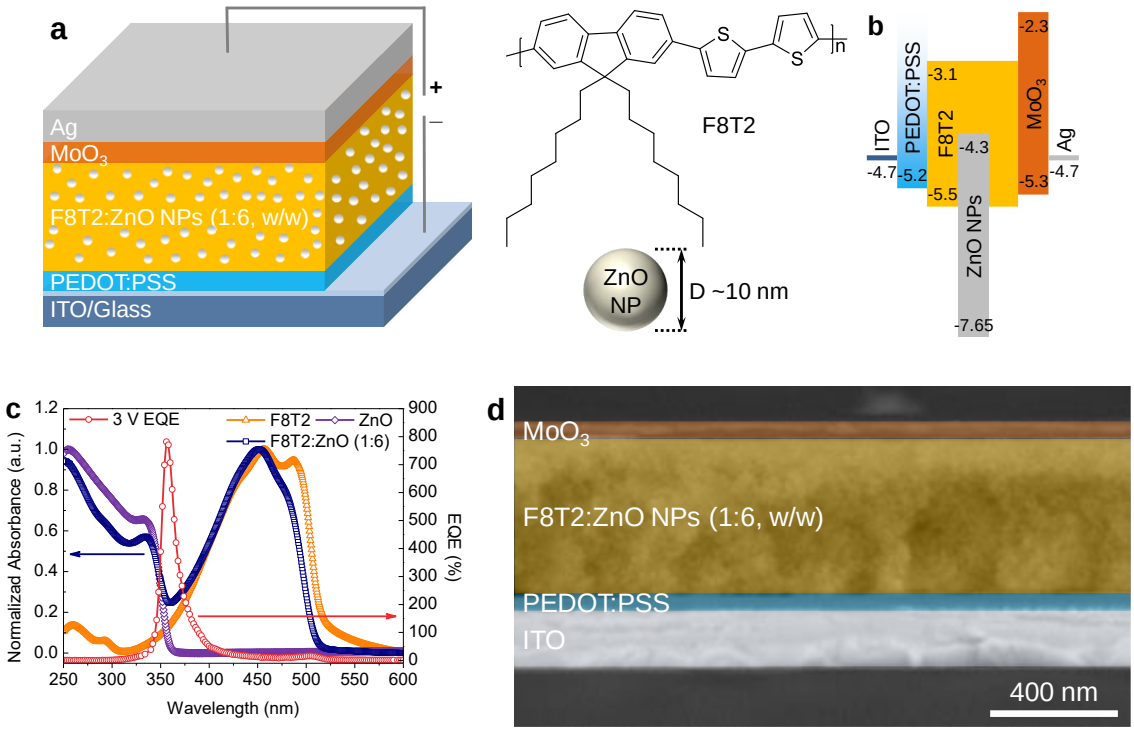

Figure 3-1 (a) Illustration of the device structure of the UV photodetector. (b) The energy level diagram of the materials employed in the UV photodetector. (c) The normalized UV-vis spectra of F8T2, ZnO NPs, and F8T2:ZnO NPs (1:6, w/w) thin films and the EQE spectrum under 3 V forward bias. (d) The cross-section SEM image of the ITO/PEDOT:PSS/F8T2:ZnO NPs (1:6, w/w)/MoO_3 thin film.

The device structure and the energy level diagram of our photodetectors are shown in Figure 3-1a and b, respectively. The transparent ITO serves as the anode, the PEDOT:PSS (~40 nm) works as the hole transport layer, the F8T2:ZnO NPs (1:6, w/w) nanocomposite film (~450 nm) serves as the active layer, MoO_3 (10 nm) functions as the hole transport/electron blocking layer, and Ag (100 nm) serves as the cathode. The cross-section SEM image of the device is shown

in Figure 3-1d. The ZnO NPs are well isolated by the F8T2 matrix in the active layer due to the aggregation. The volume ratio of F8T2:ZnO NPs nanocomposite film is estimated to be 1:1.18 as calculated from their weight ratio and the density of F8T2 (1.1 g cm^{-3}) and ZnO NPs (5.61 g cm^{-3}). The liquid crystalline polymer F8T2 is a p-type semiconductor with a hole mobility of 0.01–0.02 cm^2 V^{-1} s^{-1} and a typical band gap of 2.4 eV,.[160] ZnO is an n-type wide-band gap semiconductor with a band gap of 3.3 eV and an electron mobility on the order of 1–10 cm^2 V^{-1} s^{-1}.[161] Because of the similar energy levels of the PEDOT:PSS and MoO_3 hole transport layers and the ITO and Ag electrodes (Figure 3-1b), the photodetector exhibited a symmetric dark J-V curve under forward and reverse biases (**Figure 3-2a**). The dark current densities remained low at 7.87×10^{-7} and 1.13×10^{-6} mA/cm^2 under 3 V forward and -3 V reverse bias, respectively. The low dark current density is due to the effective blocking of hole and electron injections under both forward and reverse bias as well as the densely packed, defect-free active layer (Figure 3-1d), which reduces the current leakage. As illustrated in Figure 3-2b, under dark and forward bias, hole injection is blocked by the 0.8 eV energy barrier between ITO (work function, -4.7 eV) and F8T2 (HOMO, -5.5 eV) and electron injection is effectively blocked by the MoO_3 layer, resulting in low dark current density. Similarly, as illustrated in Figure 3-2c, hole injection is blocked by the same energy barrier between Ag and F8T2 in the dark under reverse bias. The energy barrier between ITO and ZnO conduction band is 0.4 eV, which might not be able to effectively block electron injection. While PEDOT:PSS is not commonly considered as an electron blocking layer, it has been reported that the PSS rich layer on the top surface of the PEDOT:PSS layer could dope a conjugated polymer in the active layer, forming a doped electron blocking thin layer during the thermal annealing process.[162, 163] We therefore suspect that a thin electron blocking layer could also be formed between F8T2 and PSS, which can help to block electron injection from ITO to

ZnO conduction band under reverse bias. Thus, low dark current density can also be achieved under reverse bias. The occurrence of the minimum dark current at a non-zero voltage (V_0) of -0.25 V could be due to the internal field built by PEDOT:PSS and F8T2 in the formation of the thin electron blocking layer.

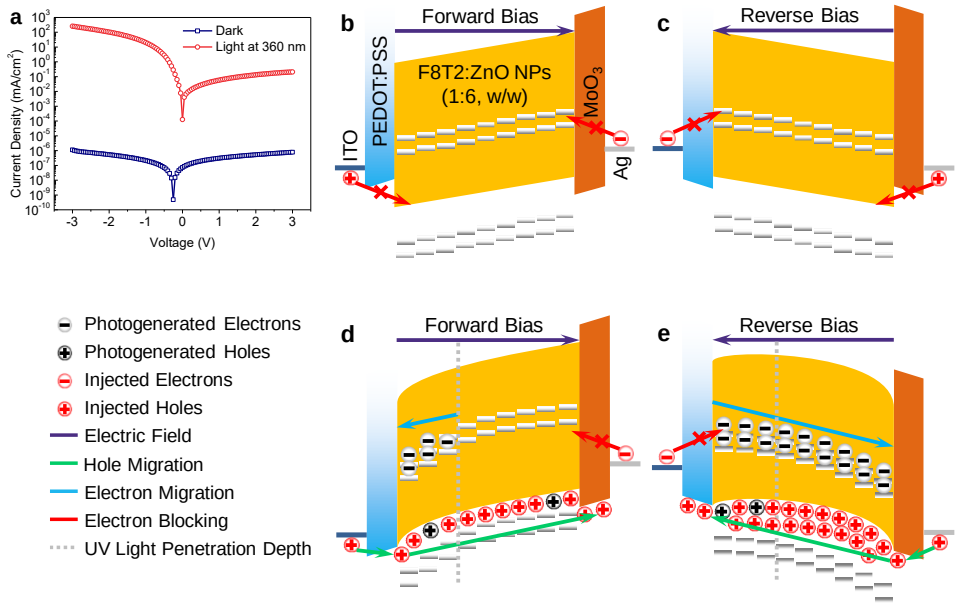

Figure 3-2 (a) The J-V curves of the device in the dark and under 360 nm illumination with an intensity of 2.46×10^{-2} mW/cm^2. (b, c) Illustrations of the device in the dark under (b) a forward bais and (c) a reverse bias. (d, e) Device working mechanism under UV illumination and (d) a forward bias or (e) a reverse bias.

Since the photoresponse of the photodetector is heavily related to the absorption of active layer materials and the distribution of ZnO NPs in the active layer, we measured the UV-Vis absorption spectra of pure F8T2 and ZnO NP thin films and the blend F8T2:ZnO NPs (1:6, w/w) thin film (Figure 3-1c), and the Zn elemental depth profiles throughout the active layer using energy-dispersive X-ray spectroscopy (EDS) and glow-discharge optical emission spectroscopy (GDOES) (**Figure 3-3**). The ZnO NP thin film absorbs light in the UV range and exhibits a sharp

optical cutoff at 360 nm. The F8T2 thin film has an absorption onset around 320 nm and a soft absorption cutoff around 530 nm with two obvious absorption peaks at 450 and 490 nm. The F8T2:ZnO NPs (1:6, w/w) thin film shows absorption in the 250 to 510 nm range with an absorption dip at 360 nm, which is between the absorption cutoff and onset of ZnO NPs and F8T2, respectively. The F8T2 absorption peak at 490 nm was obviously decreased when blended with ZnO NPs because of the disordered π-π stacking structure of the crystalline polymer by adding ZnO NPs.[164] Both EDS and GDOES showed a depletion of Zn in the active layer close to the PEDOT:PSS side and a uniform Zn distribution across the rest of the active layer. Due to surface charging, the Zn distribution close to the active layer surface could not be accurately provided by both methods.

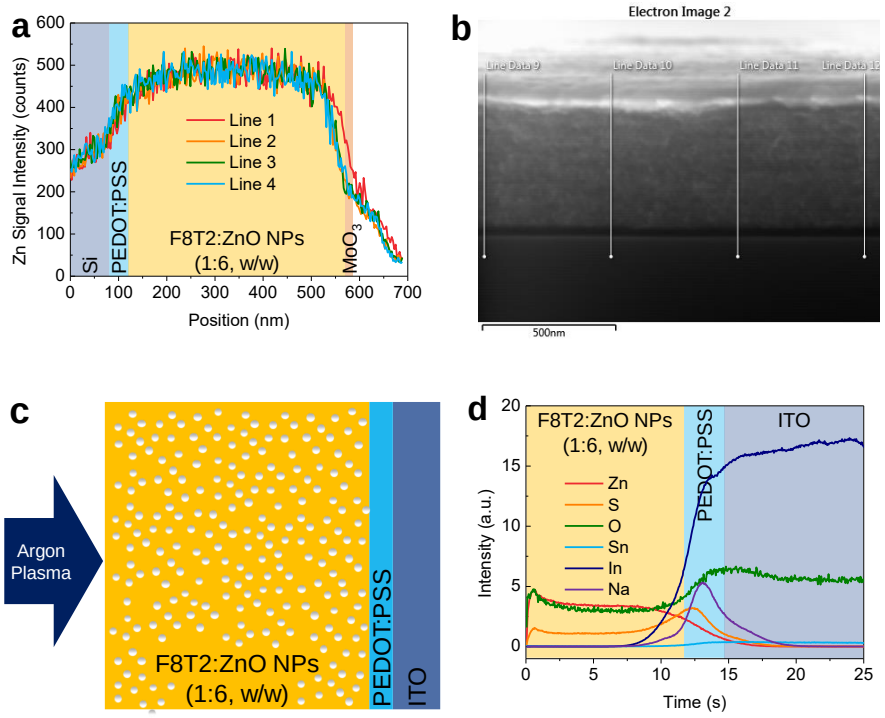

Figure 3-3 (a) The Zn distribution in the active layer obtained from energy-dispersive X-ray spectroscopy (EDS) line profiles in the cross-section line scans indicated in (b) on the sample

Si/PEDOT:PSS/F8T2:ZnO NPs (1:6, w/w)/MoO3. (c) Illustration of the sputtering of the F8T2:ZnO NPs thin film with argon plasma using glow-discharge optical emission spectroscopy (GDOES). Argon plasma was applied to sputter a crater into the F8T2:ZnO NPs (1:6, w/w), PEDOT:PSS, and ITO layer. The atomic emission of the sputtered material was measured. (d) Elemental profile as a function of time of argon plasma sputtering for the sample of glass/ITO/PEDOT:PSS/F8T2:ZnO NPs (1:6, w/w) obtained from GDOES. Both EDS and GDOES showed a depletion of Zn in the active layer close to the PEDOT:PSS side and a uniform Zn distribution across the rest of the active layer. Due to surface charging, the Zn distribution close to the active layer surface could not be accurately provided by both methods.

We calculated the light penetration depth in the active layer by Eq 3-1:[165]

$$\sigma = \frac{\lambda_0}{4\pi k}\ (nm) \qquad (3\text{-}1)$$

where λ_0 is the wavelength of the light and k is the wavelength dependent extinction coefficient of the active layer, which was measured experimentally using ellipsometer shown in **Figure 3-4**a. The light penetration depth and the measured glass/ITO/PEDOT:PSS transmittance are shown in Figure 3-4b. The transmittance approaches zero below 280 nm wavelengths and is above 80% in the wavelength range of 350 – 600 nm. The S-shaped penetration depth as a function of wavelength is mainly due to the absorption of ZnO NPs and F8T2 in the active layer.

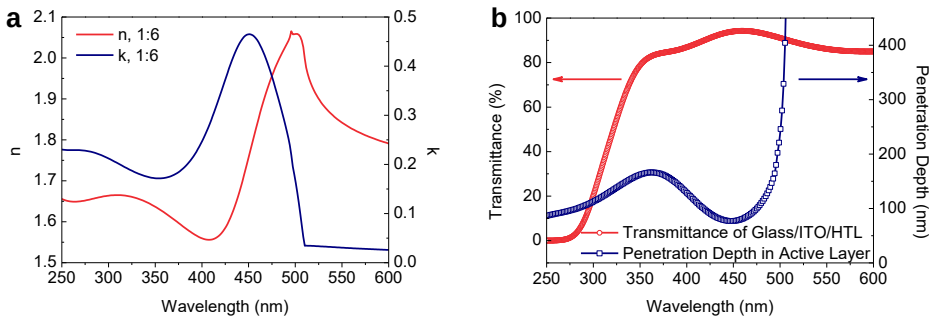

Figure 3-4 (a) Refractive index (n) and extinction coefficient (k) of the active layer of blend F8T2:ZnO NPs (1:6, w/w) obtained from ellipsometry measurements. (b) The transmittance of glass/ITO/PEDOT:PSS and the light penetration depth in the active layer as a function of wavelength.

We measured the J-V curve under 360 nm monochromatic illumination. The device exhibited a photoconductor feature with a strong rectification ratio of 1,242 under -3 V to 3 V bias. The 360 nm light at the absorption cutoff of ZnO NPs has a local maximum in the penetration depth (Figure 3-4b), and can generate excitons in ZnO NPs in the lower portion of the active layer close to the transparent ITO electrode as marked by the dash line in Figure 3-2d and e. Electron-hole pairs are separated at the ZnO NPs/F8T2 interfaces. While holes transfer in the F8T2 matrix and are collected at the Ag electrode under forward bias, electrons are trapped in ZnO NPs due to two factors: the energy barrier (1.2 eV) between the conduction band edge (-3.1 eV) of ZnO NPs and the lowest unoccupied molecular orbital (LUMO, -4.3 eV) of F8T2 (Figure 3-1b) and the disrupted electron transport pathway. In addition, the applied forward bias makes electrons more accumulated close to the PEDOT:PSS side. The consequence of this dynamic process results in a negative charge region close to the PEDOT:PSS side, causing the active layer band bending down close to the active layer/PEDOT:PSS interface. The well-aligned energy levels between the work function of ITO and the HOMOs of PEDOT:PSS and F8T2 facilitates hole injection, resulting in

the photocurrent density that is 10^5 orders of magnitude higher than the dark current density under 3 V forward bias. As illustrated in Figure 3-2e, with UV illumination and applied reverse bias, the photogenerated electrons in the ZnO NPs distributed in the lower portion of the active layer can migrate towards the Ag electrode with the aid of the applied electric field and the semi-connected electron transport channels. The electrons are trapped in the ZnO NPs during the migration through the entire active layer and a dynamic balance can be achieved, resulting in a bending in the energy level of F8T2 and hole injection from Ag electrode. More electrons were trapped in ZnO NPs close to the MoO_3/Ag side, which enhances hole tunneling injection, when the bias was increased from 0 to -1 V, resulting in a rapid increase of photocurrent density (Figure 3-2a). Despite the higher light current density exhibited under reverse bias, the dark J-V characteristics cannot return to the pristine J-V behavior and the device retained rectification behavior and high reverse dark current density after exposure to 360 nm light and reverse biases due to the change of surface defect states of ZnO NPs (**Figure 3-5**).[166-169] Therefore, the J-V characteristics indicate that our photodetector works under forward bias.

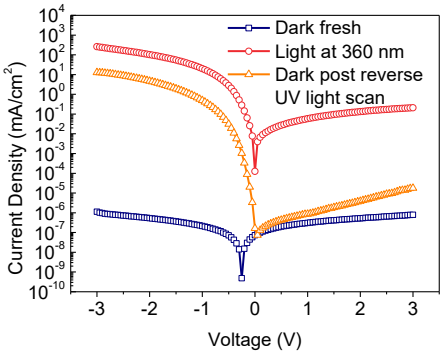

Figure 3-5 The J-V curves of the pristine ITO/PEDOT:PSS/F8T2:ZnO NPs (1:6, w/w)/MoO_3/Ag device under dark and 360 nm light illumination with the intensity of 2.46×10^{-2} mW/cm^2 and the re-measured dark J-V curve after the device was tested under 360 nm illumination and reverse bias.

3.3.2 Ultra-Narrow, UV-Selective, >100% EQEs under Low Forward Biases

We measured the photocurrent of the photodetector under the illumination of different wavelengths of light with zero and different forward biases and calculated the EQEs using Eq 3-2 by its definition:

$$EQE = \frac{(J_L - J_D)/e}{I_{in}/h\nu}\ (\%) \qquad (3\text{-}2)$$

where J_L is the photocurrent density under the illumination of different wavelengths of light, J_D is the dark current density, e is the elementary electron charge, I_{in} is the incident light intensity, h is the Plank constant and ν is the photon frequency. **Figure 3-6**a shows the EQE spectra of the photodetector under 0 and 0.5 – 3 V forward biases. Two very weak peaks centered around 358 and 504 nm exhibited under 0.5 V bias with the EQE values of 25.2 and 4.81%, respectively. While the EQE peak at 504 nm remained almost the same, the one at 358 nm increased significantly with the increase of forward bias and the values reached 283 and 782% under 2 and 3 V forward biases, respectively. The 358 nm peak also became narrower with the increase of forward bias. The FWHM decreased from 26 to 16 nm under 0.5 to 3 V forward biases, respectively.

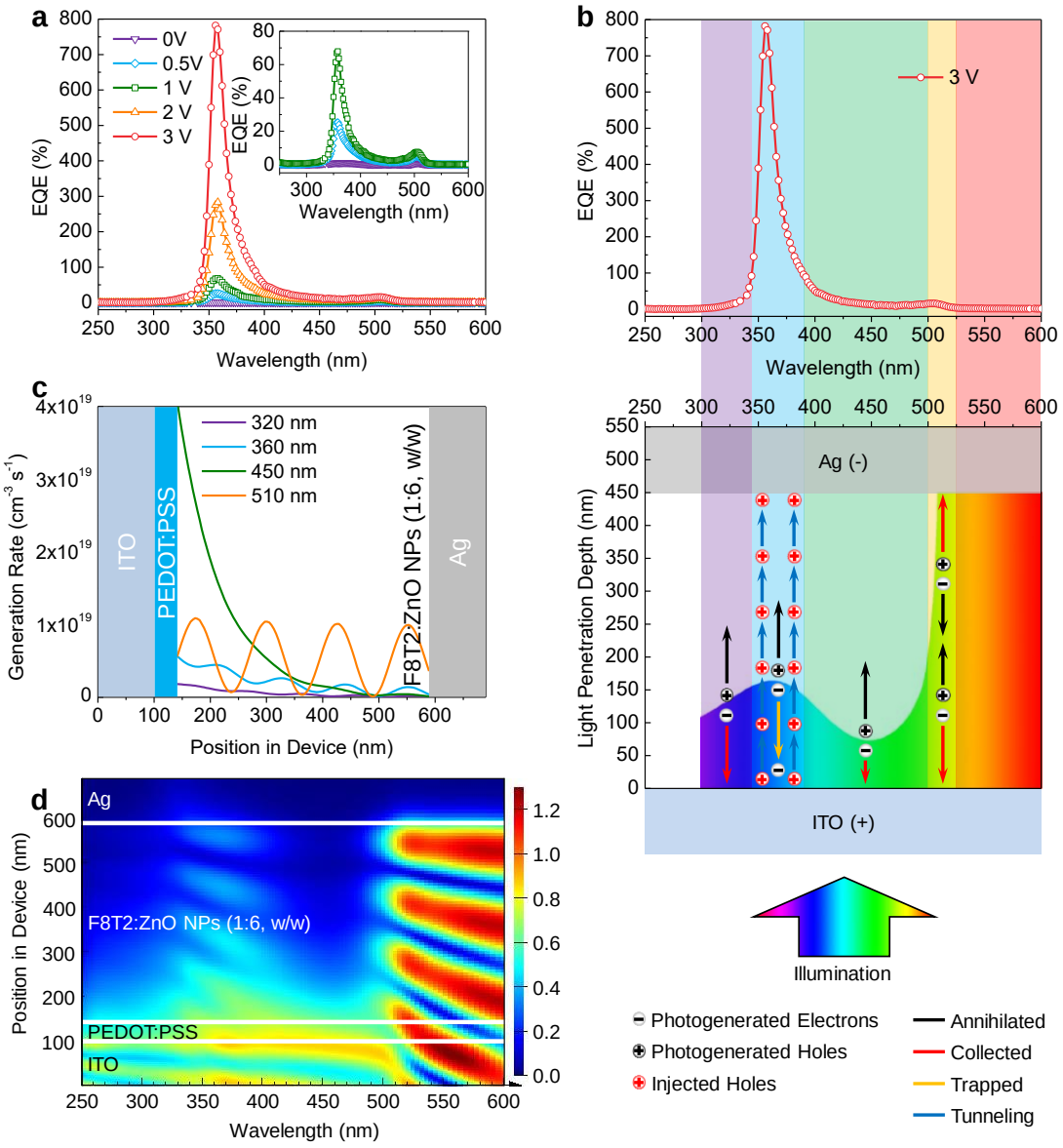

Figure 3-6 (a) EQE spectra of the device under different forward biases. The inset displays the EQE spectra under 0, 0.5 and 1 V biases. (b) The EQE spectrum under 3 V bias, and an illustration of the calculated light penetration depth, demonstrating the alignment of the EQE peak with the peak in light penetration depth around 360 nm. (Color does not represent the wavelength). (c) Exciton generation rates across the active layer for 320, 360, 450, and 510 nm lights calculated using TMM simulations under 0 V bias. (d) 3D-FDTD-simulated electric field distribution in the photodetector device between 250 and 600 nm wavelength under 0 V bias.

The working mechanism for the ultra-narrow, UV-selective, photomultiplication feature of our photodetector is proposed as illustrated in Figure 3-6b, which encompasses the effects of absorption, light penetration depth, exciton generation, charge trapping, and charge injection and collection. The photoresponse is discussed in four wavelength regions from 300 to 525 nm. Light between 300 to 340 nm has a low penetration depth due to both its short wavelength and the relatively high extinction coefficient of the blend thin film because of the strong absorption of ZnO NPs. Light in this region can generate electron-hole pairs in the ZnO NPs very close to the ITO/PEDOT:PSS side, which can separate at ZnO NPs/F8T2 interfaces. Holes transfer to F8T2 and diffuse in the F8T2 matrix towards the Ag side under a forward bias but are mostly annihilated due to the long migration length. Electrons are quickly collected by the ITO/PEDOT:PSS as they are very close to the anode and move toward the anode under forward bias. In addition, the build-in electric field between the ZnO condcution band (-4.3 eV) and the ITO work function (-4.7 eV) also facilatates the electron transfer from the ZnO conduction band to ITO. The aforementioned possible thin electron blocking layer due to PSS doped F8T2 may not effectively block electron transfer in this case. Without trapped electrons close to the ITO/PEDOT:PSS side, no F8T2 band bending occurs and hole can not inject from the anode, and thus light below 340 nm cannot induce noticeable EQE. Light between 340 and 390 nm has a longer penetration depth with the maximum depth of 166 nm, which is about 1/3 of the active layer thickness, at 360 nm wavelength. The maximum penetration depth at 360 nm corresponds to the dip in the extinction coefficient spectrum (Figure 3-4a) and the absorption spectrum (Figure 3-1c) of the blend film as it is located between the absorption cutoff and onset of ZnO NPs and F8T2, respectively. Upon charge separation, photogenerated electrons trapped in ZnO NPs in the lower 1/3 portion of the active layer, resulting in the band bending of F8T2 and hole tunneling injection from ITO anode and being collected at

Ag cathode. The photoresponse in this region is mainly due to the secondary injected holes, i.e., the photomultiplication effect, and thus exhibiting narrow, > 100% EQE. Light above 390 nm does not have enough energy to excite ZnO NPs but can generate excitons in F8T2. In the range of 390 to 500 nm, light has low penetration depth with the minimum (77 nm) at 448 nm wavelength due to the strong absorption of F8T2. Excitons can only be generated in F8T2 very close to the ITO/PEDOT:PSS side. The photogenerated electrons would again be quickly collected by the ITO electrode under a forward bias and most holes are annihilated during the migration to the Ag electrode. Therefore, there is no noticeable photoresponse. The sharp increase of the penetration depth beyond the wavelength of 500 nm is because of the low absorption of the active layer, which has a low extinction coefficient. Light between 500 nm and 525 nm, which is at the cutoff of F8T2 absorption spectrum, can penetrate through the active layer and be absorbed, albeit weakly, by F8T2, resulting in bulk exciton generation that produces a weak photoresponse.[13, 153-155] Therefore, under low forward biases of 0.5 V and 1 V, a small peak at 504 nm exhibited (Figure 3-6a) primarily due to the CCN mechanism. Unlike the photoresponse peaked at 360 nm, which is caused by injected holes and thus increases dramatically with the increase of forward bias, the photoresponse peaked at 504 nm is mainly due to bulk exciton generation and thus remains almost no change with the increase of forward bias.

To further understand the narrow UV photoresponse, we calculated the wavelength-dependent exciton generation rate and electric field distribution in the active layer upon light illumination using optical Transfer Matrix Method (TMM) and electromagnetic three-dimensional Finite-Difference Time-Domain (3D-FDTD) simulations, respectively. We calculated the exciton generation rates across the device active layer under the illumination of four representative wavelengths, corresponding to the four regions discussed above, using TMM (Figure 3-6c). The

320 nm light produces a very low exciton generation rate throughout the active layer. The 360 nm light generates a higher exciton generation rate close to the PEDOT:PSS side that decays with distance into the active layer in oscillation. Light at the wavelength of 450 nm creates a very high exciton generation rate at the PEDOT:PSS/active layer interface due to the strong absorption of F8T2 that decays quickly with distance into the active layer. The 510 nm light, which is around the absorption edge of F8T2, can penetrate through the active layer and be reflected back, establishing an interference and being weakly absorbed throughout the active layer so that it can generate excitons through the active layer. The FDTD simulation also shows four distinct electric field distributions (Figure 3-6d). The weak electric field in the active layer corresponding to the wavelengths below 340 nm and between 390-500 nm explains the low EQEs exhibited (Figure 3-6a). Like an oscillating exciton generation rate through the active layer by 360 nm light, the FDTD simulation shows an electric field fringe throughout the active layer with the illumination of light between 340 and 390 nm wavelengths. It is also noticed that a strong electric field is generated about 150 nm into the active layer from the PEDOT:PSS interface, which supports the proposed photomultiplication mechanism that is induced by hole-injection resulted from the photogenerated electron traps in the lower portion of the active layer. The FDTD simulation shows an even stronger electric filed fringe for the wavelength above 500 nm because there is no absorption in the active layer. Despite no applied bias is involved, both TMM and FDTD simulations show four distinct regions for the exciton generation rate and electric field distribution throughout the active layer with respect to wavelength, which explain the EQE characteristics.

3.3.3 Device Performance Assessment

We further evaluated the device performance by calculating the responsivity (R) and the specific detectivity (D*). The responsivity, R, as the ratio of photocurrent to intensity of incident light, was calculated from the EQE according to Eq 3-3:

$$R = \frac{EQE \times e}{hv} \ (A\,W^{-1}) \qquad (3\text{-}3)$$

where *e*, *h* and *v* are defined in Equation (2). As shown in **Figure 3-7**a, R reached a maximum of 2.24 A/W at 358 nm under 3 V forward bias. The specific detectivity, D*, which indicates the ability of a photodetector to detect low levels of incident power, can be calculated as the following Eq 3-4:

$$D^* = \frac{R\sqrt{A}}{i_{noise}} \left(Jones \ or \ \sqrt{Hz}\ cm\ W^{-1}\right) \qquad (3\text{-}4)$$

where R is the responsivity, *A* is the active area of the device, which is 0.1 cm^2 in this work, and i_{noise} is the noise current spectral density (A $Hz^{-1/2}$). The i_{noise} was calculated from the Fast Fourier Transform of measured dark current versus time as shown in **Figure 3-8**. With a low noise current value of 0.084 pA $Hz^{-1/2}$, the specific detectivity reached a maximum of 8.45×10^{12} Jones at 358 nm under 3 V forward bias, as shown in Figure 3-7b. Since the noise measurements were done after UV exposure and a slightly increased dark current was observed after UV exposure compared to the dark current of pristine device, the specific detectivity reported here has a lower value.

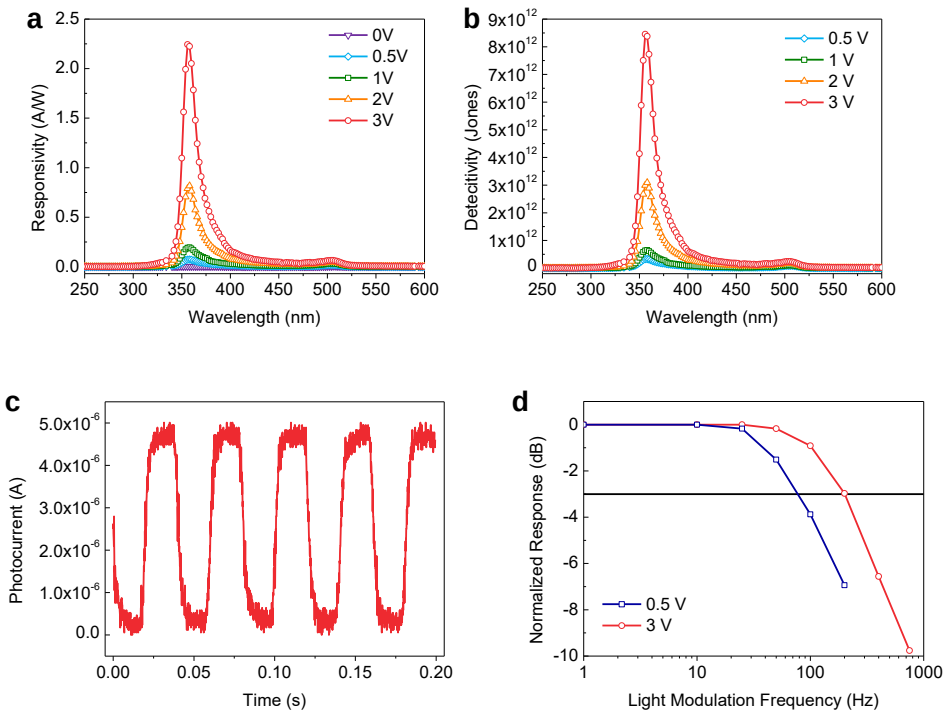

Figure 3-7 (a) Responsivity (R) and (b) specific detectivity (D*) spectra of the device under different forward biases. c) Response speed under 3 V forward bias and 360 nm light illumination with an intensity of 2.46×10^{-2} mW/cm^2. (d) Normalized response loss of the photodetector versus input light frequency under 0.5 and 3 V forward bias.

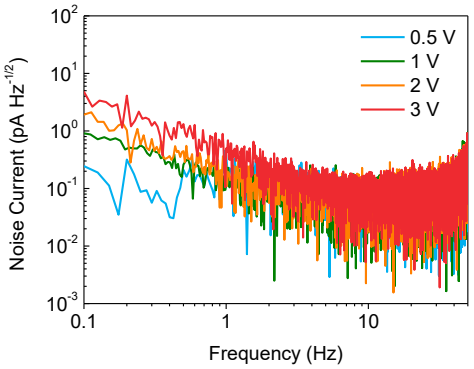

Figure 3-8 Noise current of the ITO/PEDOT:PSS/F8T2:ZnO NPs (1:6, w/w)/MoO3/Ag device under forward biases, calculated from the Fast Fourier Transform of measured dark currents,

measured after UV exposure. Generally, the noise current is evaluated as the summation of shot noise and thermal noise with the assumption that $1/f$ noise is negligible. Here, the noise current was calculated from the Fast Fourier Transform of measured dark current versus time, as shown in **Figure 3-9**. This data suggests that the measured noise current is mainly influenced by $1/f$ noise at low frequencies (f < 10 Hz), while the thermal noise dominates the noise current at high frequencies (f > 10 Hz). The photodetector device shows the similar noise current ~0.1 pA $Hz^{-1/2}$ under low reverse biases (≤ 3 V) at high frequency range.

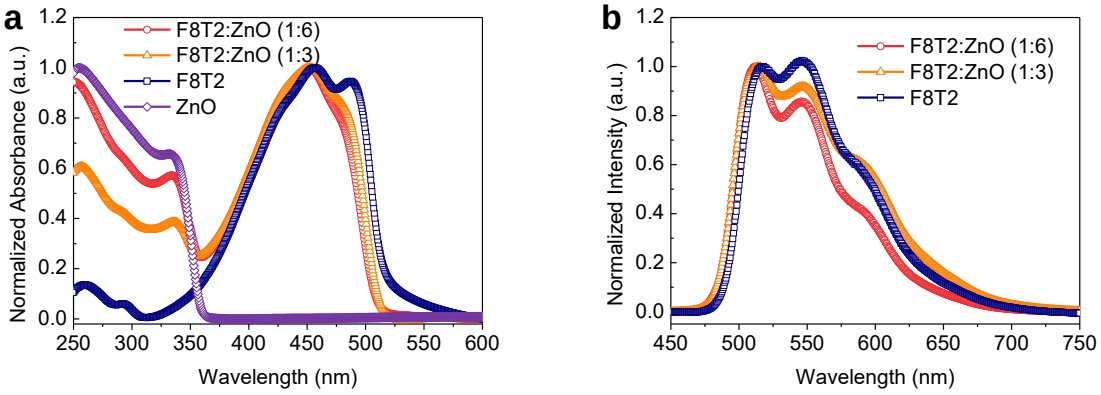

Figure 3-9 (a) Normalized UV-vis and (b) PL spectra of pure F8T2, ZnO, F8T2:ZnO NPs (1:6, w/w) and F8T2:ZnO NPs (1:3, w/w) thin films. The F8T2 absorption peak at 490 nm gradually decreases with the increase of ZnO NPs loading in the active layer, indicating the disrupted π-π stacking structure. The UV-vis and PL spectra were normalized to the highest absorption and the first PL peak, respectively.

The response time and frequency response loss are also critical for photodetector devices as in some applications such as missile detection, a fast response time is required. The response time was measured by illuminating the photodetector with 360 nm light that was turned on and off periodically with a chopper, while recording the photocurrent response with an applied forward

bias of 3 V. As shown in Figure 3-7c, the rise (fall) times are both around 6 ms as determined by the output signal changing from 10% to 90% (90% to 10%) of the peak output values. The relatively slow rise and fall times could be attributed to the hole dominated charge transport processes within F8T2, which has a hole mobility around 0.01–0.02 $cm^2\ V^{-1}\ s^{-1}$.[160] The slow response time could also be due to the trap-assisted hole tunneling working mechanism of the photodetector. The average responsivity calculated based on the response time measurement is 2.13 A/W, which is close to the value (2.24 A/W) obtained from the EQE measurement. The normalized response is calculated by Eq 3-5:

$$Normalized\ Response = 20Log\left(\frac{I}{I_0}\right)\ (dB) \qquad (3\text{-}5)$$

where I_0 and I are the photocurrent of the device under light with 0 Hz and some other, non-zero frequency, respectively. The -3 dB cutoff frequency refers to the non-zero frequency at which the amplitude of the photocurrent is decreased to $(1/2)^{0.5}$ of the value at 0 Hz. The -3 dB cutoff frequency is ~200 Hz under 3 V forward bias in our case (Figure 3-7d). This value is on the same order of magnitude as other reported photodetectors exhibiting photomultiplication, due to the electron-trapping induced hole-injection.[42, 154, 155] The device response speed is strongly dependent on the bias because of the charge carrier transit time.[170] The cutoff frequency decreased to 80 Hz when a 0.5 V forward bias was applied.

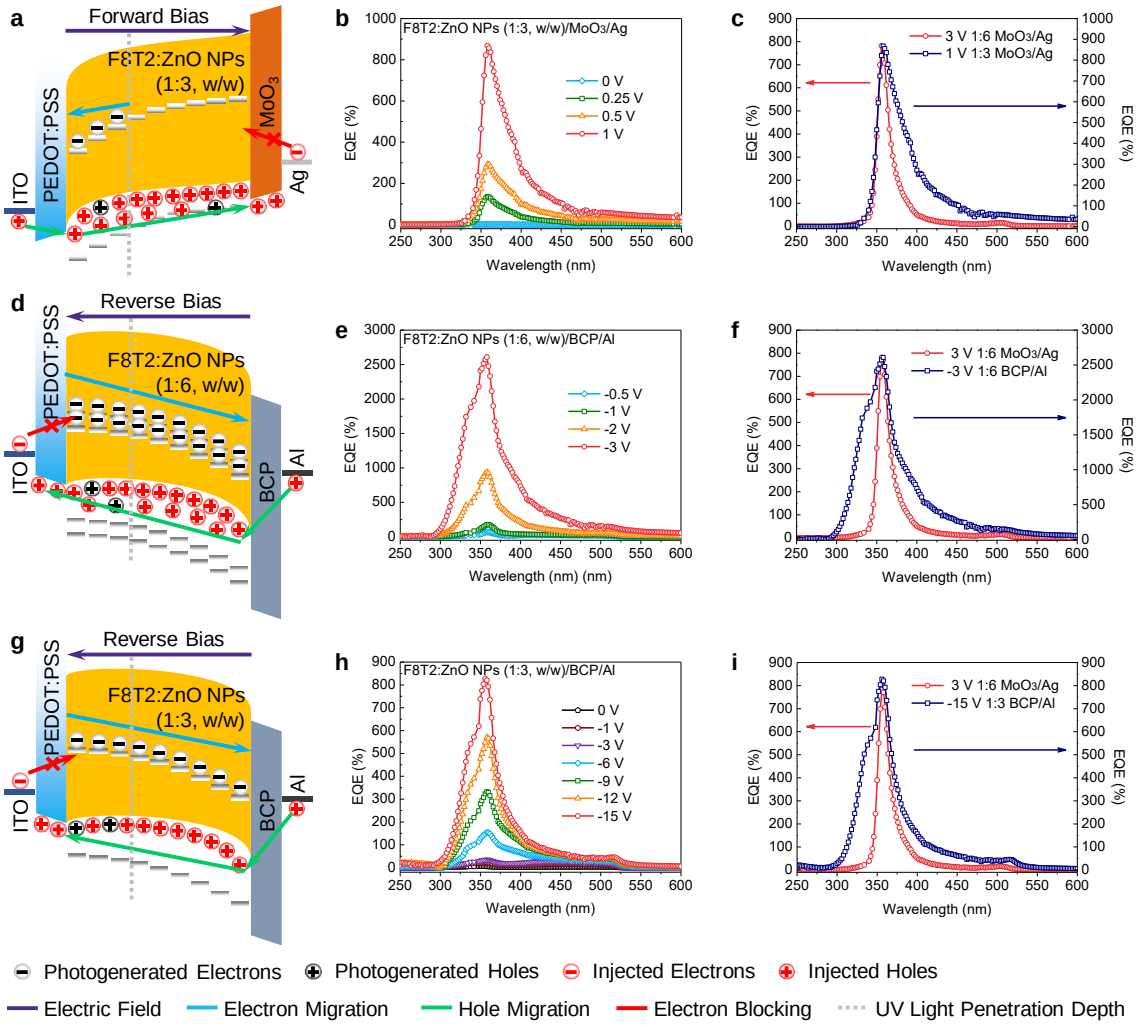

Figure 3-10 (a), (d), (g) Illustrations of charge transport and injection/blocking under forward or reserve biases of the corresponding photodetectors. (b), (e), (h) The EQE spectra of the corresponding photodetectors shown in (a), (d), (g), respectively, under different forward or reverse biases. (c), (f), (i) Comparisons of the EQE spectra of the corresponding photodetectors shown in (a), (d), (g), respectively, under forward or reverse bias, to the EQE spectrum of the feature device (labeled as 1:6 MoO_3/Ag) under 3 V forward bias.

3.3.4 Impacts of Weight Ratio and Device Structure on Device Performance

We achieved narrowband, photomultiplicative UV light detection under low forward driving voltage by utilizing the device structure of ITO/PEDOT:PSS/F8T2:ZnO NPs/MoO_3/Ag to favor hole transport. A relatively high F8T2:ZnO NPs weight ratio of 1:6 was used in the active layer to reduce visible light absorption while allowing electron trapping under UV illumination to achieve UV-selective photomultiplication. We refer this device as the "feature device" in the following discussion. To investigate the effects of F8T2:ZnO NPs weight ratio and device structure on the device performance, we fabricated photodetectors with a lower F8T2:ZnO NPs weight ratio of 1:3 and replaced the hole transport/electron blocking layer MoO_3 and the high work function electrode Ag with the electron transport/hole blocking layer bathocuproine (BCP) and the low work function electrode Al. These substitutions transform the device from a hole-only structure of ITO/PEDOT:PSS/F8T2:ZnO NPs/MoO_3/Ag to a conventional structure of ITO/PEDOT:PSS/F8T2:ZnO NPs/BCP/Al.

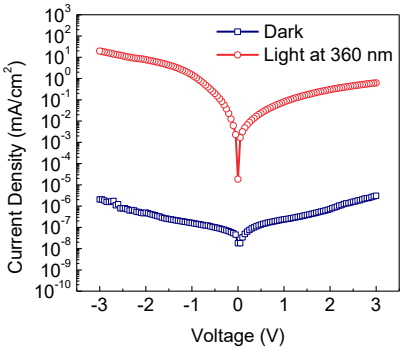

Figure 3-11 The J-V curves of the device ITO/PEDOT:PSS/F8T2:ZnO NPs (1:3, w/w)/MoO_3/Ag under dark and 360 nm light illumination with the intensity of 2.46×10^{-2} mW/cm^2

3.3.4.1 Weight Ratio in Active Layer

In **Figure 3-10**a-c, the impact of lowering the weight ratio of F8T2:ZnO NPs from 1:6 to 1:3, while keeping the ITO/PEDOT:PSS/F8T2:ZnO NPs/MoO_3/Ag device structure and the active layer thickness of 450 nm, was investigated. The basic device working mechanism of charge injection/blocking and transport under forward bias is maintained and illustrated in Figure 3-10a. However, the microstructure change of the active layer affects charge trapping/transport and ultimately the device performance. The device with a 1:3 weight ratio of F8T2:ZnO NPs exhibited a much higher peak EQE value (868%, Figure 3-10b) compared to the feature device (68%, Figure 3-2a) under 1 V forward bias. The increased EQE value under a low forward bias could be attributed to more and better crystalline F8T2 domains in the active layer due to less disruption from ZnO NPs, improving the hole transport in the active layer. The improvement of π-π stacking in F8T2 for the 1:3 weight ratio F8T2:ZnO NPs layer is supported by the UV-Vis absorption (Figure 3-9), which has a higher 490 nm absorption peak than that of the 1:6 blend film.[164] The higher amount of F8T2 in the active layer caused a relatively stronger response at longer wavelengths, leading to a broader EQE peak with a FWHM of 38 nm under 1 V forward bias, compared to the 16 nm FWHM achieved by the feature device, though this device maintained the same EQE onset at 340 nm. The J-V characteristics of the device (**Figure 3-11**) was also influenced by the change of the microstructure of the active layer. The dark J-V curve remained symmetric with slightly higher dark current densities than those of the feature device. The J-V curve produced under 360 nm monochromatic illumination exhibited a weaker rectification with the rectification ratio of 31 under ±3 V, compared to 1,241 for the feature device, because of the increased forward photocurrent and decreased reverse photocurrent. While the reduction of ZnO NPs in the active

layer leads to more, better F8T2 crystalline domains, which increases the forward photocurrent, it also reduces the amount of ZnO NP electron traps, which decreases the reverse photocurrent.

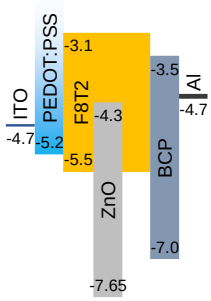

Figure 3-12 Energy diagram of the materials employed in the device with the structure of ITO/PEDOT:PSS/F8T2:ZnO NPs/BCP/Al.

3.3.4.2 Device Structure

In Figure 3-10d-f, the impact of changing the device structure to a conventional architecture while maintaining the same active layer weight ratio (1:6, w/w) and thickness (450 nm) was investigated. The conventional device works under reverse bias because of the band energy alignment (**Figure 3-12**). As illustrated in Figure 3-10d, photogenerated electrons diffuse toward Al electrode and are trapped in ZnO NPs. This bends down the energy level of F8T2 close to the top BCP/Al side and allows for hole injection from the Al electrode under illumination and reverse bias, and holes transfer through F8T2 and are collected in the ITO electrode. The J-V curves of the devices under both dark and 360 nm monochromatic light exhibited rectification due to the diode structure and strong photoresponses to the UV light under reverse bias (Figure 3-13). The conventional device, however, lost the narrowband response feature and showed broader EQE spectra, with an onset at 300 nm, a shoulder around 330 nm, and a tail at longer wavelengths (Figure 3-10e and f). Electrons generated close to the ITO/PEDOT:PSS side, by the 300 to 340

nm UV light, are able to migrate toward the BCP/Al side, causing band bending and hole injection from the Al electrode under reverse bias (Figure 3-10d). The detection window was also expanded into the visible region because absorption in F8T2 can generate trapped electrons that can migrate towards the Al electrode under reverse bias and contribute to band bending and photoresponse. Photomultiplication was easily achieved by the conventional device, with EQE values over 100% produced under -0.5 V bias and a peak EQE value of 2,609% under -3 V reverse bias at 358 nm (Figure 3-10e), which is higher than the peak EQE value of 782% produced by the feature device under 3 V forward bias (Figure 3-10f). However, the conventional device also experienced high dark current after working under UV illumination and reverse bias (**Figure 3-13**a) due to the large amount of ZnO NPs and the change of surface states.[166-169]

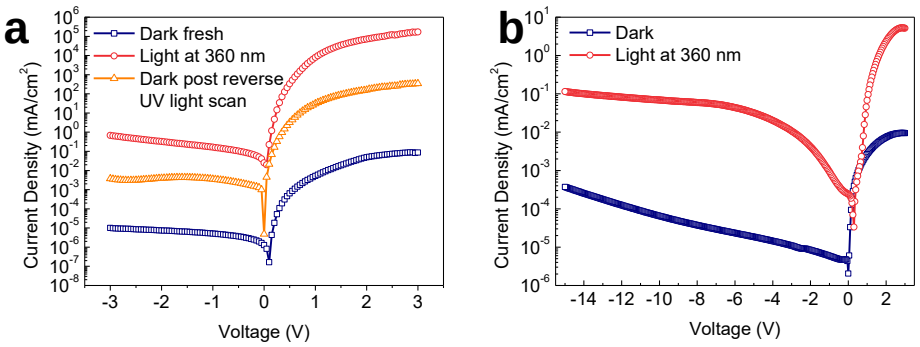

Figure 3-13 (a) The J-V curves of the pristine ITO/PEDOT:PSS/F8T2:ZnO NPs (1:6, w/w)/BCP/Al device under dark and 360 nm light illumination with the intensity of 2.46×10^{-2} mW/cm^2 and the re-measured dark J-V curve after the device was tested under 360 nm illumination and reverse bias. (b) The J-V curves of the device ITO/PEDOT:PSS/F8T2:ZnO NPs (1:3, w/w)/BCP/Al under dark and 360 nm light illumination with the intensity of 2.46×10^{-2} mW/cm^2.

Similarly, the weight ratio of F8T2:ZnO NPs also impacts the conventional device performance. In Figure 3-10g-i, the conventional device was investigated with a F8T2:ZnO NPs

weight ratio of 1:3 in the active layer, which is referred as “low weight ratio conventional device”. The same mechanisms discussed for the conventional device in Figure 3-10d-f are engaged, but lowering the F8T2:ZnO NPs weight ratio to 1:3 resulted in much lower EQE values, and higher reverse biases were required due to the reduced number of ZnO NPs electron traps. As shown in Figure 3-10h, only 828% EQE was achieved under the high reverse bias of -15 V for the low weight ratio conventional device. The low weight ratio conventional device was stable in the dark and under 360 nm illumination even up to -15 V reverse bias (Figure 3-13b), and exhibited a maximum responsivity of 2.32 A/W at 358 nm under -15 V reverse bias (**Figure 3-14**a), which is similar to 2.24 A/W produced by the feature device under 3 V bias at 358 nm. However, the noise current of the low weight ratio conventional device dramatically increased to 8.17 pA $Hz^{-1/2}$ with -15 V reverse biases (Figure 3-14b), compared to 0.084 pA $Hz^{-1/2}$ of the feature device under 3 V forward bias, resulting in the specific detectivity of 8.99×10^{10} Jones at 358 nm under -15 V reverse bias (Figure 3-14c), which is about two orders of magnitude lower than the feature device. The low weight ratio conventional device exhibited a faster response time (3 ms) based on the illumination on/off photoresponse measurement and a higher -3 dB response cutoff frequency (~340 Hz) under -12 V bias (Figure 3-14d and e). The faster response compared to the feature device could be due to the electron transport and hole blocking functions of BCP, which provides a pathway for the trapped electrons in ZnO NPs towards the Al electrode under reverse bias and relaxes the F8T2 band bending, effectively shutting down the hole tunneling.

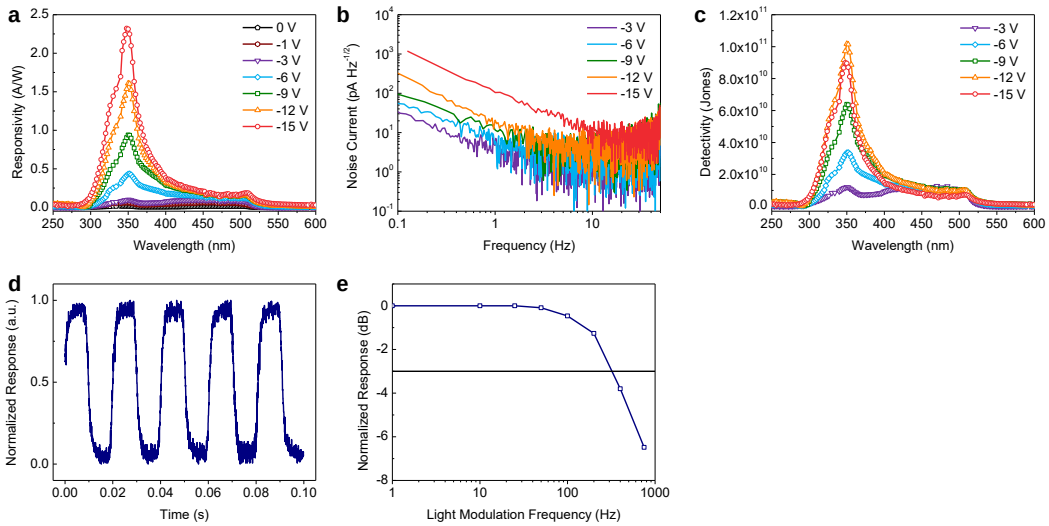

Figure 3-14. The device performance of the photodetector with the structure of ITO/PEDOT:PSS/F8T2:ZnO NPs (1:3, w/w)/BCP/Al. (a) Responsivity spectra, (b) noise current (measured after UV exposure), and (c) specific detectivity spectra under different reverse biases. The responsivity reached a maximum value of 2.32 A/W under -15 V reverse bias at 358 nm. The specific detectivity reached a maximum value of 1.02×10^{11} under -12 V reverse bias at 358 nm. (d) On/off photoresponse and (e) response loss versus input light frequency under -12 V reverse bias.

3.4 Conclusion

In conclusion, we reported a method to design photomultiplication-type narrowband UV photodetectors. The method is based on the symmetric device structure and the manipulation of light penetration depth in the active layer. We fabricated a UV-specific ultra-narrowband photodetector. The fabricated photodetector exhibited a high EQE of 782% at 358 nm under a low forward bias of 3 V and therefore a high specific detectivity of 8.45×10^{12} Jones. The ultra-narrow response window with the FWHM of 16 nm was observed. Our method offers a pathway to design and fabricate narrowband photodetectors.

Chapter 4 REVEALING STABILITY OF INVERTED PLANAR MA-FREE PEROVSKITE SOLAR CELLS AND ELECTRIC FIELD-INDUCED PHASE INSTABILITY

4.1 Introduction

Methylammonium lead triiodide ($MAPbI_3$) perovskite is one of the most studied perovskites and the PCE as high as 20% has been demonstrated for single junction solar cells.[60, 171, 172] However, $MAPbI_3$ perovskite is not an ideal option to fabricate high performance and stable single junction perovskite solar cells mainly due to its intrinsic moisture and thermal instability.[70-72, 173, 174] Formamidinium (FA) as another organic cation has been applied as a replacement for MA to solve the instability issues.[73] However, $FAPbI_3$ suffers from phase instability under room temperature. It spontaneously transfers from a photoactive α-phase to a photoinactive δ-phase at room temperature in a few days.[74] To solve the phase instability problem, alkaline cation such as Cs^+ and Rb^+ cations are introduced to partially replace the large FA cation to adjust the Goldschmidt tolerance factor.[75-84] Compare with the well-studied Cs^+ cation, the incorporation of Rb^+ in $FAPbI_3$ and the effect of Rb^+ on phase stability and device performance remain unclear. There are only a few works regarding Rb-doped MA-free perovskite solar cells and all are in the conventional device structure.[82, 84]

Beyond intrinsic phase stability problem, ion migration induced operational degradation is another critical factor that prevents the commercialization of perovskite solar cells.[175-179] Ion migration has been observed in both single component and mixed-cation/-halide perovskites, where the A-site cation and the X-site halide with low activation energy migrate spontaneously or

upon stimulation. Higher energy irradiance, temperature, and electric field have been reported to trigger the ion migration.[180] Ion migration must be mediated by the defects in perovskite solid films, such as Schottky and Frenkel defects and grain boundaries.[85, 181] In order to thoroughly prevent the degradation and meet the real-life usage requirement, it is highly demanded to fabricate MA-free perovskites with reduced defect densities.

In this work, we purposely selected mixed Cs^+ and Rb^+ and single Cs^+ as the A-site cation dopants to fabricate two types of MA-free perovskites, $Rb_{0.05}Cs_{0.1}FA_{0.85}PbI_3$ and $Cs_{0.15}FA_{0.85}PbI_3$, and investigated the effect of Rb^+ cations on device performance and long-term stability against electric field of inverted structured MA-free perovskite solar cells. We demonstrated that the incorporation of Rb^+ cations in the perovskite lattice was incomplete, but it improved the device performance despite the long-term device stability is reduced. Supported by the cross-sectional scanning electron microscopy (SEM), x-ray photoelectron spectroscopy (XPS), and time of flight secondary ion mass spectrometry (ToF-SIMS), we revealed that the degradation was due to the defect mediated I^- anion and Rb^+ and Cs^+ cation migration under electric field, and Rb cations are more vulnerable against electric field than Cs cations. In addition, we varied the precursor preparation methods to effectively control the defect densities in the resulted perovskite films, which not only impacts the device performance but also the device stability. The stabilized $Rb_5Cs_{10}FA_{85}PbI_3$ and $Cs_{15}FA_{85}PbI_3$ devices retain 68% and 92% of their initial PCEs after 30 days under N_2 protection. Our work elucidates that Rb^+ cation is a promising A-site dopant along with Cs^+ cation for stabilizing photoactive α-phase $FAPbI_3$ and enhancing device performance and stability while its migration under electric field needs to be effectively suppressed via reducing defect densities during the perovskite thin film preparation process. Our work also reveals that

simply mixing precursor solution prior to spin coating is one of the accessible methods to reduce defect densities, and thus the ion migration in perovskite solar cells.

4.2 Experimental

4.2.1 Materials

Indium tin oxide (ITO) coated glass (sheet resistance = 10 Ω sq^{-1}) was purchased from Colorado Concept Coating LLC. Poly(3,4-ethylenedioxythiophene):polystyrene sulfonate (PEDOT:PSS, CLEVIOS P VP AI 4083) was purchased from Heraeus. Lead iodide (PbI_2, for perovskite precursor, 99.99%) was purchased from Tokyo Chemical Industry. Formamidinium iodide (FAI) was purchased from Greatcell Solar. Ag evaporation pellets (99.999%) were purchased from R.D. Mathis. Dimethyl sulfoxide (DMSO, anhydrous, ≥99.9%), N,N-Dimethylformamide (DMF, anhydrous, ≥99.8%), chloroform (anhydrous, ≥99%), 2-propanol (anhydrous, 99.5%), bathocuproine (BCP, 96%), diethyl ether (DEE, ≥99.0%), RbI (99.9%), and CsI (99.999%) were purchased from Sigma-Aldrich. All the materials were used as received without further purification.

4.2.2 Thin Film Fabrication

Perovskite precursors were prepared as following: PbI_2 (1.1 M) was dissolved in DMF:DMSO 4:1 (v:v) by stirring at 80°C for 1 h. PbI_2 (1.1 M) solution was added into RbI (1 M), CsI (1 M), and FAI (1 M) to form $RbPbI_3$, $CsPbI_3$, and $FAPbI_3$ precursor solutions. $RbPbI_3$ and $FAPbI_3$ solutions were stirred at room temperature for 1 h. $CsPbI_3$ solution was stirred at 80°C for ~3.5 min then room temperature for 1 h. $Rb_{0.05}Cs_{0.1}FA_{0.85}PbI_3$ and $Cs_{0.15}FA_{0.85}PbI_3$ precursor solutions were prepared by mixing the desired volumetric ratios of the above solutions. The final precursor solution was stirred at room temperature overnight and passed 0.45 μm PTFE filter. Glass

substrates were cut into 1.5 cm × 1.5 cm pieces, then cleaned by sonication in soapy deionized (DI) water, DI water, acetone, and isopropanol for 15 min each sequentially and finally treated with 100 W oxygen plasma for 10 min. PEDOT:PSS was spin coated onto the cleaned glass substrate at 5000 rpm (ramp: 5000 rpm/s) for 60 s, followed by annealing at 150°C for 10 min in the ambient condition. The substrates were then transferred into a N_2 filled glove box. The substrates and precursor solution were placed on a 70°C hotplate and the precursors were either stirred under 500 rpm or unstirred. The heated substrate was transferred onto the spin coater, and the hot precursor solution was dropped onto the substrate. The substrate was spin at 1000 rpm for 10 s (ramp: 200 rpm/s) and 4000 rpm for 30 s (ramp: 4000 rpm/s). A 300 μL of DEE was dropped onto the substrate at the last 10 or 15 s of the entire process for $Rb_{0.05}Cs_{0.10}FA_{0.85}PbI_3$ and $Cs_{0.15}FA_{0.85}PbI_3$, respectively. The substrates were annealed at 100°C for 10 min.

4.2.3 Thin Film Characterization

Scanning electron microscopy (SEM) and energy dispersive spectroscopy (EDS) were acquired using a FEI Sirion SEM to investigate the surface morphology and elemental compositions of perovskite thin films, respectively. Two-dimensional X-ray diffraction (XRD) patterns were performed on a Bruker D8 Discover with IμS 2-D XRD System using Cu Kα radiation (λ = 1.54184 Å). Cross-sectional SEM was performed on TFS Apreo-S with Lovac without any sample pre-treatment. Ultraviolet-visible (UV-Vis) absorption spectra were collected via a Varian Cary 5000 UV-Vis-NIR spectrophotometer. Ultraviolet photoelectron spectroscopy (UPS) measurements were performed on a Kratos AXIS Ultra DLD spectrometer. A He discharge lamp source (Kratos) at an excitation energy of 21.2 eV was used in combination with a delay line detector at an electron pass energy of 5 eV. The UPS spectra for Au were acquired with a step size of 0.1 eV and a dwell time of 100 ms. The high-resolution UPS spectra and Fermi edge spectra were acquired with a

step size of 0.01 eV and a dwell time of 100 ms. X-ray photoelectron spectroscopy (XPS) measurements were performed on Kratos AXIS Ultra DLD X-ray photoelectron spectrometer. The incident X-rays were monochromatized Al Kα (KE = 1486.6 eV) operated at 10 mA and 15 kV. All XPS data were acquired at normal photoelectron takeoff angle of 0º. The survey spectra were acquired with a step size of 1.0 eV and a dwell time of 100 ms at a spectrometer pass energy of 160 eV. The high-resolution spectra were acquired with a step size of 0.1 eV and a dwell time of 425 ms for S 2p spectra and 259 ms for C 1s spectra at a spectrometer pass energy of 40 eV. Data analysis was performed using Kratos Vision Processing software (ver. 2.2.8). The binding energy scale was calibrated by assigning the lowest binding energy C1s peak to 285.0 eV. All samples were measured under ultrahigh vacuum of around 5 x 10^{-9} torr. The probing depth for both UPS and XPS was approximately 10 nm. Time of flight secondary ion mass spectrometry (ToF-SIMS, ION-TOF) was applied to gain the depth profile after the devices have been undergoing the stability tests. A beam of Ar_{1000} with 10 keV (4.4 nA) was applied for depth profiling on a raster area of 300 × 300 μm^2. A Bi^{3+} primary beam (0.01 pA) was scanned over a 100×100 μm^2 area. The data are normalized by the measured total ion counts to eliminate the artifacts from a charging ion yield in different layers.

4.2.4 Device Fabrication

ITO coated glass substrates with the size of 1.5 cm × 1.5 cm were cleaned following the same cleaning procedure as glass substrates. PEDOT:PSS and perovskite layers were fabricated as described in the thin film fabrication section. A 60 μL drop of $PC_{60}BM$ solution (15 mg/mL in chloroform) was spin coated onto the perovskite layer at 4000 rpm (ramp: 4000 rpm/s) for 60 s without annealing. A 70 μL drop of BCP solution (0.5 mg/mL in 2-propanol) was spin coated onto the $PC_{60}BM$ layer at 4000 rpm (ramp: 4000 rpm/s) for 60 s without annealing. The devices were

finished by the deposition of a 150 nm Ag layer at the rate of 0.2 nm/s with a mask to a final device size of 0.0314 cm^2. The thermal evaporation processes were performed in a background vacuum less than 2×10^{-6} Torr.

4.2.5 Device Characterization

The photocurrent density-voltage (J−V) measurements were performed in a N_2 filled glove box and recorded by a Keithley 2400 source meter from -0.5 V to 1.5 V (forward scan) or 1.5 V to -0.5 V (reverse scan) under illumination by a 450 W oriel Xenon lamp with a AM 1.5G filter solar simulator (100 mW/cm^2). The light intensity was calibrated with a standard Si photodiode equipped with KG-5 filter. The calibration diode was calibrated by the National Renewable Energy Laboratory. The EQE spectra were measured using a setup consisting of a Xenon lamp (Oriel, 300W) as a light source, a monochromator (Newport Cornerstone 130), a mechanical chopper (Stanford Research Systems Inc.) with a frequency of 200 Hz, a lock-in amplifier (Stanford Research Corp SR830), and a NIST-certified Si photodiode (Thorlabs FDS 1000CAL) for calibration. The EQE spectra were integrated over AM 1.5G photon flux to attain photocurrent density.

4.3 Results and Discussion

4.3.1 MA-Free Perovskite Solar Cells Characterization

One-step solution process of hot casting with anti-solvent was applied to fabricate $Rb_{0.05}Cs_{0.10}FA_{0.85}PbI_3$ and $Cs_{0.15}FA_{0.85}PbI_3$ perovskite thin films,[171] which are named as Rb5Cs10 and Cs15, respectively. The perovskite films prepared using well-mixed precursor solutions denoted as Rb5Cs10-M or Cs15-M while those without stirring as Rb5Cs10-U or Cs15-U. The perovskite solar cells were fabricated in an inverted structure as

ITO/PEDOT:PSS/Perovskite/$PC_{60}BM$/BCP/Ag, where perovskite active layers are Rb5Cs10-M, Rb5Cs10-U, Cs15-M and Cs15-U, respectively.

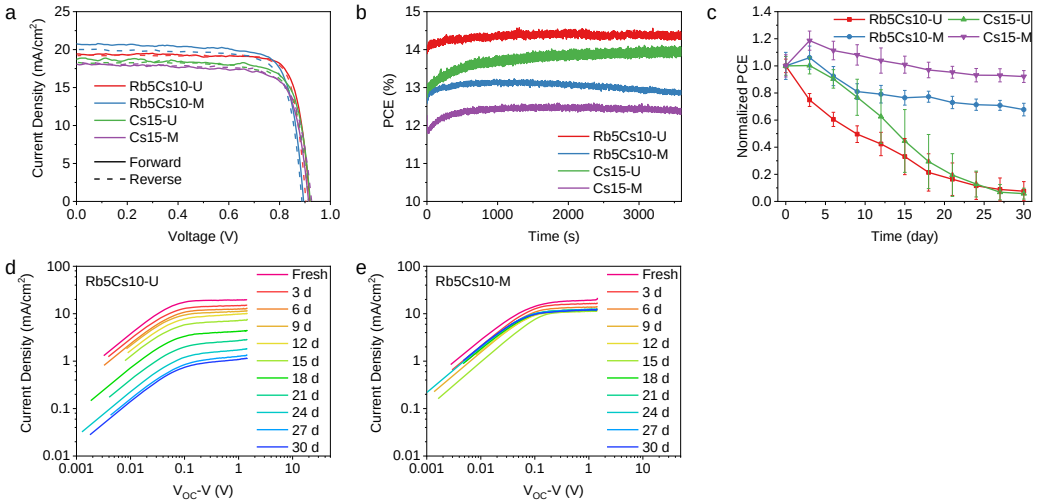

Figure 4-1 (a) J-V characteristics, (b) PCE versus time at the maximum power output, and (c) normalized PCE versus time for the solar cells based on Rb5Cs10-U, Rb5Cs10-M, Cs15-U and Cs15-M perovskite active layers. (d, e) Photocurrent density versus effective voltage of the solar cells with Rb5Cs10-U and Rb5Cs10-M active layers, respectively, by tracking the same device over 30 days.

Table 4-1. Average photovoltaic parameters of the perovskite solar cells based on different active layers.

Active Layer	Jsc (mA/cm^2)	Voc (V)	FF	PCE (%)
Rb5Cs10-U	17.65±0.72	0.93±0.01	0.81±0.01	13.22±0.52
Rb5Cs10-M	17.00±1.10	0.92±0.02	0.74±0.02	11.52±1.10
Cs15-U	18.16±0.70	0.91±0.01	0.74±0.02	12.17±0.84
Cs15-M	15.04±0.84	0.90±0.02	0.67±0.03	9.05±0.68

Figure 4-1a shows the current density-voltage (J-V) characteristics of the devices under forward and reversed scans and the device performance parameters are summarized in **Table 4-1**. All devices show ignorable hysteresis. Devices fabricated with un-mixed precursor solutions exhibit better performance than their counterparts with mixed precursor solutions. Rb5Cs10-U devices show a J_{SC} of 17.65 mA/cm^2, a V_{OC} of 0.93 V, an FF of 0.81, and a PCE of 13.22%. The Rb5Cs10-M devices give a slightly reduced J_{SC} of 17.00 mA/cm^2 and V_{OC} of 0.92 V, while a heavily reduced FF of 0.74, which results in a reduced PCE of 11.52%. The Cs15-U and Cs15-M devices show a similar trend, with J_{SC} reduced from 18.16 to 15.04 mA/cm^2, V_{OC} from 0.91 to 0.90 V, FF from 0.74 to 0.67, and in sum, PCE from 12.17 to 9.05%. The EQE spectra (**Figure 4-2**) of Rb5Cs10-M device shows a sharp cutoff at around 830 nm and an integrated photocurrent density of 17.30 mA/cm^2. The incorporation of Rb^+ cation boosts up the device performance regardless of mixed or un-mixed precursor solutions. All devices exhibit good short-term stability at the maximum power output (MPP) over one-hour measurement.

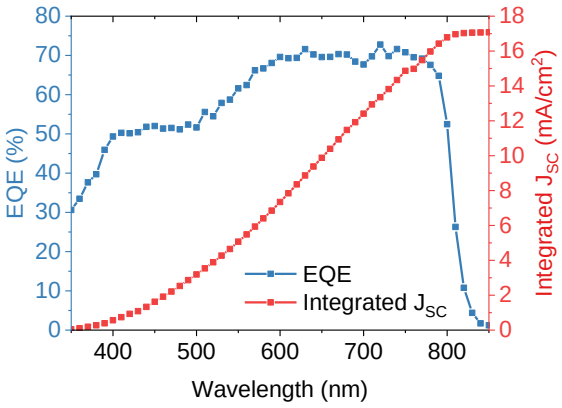

Figure 4-2 The external quantum efficiency (EQE) spectrum versus wavelength and the integrated current density from the EQE spectrum of the Rb5Cs10-M device.

The long-term device stability was evaluated by measuring the J-V curves every 3 days for 30 days. The devices were stored in a N_2 glove box without encapsulation in dark between measurements. As shown in Figure 4-1c, the PCEs of both Cs15-U and Rb5Cs10-U devices drop significantly to less than 10% of the initial values over the 30 days testing period. The Cs15-U devices show a relatively improved stability in the first 20 days than the Rb5Cs10-U devices. The Cs15-M devices exhibit even increased PCEs in the first 15 days with a peak PCE about 20% higher than the initial values on the 3rd day. The PCEs retain 92% of the initial values at the end of 30 days. The Rb5Cs10-M devices also exhibit an initial PCE increase in the first 3 days but a quick drop of PCE in the next 6 days and then maintain 68% of the PCEs to the end of 30 days. The losses of PCEs are mainly due to the decrease of J_{SC}'s as the V_{OC}'s remain unchanged over the 30 days for all devices and the FFs even increase for the Rb5Cs10-M and Cs15-M devices (**Figures 4-3**a-c).

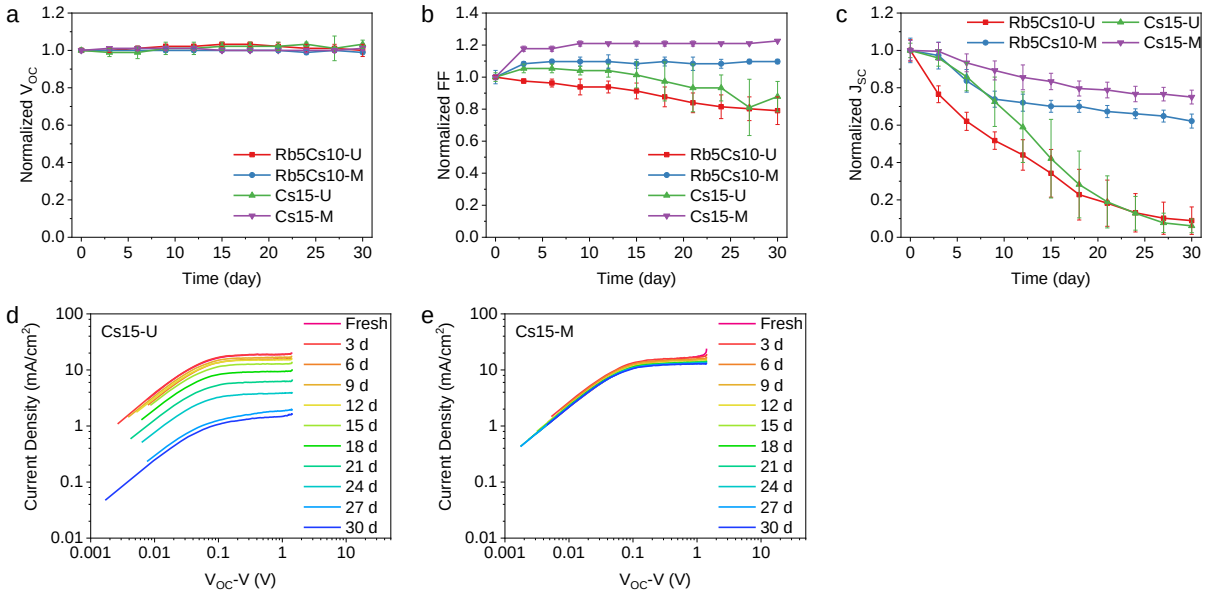

Figure 4-3 Normalized (a) V_{OC}, (b) FF, and (c) J_{SC} of the solar cells with Rb5Cs10-U and Rb5Cs10-M and Cs15-U and Cs15-M active layers stored in a N_2 filled glove box in dark at room

temperature with a testing interval of 3 days for 30 days. (d, e) Photocurrent density versus effective voltage of the solar cells with Cs15-U and Cs15-M active layers, respectively, by tracking the same device over 30 days.

The reduction of J_{SC} is generally attributed to interfacial degradation and/or active layer degradation. The interfacial degradation refers to the generation of deep trap states at the perovskite/transport layer interfaces, or the degradation of the transport layers.[182-184] Both types of the interfacial degradation would affect the charge carrier extraction but not the charge carrier generation and transport in the active layer. On the other hand, active layer degradation, such as phase degradation and decomposition, would significantly reduce the active layer light absorption and directly impact on the charge carrier generation and transport.[185] To identify which degradation could be the key factor for J_{SC} decrease, we first evaluated the charge extraction of the devices over time. We plotted the photocurrent density versus effective voltage for Rb5Cs10-U and Rb5Cs10-M devices in a 3-day interval for 30 days as shown in Figures 4-1d and e, respectively. The effective voltage is defined as the voltage applied on the active layer, given by the open circuit voltage minors the externally applied voltage (V_{OC}-V). When the effective voltage equals zero, the photogenerated charge carriers have no driving force to flow to the external circuit and therefore recombine in the active layer, exhibiting no photocurrent density. With the increasing of effective voltage, photogenerated charge carriers start to flow to the external circuit under the electric field, and the photocurrent density increase linearly with the increased effective voltage till the turning point. At the photocurrent density plateau region, all the photogenerated charge carriers are extracted by the effective voltage and the current flow is only limited by the generation rate of the charge carrier in the active layer. In Figures 4-1d and e, the photocurrent densities reach the plateaus at a low effective voltage of 0.1-0.2 V, suggesting that charge carriers are swept out

efficiently and interfacial charge extraction is not a limiting factor of the device performance.[186] In addition, the plateau effective voltage, at which the photocurrent densities reach the plateaus, does not change over the storage time, indicating that the reduction of J_{SC} is not caused by the interfacial degradation. The Rb5Cs10-U device exhibits a decreased plateau current density at high effective voltage over the 30 days testing, indicating that the charge carrier generation rate in the active layer is the reason of the device degradation. In contrast, the plateau current density of the Rb5Cs10-M device decreases in the first 9 days and then maintains almost the same in the following 21 days, suggesting that the charge generation rate is maintained at the similar level. Similarly, both Cs15-U and Cs15-M devices exhibit the constant plateau effective voltage of 0.1-0.2 V over the 30 days, while the plateau current density of Cs15-U significantly decreases and that of Cs15-M remains constant (Figures 4-3d and e). The decreased plateau current density again indicates the reduced charge generation rate in the active layer.

4.3.2 MA-Free Perovskite Thin Films Characterization

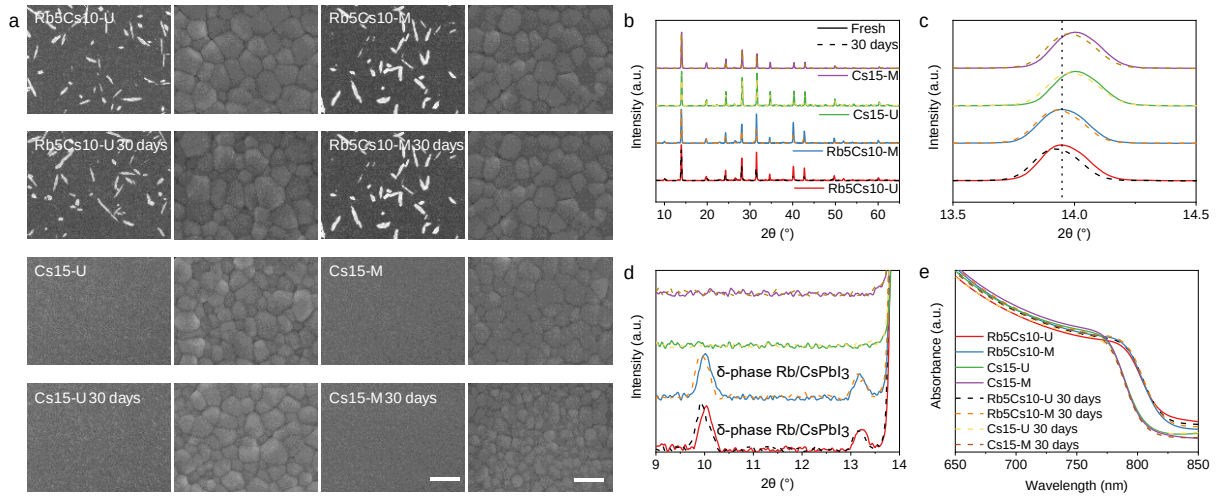

Figure 4-4 (a) SEM images, (b-d) XRD patterns, and (e) UV-Vis absorption spectra of Rb5Cs10-U and Rb5Cs10-M, and Cs15-U and Rb5Cs10-M thin films on glass/PEDOT:PSS substrates that

are freshly prepared and after stored in dark under N_2 protection for 30 days. Scale bars are 5 μm and 500 nm for the low and high magnification images, respectively.

To fully understand the impacts of mixed Rb^+ and Cs^+ cation versus single Cs^+ cation doping in the A-site of $FAPbI_3$ as well as the precursor preparation methods on MA-free device performance and stability, we characterized freshly made and aged thin films as well as the active layers after device stability tests. SEM images (**Figure 4-4**a), XRD patterns (Figure 4-4b-d) and UV-Vis spectra (Figure 4-4e) show that there are no significant differences in film morphology, crystalline phase and optical band gap for Rb5Cs10-U and Rb5Cs10-M films or Cs15-U and Cs15-M films. However, differences are observed for perovskites with or without Rb. White rods present on both Rb5Cs10-U and Rb5Cs10-M films but not on Cs15-U and Cs15-M films (Figure 4-4a). The energy dispersive spectroscopy (EDS) of the Rb5Cs10-U thin film shows the white rod regions have higher amount of Cs and Rb, especially Rb, while less FA content (indicated by element N) compared to these element contents in the background regions (**Figure 4-5** and **Table 4-2)**. Giving the same total 15% substitutional quantity of small cations for FA cations and the smaller radius of Rb^+ (1.52 Å) than Cs^+ (1.67 Å), the (110) peak of a Rb5Cs10 thin film should appear at the higher diffraction angle than that of a Cs15 thin film if all small cations are integrated into the perovskite lattice. However, Figure 4-4c shows that the (110) peaks of the Rb5Cs10 thin films are at 13.94° compared to 14.00° for the Cs15 thin films, indicating that less Cs^+ and Rb^+ cations are integrated into the perovskite lattices.[75] In addition, two extra peaks, corresponding to the δ-phase Rb/$CsPbI_3$,[82, 84, 178, 187, 188] present at 10.04° and 13.22° for the Rb5Cs10-U thin film and at 10.02° and 13.18° for the Rb5Cs10-M thin film (Figure 4-4d). The EDS and XRD results indicate that the white rods could be enriched δ-phase Rb/$CsPbI_3$ segregated from the Rb5Cs10 perovskites. The UV-Vis spectra show that the absorption cutoffs of Rb5Cs10 perovskite thin films

are around 832 nm, exhibiting an obvious red shift comparing with the cutoffs around 821 nm for Cs15 thin films, which is attributed to the less incorporation of small Cs^+ and Rb^+ cations in the perovskite lattice.[64, 84] The SEM, EDS, XRD and UV-Vis results reveal that Rb^+ cation is less effectively integrated into the $FAPbI_3$ lattice than Cs^+ cation and co-doping Rb^+ with Cs^+ could even induce the segregation of Cs^+ cation along with Rb^+ cation, forming mixed δ-phase Rb/$CsPbI_3$ white rods on the Rb5Cs10 films.

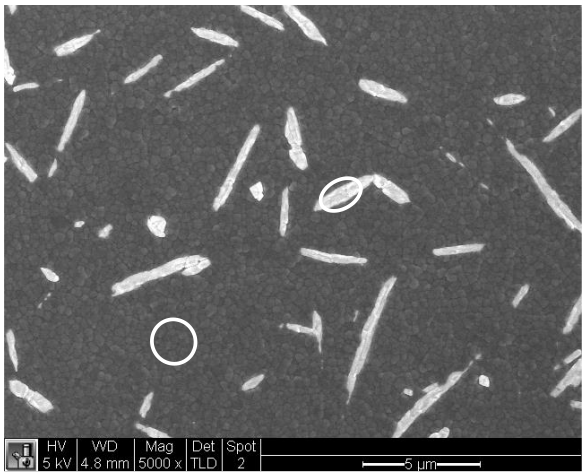

Figure 4-5 SEM image of Rb5Cs10-U perovskite thin film. EDS data were collected from the thin film background and while rod region indicated by white circles.

Table 4-2 Molar percentage of the elements in the Rb5Cs10-U perovskite thin film averaged from 3 EDS scans. Due to the low accuracy of the EDS experiment for perovskite thin films, the values reflect only the relative rather than accurate amount of the elements.

Region	I	Pb	C	N	Cs	Rb
Background	30%	11%	37%	20%	1-2%	<1%
White rods	33%	12%	39%	9%	4%	3%

To rule out the effect of mixed Rb^+ and Cs^+ cation doping and single Cs^+ cation doping on $FAPbI_3$ perovskite phase stability, we conducted SEM, XRD, and UV-Vis s experiments after

storing all four thin films under N_2 protection in dark for 30 days. SEM images show white crumbs present on the aged Rb5Cs10-U perovskite grains, which is similar to the feature reported previously, [84] while no obvious morphology changes for the other three films. XRD patterns show a 0.02° down-shift of the (110) peak for all films, indicating a slight segregation of small cations upon storage. In addition, the peak corresponding to the δ-phase Rb/$CsPbI_3$ also shifts from 10.04° to 9.92° and from 10.02° to 9.94° for the Rb5Cs10-U and Rb5Cs10-M film, respectively, indicating that more Cs^+ cations segregate out of the Rb5Cs10-U film than the Rb5Cs10-M film because the lattice parameter of $CsPbI_3$ is larger than $RbPbI_3$. There are no obvious differences at the absorption edges for all thin films after storage (Figure 4-4e). The aging results indicate that single Cs^+ cation doped Cs15 perovskites are stable regardless how the precursor solutions were prepared. In contrast, the phase stability of mixed Rb^+ and Cs^+ cation doped Rb5Cs10 perovskites is influenced by the means that the precursor solutions were prepared. A well-mixed precursor solution leads to a more stable Rb5Cs10 perovskite while an unmixed precursor solution results in more segregation of small cations.

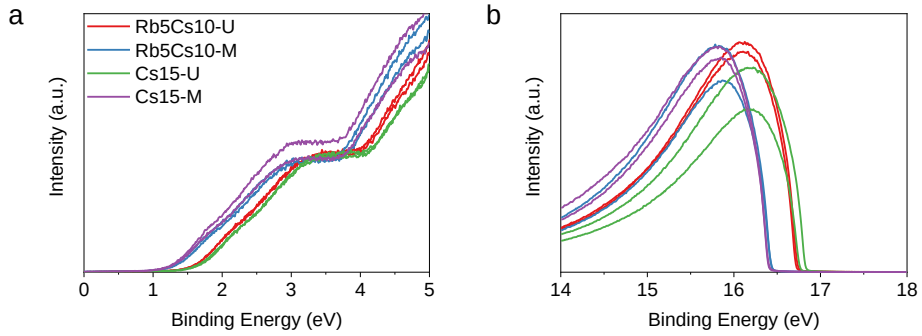

Figure 4-6 UPS spectra of Rb5Cs10-U and Rb5Cs10-M, and Cs15-U and Cs15-M thin films in (a) the valence band edge region and (b) the secondary electron cut-off region. Two scans were performed on each sample to ensure the consistency.

Table 4-3 The work function (WF), valence band maximum (VBM), optical band gap, and conduction band minimum (CBM) of four MA-free perovskites. The VBM and optical band gaps were defined by fitting the UPS and UV-Vis spectra in a log scale. The data for each sample are the averages of two UPS scans.

	WF (eV)	VBM (eV)	Optical Bandgap (eV)	CBM (eV)
Rb5Cs10-U	-4.41	-5.68	1.49	-4.19
Rb5Cs10-M	-4.69	-5.63	1.49	-4.14
Cs15-U	-4.34	-5.64	1.51	-4.13
Cs15-M	-4.72	-5.67	1.51	-4.16

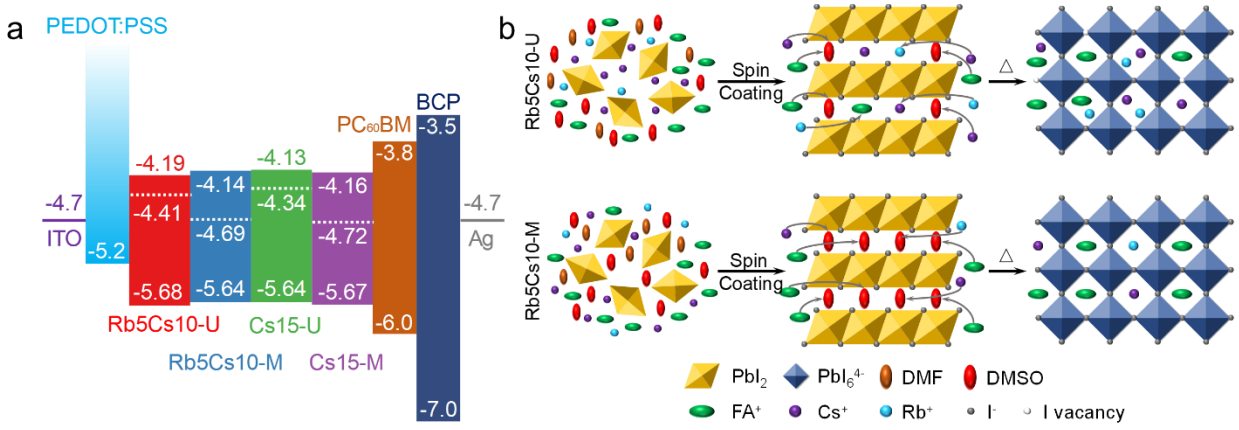

Figure 4-7 (a) Energy level diagram of the materials in the inverted structured perovskite solar cells. The valence band maxima (VBM) and Fermi levels (dotted lines) of all perovskite films were obtained from UPS while the conduction band minima (CBM) were estimated by adding the VBM and optical band gaps obtained from the UV-Vis absorption spectra. (b) Schematic illustration of unmixed and mixed precursor solutions resulting in the A-site interstitial defects in the Rb5Cs10-U film but less defects in the Rb5Cs10-M film.

We investigated the band structures of these four perovskites using ultraviolet photoelectron spectroscopy (UPS) (**Figure 4-6**) and determined their valence band maxima (VBM) and Fermi levels (**Table 4-3**). The conduction band minima (CBM) were calculated by adding the optical band gaps to the VBM. **Figure 4-7**a shows the derived energy level diagram of four perovskite films along with the transport layer and electrode materials. Both Rb5Cs10-U and Cs15-U perovskites show a strong n-type semiconductor feature with the Fermi levels 0.52 and 0.54 eV above the middle band gap, respectively, while both Rb5Cs10-M and Cs15-M perovskites show a weak n-type feature with the Fermi levels 0.2 eV above the middle band gap. Previous studies of $MAPbI_3$ perovskite show that at least six types of point defects can cause n-type doping.[142] They are I^- vacancy (V_I), MA^+ and Pb^{2+} interstitial sites (MA_i and Pb_i), cation substitution (Pb_{MA}), and antisite substitution (MA_I and Pb_I). Except the interstitial site Pb_i and antisite substitution Pb_I causing deep level traps, all others make shallow level traps and the formation energy of these point defects is low. Experiments have demonstrated that $MAPbI_3$ can be tuned from p-type to n-type by adjusting the MAI and PbI_2 concentration ratio from 0.3 to 1.7 in the precursor solution or creating Pb^{2+} rich and MA^+ and I^- deficiency through thermal annealing to remove MAI.[138] $MAPbI_3$ was heavily n-doped with a high electron concentration of 2.8×10^{17} cm^{-3} even with the stoichiometric ratio. At room temperature, the MA^+ interstitial defect has the highest concentration of 1×10^{12} cm^{-3} and the I^- vacant defect concentration is about five orders of magnitude lower.[189] The n-type doping level difference of our perovskite films revealed by UPS could be related to the formation of point defects in making Rb5Cs10-U and Cs15-U perovskite films and Rb5Cs10-M and Cs15-M perovskite films because the only difference is that the precursor solutions were magnetically stirred or not prior to spin coating. As illustrated in Figure 4-7b, in the unmixed precursor solution, PbI_2 octahedrons are most surrounded by Rb^+ and Cs^+

cations due to their high affinity to PbI_2. In contrast, in the well-mixed precursor solution, PbI_2 octahedrons are surrounded by more homogeneously distributed DMSO and DMF solvent molecules. The PbI_2-DMSO intermediates were formed after the anti-solvent DEE washes off the majority of DMSO and DMF solvent molecules and the perovskite structure with corner-sharing octahedrons was formed by extracting DMSO molecules and diffusion of A-site cations during thermal annealing.[190, 191] For Rb5Cs10-U and Cs15-U samples, Rb^+ and Cs^+ cations have partially fill the spaces between the PbI_2-DMSO intermediates, and some Rb^+ and Cs^+ cations are trapped in the interstitial A-sites after annealing, resulting in more defects and strong n-type perovskites. For Rb5Cs10-M and Cs15-M samples, DMSO molecules slow down the interdiffusion process and crystallization, resulting in less defects, and thus weak n-doping. The UPS results reveal that both Rb5Cs10-U and Cs15-U perovskites are stronger n-doped than Rb5Cs10-M and Cs15-M perovskites, which could be attributed to more A-site interstitials in perovskite films made by unmixed precursor solutions. The heavily n-doping and possible higher electron concentration in Rb5Cs10-U and Cs15-U perovskites yield the better device performance, especially larger Jsc's for Rb5Cs10-U and Cs15-U devices (Figure 4-1a and Table 4-1).

4.3.3 Revealing the Electric Field-Induced Ion Migration

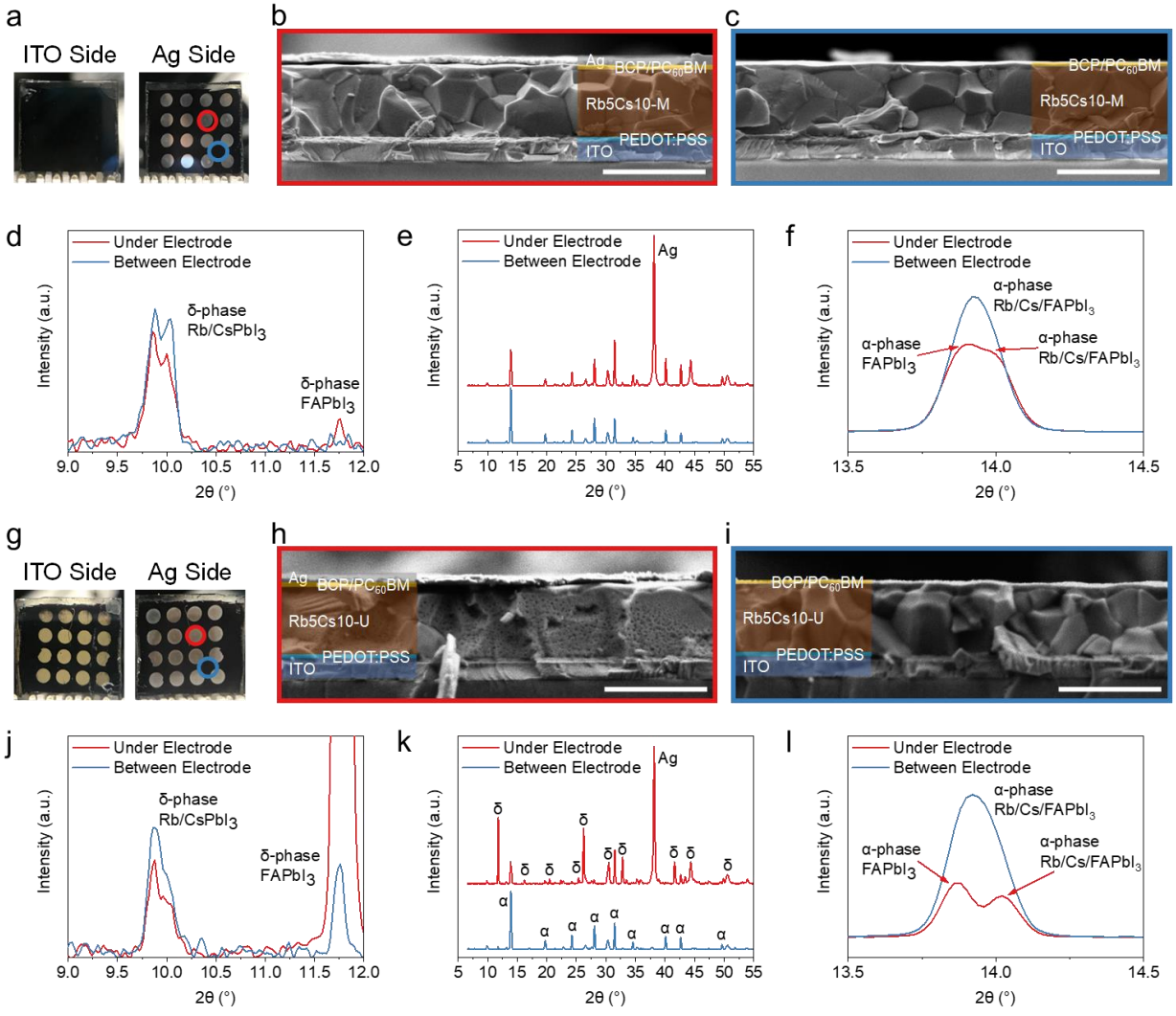

Figure 4-8 (a, g) Photographs of the ITO side and Ag side of the solar cells with Rb5Cs10-M and Rb5Cs10-U active layers, respectively. (b, c, h, i) Cross-sectional SEM images of the solar cells with Rb5Cs10-M and Rb5Cs10-U active layers in the areas between Ag electrodes (blue circles and blue frames) and under Ag electrodes (red circles and red frames). (d-f, j-l) XRD patterns taken from the areas between Ag electrodes and under electrodes of the solar cells with Rb5Cs10-M and Rb5Cs10-U active layers. The devices are those that have been tested in a 3-day interval for 30 days.

Since co-doping Rb^+ with Cs^+ induced more phase segregation and PCE decrease over time, we further characterized the perovskite active layers after the Rb5Cs10-M and Rb5Cs10-U devices have been tested in a 3-day interval for 30 days. **Figure 4-8**a shows the photographs of the front-side (Ag electrode) and back-side (glass/ITO) of the Rb5Cs10-M devices after 30 days testing. The back-side photograph shows black color in the entire active layer film, indicating that Rb5Cs10-M perovskite is photoactive α-phase. We took the cross-sectional SEM images specifically in the areas under an Ag electrode (Figure 4-8b) and between Ag electrodes (Figure 4-8c). The SEM images show that the Rb5Cs10-M perovskite thin films have a thickness of approximately 700 nm with nice polycrystalline structures and clear grain boundaries in both areas. We also acquired the XRD patterns in these two areas (Figures 4-8d-f). There are no obvious differences in the overall XRD patterns except some peak intensity changes and an Ag diffraction peak centered at 38.12° in the XRD pattern taken under the Ag electrode (Figure 4-8e). However, some changes are observed in the zoom-in low angle region and the (110) peak. Figure 4-8d shows a tiny δ-phase $FAPbI_3$ peak centered at 11.76° in the XRD pattern taken under the Ag electrode but not present between electrodes. Figure 4-8f shows that the (110) peak in the XRD pattern taken from the area between electrodes still maintains a single peak of α-phase while it slightly splits into two peaks collected under the electrode with one peak corresponding to $FAPbI_3$-rich phase while another corresponding to more Rb^+ and Cs^+ in $FAPbI_3$.[192] Even the single peak from the area between electrodes also shifts slightly to the low angle centered at 13.92° compared to 13.94° for the film that has been stored in a N_2 glove box for 30 days (Figure 4-4c). The XRD results indicate that phase segregation occurs in the Rb5Cs10-M active layer, especially under the Ag electrode during the course of device testing. The emerging δ-phase $FAPbI_3$ in the active layer

under the Ag electrode could be due to the phase transition of small clusters of pure α-phase $FAPbI_3$ that are formed in the Rb5Cs10-M film.

A dramatically visual difference is shown by photographs in Figure 4-8g. Devices containing the Rb5Cs10-U active layer show a see-through photograph taken from the glass/ITO side after 30 days testing. The Rb5Cs10-U active layer turns to yellow under the Ag electrodes, making the electrodes can be seen from the back-side. However, the Rb5Cs10-U active layer between electrodes remains black. The cross-sectional SEM image taken under the electrode shows pinholes in grains and blurry grain boundaries (Figure 4-8h), in comparison to dense grains and clear grain boundaries exhibited in the SEM image between Ag electrodes (Figure 4-8i). The overall XRD patterns in Figure 4-8k show the coexistence of photoactive α-phase and photoinactive δ-phase perovskites in the active layer under the electrode, while mainly photoactive α-phase perovskite in the active layer between electrodes. Much stronger δ-phase $FAPbI_3$ peak at 11.76° exhibit in the active layer under the electrode than between electrodes (Figure 4-8j). The α-phase (110) peak of the Rb5Cs10-U active layer under the electrode splits into two peaks, centered at 13.86° and 14.02°, as shown in Figure 4-8l. The two peaks could be referred to pure α-phase $FAPbI_3$ and the α-phase $FAPbI_3$ with highly incorporated Rb^+ and Cs^+ cations.[192] The content of Rb^+ and Cs^+ cations is even higher than the freshly made films because the (110) peak is shifted to 14.02° comparing to the location at 13.94°. The SEM images, particularly, XRD patterns suggest that a phase segregation occurs in the Rb5Cs10-U active layer under the electrodes because of the built-in internal electric field and the applied external electric filed, resulting in the coexistence of relatively pure α-phase $FAPbI_3$ crystals and highly incorporated Rb^+/Cs^+ α-phase Rb/$CsFAPbI_3$ crystals. The relatively pure α-phase $FAPbI_3$ crystals are not stable at room

temperature, transferring from the black photoactive α-phase to the yellow photoinactive δ-phase. Apparently, ions must migrate in this process.

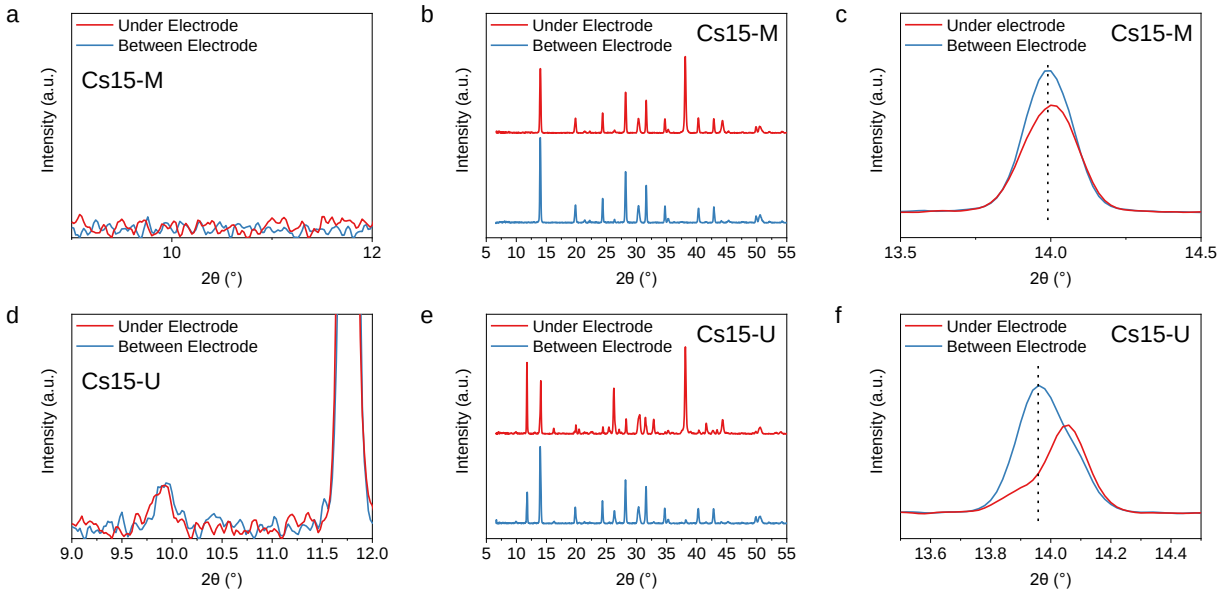

Figure 4-9 XRD patterns taken from the areas between Ag electrodes and under the electrode of the solar cells with (a-c) Cs15-M and (d-f) Cs15-U active layers. The devices have been tested in a 3-day interval for 30 days.

The Cs15-M and Cs15-U devices show the similar visual pictures as the Rb5Cs10-M and Rb5Cs10-U devices after testing for 30 days and their XRD patterns are shown in **Figure 4-9**. The active layer of the Cs15-M devices remains pure photoactive α-phase in both under the electrode and between electrodes areas. Unlike Rb5Cs10-U devices, strong δ-phase $FAPbI_3$ peak at 11.76°, besides α-phase $FAPbI_3$ peaks, presents in the active layer of the Cs15-U device no matter under the electrode and between electrodes. The (110) peak down-shifts for the active layer between electrodes while it splits into two peaks for the active layer under the electrode, corresponding to pure α-phase $FAPbI_3$ and α-phase $FAPbI_3$ heavily doped by Cs^+ cation. In addition, the δ-phase $CsPbI_3$ peak at 9.94° appeared in both under the electrode and between electrodes areas. Since no

δ-phase $CsPbI_3$ peak was observed in the Cs15-U thin film after 30 days storage (Figure 4-4d), the formation of δ-phase $CsPbI_3$ after 30 days testing of the C15-U device could be due to the electric field induced cation migration.

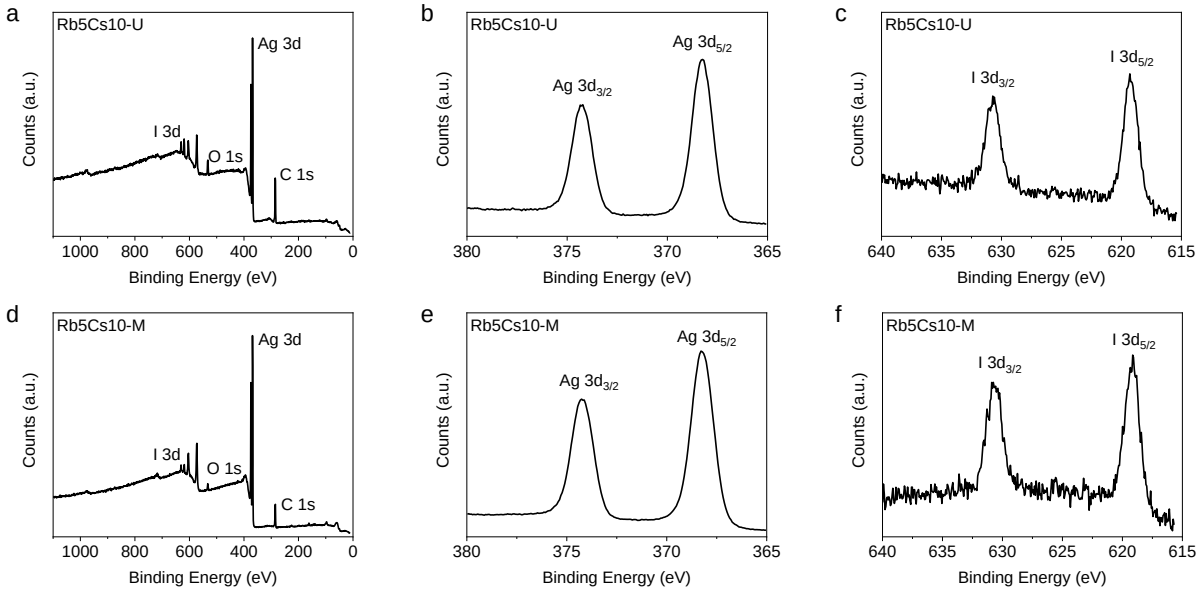

Figure 4-10 Survey and high-resolution Ag 3d and I 3d XPS spectra of (a-c) Rb5Cs10-U and (d-f) Rb5Cs10-M. The Ag electrodes were carefully peeled off from the devices after testing for 30 days and the XPS measurements were conducted at the Ag electrode side touching the ETL.

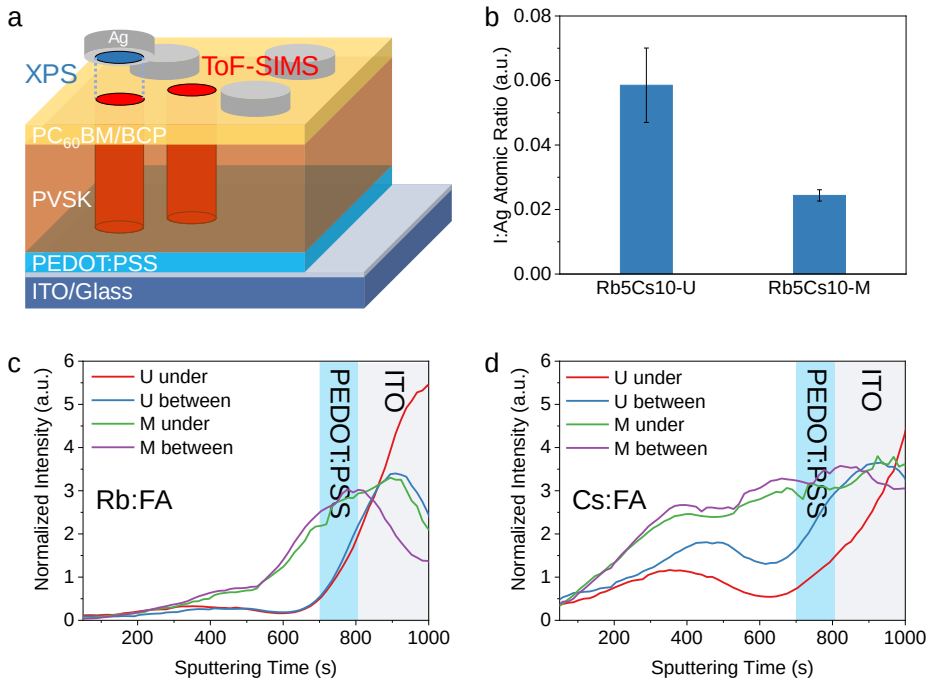

Figure 4-11 (a) Schematic illustration of the regions where XPS and ToF-SIMS experiments were performed indicated by blue and red, respectively. (b) Atomic ratio of I to Ag determined by XPS measured at the peel-off Ag electrodes from the Rb5Cs10-M and Rb5Cs10-U devices after testing for 30 days. (c) The Rb to FA and (d) Cs to FA content ratio profiles determined by ToF-SIMS for the Rb5Cs10-M and Rb5Cs10-U devices in the regions between electrodes and under the electrode.

To find the evidence of ion migration, we first characterized the chemical components of the Ag electrodes at the side touching the electron transfer layer (ETL). The Ag electrodes were carefully peeled off and the survey and high-resolution XPS scans (**Figure 4-10**) were taken at the Ag electrode side contacting the ETL as illustrated in **Figure 4-11**a. The survey scans (Figures 4-10a and d) show iodine signal on the Ag electrode but no Rb and Cs signals. The core level spectra of I 3d and Ag 3d (Figures 4-10b, c, e, and f) show the binding energy of 619.2 eV and 368.2 eV for I $3d_{5/2}$ and Ag $3d_{5/2}$, respectively, corresponding to I^- in AgI compound and Ag^+ in the hybrid of AgI and Ag.[193] The I:Ag atomic ratios on the Ag electrodes were calculated by integrating the

peak areas of Ag 3d and I 3d in the survey scans. More than the twice of the I:Ag atomic ratio was found on the Ag electrode from the Rb5Cs10-U device compared to the Rb5Cs10-M device (Figure 4-11b). Forming AgI in the Ag electrode due to iodide ion migration have been reported in previous studies.[193-195] The higher I:Ag atomic ratio on the Ag electrode from the Rb5Cs10-U device and the strong n-type doping of Rb5Cs10-U films shown by the UPS results demonstrate that more halide vacancies exist in the Rb5Cs10-U film than in the Rb5Cs10-M film. We further used ToF-SIMS to characterize the elemental depth profiles in the regions under the electrode and between electrodes for both Rb5Cs10-U and Rb5Cs10-M devices (**Figure 4-12**). The Rb:FA and Cs:FA cation ratio profiles are shown in Figures 4-11c and d, respectively. Clearly, Rb^+ cations show a strong diffusion direction towards the PEDOT:PSS and ITO layers. The Rb content in the Rb5Cs10-U active layer is less than that in the Rb5Cs10-M active layer because more Rb^+ cations have diffused into the PEDOT:PSS and ITO layers. For both Rb5Cs10-U and Rb5Cs10-M active layers, more Rb present in the PEDOT:PSS and ITO layers in the region under the electrodes. Similarly, Cs^+ cations also diffuse towards the PEDOT:PSS and ITO layers, leaving a Cs depletion zone in the active layer close to the ETLs. The Rb5Cs10-U active layer has a lower Cs content than the Rb5Cs10-M active layer. The Cs content is lower in the regions under the electrodes, especially for the Rb5Cs10-U active layer. The XPS and ToF-SIMS results show that after testing the devices in a 3-day interval for 30 days, iodide anions present in the Ag electrodes while Rb^+ and Cs^+ cations in the PEODT:PSS and ITO layers, the consequence of anion and cation migration in the opposite directions. The applied external electric field accelerates these ion migrations and the active layer, prepared with the unmixed precursor solutions, exhibit more serious Rb^+ and Cs^+ cation and I^- anion deficiency in the active layer.

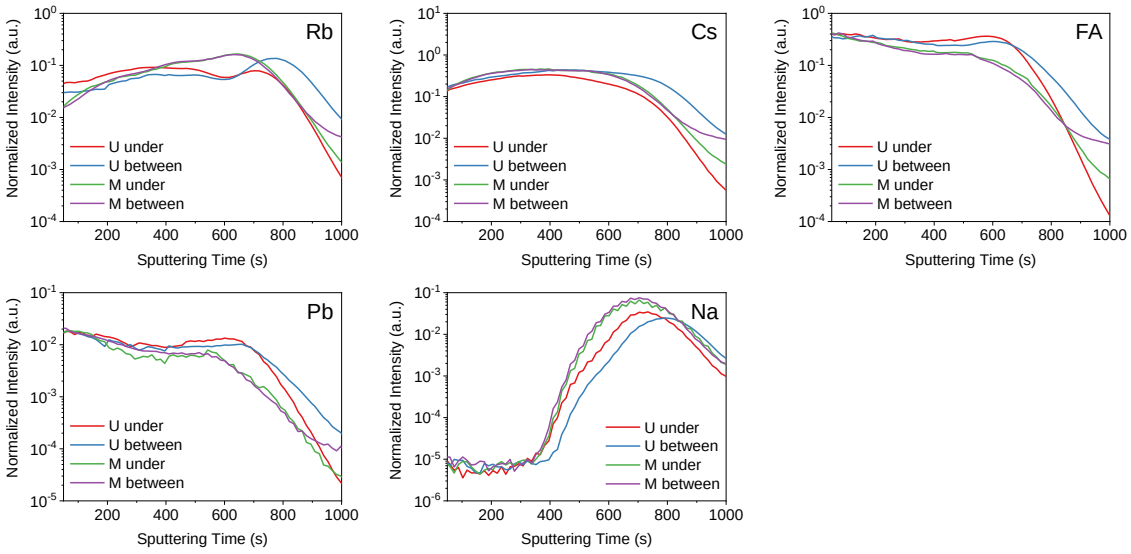

Figure 4-12 Normalized ToF-SIMS profiles of Rb, Cs, FA, Pb, and Na elements acquired from the areas under the electrodes and between electrodes of the solar cells tested for 30 days with Rb5Cs10-U and Rb5Cs10-M active layers.

The comprehensive characterizations of both stand-alone perovskite films and the perovskite active layers in the inverted structured devices allow us to understand the device performance and the stability related to the mixed Rb^+ and Cs^+ and single Cs^+ cation doping as well as the precursor solution preparation methods induced defects in $Rb_{0.05}Cs_{0.10}FA_{0.85}PbI_3$ and $Cs_{0.15}FA_{0.85}PbI_3$ perovskites. The device performances were significantly improved by replacing 5% of Cs^+ cation in $Cs_{0.15}FA_{0.85}PbI_3$ with Rb^+ forming $Rb_{0.05}Cs_{0.10}FA_{0.85}PbI_3$, even though Rb^+ cations were not completely integrated into the perovskite lattice and $Rb/CsPbI_3$ phase was observed on the perovskite surface. The improved device performance of $Rb_{0.05}Cs_{0.10}FA_{0.85}PbI_3$ than $Cs_{0.15}FA_{0.85}PbI_3$ was also observed in the conventional structured devices and the white segregation of $Rb/CsPbI_3$ phase presented on the $Rb_{0.05}Cs_{0.10}FA_{0.85}PbI_3$ thin film.[84] The difficulty to integrate Rb^+ cation into perovskites lattices has been reported in a variety perovskites from $MAPbI_3$, $FAPbI_3$, $MA/FAPbI_3$ to $MA/FAPb(I/Br)_3$ with single Rb^+ cation or mixed Rb^+ and Cs^+

cation.[82-84, 196-198] Nonetheless, even a small amount of Rb^+ integration can increase charge carrier mobility and slow down charge recombination,[82, 196, 197] which could also be the underline factors improving the device performance of our Rb5Cs10-M and Rb5Cs10-U devices. The better device performance of the Rb5Cs10-U and Cs15-U devices than the Rb5Cs10-M and Cs15-M devices benefits from the heavily n-doping of these perovskites, which increases electron carrier concentration, improves the charge carrier transport, and eventually enhances the J_{SC} and FF.[138] It has also been reported that the benign defects in the perovskite could improve the performance by aggregating at the perovskite/transport layer interface and heal the deep defects, therefore, improve the charge carrier collection.[199]

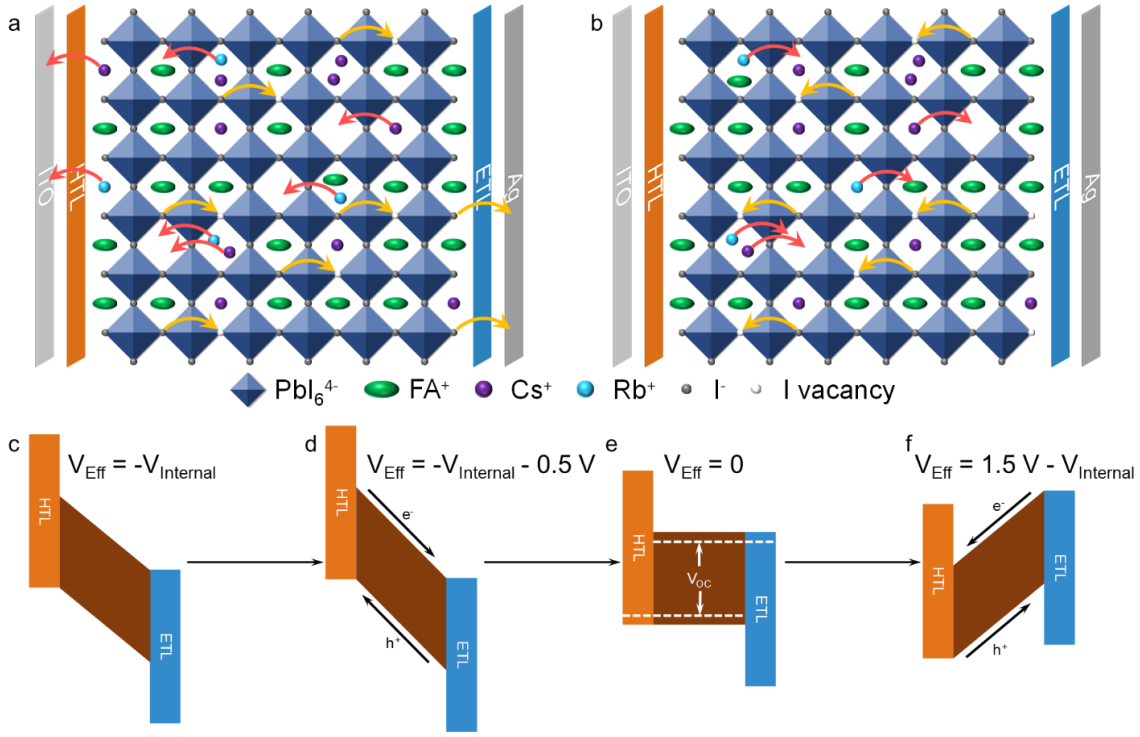

Figure 4-13 Schematic illustration of ion migration in the perovskite film under (a) negative effective electric filed and (b) positive electric field. Effective electric field applied on the perovskite active layer following the testing sequence: (c) under dark without external bias, and

under illumination with (d) -0.5 V reverse external bias, (e) Voc forward external bias, and (f) +1.5 V forward external bias.

Even though both Rb^+ cation incorporation and benign defects in the perovskites make the positive impacts on the initial device performance, they cause the long-term instability of the devices due to ion migration under electric field. The n-type doping nature of these perovskites means the presence of many types of point defects, particularly, halide vacancies and A-site cation interstitial sites as illustrated in **Figures 4-13**a and b. Other types of defect such as A-site vacancy and grain boundary defects may also exist in the perovskite and serve as the cation migration channel. The effective voltage (V_{eff}) is the actual voltage applied to the active layer involving both built-in internal electric field and applied external voltage. When the device is in dark and no applied external voltage, the active layer experienced a built-in internal field (Figure 4-13c). When we conducted the stability test in a 3-day interval for 30 days, the devices were always swapped from -0.5 V to 1.5 V. The effective voltage is even stronger under an applied reverse external bias (-0.5 to < 0 V, Figure 6d). In both cases, as illustrated in Figure 4-13a, I^- anions move towards the Ag electrode side mediated by the halide vacancies, and interstitial (even some A-site) small Cs^+, and especially Rb^+ cations migrate toward the ITO electrode side via different path ways,[181] while large FA^+ cations mainly remain in their positions because of the hydrogen bonding with iodide atoms. When the applied external voltage is equal to Voc, the effective voltage is equal to zero, no ion migrations occurs but this is a very short period. When the device is under a forward external bias (0 – 1.5 V, Figure 4-13f), the effective voltage applied to the active layer is reversed. Consequently, Rb^+ and Cs^+ cations and I^- anions migrate in the opposite directions as illustrated in Figure 4-13b. Since the devices were stored in dark during the course of 30 days testing, the active layers were experienced a constant built-in voltage, which drives the slow migration of Rb^+ and

Cs^+ cations towards the ITO electrode side and I^- anions towards the Ag electrode side and they even diffuse through the transport layers and are permanently captured in electrodes. Therefore, after 30 days device testing, iodide element is testable in the Ag electrode by XPS and enriched Rb and Cs elements in the ITO side shown by ToF-SIMS. In contrast, in the conventional structured devices, the migrated cations and anions accumulate at the HTL/perovskite and ETL/perovskite interfaces. Under illumination and open circuit voltage, light induced self-pooling makes ions redistribution in the active layer, which has been attributed to the origin of hysteresis.[200] The losses of materials in the active layer under dark and reverse applied external voltage create more defects, which facilitates ion migration under the applied higher forward external bias. Consequently, small clusters with relative pure α-phase $FAPbI_3$ are formed in the active layer, which are easily transferred to the thermodynamically more stable δ-phase $FAPbI_3$ under room temperature. To further confirm our hypothesis regarding the effect of electric field on the device stability, we also performed the stability test on the Rb5Cs10-U device with longer testing intervals, 15 days and 30 days (**Figure 4-14**). The PCEs at the 30 days retain 20% and over 40% of the initial PCEs for the devices tested in a 15-day and 30-day interval, respectively, while the PCE is below 10% of the initial PCE for the devices tested in a 3-day interval. The reduced PCEs are again mainly due to the decrease of J_{SC}'s. These results confirm that the electric field plays a crucial role in the ion migration process. In the inverted structured devices, the migrated small inorganic cations and halide anions are captured in electrodes, creating more defects in perovskite. A frequently applied electric field accelerates phase segregation, creating small clusters of pure α-phase $FAPbI_3$, which transfers to photo-inactive δ-phase $FAPbI_3$ under room temperature, and finally resulting in the degradation of device. We should point out that the reported long-term device stability based on MA-free $Rb_{0.05}Cs_{0.10}FA_{0.85}PbI_3$ perovskite was achieved in the

conventional structured device and the device was tracking under continuous maximum power point, at which the applied voltage is close to Voc and thus, ion migration is physically suppressed.[84] The further improved stability by applying PMMA in both HTL/perovskite and ETL/perovskite interfaces could be due to the mitigation of ion diffusion into transport layers.

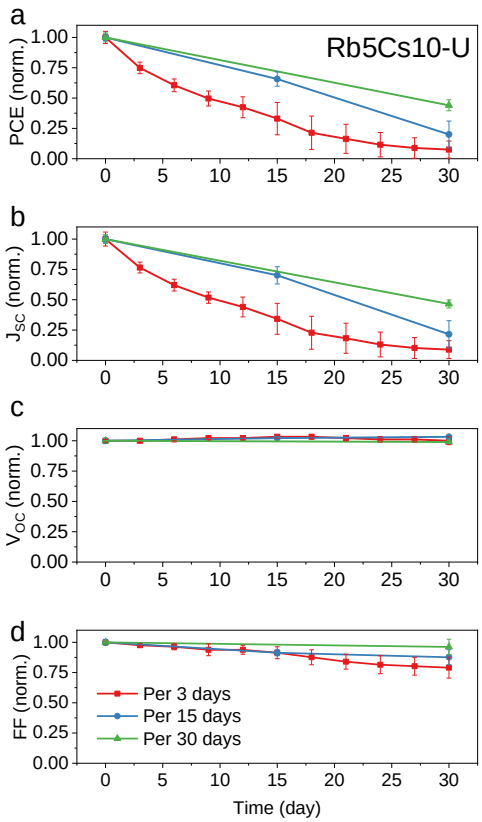

Figure 4-14 Normalized (a) PCE, (b) J_{SC}, (c) V_{OC}, and (d) FF of solar cells with a Rb5Cs10-U active layer stored in N_2 filled glove box under room temperature for 30 days with the testing intervals of 3, 15, and 30 days for the first 30 days.

4.4 Conclusion

In conclusion, we prepared two types of MA-free perovskite, $Rb_{0.05}Cs_{0.10}FA_{0.85}PbI_3$ and $Cs_{0.15}FA_{0.85}PbI_3$, and investigated the effect of Rb^+ on the device performance and long-term

device stability against electric field. We demonstrated that the incorporation of Rb^+ cation in the perovskite lattice was incomplete, but it improved the device performance even though reduced the long-term device stability. We revealed that the degradation of the inverted structured devices was due to phase segregation caused by ion migration under electric field and the losses of I^- anions and Rb^+ and Cs^+ cations captured by the electrodes. We showed that by stirring the precursor solution prior to spin coating, the defect density in the perovskite was significantly reduced and the device long-term stability was improved. The stabilized $Rb_{0.05}Cs_{0.10}FA_{0.85}PbI_3$ and $Cs_{0.15}FA_{0.85}PbI_3$ devices retained 68% and 92% of the initial PCE, respectively, after 30 days under N_2 protection. Our work elucidates that co-doping Rb^+ with Cs^+ cation is still promising for $FAPbI_3$ but ion migration under electric field needs to be suppressed. Our work also reveals that mixing precursor solution prior to spin coating is one of the accessible methods to reduce the defect densities, therefore the ion migration in the perovskite solar cells. Our work sheds a light on the solution of the operational instability of perovskite solar cells and paves the pathway for their industrialization.

Chapter 5 CHEMICAL POLYMERIZATION OF HYDROXYMETHYL AND CHLOROMETHYL FUNCTIONALIZED PEDOT:PSS

5.1 Introduction

Conducting polymers have gained enormous attention since the first report in 1977.[201] Poly(3, 4-ethylenedioxythiophene) (PEDOT) is one of the most successful conducting polymers because of its flexibility, high transparency and conductivity, and great thermal and environmental stability.[202] PEDOT can be synthesized with different methods, such as electrochemical polymerization, transition metal-mediated coupling polymerization, and oxidative chemical polymerization.[202] Electrochemical polymerization offers the advantages of the use of a small amount of monomers and short polymerization time but the films can only be formed on conductive substrates, making it difficult to fabricate large area, uniform PEDOT thin films.[203, 204] Transition metal-mediated coupling polymerization yields neutral but typically low molecular weight PEDOT.[205, 206] Oxidative chemical polymerization is considered as the most practical method because it produces PEDOT in the form of conductive ink, which can be coated onto various substrates, either conductive or non-conductive, or printed into different patterns using ink-jet printer or other priting technologies.[207, 208] The most commonly used PEDOT, "Baytron P", was developed by Bayer AG company in 1988.[209] The "Baytron P" was synthesized by chemically polymerizing 3,4-ethylenedioxythiophene (EDOT) monomer in the presence of polyelectrolyte poly(styrene sulfonate) (PSS). The negatively charged PSS serves as the counterion to balance or to dope the positive charge of the oxidized PEDOT. In addition, the hydrophilic PSS forms a shell

wrapping around the hydrophobic PEDOT core, resulting in a core-shell structure of PEDOT:PSS to be dispersed in water.[94, 210] Many applications of PEDOT:PSS have been developed such as solar cells,[88, 211-214] photodetectors,[44, 45] light-emitting diodes,[215] smart windows,[216] biosensors,[217, 218], fuel cells,[219, 220] and wearable electronics.[221, 222]

The conventional PEDOT:PSS, however, lacks functionality, which is particularly important in bioelectronics and biosensing. For example, the PEDOT:PSS electrode induced inflammatory response and scar formation when implanted in living tissues, thereby insulating the electrode from targeted tissues.[223] The functionality of PEDOT:PSS can be introduced by changing the counterion PSS or adding a functional group onto the ethylenedioxy ring in the PEDOT backbone.[224] PSS counterions have been replaced to other polyelectrolytes such as dextran sulfate,[225] heparin,[226] and sulfonated lignin,[227] or small molecules such as tosylate[228] and chloride,[219] to improve the PEDOT biocompatibility, conductivity, and thermoelectric properties. PEDOTs with the functional group added onto the ethylenedioxy ring are mostly polymerized from the functionalized EDOT monomer via the electrochemical polymerization method.[229-231] The difficulty for applying oxidative chemical polymerization to the functionalized EDOT monomers comes from the change of oxidative potential and the interaction with the oxidant, and counterion because of the introduction of a functional group onto the ethylenedioxy ring. In order to develop functionalized PEDOT:PSS conducting polymers using oxidative chemical polymerization method, it is crucial to understand the polymerization mechanism, especially the interaction between functionalized EDOT monomer and anionic counterion and oxidant during the reaction.

In this work, we introduced a hydroxymethyl (-MeOH) and a chloromethyl (-MeCl) function group to the oxyethylene ring of EDOT to obtain hydroxymethylated-3,4-

ethylenedioxythiophene (EDOT-MeOH) and chlorylmethylated-3,4-ethylenedioxythiophene (EDOT-MeCl) monomer, respectively, and used oxidative chemical polymerization to synthesize PEDOT:PSS, functionalized PEDOT-MeOH:PSS and PEDOT-MeCl:PSS. In oxidative chemical polymerization, the interaction between ferric ions (Fe^{3+}) and monomers is a critical step because Fe^{3+} ions first oxidize monomers to form polymers, and the couples of ferrous ions (Fe^{2+}) and Fe^{3+} ions catalyze the decomposition of persulfate ions ($S_2O_8^{2-}$) into sulfate radicals (SO_4^{-}) that oxidize polymers together with Fe^{3+} ions.[229, 232] Polyelectrolyte PSS also plays a key role in the reaction. In the initial stage of reaction, the the surface charge of PSS and the interaction of PSS and monomers directly affect how Fe^{3+} ions attack monomers, while in the later stage of reaction, the interaction of counterion PSS and polymers impacts the doping efficiency and dispersibility of conducting polymers.[207] We showed that for the polymerization of EDOT, the acidity of the reaction solution determines the protonation/deprotonation of PSS, and dispersibility of conducting polymers. Neutralized PSSH, by adding equal molar of KOH, allows Fe^{3+} ions selectively polymerize EDOT monomers inside PSS micelles because of the electrostatic interaction of negatively charged PSS^- and Fe^{3+}, yielding PSS doped, well-dispersed PEDOT:PSS in water. Acidic PSSH, by adding partial or no KOH, makes Fe^{3+} ions polymerize EDOT monomers both inside PSS micelles and in the water phase, yielding the mixtures of PSS doped, water-dispersible PEDOT:PSS and SO_4^{2-} doped, water-non-dispersible PEDOT:SO_4 precipitates. For the polymerization of EDOT-MeOH and EDOT-MeCl, the function group not only changes the oxidation potential but also affects the interaction of monomers with PSS, and thereby the dispersibility, conductivity, and morphology of final products. Because of the high electronegativity of -OH and -Cl, triple amount of oxidant, compared to the polymerization of EDOT, had to be used to polymerize and oxidize PEDOT-MeOH and PEDOT-MeCl. EDOT-MeCl

monomers tended to be away from PSS due to the electrostatic repulsion. As a result, PEDOT–MeCl were doped by both PSS and sulfate (SO_4^{2-}), yielding a mixture of water-dispersible PEDOT-MeCl:PSS and non-dispersible PEDOT-MeCl:SO_4 precipitates. EDOT-MeOH monomers can form hydrogen bonding with PSS, making EDOT-MeOH monomers stay inside PSS micelles or closer to PSS. Therefore, PEDOT-MeOH polymers were mainly doped by PSS, yielding a homogeneous PEDOT-MeOH:PSS-water mixture. We further studied the surface morphology, oxidation level, and the conductivity of synthesized conducting polymers, and correlated them to the proposed polymerization mechanisms.

5.2 Experimental Section

5.2.1 Materials

3,4-Ethylenedioxythiophene (EDOT, 97%), sodium persulfate ($Na_2S_2O_8$, ≥ 98%), iron(III) sulfate hydrate ($Fe_2(SO_4)_3$, 97%), poly(4-styrenesulfonic acid) solution (PSSH, M_w ~ 75,000, 18 wt% in H_2O), hydrochloric acid (HCl, 37 wt%), 3,4-dimethoxythiophene (97%), 3-chloro-1,2-propanediol (98%), p-toluenesulfonic acid monohydrate (PTSA, ≥ 98.5%), toluene (≥ 99.5%), sodium acetate anhydrous (CH_3COONa, > 99%), and dimethyl sulfoxide (DMSO, ≥ 99.9%) were purchased from Sigma-Aldrich. Potassium hydroxide (KOH), dichloromethane (DCM), sodium hydroxide (NaOH), and chloroform-d ($CDCl_3$) were purchased from Fisher Scientific. Cation exchanger LEWATIT S108H and anion exchanger LEWATIT MP62 were kindly provided by LANXESS. Commercial PEDOT:PSS Clevios P VP AI 4083 was purchased from Heraeus. All the materials were used as received without further purification.

5.2.2 Synthesis of Functionalized EDOT Monomers

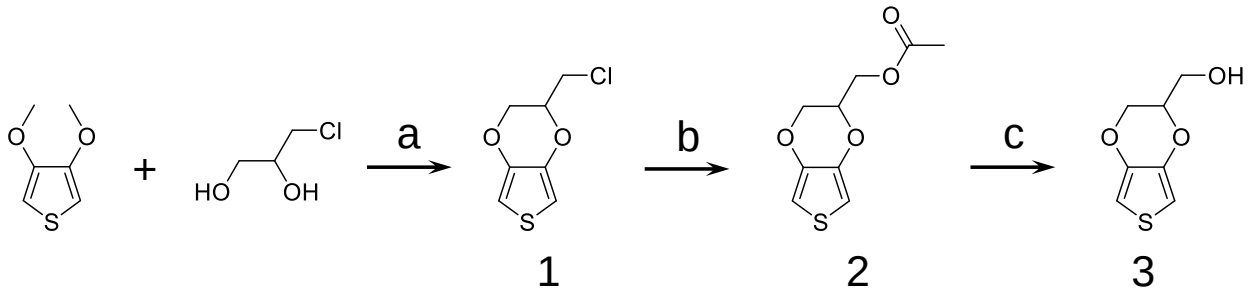

Scheme 5-1 Synthetic route of the chloromethyl and hydroxymethyl functionalized EDOT monomers.

The synthetic route of functionalized EDOT monomers is illustrated in **Scheme 5-1**. The experimental details were adopted from previous studies with some modification.[233, 234] (a) 3,4-dimethoxythiophene (5 g), 3-chloro-1,2-propanediol (12 g), PTSA (0.676 g), toluene (118 mL) were added into a three-neck flask. The system was purged with N_2 flow for 30 min and stirred vigorously at 95 °C under N_2 protection for 24 h. After removing of toluene under reduced pressure, the residue was purified by column chromatography (silica gel, hexane/DCM = 8/2 v/v) to give the product **1**, 2-(chloromethyl)-2,3-dihydrothieno[3,4-b][1,4]dioxine (EDOT-MeCl). ^{1}H NMR (300 MHz, $CDCl_3$, ppm): δ 6.38 (s, 2H, Th), 4.42-4.14 (m, 3H, -O-CH_2-CH-O-), and 3.65-3.78 (m, 2H, -CH_2-Cl). The yield of EDOT-MeCl was 46%. (b) EDOT-MeCl (0.5 g), CH_3COONa (0.323 g), and DMSO (7.9 mL) were added into a flask. The solution mixture was stirred at 120 °C for 2 h. The mixture was poured into DI water (15 mL) and extracted with DCM (60 mL). (c) After removing DCM under reduced pressure, the product **2** was added to a solution of NaOH (0.367 g) in DI water (10.5 mL). The mixture was refluxed for 1 h and then cooled to room temperature, and DI water (5.8 mL) was added. The mixture was acidified and extracted with DCM. The solvent was removed under reduced pressure and column chromatography (silica gel, hexane/DCM = 8/2

v/v) was performed to give the product **3**, 2-(hydroxymethyl)-2,3-dihydrothieno[3,4-b][1,4]dioxine (EDOT-MeOH). ^{1}H NMR (300 MHz, $CDCl_3$, ppm): δ 6.36 (s, 2H, Th), 4.08-4.27 (m, 3H, -O-CH_2-CH-O-), and 3.85-3.92 (m, 2H, -CH_2-OH). The step and global yield of EDOT-MeOH was 78% and 36%, respectively.

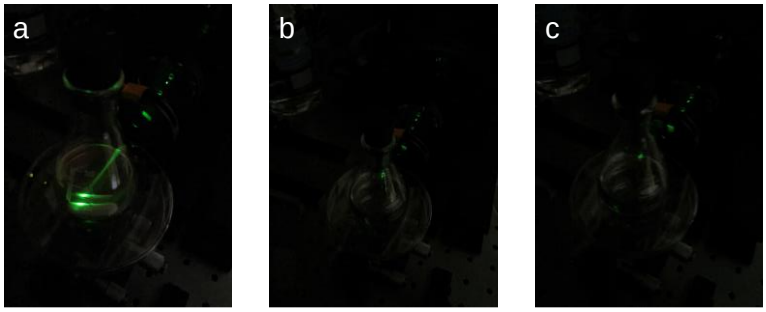

Figure 5-1 Tyndall effect experiments of (a) EDOT-PSS-water mixture, (b) PSS-water solution, and (c) water. EDOT-PSS-water forms an emulsion and shows a visible light beam passes the mixture.

5.2.3 Oxidative Chemical Polymerization

PSSH (3 mL) was mixed with DI water (21 mL) for 20 min. Various molar amounts of KOH was dissolved in DI water (2 mL) and added into the mixture solution. EDOT (0.1 g) or equal molar amount of functionalized EDOT was added into the mixture solution and stirred vigorously for 20 min to form an emulsion (**Figure 5-1**). $Na_2S_2O_8$ (0.25 g for EDOT, or 0.75 g for functionalized EDOT) and $Fe_2(SO_4)_3$ (0.00187 g for EDOT, or 0.00561 g for functionalized EDOT) was dissolved in DI water (1 mL), respectively, and added into the emulsion sequentially. The emulsion was stirred vigorously under room temperature for 24 h until the UV-Vis absorption intensity of the solution does not change. UV-Vis absorption was collected using a Varian Cary 5000 UV-Vis-NIR spectrophotometer by diluting 100 μL sample with 3.5 mL DI water. S108H

and MP62 ion exchanger resins (4.5 g and 6.5 g, respectively) were added into the solution, stirred for 2 h, and removed by vacuum filtration. The product solution was in dark blue color.

5.2.4 Fabrication and Characterization of Polymer Thin Films

Glass substrates were first cut into 15 mm × 15 mm pieces, then cleaned sequentially by sonication in soapy DI water, DI water, acetone, and isopropanol for 15 min each and then treated with 100 W oxygen plasma for 10 min. PEDOT:PSS or functionalized PEDOT:PSS was treated with ultrasonic for 5 min and spin-coated onto a clean glass substrate at 1000, 3000, and 5000 rpm, and annealed at 150 °C for 10 min for Raman, conductivity, and atomic force microscope (AFM) measurements, respectively. The morphology of PEDOT:PSS and functionalized PEDOT:PSS thin films were characterized by tapping mode AFM (TM-AFM) using a Digital Multimode AFM equipped with a Nanoscope IVa controller. Conductivity was measured by Jandel Cylindrical four-point probe connected with a Keithley 2450 SourceMeter. Film thickness was characterized by Olympus OLS41 profilometer. Raman spectroscopic measurement was performed on Thermo Scientific DXR2 Raman Microscope with a 532 nm green laser. The laser power applied was between 1-5 mW to avoid damaging polymer thin films, and a 10x (N.A. = 0.25) or 50x (N. A. = 0.50) objective lens was used to focus the laser on the sample. Raman spectra were fitted using PeakFit with the assumption of 50% Gaussian and 50% Lorentzian component peaks.

5.3 Results and Discussion

5.3.1 Oxidative Chemical Polymerization of PEDOT:PSS and Functionalized PEDOT:PSS

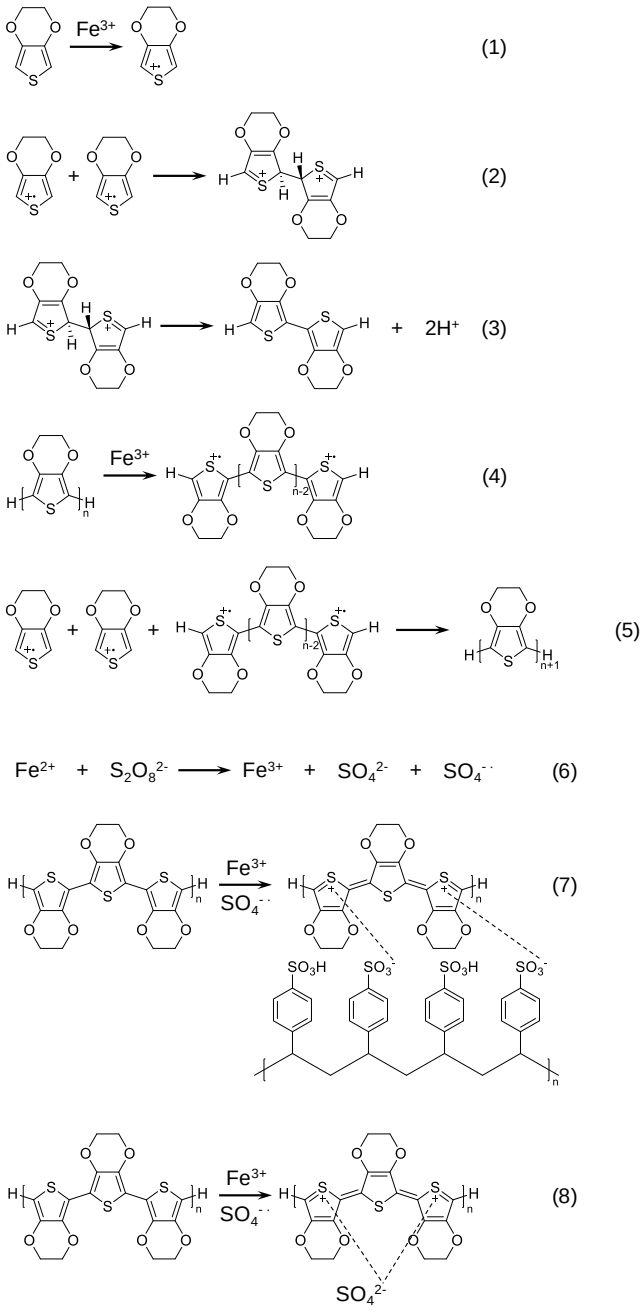

Scheme 5-2 Schematic description of the oxidative step-growth polymerization of EDOT into PEDOT and doping of PEDOT: (1) oxidation of EDOT to form cation radical; (2) dimerization of

cation radical; (3) deprotonation to form dimer; (4, 5) further polymerization from n-mer to (n+1)-mer; (6) Fe^{3+} regeneration and $SO_4^{-\cdot}$ radical formation; (7, 8) oxidation of PEDOT backbone and doping with PSS^- or SO_4^{2-} counterion, respectively.

Scheme 5-2 shows the reaction processes in the oxidative chemical polymerization using EDOT as an example. Generally, $Fe_2(SO_4)_3$ and $Na_2S_2O_8$ are added in the EDOT oxidative chemical polymerization to initiate the step-growth polymerization of PEDOT, and to regenerate $Fe_2(SO_4)_3$ and oxidize PEDOT polymers, respectively.[235-237] Fe^{3+} ions oxidizes an EDOT monomer into a cation radical that dimerizes and is stabilized by the removal of two protons. Dimers can also be oxidized by Fe^{3+} ions to form cation radicals and chain-growth processes as a classical stepwise polymerization. The reduced Fe^{2+} ions are oxidized by the excess amount of $S_2O_8^{2-}$ ions, which regenerate Fe^{3+} ions and produces $SO_4^{-\cdot}$. The formed PEDOT polymers are oxidized by $SO_4^{-\cdot}$ anion radicals and Fe^{3+} ions to become positively charged, which are balanced by PSS^- or SO_4^{2-} counterions.

Polyelectrolyte PSSH has hydrophobic carbon backbone and hydrophilic sulfonic acid groups ($-SO_3H$) along the backbone, resulting in a micelle-like structure in water with the carbon backbone toward the inner part of the micelles and $-SO_3H$ groups outside. For EDOT monomers, upon adding hydrophobic EDOT monomers, they could either diffuse into the PSSH micelles forming a dissolvable emulsion or leave in water phase forming oil droplets as illustrated in **Figure 5-2**a. Since the step-growth polymerization is initiated by Fe^{3+} ions, deprotonation of $-SO_3H$ groups outside the PSS micelles by adding base could affect whether the EDOT polymerization occurs preferably inside the micelles or in oil droplets in the water phase. Therefore, we proposed a base-dependent mechanism based on emulsion polymerization.[238]

As illustrated in Figure 5-2b, adding equal molar base deprotonates PSSH, resulting in a negatively charged micelle surfaces. Electrostatic force drives positively charged Fe^{3+} ions to the micelle surfaces, initiating the polymerization of EDOT predominately inside the micelles. EDOT monomers in the water phase could continuously diffuse into the micelles as the polymerization processes. In the meantime, self-released protons during the polymerization protonate sulfonate ($–SO_3^-$) groups outside the micelles, reducing the driving force for Fe^{3+} attaching micelles surfaces, and thus resulting in more polymerization in the water phase. $SO_4^{-\cdot}$ anion radicals could diffuse into the micelles or approach PEDOT in the water phase and oxidize the polymerized PEDOT together with Fe^{3+} ion. The presence of $–SO_3^-$ groups outside the emulsion could hinder the diffusion of $SO_4^{-\cdot}$ anion radicals into the emulsion, and thus limit the oxidation of PEDOT in the emulsion. But this electrostatic effect is reduced with the $–SO_3^-$ groups becoming protonated during the course of polymerization. Polyelectrolyte PSS^- and small SO_4^{2-} serve as counterions for oxidized PEDOT in the emulsion and in the water phase, respectively. Thus, the final product under the reaction with the adding of equal molar base is dominated by dispersible PSS^- doped PEDOT mixed with a small amount of non-dispersible SO_4^{2-} doped PEDOT. When the product is spin-coated on substrates and transforms into a solid state after thermal annealing, the short PEDOT chains with 6-18 segments stay attached on long PSS chains, and PSS dominates the PEDOT:PSS grain boundaries.

Without adding base, as illustrated in Figure 5-2c, protonated $–SO_3H$ groups, which are outside the PSS-EDOT micelles, have no electrostatic attraction to Fe^{3+} ions, leading to the initiation of the polymerization of EDOT both inside the micelles and in the water phase without preference. The oxidation also occurs both in the micelles and in the water phase. As a result, the product has more non-dispersible PEDOT doped by SO_4^{2-} than dispersible PSS^- doped PEDOT.

When transforms into a solid state, the SO_4^{2-} doped PEDOT polymers stay in between the PEDOT:PSS grains.

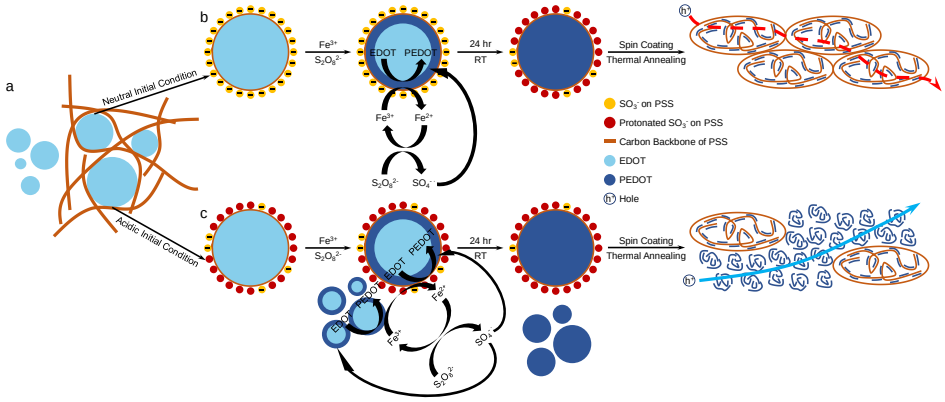

Figure 5-2 Schematic illustration of PEDOT:PSS polymerization mechanism under neutral and acidic initial condition via $Fe^{3+}/S_2O_8^{2-}$ system. (a) The initial emulsion structure of EDOT monomers and PSS chains. (b) Polymerization under a neutral initial condition achieved by adding equal molar base, resulting in the product dominated by stable, well-dispersed PSS^- doped PEDOT. Upon spin coating and thermal annealing, PEDOT:PSS grains surrounded by PSS, which hinders the hole transport. (c) Polymerization under an acidic initial condition by adding less or no base, resulting in the product with a notable amount of non-dispersible SO_4^{2-} doped PEDOT in addition to stable, well-dispersed PSS- doped PEDOT. Upon spin coating and thermal annealing, PEDOT:PSS grains surrounded by the SO_4^{2-} doped PEDOT polymers, which allows hole transport.

Table 5-1 The molar ratios of reactants in the EDOT(-X) polymerization and the water dispersibility and color of the products.

Monomer	KOH: PSSH	PSSH: EDOT-X	$Na_2S_2O_8$: EDOT-X	$Fe_2(SO_4)_3$: EDOT-X	Water Dispersibility	Product Color
EDOT	1.0	4.64	1.49	0.0067	Dispersible	Dark blue
	0.75	4.64	1.49	0.0067	Partially dispersible	Dark blue
	0.5	4.64	1.49	0.0067	Partially dispersible	Dark blue
	0	4.64	1.49	0.0067	Partially dispersible	Dark blue
	0	0*	1.49	0.0067	Non-dispersible	Dark blue
EDOT-MeCl	0	4.64	1.49	0.0067	Partially dispersible	Yellow (color of PSSH)
	1	4.64	4.47	0.0201	Partially dispersible	Grey-green
	0	4.64	4.47	0.0201	Patrially dispersible	Dark blue
EDOT-MeOH	0	4.64	1.49	0.0067	Dispersible	Yellow (color of PSSH)
	1	4.64	4.47	0.0201	Dispersible	Grey-green
	0	4.64	4.47	0.0201	Dispersible	Dark blue

* PSSH was not added but an equal molar amount of HCl was added to adjust the initial pH value to be the same as that in the batch without KOH.

In this study, we used PSSH and adjusted the molar ratio of KOH:PSSH in the reactions, which allows us to investigate the effect of deprotonation of PSSH on the polymerization using EDOT monomer. To verify the proposed mechanism, we performed the polymerization of EDOT by adding different amount of KOH into the solution at the beginning of reactions to control the

deprotonation of PSSH. The molar ratio between KOH and PSSH are 1, 0.75, 0.5, and 0. The mass ratio between PSSH and EDOT is 6:1, which is the same as that for the commercial PEDOT:PSS AI 4083. The molar ratios of reactants are listed in **Table 5-1**. A well-dispersed dark blue solution was obtained for the PEDOT:PSS synthesized with the KOH:PSSH molar ratio of 1 because almost fully deprotonated $-SO_3^-$ groups make the polymerization mainly following the process described in Fig. 5-2b. Without adding KOH and with the KOH:PSSH molar ratios of 0.5 and 0.75, the final dark blue solutions have some sediments, which could be attributed to the protonated or partially protonated $-SO_3^-$ groups, making the process dominated by the mechanism described in Fig. 5-2c. To verify the sediments are SO_4^{2-} doped PEDOT, a batch of reaction was conducted without adding PSSH but adding equal molar amount of HCl. In this way, polyelectrolyte PSS^- is completely eliminated from the solution and the oxidized PEDOT can only be doped by SO_4^{2-} or Cl^-. Indeed, the product is a completely non-dispersible dark blue mixture.

The UV-Vis absorption spectra of the synthesized PEDOT:PSS and commercial AI 4083 PEDOT:PSS are shown in **Figure 5-3**. The polaron and bipolaron absorption range at 700-900 and beyond 1200 nm, respectively, appear in all samples with PSS, indicating the polymerization and oxidation of PEDOT:PSS.[239] PEDOT synthesized without PSS exhibit a blue-shifted polaron absorption and reduced bipolaron absorption intensity. Since the polaron and bipolaron absorptions are due to the oxidation formed sub-bandgap state and the absorptions become narrower with higher oxidation level,[90, 240] the blue-shifted polaron absorption and reduce bipolaron absorption intensity indicate that the PEDOT is not effectively oxidized or doped by SO_4^{2-} or Cl^-.

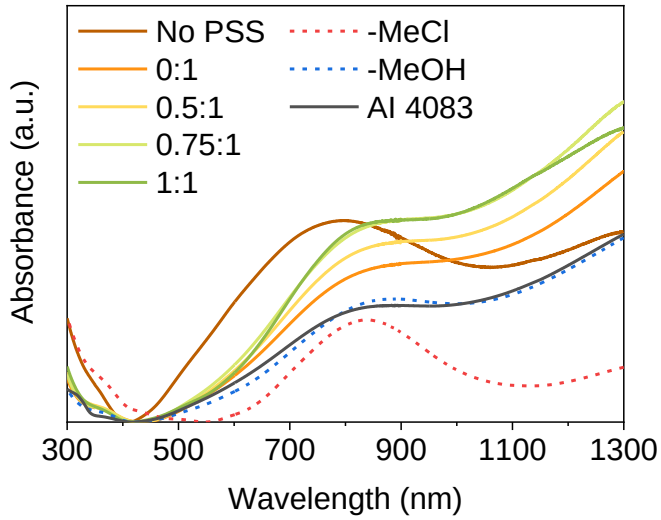

Figure 5-3 UV-Vis spectra of the synthesized PEDOT:PSS with different KOH:PSSH molar ratios and without PSS, and the PEDOT-MeOH:PSS and PEDOT-MeCl:PSS synthesized with no base and triple amount of oxidant, as well as the commercial AI 4083 PEDOT:PSS. Spectra are normalized by matching the lowest absorption point.

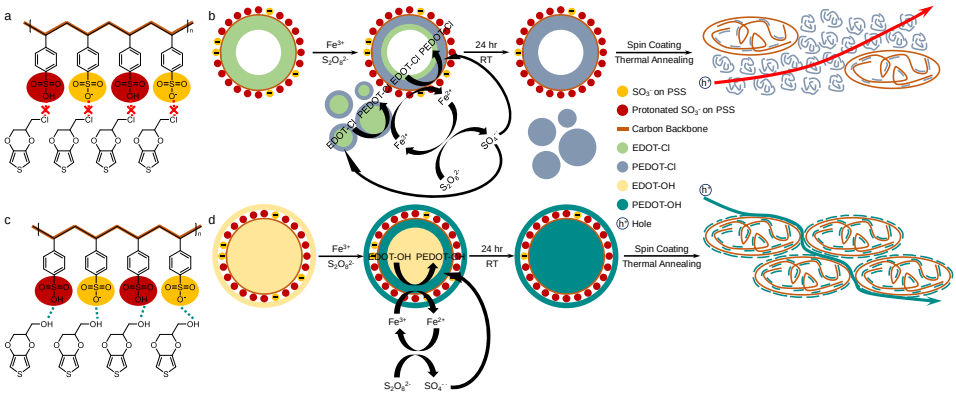

Figure 5-4 (a) Schematic illustration of strong repulsion between EDOT-MeCl monomer and protonated or deprotonated PSS because of the high electronegativity of the -MeCl function group. (b) PEDOT-MeCl polymerization under an acidic initial condition, resulting in the product with a mixture of non-dispersible SO42- doped PEDOT-MeCl and stable, well-dispersed PSS- doped PEDOT-MeCl. Upon spin coating and thermal annealing, PEDOT-MeCl:PSS grains surrounded

by poorly SO_4^{2-} doped PEDOT-MeCl polymers. (c) Schematic illustration of hydrogen bonding between EDOT-MeOH monomer and protonated or deprotonated PSS. (d) PEDOT-MeOH polymerization under an acidic initial condition, resulting in stable, well-dispersed PSS- doped PEDOT-MeOH. Upon spin coating and thermal annealing, PEDOT-MeOH:PSS domains are surrounded by PSS attached with PEDOT-MeOH, which allows hole transport through the thin layer of PEDOT-MeOH between PEDOT-MeOH:PSS domains.

We introduced functional groups of -MeCl and -MeOH to the oxyethylene ring of EDOT and synthesized EDOT-MeCl and EDOT-MeOH monomers as shown in Scheme 5-1. The introduction of -MeCl and -MeOH groups to EDOT causes drastically different molecular interactions with PSS, leading to different reaction mechanisms and thus final products. As illustrated in **Figure 5-4**a, the EDOT-MeCl monomers tend to repulse either protonated or deprotonated PSS due to the high electronegativity introduced by the -MeCl functional group, making EDOT-MeCl monomers hard to diffuse into PSSH micelles. Hence, as illustrated in Fig. 5-4b, most of EDOT-MeCl monomers are polymerized via the step-growth polymerization initiated by Fe^{3+} in the water phase, and only a small amount of them are polymerized inside the PSS micelle. The strong electronegativity of -MeCl also makes it hard to be doped by negatively charged PSS^- or SO_4^{2-} in PSS micelles or water, respectively, due to the strong electrostatic repulsion. As a result, the final PEDOT-MeCl is lightly doped by either PSS^- or SO_4^{2-} counterions. When forms into a solid state, poorly SO_4^{2-} doped PEDOT-MeCl polymers stay in between PEDOT-MeCl:PSS domains. Unlike EDOT-MeCl monomer, EDOT-MeOH can form hydrogen bonding with the oxygen or hydrogen atoms in the deprotonated or protonated sulfonate group of PSS counterion (Fig. 5-4c), respectively, as well as water, making EDOT-MeOH monomers easily diffuse into the PSS micelle or in the peripheral of the micelle (Fig. 5-4d). No obvious oil droplets

were formed when mixing PSSH and EDOT-MeOH in water. The step-growth polymerization predominately occurs at PSS micelles, and so does the oxidization, resulting in stable PEDOT-MeOH:PSS. When transforms into a solid state, short PEDOT-MeOH chains are attached on PSS chain at the PEDOT-MeOH:PSS grain boundaries.

We polymerized EDOT-MeCl and EDOT-MeOH using the same molar ratios of reactants as those used in the polymerization of EDOT and without adding KOH (Table 5-1). However, the color of the solutions remained yellow as the color of PSSH over 24 h, indicating that no polymerization occurred. The electron-pulling effect caused by chloride or oxygen atom raises the oxidation potential and makes it harder to remove an electron from the monomer thiophene ring by Fe^{3+} and $SO_4^{-\cdot}$ (Scheme 5-2).[241] Therefore, we tripled the molar ratios of $Na_2S_2O_8$ and $Fe_2(SO_4)_3$ to monomers, and added KOH in a 1:1 KOH:PSSH molar ratio. This condition resulted in both solutions turning into a gray-green color in 24 h, indicating that short-chain PEDOT-MeCl and PEDOT-MeOH might be formed and the doping level is low. It has been reported that the acidity of the reaction solution influences the reaction kinetics and adding base has been used to adjust the reaction kinetics.[236, 242] Therefore, we conducted another batch of polymerization by keeping the high molar ratios of $Na_2S_2O_8$ and $Fe_2(SO_4)_3$ to monomers but without adding KOH. Under this condition, both solutions turned into dark blue color and the reactions completed after 24 h. The PEDOT-MeCl:PSS solution had some precipitates while the PEDOT-MeOH:PSS solution was homogeneous. The PEDOT-MeOH:PSS solution shows both polaron and bipolaron peaks in the UV-Vis absorption spectrum, similar to those in commercial AI 4083 PEDOT:PSS (Fig. 5-3). For PEDOT-MeCl:PSS, a clear polaron absorption is shown at 700-900 nm and a low rising bipolaron tail presents above ~1200 nm, indicating its low doping level.

5.3.2 Surface Morphology of PEDOT:PSS and Functionalized PEDOT:PSS

Surface morphology of the thin films of synthesized PEDOT:PSS, PEDOT-MeCl:PSS and PEDOT-MeOH:PSS as well as commercial AI 4083 PEDOT:PSS coated on glass substrates were characterized using TM-AFM. To gain the surface morphology of each sample, we acquired both large area (10 μm × 10 μm) and small area (1 μm × 1 μm) topographic AFM images, which are shown in **Fig. 5-5**. The impact of adding KOH in the polymerization of PEDOT:PSS on the final products can be observed from the surface morphology of thin films. The thin film of the PEDOT:PSS synthesized without adding KOH exhibits a very rough surface morphology presenting elongated aggregates with the height exceeding 100 nm and a square root mean roughness (Rq) of 21 nm in the large area image (Fig. 5-5a) because of the existence of SO_4^{2-} doped non-dispersible PEDOT as illustrated in Fig. 5-2c. Adding KOH in the polymerization solution improves the surface morphology gradually, showing small aggregates with the height around 50 nm and reduced Rq values of 8.52 and 7.98 nm for the thin films of the PEDOT:PSS synthesized with 0.5 and 0.75 KOH:PSSH molar ratios (Figs. 5-5b and c), respectively. This also demonstrates the trend that more PEDOT polymers are doped by PSS^- because of the process described in Fig. 5-2b becomes dominant. Further increased the molar ratio of KOH:PSSH to 1, the morphology of the thin film was significantly improved with the surface roughness (Rq = 1.24 nm) (Fig. 5-5d), which is close to the commercial AI 4083 PEDOT:PSS (Rq = 1.09 nm) (Fig. 5-5k). Figure 5-5d shows only some small aggregates on the surface with a height around 20 nm. Fine-line features are shown in Figs. 5-5d and k, which could be due to well-dispersed PEDOT:PSS. Line features are also shown in Figs. 5-5b and c, indicating more PSS doped PEDOT in the products. Figures 5-5e-h, and n are the small area images taken from the flat area of the large area images. PEDOT:PSS synthesized without and with 0.5 and 0.75 molar ratio KOH exhibits

clear domain contrast and particle-like structures (Figs. 5-5e-g), which refer to the PEDOT doped by SO_4^{2-} as illustrated in Fig. 5-2c. While for commercial AI 4083 and PEDOT:PSS synthesized with KOH:PSSH ratio of 1, no particle-like structures are observed and the films exhibit smooth uniform morphologies with fine-line structure (Figs. 5-5h and n), which is due to the disperisble PSS doped PEDOT as illustrated in Fig. 5-2b.

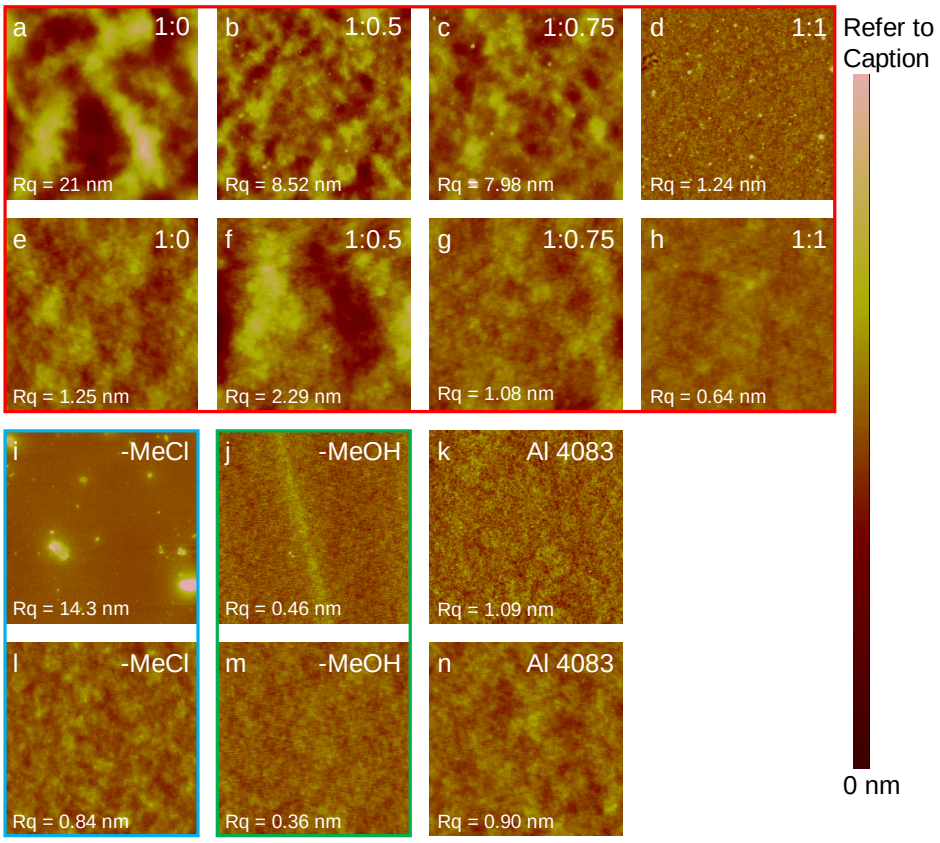

Figure 5-5 Topographic AFM images of the thin films of PEDOT:PSS synthesized with the KOH:PSSH molar ratio of 0 (a, e), 0.5 (b, f), 0.75 (c, g), and 1 (d, h), PEDOT-MeCl:PSS (i,l), PEDOT-MeOH:PSS (j, m), and the commercial AI 4083 PEDOT:PSS (k, n). Image sizes are 10 μm × 10 μm for (a-d, i-k) and 1 μm × 1 μm for (e-h, l-n). The Z scales are as following: for synthesized PEDOT:PSS,150 nm (a), 100 nm (b, c), and 20 nm (d-h); for PEDOT-MeCl:PSS, 150

nm (i) and 10 nm (l); for PEDOT-MeOH:PSS, 10 nm (j, m); for commercial AI 4083 PEDOT:PSS, 20 nm (k, n).

Figure 5-5i shows the large area scan AFM image of the PEDOT-MeCl:PSS thin film, which has aggregates in different sizes with height above 150 nm but a relatively smooth background. The large aggregates are attributed to the poorly SO_4^{2-} doped PEDOT-MeCl as described in Fig. 5-4b. The PEDOT-MeOH:PSS thin film has a smooth and uniform morphology without any aggregates and a low Rq of 0.46 nm in the large area scan AFM image (Fig. 5-5j). The zoom-in image of PEDOT-MeCl:PSS sample (Fig. 5-5l) shows domain contrast and particle-like structure similar to PEDOT:PSS synthesized without KOH, which could be attributed to the aggregated PEDOT-MeCl polymers that are poorly doped by SO_4^{2-}. The small area scan image of PEDOT-MeOH:PSS, however, shows a very smooth and uniform morphology with the lowest Rq of 0.36 nm and more fine-line features (Fig. 5-5m), indicating well dispersed PEDOT-MeOH along PSS.

5.3.3 Oxidation and doping level of PEDOT:PSS and functionalized PEDOT:PSS

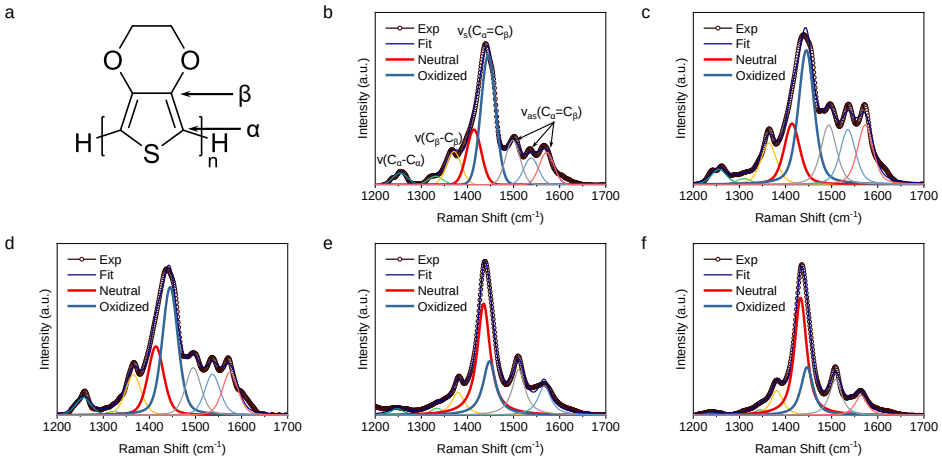

Figure 5-6 (a) PEDOT structure showing α and β carbon atoms on the thiophene ring. (b-f) Raman spectra along with the spectral deconvolution of the thin films for (b) commercial AI 4083

PEDOT:PSS, PEDOT:PSS synthesized with (c) 1:1 and (d) 0:1 KOH:PSSH molar ratio, (e) PEDOT-MeCl:PSS, and (f) PEDOT-MeOH:PSS.

To further investigate the effect of KOH and functional groups on the oxidation and doping level of synthesized PEDOT:PSS and functionalized PEDOT-MeCl:PSS and PEDOT-MeOH:PSS, respectively, we acquired Raman spectra of these products as shown in **Figure 5-6**. In the spectral window of 1200-1700 cm^{-1}, peaks are mainly due to the vibrational modes related to C_α and C_β on the thiophene ring (Fig. 5-6a). The Raman peak assignment of the synthesized PEDOT:PSS and the commercial AI 4083 sample is listed in **Table 5-2** and are labeled in Fig. 5-6b. Briefly, the peaks in the ranges of 1258-1267 cm^{-1} and 1364-1368 cm^{-1} refer to the C_α-$C_{\alpha'}$ inter-ring stretching and the C_β-C_β stretching, respectively. The most intense peak at 1429-1443 cm^{-1} is related to the C_α=C_β symmetrical stretching, which can be deconvoluted into two separated bands, centered at 1414 and 1445 cm^{-1} due to the C_α=C_β symmetrical stretching from the PEDOT in neutral and oxidized state, respectively.[243-245] The C_α=C_β asymmetrical stretching occupies a board range from 1496-1571 cm^{-1}. The highly oxidized PEDOT usually has three C_α=C_β asymmetrical stretching peaks while the less oxidized PEDOT usually has two.[246] The spectra were fitted and the ratios of oxidized to neutral (O:N) state in the PEDOT backbone of different samples were estimated from the area of the peaks corresponding to the C_α=C_β symmetry stretching modes of oxidized and neutral state.

Table 5-2 Raman peak assignment of the synthesized PEDOT:PSS and commercial AI 4083 PEDOT:PSS excited by 532 nm laser. The unit is cm^{-1}. The wavenumbers of each peak are from the experimentally measured Raman spectra, not the fittings.

Assignment	AI 4083	1:1 KOH:PSSH	0:1 KOH:PSSH			No PSSH before Ion Exchange	No PSSH after Ion Exchange
			Mixture	Solution	Sediment		
$\nu(C_\alpha\text{-}C_\alpha)$ inter-ring	1258	1261	1260	1262	1259	1267	1267
$\nu(C_\beta\text{-}C_\beta)$	1368	1364	1366	1366	1364	1367	1367
$\nu_s(C_\alpha=C_\beta)$	1439	1438	1437	1443	1429	1438	1437
$\nu_{as}(C_\alpha=C_\beta)$	1499	1496	1495	1502	1489	1498	
							1510
	1535	1536	1536	1538	1534		
							1564
	1566	1571	1570	1569	1570	1567	

The thin film of PEDOT:PSS synthesized with a 1:1 KOH:PSSH molar ratio has an O:N ratio of 2.20 (Fig. 5-6c), which is similar to the O:N ratio of 2.35 for the commercial AI 4083 PEDOT:PSS. The high O:N ratio indicates that the PEDOT is effectively oxidized and doped by PSS counterion. While the O:N ratio reduces to 1.86 (Fig. 5-6d) for the thin film of sonicated PEDOT:PSS synthesized with a 0:1 KOH:PSSH molar ratio. We centrifuged the solution of PEDOT:PSS synthesized with a 0:1 KOH:PSSH molar ratio to separate the homogeneous solution and the sediment and acquired the Raman spectra of each part (**Figure 5-7**a and b). The thin film made from the homogeneous solution exhibits an O:N ratio of 2.62, which is higher compared with that of the thin film of AI 4083 and PEDOT:PSS synthesized with a 1:1 KOH:PSSH molar ratio. The improved O:N ratio of the 0:1 KOH:PSSH homogeneous sample is due to the higher

reactivity of Fe^{3+} and $SO_4^{-\cdot}$ under acidic environment,[236, 247, 248] which makes the PEDOT highly oxidized. However, the sediment exhibits a much lower O:N ratio of 1.32. The low O:N ratio of the sediment might be attributed to the bivalent SO_4^{2-} counterions cannot effectively dope the oxidized PEDOT,[244] and these small ions are easily removed in the ion exchange process, further dedoping the PEDOT. For PEDOT synthesized without adding PSS but adding HCl, PEDOT can only be doped by small SO_4^{2-} and Cl^- ions. The O:N ratio further reduces to 0.71 (Fig. 5-7c) and 0.49 (Fig. 5-7d) before and after ion exchange, respectively. There are only two peaks shown in the C_α=C_β asymmetrical stretching range, indicating that the PEDOT is not effectively oxidized and doped. The Raman results of PEDOT without PSS agree with the observation of blue-shifted polaron absorption and low bipolaron absorption in the UV-Vis spectrum (Fig. 5-3).

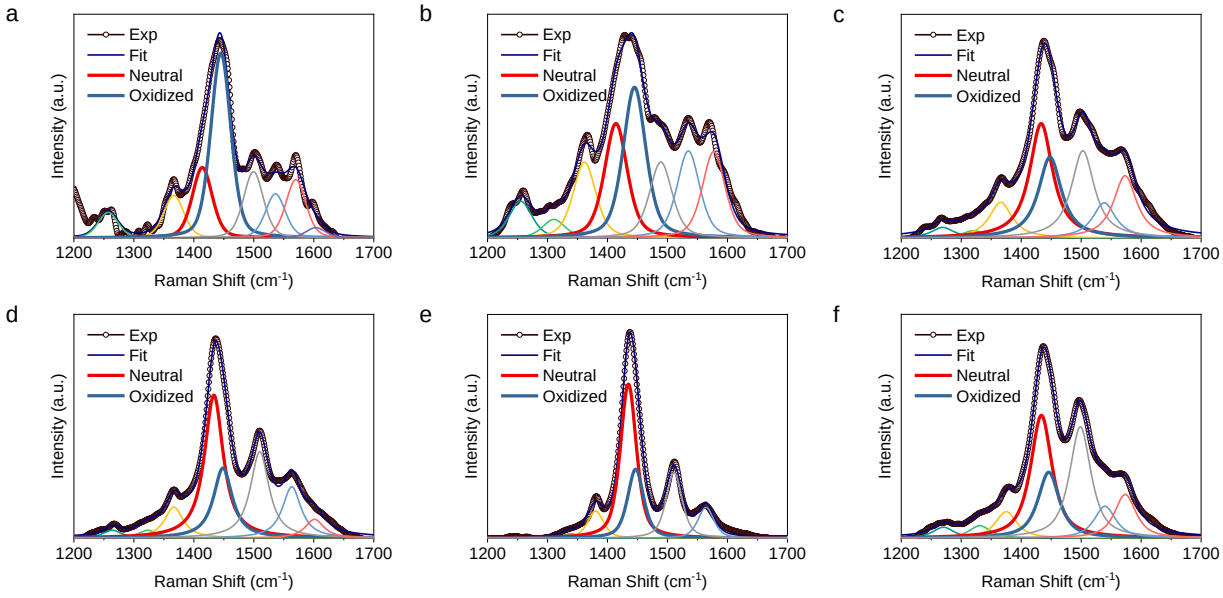

Figure 5-7 Raman spectra along with the spectral deconvolution of the thin films for (a) the top homogeneous solution and (b) the bottom sediment of PEDOT:PSS synthesized with a 0:1 KOH:PSSH molar ratio after centrifugation. PEDOT synthesized without adding PSSH (c) before

and (d) after ion exchange. (e) Top homogeneous solution and (f) bottom sediment of PEDOT-MeCl:PSS after centrifugation.

Table 5-3 Raman peak assignment of the synthesized PEDOT-MeCl:PSS and PEDOT-MeOH:PSS thin films excited by 532 nm laser. The unit is cm^{-1}. The wavenumbers of each peak are from the experimentally measured Raman spectra, not the fittings.

Assignment	PEDOT-MeCl:PSS			PEDOT-MeOH:PSS
	Mixture	Solution	Sediment	
$\nu(C_\alpha\text{-}C_\alpha)$ inter-ring	1244	N.A.	1277	1240
$\nu(C_\beta\text{-}C_\beta)$	1382	1381	1379	1381
$\nu_s(C_\alpha{=}C_\beta)$	1438	1437	1437	1435
$\nu_{as}(C_\alpha{=}C_\beta)$	1510	1512	1496	1508
	1566	1562	1566	1563

Regarding functionalized PEDOT, since PEDOT-MeCl:PSS is a mixture of dispersible PSS doped PEDOT-MeCl and non-dispersible SO_4^{2-} doped PEDOT-MeCl, we collected the Raman spectra of the thin films formed from the sonicated mixture as well as from the top homogeneous solution and bottom sediment that were separated by centrifugation. The Raman peak assignments of the synthesized PEDOT-MeCl:PSS and PEDOT-MeOH:PSS samples are listed in **Table 5-3**. The C_α-C_α inter-ring stretching peaks of functionalized PEDOT:PSS are in the range of 1240-1277 cm^{-1}. The $\nu(C_\beta\text{-}C_\beta)$ peaks are in the range of 1379-1381 cm^{-1}, which are blueshift compared to 1368 cm^{-1} for commercial AI 4083 and synthesized PEDOT:PSS. The blueshift of $\nu(C_\beta\text{-}C_\beta)$ peaks is possibly due to the introduction of -MeCl and -MeOH functional groups, which makes the dioxyring stiffer. The most intense peaks at 1435-1437 cm^{-1} are also attributed to the $C_\alpha{=}C_\beta$ symmetrical stretching, which can be deconvoluted into neutral and oxidized PEDOT-MeCl and PEDOT-MeOH. The $C_\alpha{=}C_\beta$ asymmetrical stretching occupies a broad

range from 1496-1566 cm^{-1}. All the functionalized PEDOT-MeCl:PSS and PEDOT-MeOH:PSS samples exhibit two peaks in the $C_\alpha=C_\beta$ asymmetrical stretching range, which indicates that the doping level is not as high as PEDOT:PSS samples even though triple amount of $Fe_2(SO_4)_3$ and $Na_2S_2O_8$ were used.

The O:N ratios are 0.48, 0.45 and 0.54 for the films prepared with the sonicated PEDOT-MeCl:PSS mixture, the homogeneous solution and the sediment of PEDOT-MeCl:PSS, respectively. These ratios are far below those for PEDOT:PSS. This is mainly due to the low doping level resulted from the aforementioned electron-pulling effect introduced by the -MeCl and the repulsive force between -MeCl group and PSS^- or SO_4^{2-} counterions. The C_α-C_α inter-ring stretching peak of PEDOT-MeCl:PSS almost disappears in the top homogeneous solution while still exists centered at 1277 cm^{-1} in the sediment. This result supports our hypothesis that EDOT-MeCl monomers are hard to form emulsions with PSS and the step-growth polymerization of EDOT-MeCl monomers mainly takes place in the water phase, producing a relatively longer PEDOT-MeCl in the water phase. PEDOT-MeOH:PSS also shows a low O:N ratio of 0.41 because of the electron-pulling effect introduced by –MeOH, making PEDOT-MeOH hard to be oxidized. The C_α-C_α inter-ring stretching peak for PEDOT-MeOH:PSS is slightly stronger than PEDOT-MeCl:PSS. This is mainly due to the hydrogen bonding between EDOT-MeOH monomers, making them stay close to each other and helping polymerization.

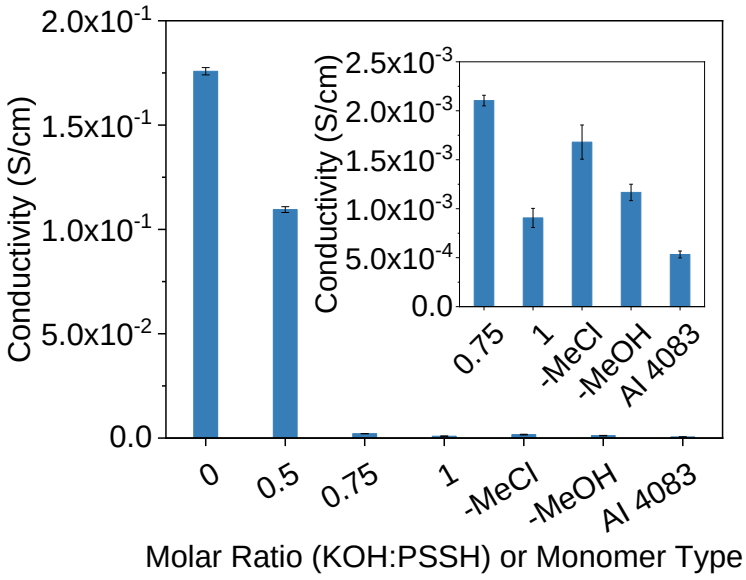

Figure 5-8 Conductivity of the thin films of the PEDOT:PSS synthesized with varied KOH:PSSH molar ratios, PEDOT-MeCl:PSS, PEDOT-MeOH:PSS, and commercial AI 4083 PEDOT:PSS. The inset displays the zoom-in graph for five samples with low conductivities.

5.3.4 Conductivity of PEDOT:PSS and Functionalized PEDOT:PSS

The protonation-state of PSS related different reaction processes also impact the conductivity of PEDOT:PSS thin films. The thin films of synthesized PEDOT:PSS were made by spin coating the sonicated PEDOT:PSS solutions, including precipitates, for conductivity measurements. The conductivity of the thin film of each sample was measured through the four-point probe measurement and are plotted in **Fig. 5-8**. The conductivity of synthesized PEDOT:PSS thin films decreased with the increasing of KOH:PSSH molar ratio. The conductivity exhibited the highest value of 1.76 × 10^{-1} S/cm for the thin film synthesized without adding KOH. The conductivity decreased slightly to 1.10× 10^{-1} S/cm by adding KOH with the KOH:PSSH molar ratio of 0.5. The conductivity decreased significantly by two to three orders of magnitudes to the

values of 2.10×10^{-3} and 9.06×10^{-4} S/cm when the molar ratio of KOH:PSSH was increased to 0.75 and 1, respectively.

Basically, electrical conductivity (σ) is the product of carrier charge (e), carrier concentration (n) (cm^{-3}) and carrier mobility μ ($cm^2\ V^{-1}\ s^{-1}$), expressed as $\sigma = ne\mu$, where e is a constant, n and μ can be modified via varying polymerization conditions. As π-conjugated polymers, the carrier concentration and carrier mobility of PEDOT, PEDOT-MeCl, and PEDOT-MeOH are highly determined by the oxidative state, the chain-length, and the co-plane and packing of the polymer backbone. In addition, because PEDOT, PEDOT-MeCl, and PEDOT-MeOH are doped by PSS or SO_4^{2-}, the structure and morphology of the polymer complex place an important role in determining the electrical conductivity. Previous studies showed that the conductivity of PEDOT thin films is mainly determined by the charge carrier hopping distance between PEDOT backbones, or carrier mobility, which is strongly affected by the amount of counterions, especially whether the counterions are polyelectrolytes or small anions.[242] Doping level, or carrier concentration, has relatively less impact on the conductivity since the oxidation level of PEDOT is limited.[242] Some post-treatment were applied to replace PSS with SO_4^{2-} or organic acid,[249, 250] and several orders of magnitude enhancement of conductivity were achieved. Therefore, we attribute the high conductivity of the samples synthesized without or with 0.5 molar ratio KOH to the existence of SO_4^{2-} doped PEDOT domains, which allows charge transport easily without blocking by nonconductive PSS domains (Fig. 5-2c). For PEDOT:PSS synthesized with KOH:PSSH ratio of 0.75 or 1, the oxidized PEDOT polymers are mainly doped by nonconductive PSS^- counterions. Large, hydrophilic polyelectrolyte PSS^- counterions stabilize the hydrophobic, conductive PEDOT polymers in water by forming PEDOT-core PSS-shell structures. Charge transport between PEDOT domains is significantly hindered by nonconductive PSS-shells (Fig. 5-

2b), resulting in low conductivities. Commercial AI 4083 PEDOT:PSS has high water dispersibility and homogeneity, benefits from the well-formed PEDOT-core PSS-shell structure. Therefore, commercial AI 4083 PEDOT:PSS thin film exhibits the lowest conductivity with a value of 5.33×10^{-4} S/cm compared to all synthesized PEDOT:PSS.

We measured the conductivity of the synthesized PEDOT-MeCl:PSS and PEDOT-MeOH:PSS thin films. The PEDOT-MeCl:PSS was sonicated before spin coating and the film contains non-dispersible portion. The conductivity of PEDOT-MeCl:PSS is 1.68×10^{-3} S/cm, higher than that of AI 4083 PEDOT:PSS (5.33×10^{-4} S/cm) while much lower than PEDOT:PSS synthesized with 0:1 KOH:PSSH ratio (1.76×10^{-1} S/cm) with similar morphology. The low conductivity of PEDOT-MeCl:PSS is mainly due to the low oxidation and doping level caused by the electron-pulling -MeCl functional group. Even though the non-dispersible portion was included in the sample, this portion of PEDOT-MeCl is also poorly doped by small counterion SO_4^{2-}, which does not benefit the conductivity. The conductivity of PEDOT-MeOH:PSS is 1.17×10^{-3} S/cm, which is higher than the conductivity AI 4083 PEDOT:PSS (5.33×10^{-4} S/cm) and PEDOT:PSS synthesized with 1:1 KOH:PSSH (9.06×10^{-4} S/cm) with similar smooth morphology. The increased conductivity could be due to the hole transport pathway formed by the thin layer of PEDOT-MeOH attached to the PSS shells as illustrated in Fig. 5-4d.

5.4 Conclusion

In conclusion, we studied the effect of base and functional groups on the oxidative chemical polymerization of EDOT and functionalized EDOT-MeCl and EDOT-MeOH monomers, and the oxidation and doping level, morphology and conductivity of the synthesized polymer thin films. For the polymerization of EDOT, the protonation state of PSS is critical to the dispersibility and morphological and electronic properties of PEDOT:PSS. Neutralized PSSH, by adding equal

molar of KOH, allows Fe^{3+} ions selectively polymerize EDOT monomers inside PSS micelles, yielding PSS doped, well-dispersed PEDOT:PSS in water. These PEDOT:PSS films are smooth but the conductivity is low (9.06×10^{-4} S/cm), in the same range of commercial AI 4083 PEDOT:PSS, because of the nonconductive PSS shells around the PEDOT dominated domains. Acidic PSSH, by adding partial or no KOH, makes Fe^{3+} ions polymerize EDOT monomers both inside PSS micelles and in the water phase, yielding the mixtures of PSS doped, dispersible PEDOT:PSS and SO_4^{2-} doped, non-dispersible PEDOT:SO_4. The films made from these products exhibit particles and two to three orders of magnitude enhanced conductivity (1.10×10^{-1} and 1.76×10^{-1} S/cm) because of the existence of SO_4^{2-} doped PEDOT domains, which allows hole transport easily without the blocking of nonconductive PSS. All the synthesized PEDOT:PSS have relative high oxidation and doping levels, presented by the peak area ratios in the range of 2.2-2.7 corresponding to the oxidized and neutral C_α=C_β symmetrical stretching modes in Raman spectroscopy. Introducing -MeOH and -MeCl functional group to EDOT monomer, the electron-pulling property of these functional groups raise the oxidative potential of the monomers, and thus higher amount of oxidant is required for the polymerization of EDOT-MeCl and EDOT-MeOH. The repulsive force between EDOT-MeCl monomer and PSS or SO_4^{2-} counterion strongly hinder the oxidation and doping process, resulting in the mixture of PSS doped, water-dispersible PEDOT-MeCl and SO_4^{2-} doped, water-non-dispersible PEDOT-MeCl. The thin films of PEDOT-MeCl have large particles and low conductivity of 1.68×10^{-3} S/cm compared to PEDOT:PSS synthesized without adding KOH with the similar aggregation morphology. The hydrogen bonding between EDOT-MeOH monomer and PSS counterion as well as among EDOT-MeOH monomers makes the polymerization and doping processes easily, yielding PSS doped, water-dispersible PEDOT-MeOH. The PEDOT-MeOH:PSS thin films are very smooth and the conductivity ($1.17 \times$

10^{-3} S/cm) is higher than commercial AI 4083 with the similar smooth morphology because of a thin layer of PEDOT-MeOH attached along the PSS in grain boundaries. The oxidation and doping levels of PEDOT-MeCl and PEDOT-MeOH are low, revealed by the low peak area ratios in the range of 0.4-0.5 corresponding to the oxidized and neutral $C_\alpha=C_\beta$ symmetrical stretching modes. This study sheds light on the polymerization of PEDOT with functional groups and provides a guideline for the synthesis of functionalized PEDOT conducting polymers with polyelectrolyte using oxidative chemical polymerization.

Chapter 6 CONCLUSIONS AND OUTLOOK

6.1 Conclusions

This thesis focuses on the development of the next generation optoelectronic devices, including photodetectors and solar cells. To achieve the goal, novel optoelectronic materials including $CH_3NH_3PbCl_3$ and MA-free perovskites, F8T2 and functionalized PEDOT:PSS conducting polymers, and ZnO NPs were either synthesized and/or applied directly for device fabrication.

To explore the potential of perovskite materials in UV light detection, pinhole-free $CH_3NH_3PbCl_3$ perovskite thin films were fabricated via a two-step spin coating and solvent-vapor-assisted thermal annealing method under low temperature for the first time. Prototypical UV photodetectors were fabricated and showed strong photoresponse in 300-400 nm region. The results demonstrated that low-temperature solution-processed $CH_3NH_3PbCl_3$ perovskite thin films offer a great potential for making flexible, lightweight visible-blind UV-A photodetectors. The design and fabrication of narrowband photomultiplication type photodetectors using novel organic-inorganic hybrid materials is challenging due to the broad absorption range of organic and inorganic semiconductor materials. To counter this challenge, nanocomposite thin films containing the wide bandgap conducting polymer F8T2 blended with wide bandgap ZnO NPs are served as the active layers of the photodetectors. Narrowband UV photodetectors with high gain and low driving voltage were demonstrated by adopting a symmetric device structure, controlling the active layer composition and microstructure, and manipulating the light penetration depth in the active layer. The fabricated photodetector exhibits a high external quantum efficiency (EQE) of 782% at 358 nm under a low forward bias of 3 V with the FWHM of 16 nm. The impacts of the F8T2:ZnO

NPs weight ratio and device structure on the UV-selectivity and device performance are investigated and discussed. The designing method offers a broadly applicable pathway to design and fabricate narrowband UV photodetectors.

The instability of perovskite materials, including intrinsic and operational instability, strongly hinders its applications in real-life. Along the research, we realized that the MA cation is one of the major sources of the intrinsic instability. To solve the problem, two types of MA-free perovskites, $Rb_{0.05}Cs_{0.1}FA_{0.85}PbI_3$ and $Cs_{0.15}FA_{0.85}PbI_3$ were fabricated and the effect of Rb^+ on the solar cell device performance and long-term stability were investigated. The defect-mediated cation and anion migration under electric field was revealed and the Rb^+ is identified to be more vulnerable compared to Cs^+. By simply mixing the precursor solution before spin coating, the defect states in both types of perovskite were significantly reduced and device stabilities against electric field were improved. The modified precursor solution provides devices with $Rb_{0.05}Cs_{0.1}FA_{0.85}PbI_3$ and $Cs_{0.15}FA_{0.85}PbI_3$ active layer that retains 68% and 92% of their initial PCE, respectively, over 30 days under N_2 protection. The work sheds a light on the solution of the operational instability of perovskite solar cells and paves the pathway for their industrialization.

PEDOT:PSS conducting polymer has been applied in the previous photodetector and solar cell devices in this thesis. For further improvement of the device performance, we introduced a -MeOH and a -MeCl function group to the oxyethylene ring of EDOT monomer to obtain EDOT-MeOH and EDOT-MeCl monomer, respectively. Oxidative chemical polymerization was applied to synthesize pristine PEDOT:PSS, PEDOT-MeCl:PSS, and PEDOT-MeOH:PSS. The polymerization mechanism of PEDOT:PSS and effects of functional group on the polymerization were revealed. The integration of the PEDOT-MeCl:PSS and PEDOT-MeOH:PSS into perovskite solar cells has been demonstrated by our lab mates. The study provides a guideline for the synthesis

of functionalized PEDOT conducting polymers with polyelectrolyte counterions using oxidative chemical polymerization, and is broadly applicable in various PEDOT:PSS based electronics beyond photodetectors and solar cells, such as bio-sensors.

6.2 Outlook

This thesis explores the synthesis, optimization, and application of several novel optoelectronic materials, and reveals a lot of research areas for the community to explore.

$CH_3NH_3PbCl_3$ perovskite is an attractive material for UV detection. This thesis focuses on the fabrication of $CH_3NH_3PbCl_3$ perovskite thin films using solution process. The prototypical UV photodetector performance is still not comparable to the state-of-the-art photodetector based on inorganic materials. The reason lies in the poor energy level alignment between the $CH_3NH_3PbCl_3$ and the commercially available charge carrier transport layers. Future research direction could be developing visible-blind electron and hole transport layers with improved energy level alignment with the $CH_3NH_3PbCl_3$. Beyond photodetector, blue LED and laser, transparent solar window, and tandem solar cells could also be developed based on the $CH_3NH_3PbCl_3$ perovskite thin films reported in this thesis. The narrowband UV photodetector based on F8T2:ZnO NCs reported in the thesis have already shown narrowband detection, high sensitivity, and low driving voltage features. Further research would mainly focus on the integration with other optoelectronic devices, such as scintillator, to fabricate γ-ray or x-ray detectors.

The MA-free perovskite solar cells reported in this thesis exhibit satisfactory stability. To improve the device performance, the integration of functionalized PEDOT:PSS would be one of the future research directions. The functional groups on the PEDOT chain could passivate positive charged ionic defects and form hydrogen bond with perovskite, respectively, and improve the hole

transport at the perovskite/HTL interface. Theoretically, zwitterionic molecules or polymers and Lewis acid and base could be mixed into perovskite precursor or coated onto perovskite layer to passivate positively and negatively charged ionic defect simultaneously. In Appendix B, however, no positive results were observed. Ammonium halide salts commonly serves as the component of perovskite materials could also be applied to passivate the A-site and halide ionic defects in perovskite. In the Appendix B, preliminary results have shown the effect of ethylenediammonium iodide on the improvement of device performance. Future research could focus on adjusting the carbon spacer length of diammonium iodide salt and changing the number of ammonium group on the molecule.

The oxidative chemical polymerization mechanism of PEDOT:PSS and functionalized PEDOT:PSS reported in this thesis opens a broad research area with almost endless number of functional groups to be installed onto the PEDOT:PSS. The electronegative functional group such as -MeCl and -MeOH reduce the conductivity and increase the work function of PEDOT:PSS. In Appendix A, the synthesis and characterization of PEDOT:PSS with bromomethyl functional group (-MeBr) was demonstrated and further confirmed the hardness of oxidative polymerization on PEDOT with electronegative functional group. To improve the conductivity, electropositive functional group -dimethylaminomethyl (-MeDMA) could be introduced. The functionalized PEDOT:PSS could also serve as the active layer of electrochemical biosensor devices to specifically detect molecular that interact/resist with its functional groups.

Appendix A SYNTHESIS AND OXIDATIVE POLYMERIZATION OF BROMOMETHYL AND DIMETHYLAMINOMETHYL FUNCTIONALIZED 3,4-ETHYLENEDIOXYTHIOPHENE

A.1 Introduction

In this thesis work, the synthesis and chemical polymerization of -MeCl and -MeOH functionalized EDOT monomers were performed to demonstrate the effect of functional group on the polymerization mechanism. However, based on the results reported by our lab mates, the performance of the perovskite solar cells based on these two novel HTLs only exhibit slight improvement compared with the commercial available PEDOT:PSS, even after some HTL post-treatments. The unsatisfactory performance might relate to the intrinsic low conductivities of these two functionalized PEDOT:PSS due to the highly electronegative (electron-withdrawing) functional groups,[1] and the poor surface morphology of the -MeCl functionalized PEDOT:PSS could also hinder the growth of perovskite thin film. To solve the problem, bromomethyl (-MeBr) and dimethylaminomethyl (-MeDMA) will be introduced to the EDOT monomer. The -MeBr functional group has less electronegativity compared with the -MeCl, therefore the oxidation and doping process would be more effective and the electrical conductivity of the synthesized PEDOT-MeBr:PSS is expected to be higher than the current PEDOT-MeCl:PSS. The -MeDMA is an electron-donating functional group, and it could promote the oxidation and doping of PEDOT-MeDMA:PSS and results in an improved conductivity even compared with the commercial available PEDOT:PSS.

A.2 Experimental Section

A.2.1 Materials

3,4-Ethylenedioxythiophene (EDOT, 97%), sodium persulfate ($Na_2S_2O_8$, ≥ 98%), iron(III) sulfate hydrate ($Fe_2(SO_4)_3$, 97%), poly(4-styrenesulfonic acid) solution (PSSH, M_w ~ 75,000, 18 wt% in H_2O), 3,4-dimethoxythiophene (97%), 3-bromo-1,2-propanediol (97%), dimethylamine solution (2M in THF), dimethylamine solution (40 wt% in water), p-toluenesulfonic acid monohydrate (PTSA, ≥ 98.5%), toluene (≥ 99.5%), sodium acetate anhydrous (CH_3COONa, > 99%), and dimethyl sulfoxide (DMSO, ≥ 99.9%) were purchased from Sigma-Aldrich. Potassium hydroxide (KOH), dichloromethane (DCM), acetonitrile, and chloroform-d ($CDCl_3$) were purchased from Fisher Scientific. Cation exchanger LEWATIT S108H and anion exchanger LEWATIT MP62 were kindly provided by LANXESS. Commercial PEDOT:PSS Clevios P VP AI 4083 was purchased from Heraeus. All the materials were used as received without further purification.

A.2.2 Synthesis of Functionalized EDOT Monomers

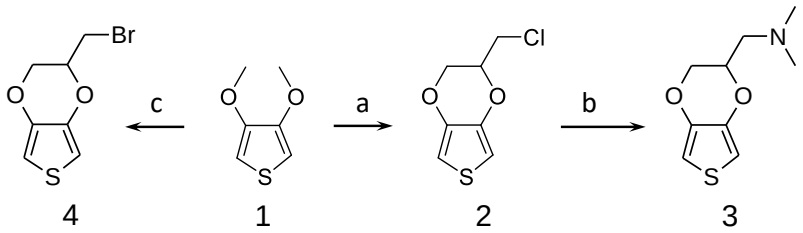

Scheme A-1 Synthetic routes of the bromomethyl and dimethylaminomethyl functionalized EDOT monomers.

The synthetic route of functionalized EDOT monomers is illustrated in **Scheme 5-1**. The experimental details were adopted from previous studies with some modification.[2-4] (a) 3,4-

dimethoxythiophene (5 g), 3-chloro-1,2-propanediol (12 g), PTSA (0.676 g), toluene (118 mL) were added into a three-neck flask. The system was purged with N_2 flow for 30 min and stirred vigorously at 95 °C under N_2 protection for 24 h. After removing of toluene under reduced pressure, the residue was purified by column chromatography (silica gel, hexane/DCM = 8/2 v/v) to give the product **2**, 2-(chloromethyl)-2,3-dihydrothieno[3,4-b][1,4]dioxine (EDOT-MeCl). ^{1}H NMR (300 MHz, $CDCl_3$, ppm): δ 6.38 (s, 2H, Th), 4.42-4.14 (m, 3H, -O-CH_2-CH-O-), and 3.65-3.78 (m, 2H, -CH_2-Cl). The yield of EDOT-MeCl was 46%.

(b) EDOT-MeCl (1 g), dimethylamine (40 wt% in water, 5.92 mL), and acetonitrile (5.92 mL) were added into a Schlenk flask. The solution mixture was stirred at 80 °C for 2 days. Another 5.92 mL dimethylamine was added into the flask and the solution mixture was stirred at 80 °C for another 2 days. After removing acetonitrile under reduced pressure, DCM was applied to extract the product and Na_2SO_4 was added into the mixture to remove water. the residue was purified by column chromatography (silica gel, MeOH/DCM = 1/10 v/v) to give the product **3,** 2-(dimethylaminomethyl)-2,3-dihydrothieno[3,4-b][1,4]dioxine (EDOT-MeDMA). ^{1}H NMR (300 MHz, $CDCl_3$, ppm): δ 6.30-6.40 (s, 2H, Th), 3.90-4.40 (m, 3H, -O-CH_2-CH-O-), and 2.40-2.70 (m, 2H, -CH_2-N), 2.31 (s, 6H, -N-C_2H_6).

(c) 3,4-dimethoxythiophene (4 g), 3-bromo-1,2-propanediol (5 g), PTSA (0.53 g), toluene (72 mL) were added into a three-neck flask. The system was purged with N_2 flow for 30 min and stirred vigorously at 105 °C under N_2 protection for 24 h. After removing of toluene under reduced pressure, the residue was purified by column chromatography (silica gel, hexane/DCM = 8/2 v/v) to give the product **4**, 2-(bromomethyl)-2,3-dihydrothieno[3,4-b][1,4]dioxine (EDOT-MeBr). ^{1}H NMR (300 MHz, $CDCl_3$, ppm): δ 6.38 (s, 2H, Th), 4.45-4.15 (m, 3H, -O-CH_2-CH-O-), and 3.48-3.61 (m, 2H, -CH_2-Br). The yield of EDOT-MeBr was 44%.

A.2.3 Oxidative Chemical Polymerization

PSSH (2.4 mL) was mixed with DI water (3 mL) for 20 min. NaOH (0.0522 g) was dissolved in DI water (1.2 mL) and added into the mixture solution. EDOT-MeBr (0.1323 g) was added into the solution mixture and stirred vigorously for 20 min to form an emulsion. $Na_2S_2O_8$ (0.6029 g) and $Fe_2(SO_4)_3$ (0.01125 g) was dissolved in DI water (1.2 mL), respectively, and added into the emulsion sequentially. The emulsion was stirred vigorously under 45 °C for 5 h until the UV-Vis absorption intensity of the solution does not change. UV-Vis absorption was collected using a Varian Cary 5000 UV-Vis-NIR spectrophotometer by diluting 50 μL sample with 3.5 mL DI water. S108H and MP62 ion exchange resins (4.5 g and 6.5 g, respectively) were added into the solution, stirred for 1 h, and removed by vacuum filtration. The product solution was in dark green color.

A.2.4 Fabrication and Characterization of Polymer Thin Films

Glass substrates were first cut into 15 mm × 15 mm pieces, then cleaned sequentially by sonication in soapy DI water, DI water, acetone, and isopropanol for 15 min each and then treated with 100 W oxygen plasma for 10 min. PEDOT-MeBr:PSS was treated with ultrasonic for 5 min passed 0.45 nylon filter, and spin-coated onto a clean glass substrate at 3000, and 5000 rpm, and annealed at 150 °C for 10 min for conductivity and atomic force microscope (AFM) measurements, respectively. The morphology of PEDOT:PSS and functionalized PEDOT:PSS thin films were characterized by tapping mode AFM (TM-AFM) using a Digital Multimode AFM equipped with a Nanoscope IVa controller. Conductivity was measured by Jandel Cylindrical four-point probe connected with a Keithley 2450 SourceMeter. Film thickness was characterized by Olympus OLS41 profilometer.

A.3 Results and Discussion

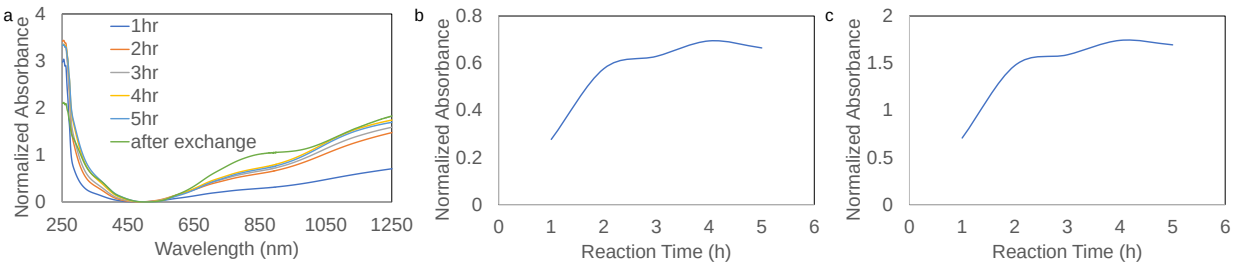

Figure A-1 (a) UV-vis spectra of PEDOT-MeBr:PSS with different reaction time and after ion exchange. (b) Bipolaron (1250 nm) and (c) polaron peaks (850 nm) absorption intensity versus reaction time. Spectra are normalized by matching the lowest absorption point.

The PEDOT-MeBr:PSS polymerization process was tracked by the UV-vis absorption spectra with a interval of 1 hour. As shown in **Figure A-1**a, the absorption stopped increasing at the 5-hour. The result is also reflected by the bipolaron and polaron peak intensity versus reaction time as shown in Figure A-1b and c, indicating the stop of the oxidative polymerization. Figure A-1a also shows both bipolaron and polaron peak intensity increase after the ion exchange process, unlike the case of PEDOT:PSS, PEDOT-MeCl:PSS, and PEDOT-MeOH:PSS. The concentration of the PEDOT-MeBr:PSS solution was intentionally increased to promote the polymerization process. During the ion exchange and filtration process, water might be absorbed by the ion exchanger and filter paper and the solution became even more concentrated and viscous, which could be the reason of the increased bipolaron and polaron peaks.

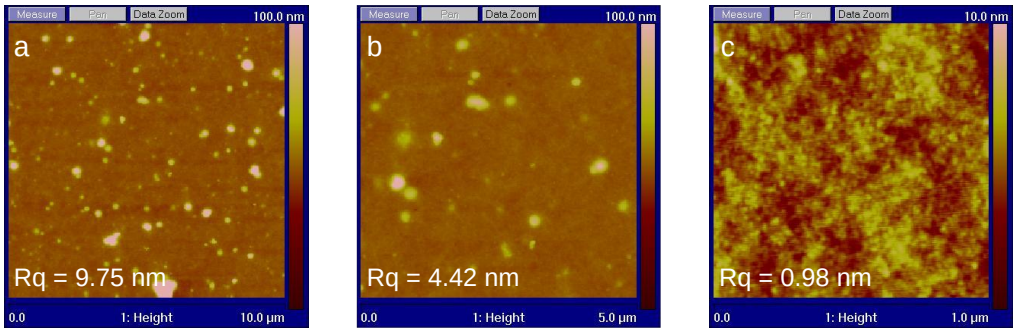

Figure A-2 Topographic AFM images of the synthesized PEDOT-MeBr:PSS thin films with the image size of (a) 10 µm × 10 µm, (b) 5 µm × 5 µm, and (c) 1 µm × 1 µm.

Surface morphology of the PEDOT-MeBr :PSS thin film was characterized by TM-AFM. Large, medium, and small area topographic AFM images were acquired as shown in **Figure A-2**a-c. Large aggregates with the diameter of around 0.3 µm can be found on large and medium AFM images with the PEDOT-MeBr:PSS solution mixture passed through the 0.45 µm nylon filter prior to the spin coating. The zoom-in image of PEDOT-MeBr:PSS sample (Figure A-2c) shows domain contrast and particle-like structure similar to PEDOT-MeCl:PSS, which could be attributed to the aggregated PEDOT-MeBr polymers that are poorly doped by SO_4^{2-}. The AFM results indicate that despite the reduce electronegativiey of -MeBr compare with -MeCl and the add of NaOH into PSSH to release PSS^- prior to the polyermization, the EDOT-MeBr monomers still tend to repluse the PSS counter during the polymerization process, and finally result in PEDOT-MeBr poorly doped by SO_4^{2-} counterion and large non-dispersible aggregates on the surface. The conductivity of the syntehsized PEDOT-MeBr:PSS is charasized to be 6.25×10^{-4} S/cm, which is lower than the 1.68×10^{-3} S/cm for PEDOT-MeCl:PSS. Since NaOH was added to partially neutralize PSSH prior to the polymerization, the reduced conductivity can be attributed to the reduced oxidant activity due to decreases solution acidity.

All the above reuslts tell that when selecting EDOT monomer functinoal group for oxidative chemcial polymerizaiton, it is recommonded to have electron-donating group (e.g. EDOT-MeDMA) instead of electron-withdrawing group (e.g. EDOT-MeCl and EDOT-MeBr). It is also recommonded to have the functional group that can attract PSS counterion (e.g. EDOT-MeOH through hydrogen bonding) over that will repluse PSS counterion (e.g. EDOT-MeCl and EDOT-MeBr through electrostaic force).

Appendix B PASSIVATING IONIC DEFECTS IN MA-FREE PEROVSKITE USING ZWITTERIONIC MOLECULES, LEWIS ACID AND BASE, AND ETHYLENEDIAMMONIUM DIIODIDE

B.1 Introduction

This thesis has demonstrated MA-free perovskite solar cells in inverted device structure with improved operational stability against electric field. But the PCE reported in this work (maximum ~15%) is of the device is not comparable to the highest reported PCE in this field (25.2%).[5] Despite we have reduce the defect density through mixing the precursor prior to the spin coating process, there is still possibly some ionic defect due to the soft ionic nature of perovskite material. Defect passivation was firstly demonstrated by Snaith et al using Lewis acid and base, which has electron withdrawing and donating group, respectively.[6] Zwitterionic molecules consist both positively and negatively charged ions on the same molecule are among the most popular materials in the biochemistry and biomaterial areas.[7] Recently, researchers have applied zwitterionic molecules to passivate the ionic defect in perovskites.[8, 9] Ammonium iodide salts such as MAI and FAI are commonly applied to synthesize perovskite materials. Works have been reported where ammonium iodide salts are applied to passivate perovskite ionic defect or even form stable low dimension perovskite materials.[10] With the objective of improving the perovskite solar cell performance, several zwitterionic molecules and ethylenediammonium diiodide were attempted to be integrated into the perovskite.

B.2 Experimental Section

B.2.1 Materials

Indium tin oxide (ITO) coated glass (sheet resistance = 10 Ω sq^{-1}) was purchased from Colorado Concept Coating LLC. Poly(3,4-ethylenedioxythiophene):polystyrene sulfonate (PEDOT:PSS, CLEVIOS P VP AI 4083) was purchased from Heraeus. Lead iodide (PbI_2, for perovskite precursor, 99.99%), 3-hydroxytyramine hydrochloride (dopamine HCl, >98%), and 3-(3,4-dihydroxyphenyl)-L-alanine (L-dopa, >98%) were purchased from Tokyo Chemical Industry. Formamidinium iodide (FAI) was purchased from Greatcell Solar. Ag evaporation pellets (99.999%) were purchased from R.D. Mathis. Dimethyl sulfoxide (DMSO, anhydrous, ≥99.9%), N,N-Dimethylformamide (DMF, anhydrous, ≥99.8%), chloroform (anhydrous, ≥99%), 2-propanol (anhydrous, 99.5%), [2-(Methacryloyloxy)ethyl]dimethyl-(3-sulfopropyl)ammonium hydroxide (SBMA, 95%), bathocuproine (BCP, 96%), diethyl ether (DEE, ≥99.0%), RbI (99.9%), and CsI (99.999%) were purchased from Sigma-Aldrich. Ethylenediammonium diiodide ($EDAI_2$) was purchased from Milipore. All the materials were used as received without further purification.

B.2.2 Device Fabrication

ITO coated glass substrates with the size of 1.5 cm × 1.5 cm were cleaned by sonication in soapy deionized (DI) water, DI water, acetone, and isopropanol for 15 min each sequentially and finally treated with 100 W oxygen plasma for 10 min. PEDOT:PSS was spin coated onto the cleaned glass substrate at 5000 rpm (ramp: 5000 rpm/s) for 60 s, followed by annealing at 150°C for 10 min in the ambient condition. The substrates were then transferred into a N_2 filled glove box. Perovskite precursors were prepared as following: PbI_2 (1.1 M) was dissolved in DMF:DMSO 4:1 (v:v) by stirring at 80°C for 1 h. PbI_2 (1.1 M) solution was added into RbI (1 M), CsI (1 M),

and FAI (1 M) to form $RbPbI_3$, $CsPbI_3$, and $FAPbI_3$ precursor solutions. $RbPbI_3$ and $FAPbI_3$ solutions were stirred at room temperature for 1 h. $CsPbI_3$ solution was stirred at 80°C for ~3.5 min then room temperature for 1 h. Passivation molecules were dissolved in the DMF:DMSO 4:1 solvent and stirred overnight. $Rb_{0.05}Cs_{0.1}FA_{0.85}PbI_3$ precursor solution was prepared by mixing the desired volumetric ratios of the above solutions. The final precursor solution was stirred at room temperature overnight and passed 0.45 μm PTFE filter. The substrates and precursor solution were placed on a 70°C hotplate and the precursors were unstirred. The heated substrate was transferred onto the spin coater, and the hot precursor solution was dropped onto the substrate. The substrate was spin at 1000 rpm for 10 s (ramp: 200 rpm/s) and 4000 rpm for 30 s (ramp: 4000 rpm/s). A 300 μL of DEE was dropped onto the substrate at the last 10 or 15 s of the entire process for $Rb_{0.05}Cs_{0.10}FA_{0.85}PbI_3$ and $Cs_{0.15}FA_{0.85}PbI_3$, respectively. The substrates were annealed at 100°C for 10 min. The passivation layer was prepared by dissolving target molecules in 2-propanol overnight and spin coat onto perovskite directly with at 4000 rpm for 60 s (ramp: 4000 rpm/s) with or without annealing at different temperature for 10 min. A 60 μL drop of $PC_{60}BM$ solution (15 mg/mL in chloroform) was spin coated onto the perovskite layer or passivation layer at 4000 rpm (ramp: 4000 rpm/s) for 60 s without annealing. A 70 μL drop of BCP solution (0.5 mg/mL in 2-propanol) was spin coated onto the $PC_{60}BM$ layer at 4000 rpm (ramp: 4000 rpm/s) for 60 s without annealing. The devices were finished by the deposition of a 150 nm Ag layer at the rate of 0.2 nm/s with a mask to a final device size of 0.0314 cm^2. The thermal evaporation processes were performed in a background vacuum less than 2×10^{-6} Torr.

B.2.3 Device Characterization

The photocurrent density-voltage (J−V) measurements were performed in a N_2 filled glove box and recorded by a Keithley 2400 source meter from -0.5 V to 1.5 V (forward scan) or 1.5 V

to -0.5 V (reverse scan) under illumination by a 450 W oriel Xenon lamp with a AM 1.5G filter solar simulator (100 mW/cm^2). The light intensity was calibrated with a standard Si photodiode equipped with KG-5 filter. The calibration diode was calibrated by the National Renewable Energy Laboratory.

B.3 Results and Discussion

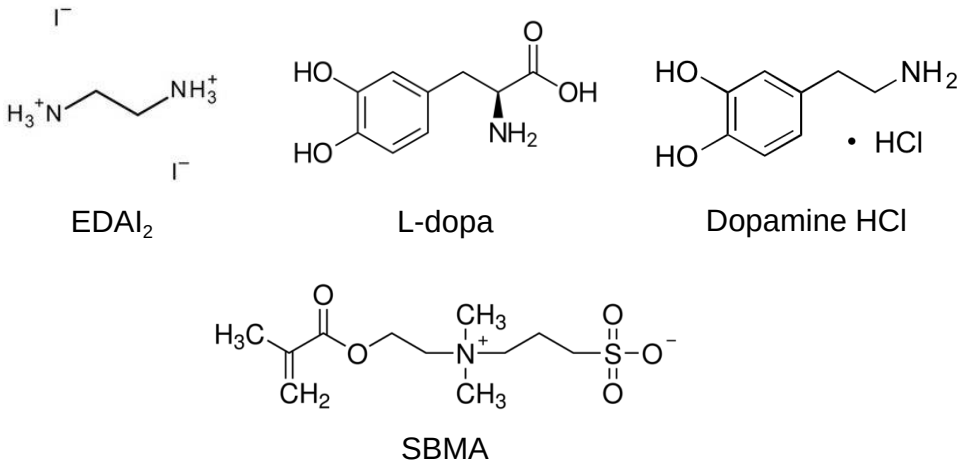

Figure B-1 Chemical structure of the molecules applied to passivate perovskite ionic defects.

Ammonium iodide salt $EDAI_2$, molecules contain both Lewis acid and base L-dopa and dopamine HCl, and zwitterionic molecule SBMA were applied to passivate perovskite ionic defect by mixing into perovskite precursor or spin coating onto the perovskite layer. **Figure B-2** shows the effect of each passivation materials by serving as the passivation layer or mixing into perovskite precursor. The only improvement was observed by using $EDAI_2$ as passivation layer on the top of the perovskite layer. The averaged device efficiency was increased from 8.22% to 11.19% and 12.04% with and without post-annealing for the passivation layer. Based on the results, we elucidate that spin coat $EDAI_2$ onto the perovskite layer have a better passivation function over

other molecules and treatment method reported here. Future work could focus on changing the carbon spacer length or adjusting the number of ammoniums on the molecule.

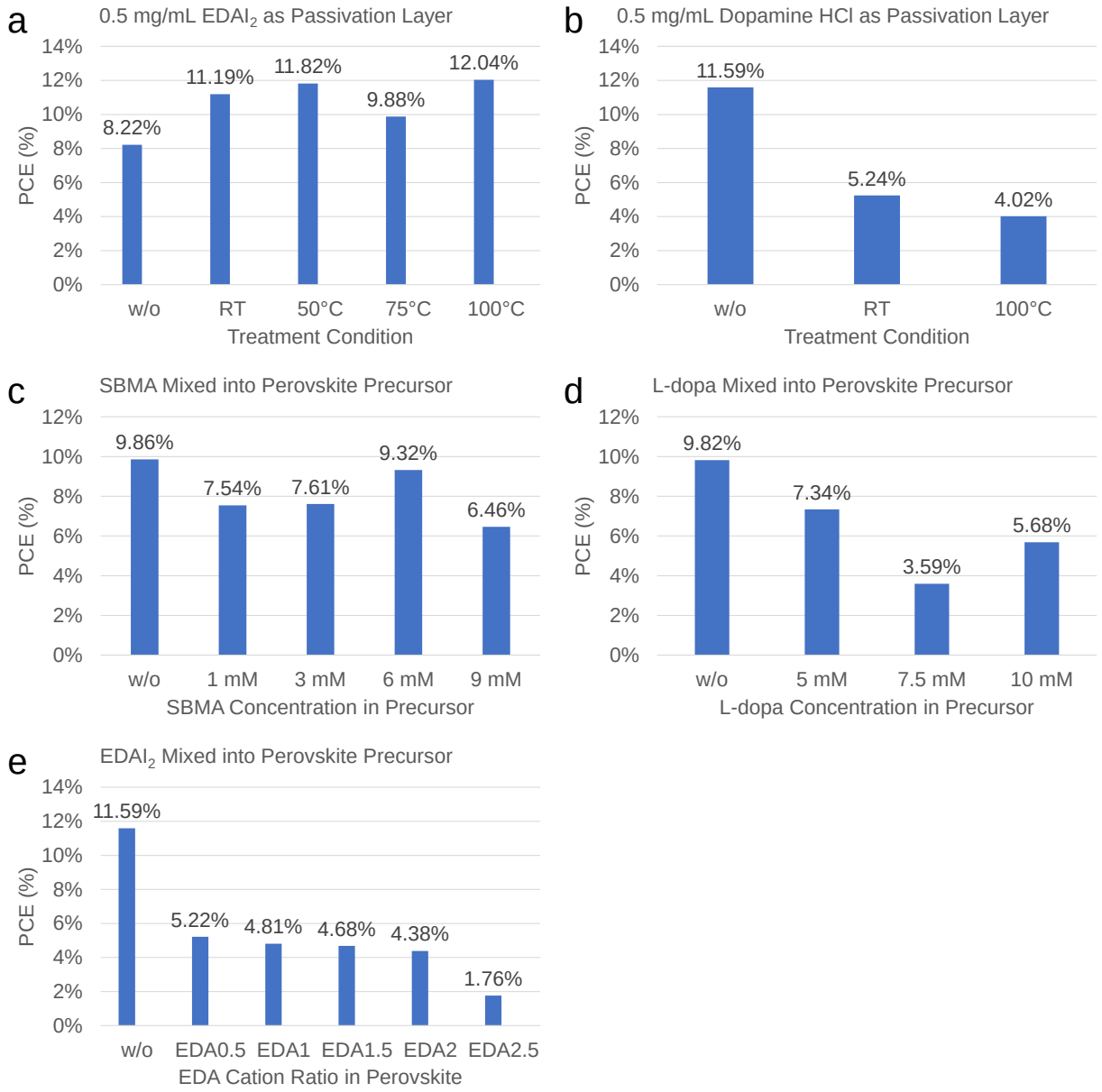

Figure B-2 $Rb_5Cs_{10}FA_{85}PbI_3$ perovskite solar cell device performance using different passivation method. The PCE fluctuation of the reference cell w/o any treatment was due to the degradation of FAI possible contamination of PbI_2 from the contaminated thermal evaporator.

REFERENCES

1. Sweeney, S. J.; Mukherjee, J., *Optoelectronic Devices and Materials*. Springer, Cham: 2017.

2. Kao, C. K., *The Impact of Optoelectronics Technology on the Information Society*. Springer, Dordrecht: 1989.

3. Khan, S.; Lorenzelli, L.; Dahiya, R. S., Technologies for Printing Sensors and Electronics Over Large Flexible Substrates: A Review. *Ieee Sensors Journal* **2015,** *15* (6), 3164-3185.

4. Huang, Q. J.; Zhu, Y., Printing Conductive Nanomaterials for Flexible and Stretchable Electronics: A Review of Materials, Processes, and Applications. *Advanced Materials Technologies* **2019,** *4* (5).

5. International Energy Agency. https://www.iea.org/publications/freepublications/.

6. Bisquert, J., *The Physics of Solar Cells*. CRC Press: 2018.

7. Mora-Sero, I., How Do Perovskite Solar Cells Work? *Joule* **2018,** *2* (4), 585-587.

8. Monroy, E.; Omnes, F.; Calle, F., Wide-bandgap semiconductor ultraviolet photodetectors. *Semiconductor Science and Technology* **2003,** *18* (4), R33-R51.

9. Razeghi, M.; Rogalski, A., Semiconductor ultraviolet detectors. *Journal of Applied Physics* **1996,** *79* (10), 7433-7473.

10. Liao, M. Y.; Koide, Y.; Alvarez, J., Photovoltaic Schottky ultraviolet detectors fabricated on boron-doped homoepitaxial diamond layer. *Applied Physics Letters* **2006,** *88* (3), 3.

11. Sandvik, P.; Brown, D.; Fedison, J.; Matocha, K.; Kretchmer, J., Dual-SiC photodiode devices for simultaneous two-band detection. *Journal of the Electrochemical Society* **2005,** *152* (3), G199-G202.

12. Carrano, J. C.; Li, T.; Grudowski, P. A.; Eiting, C. J.; Dupuis, R. D.; Campbell, J. C., High quantum efficiency metal-semiconductor-metal ultraviolet photodetectors fabricated on single-crystal GaN epitaxial layers. *Electronics Letters* **1997,** *33* (23), 1980-1981.

13. Armin, A.; Jansen-van Vuuren, R. D.; Kopidakis, N.; Burn, P. L.; Meredith, P., Narrowband light detection via internal quantum efficiency manipulation of organic photodiodes. *Nature Communications* **2015,** *6*, 8.

14. Baeg, K. J.; Binda, M.; Natali, D.; Caironi, M.; Noh, Y. Y., Organic Light Detectors: Photodiodes and Phototransistors. *Advanced Materials* **2013,** *25* (31), 4267-4295.

15. Miao, J. L.; Zhang, F. J., Recent progress on highly sensitive perovskite photodetectors. *Journal of Materials Chemistry C* **2019,** *7* (7), 1741-1791.

16. Konstantatos, G.; Sargent, E. H., Nanostructured materials for photon detection. *Nature Nanotechnology* **2010,** *5* (6), 391-400.

17. Assefa, S.; Xia, F. N. A.; Vlasov, Y. A., Reinventing germanium avalanche photodetector for nanophotonic on-chip optical interconnects. *Nature* **2010,** *464* (7285), 80-U91.

18. Medintz, I. L.; Uyeda, H. T.; Goldman, E. R.; Mattoussi, H., Quantum dot bioconjugates for imaging, labelling and sensing. *Nature Materials* **2005,** *4* (6), 435-446.

19. Tan, C. L.; Mohseni, H., Emerging technologies for high performance infrared detectors. *Nanophotonics* **2018,** *7* (1), 169-197.

20. Chen, H. Y.; Liu, K. W.; Hu, L. F.; Al-Ghamdi, A. A.; Fang, X. S., New concept ultraviolet photodetectors. *Materials Today* **2015,** *18* (9), 493-502.

21. Piels, M.; Bower, J. E., *Photodetectors: Materials, Devices and Applications*. Woodhead Publishing: 2015.

22. M., C., *Photodetectors: Materials, Devices*

and Applications. Woodhead Publishing: 2015.

23. Sobhani, A.; Knight, M. W.; Wang, Y. M.; Zheng, B.; King, N. S.; Brown, L. V.; Fang, Z. Y.; Nordlander, P.; Halas, N. J., Narrowband photodetection in the near-infrared with a plasmon-induced hot electron device. *Nature Communications* **2013,** *4*, 6.

24. Zheng, E.; Yuh, B.; Tosado, G. A.; Yu, Q., Solution-processed visible-blind UV-A photodetectors based on CH3NH3PbCl3 perovskite thin films. *Journal of Materials Chemistry C* **2017,** *5* (15), 3796-3806.

25. Seo, H.; Aihara, S.; Kubota, M.; Egami, N., Improvement in Photoconductive Properties of Coumarin 30-Evaporated Film by Fullerene Doping for Blue-Sensitive Photoconductors. *Japanese Journal of Applied Physics* **2010,** *49* (11).

26. Wang, W. B.; Zhang, F. J.; Li, L. L.; Gao, M. L.; Hu, B., Improved Performance of Photomultiplication Polymer Photodetectors by Adjustment of P3HT Molecular Arrangement. *Acs Applied Materials & Interfaces* **2015,** *7* (40), 22660-22668.

27. Li, L. L.; Zhang, F. J.; Wang, W. B.; An, Q. S.; Wang, J.; Sun, Q. Q.; Zhang, M., Trap-Assisted Photomultiplication Polymer Photodetectors Obtaining an External Quantum Efficiency of 37500%. *Acs Applied Materials & Interfaces* **2015,** *7* (10), 5890-5897.

28. Li, L. L.; Zhang, F. J.; Wang, W. B.; Fang, Y. J.; Huang, J. S., Revealing the working mechanism of polymer photodetectors with ultra-high external quantum efficiency. *Physical Chemistry Chemical Physics* **2015,** *17* (45), 30712-30720.

29. Li, L. L.; Zhang, F. J.; Wang, J.; An, Q. S.; Sun, Q. Q.; Wang, W. B.; Zhang, J.; Teng, F., Achieving EQE of 16,700% in P3HT: PC71BM based photodetectors by trap-assisted photomultiplication. *Scientific Reports* **2015,** *5*, 7.

30. Esopi, M. R.; Calcagno, M.; Yu, Q. M., Organic Ultraviolet Photodetectors Exhibiting Photomultiplication, Low Dark Current, and High Stability. *Advanced Materials Technologies* **2017,** *2* (8), 9.

31. Miao, J. L.; Zhang, F. J.; Du, M. D.; Wang, W. B.; Fang, Y., Photomultiplication type narrowband organic photodetectors working at forward and reverse bias. *Physical Chemistry Chemical Physics* **2017,** *19* (22), 14424-14430.

32. Li, H. G.; Wu, G.; Chen, H. Z.; Wang, M., Spectral response tuning and realization of quasi-solar-blind detection in organic ultraviolet photodetectors. *Organic Electronics* **2011,** *12* (1), 70-77.

33. Zhu, H. L.; Choy, W. C. H.; Sha, W. E. I.; Ren, X. G., Photovoltaic Mode Ultraviolet Organic Photodetectors with High On/Off Ratio and Fast Response. *Advanced Optical Materials* **2014,** *2* (11), 1082-1089.

34. Yuan, Y. B.; Huang, J. S., Ultrahigh Gain, Low Noise, Ultraviolet Photodetectors with Highly Aligned Organic Crystals. *Advanced Optical Materials* **2016,** *4* (2), 264-270.

35. Wang, W. B.; Zhang, F. J.; Bai, H. T.; Li, L. L.; Gao, M. L.; Zhanga, M.; Zhan, X. W., Photomultiplication photodetectors with P3HT: fullerene-free material as the active layers exhibiting a broad response. *Nanoscale* **2016,** *8* (10), 5578-5586.

36. Wang, X.; Wang, H. Y.; Zhou, D. L.; Jin, H.; Yu, J. S., Semitransparent indium-tin-oxide-free non-fullerene organic photodetectors with double-side ultraviolet selective responses. *Materials Letters* **2018,** *230*, 289-292.

37. Xu, R. L.; Zhang, D. Z.; He, L. J.; Li, K. Z.; Ruan, S. P.; Zhang, H. F.; Zhou, J. R.; Chen, Y., A PFTBT modified visible-blind ultraviolet photodetector with a narrow detecting range and high responsivity. *Nanotechnology* **2018,** *29* (46).

38. Guo, F. W.; Yang, B.; Yuan, Y. B.; Xiao, Z. G.; Dong, Q. F.; Bi, Y.; Huang, J. S., A nanocomposite ultraviolet photodetector based on interfacial trap-controlled charge injection. *Nature Nanotechnology* **2012,** *7* (12), 798-802.

39. Shao, D. L.; Sun, X.; Xie, M.; Sun, H. T.; Lu, F. Y.; George, S. M.; Lian, J.; Sawyer, S., ZnO quantum dots-graphene composite for efficient ultraviolet sensing. *Materials Letters* **2013,** *112*, 165-168.

40. Shao, D. L.; Yu, M. P.; Sun, H. T.; Xin, G. Q.; Lian, J.; Sawyer, S., High-Performance Ultraviolet Photodetector Based on Organic-Inorganic Hybrid Structure. *Acs Applied Materials & Interfaces* **2014,** *6* (16), 14690-14694.

41. Shen, L.; Fang, Y. J.; Dong, Q. F.; Xiao, Z. G.; Huang, J. S., Improving the sensitivity of a near-infrared nanocomposite photodetector by enhancing trap induced hole injection. *Applied Physics Letters* **2015,** *106* (2), 4.

42. Azadinia, M.; Fathollahi, M. R.; Mosadegh, M.; Boroumand, F. A.; Mohajerani, E., Improved performance of photoconductive gain hybrid UV detector by trap state engineering of ZnO nanoparticles. *Journal of Applied Physics* **2017,** *122* (15), 10.

43. Esopi, M. R.; Zheng, E. J.; Zhang, X. Y.; Cai, C.; Yu, Q. M., Tuning the spectral response of ultraviolet organic-inorganic hybrid photodetectors via charge trapping and charge collection narrowing. *Physical Chemistry Chemical Physics* **2018,** *20* (16), 11273-11284.

44. Zhang, X. Y.; Zheng, E. J.; Esopi, M. R.; Cai, C.; Yu, Q. M., Flexible Narrowband Ultraviolet Photodetectors with Photomultiplication Based on Wide Band Gap Conjugated Polymer and Inorganic Nanoparticles. *Acs Applied Materials & Interfaces* **2018,** *10* (28), 24064-24074.

45. Zheng, E. J.; Zhang, X. Y.; Esopi, M. R.; Cai, C.; Zhou, B. Y.; Lin, Y. Y.; Yu, Q. M., Narrowband Ultraviolet Photodetectors Based on Nanocomposite Thin Films with High Gain and Low Driving Voltage. *Acs Applied Materials & Interfaces* **2018,** *10* (48), 41552-41561.

46. Fang, Y. J.; Dong, Q. F.; Shao, Y. C.; Yuan, Y. B.; Huang, J. S., Highly narrowband perovskite single-crystal photodetectors enabled by surface-charge recombination. *Nature Photonics* **2015,** *9* (10), 679-+.

47. Saidaminov, M. I.; Haque, M. A.; Savoie, M.; Abdelhady, A. L.; Cho, N.; Dursun, I.; Buttner, U.; Alarousu, E.; Wu, T.; Bakr, O. M., Perovskite Photodetectors Operating in Both Narrowband and Broadband Regimes. *Advanced Materials* **2016,** *28* (37), 8144-8149.

48. Li, L. L.; Deng, Y. H.; Bao, C. X.; Fang, Y. J.; Wei, H. T.; Tang, S.; Zhang, F. J.; Huang, J. S., Self-Filtered Narrowband Perovskite Photodetectors with Ultrafast and Tuned Spectral Response. *Advanced Optical Materials* **2017,** *5* (22), 6.

49. Chen, Z.; Li; Chenglong; Zhumekenov; Ayan; Zheng; Xiaopeng; Yang; Chen; Yang, H.; He, Y.; Turedi; B; ekir; Mohammed ; Omar; Shen, L.; Bakr; Osman, Solution-Processed Visible-Blind Ultraviolet Photodetectors with Nanosecond Response Time and High Detectivity *Advanced Optical Materials* **2019**, 1900506.

50. Gong, J.; Darling, S. B.; You, F. Q., Perovskite photovoltaics: life-cycle assessment of energy and environmental impacts. *Energy & Environmental Science* **2015,** *8* (7), 1953-1968.

51. Kumar, M.; Kumar, A., Performance assessment and degradation analysis of solar photovoltaic technologies: A review. *Renewable & Sustainable Energy Reviews* **2017,** *78*, 554-587.

52. Green, M. A.; Ho-Baillie, A.; Snaith, H. J., The emergence of perovskite solar cells. *Nature Photonics* **2014,** *8* (7), 506-514.

53. Lin, Q. Q.; Armin, A.; Nagiri, R. C. R.; Burn, P. L.; Meredith, P., Electro-optics of perovskite solar cells. *Nature Photonics* **2015,** *9* (2), 106-112.

54. Xing, G. C.; Mathews, N.; Sun, S. Y.; Lim, S. S.; Lam, Y. M.; Gratzel, M.; Mhaisalkar, S.; Sum, T. C., Long-Range Balanced Electron- and Hole-Transport Lengths in Organic-Inorganic CH3NH3PbI3. *Science* **2013,** *342* (6156), 344-347.

55. Wehrenfennig, C.; Eperon, G. E.; Johnston, M. B.; Snaith, H. J.; Herz, L. M., High Charge Carrier Mobilities and Lifetimes in Organolead Trihalide Perovskites. *Advanced Materials* **2014,** *26* (10), 1584-1589.

56. Mosconi, E.; Etienne, T.; De Angelis, F., Rashba Band Splitting in Organohalide Lead Perovskites: Bulk and Surface Effects. *Journal of Physical Chemistry Letters* **2017,** *8* (10), 2247-2252.

57. Dou, L. T.; Yang, Y.; You, J. B.; Hong, Z. R.; Chang, W. H.; Li, G., Solution-processed hybrid perovskite photodetectors with high detectivity. *Nature Communications* **2014,** *5*, 6.

58. Stranks, S. D.; Snaith, H. J., Metal-halide perovskites for photovoltaic and light-emitting devices. *Nature Nanotechnology* **2015,** *10* (5), 391-402.

59. Xing, G. C.; Mathews, N.; Lim, S. S.; Yantara, N.; Liu, X. F.; Sabba, D.; Gratzel, M.; Mhaisalkar, S.; Sum, T. C., Low-temperature solution-processed wavelength-tunable perovskites for lasing. *Nature Materials* **2014,** *13* (5), 476-480.

60. Liu, M. Z.; Johnston, M. B.; Snaith, H. J., Efficient planar heterojunction perovskite solar cells by vapour deposition. *Nature* **2013,** *501* (7467), 395-+.

61. Tosado, G. A.; Lin, Y.-Y.; Zheng, E.; Yu, Q., Impact of cesium on the phase and device stability of triple cation Pb–Sn double halide perovskite films and solar cells. *Journal of Materials Chemistry A* **2018**.

62. NREL Efficiency chart. https://www.nrel.gov/pv/assets/images/efficiency-chart.png.

63. Lee, J. H.; Bristowe, N. C.; Lee, S. H.; Bristowe, P. D.; Cheetham, A. K.; Jang, H. M., Resolving the Physical Origin of Octahedral Tilting in Halide Perovskites. *Chemistry of Materials* **2016,** *28* (12), 4259-4266.

64. Prasanna, R.; Gold-Parker, A.; Leijtens, T.; Conings, B.; Babayigit, A.; Boyen, H. G.; Toney, M. F.; McGehee, M. D., Band Gap Tuning via Lattice Contraction and Octahedral Tilting in Perovskite Materials for Photovoltaics. *Journal of the American Chemical Society* **2017,** *139* (32), 11117-11124.

65. McMeekin, D. P.; Sadoughi, G.; Rehman, W.; Eperon, G. E.; Saliba, M.; Horantner, M. T.; Haghighirad, A.; Sakai, N.; Korte, L.; Rech, B.; Johnston, M. B.; Herz, L. M.; Snaith, H. J., A mixed-cation lead mixed-halide perovskite absorber for tandem solar cells. *Science* **2016,** *351* (6269), 151-155.

66. Berhe, T. A.; Su, W. N.; Chen, C. H.; Pan, C. J.; Cheng, J. H.; Chen, H. M.; Tsai, M. C.; Chen, L. Y.; Dubale, A. A.; Hwang, B. J., Organometal halide perovskite solar cells: degradation and stability. *Energy & Environmental Science* **2016,** *9* (2), 323-356.

67. Chen, Q.; De Marco, N.; Yang, Y.; Song, T. B.; Chen, C. C.; Zhao, H. X.; Hong, Z. R.; Zhou, H. P., Under the spotlight: The organic-inorganic hybrid halide perovskite for optoelectronic applications. *Nano Today* **2015,** *10* (3), 355-396.

68. Ono, L. K.; Juarez-Perez, E. J.; Qi, Y. B., Progress on Perovskite Materials and Solar Cells with Mixed Cations and Halide Anions. *Acs Applied Materials & Interfaces* **2017,** *9* (36), 30197-30246.

69. Aristidou, N.; Sanchez-Molina, I.; Chotchuangchutchaval, T.; Brown, M.; Martinez, L.; Rath, T.; Haque, S. A., The Role of Oxygen in the Degradation of Methylammonium Lead

Trihalide Perovskite Photoactive Layers. *Angewandte Chemie-International Edition* **2015,** *54* (28), 8208-8212.

70. Christians, J. A.; Herrera, P. A. M.; Kamat, P. V., Transformation of the Excited State and Photovoltaic Efficiency of CH3NH3PbI3 Perovskite upon Controlled Exposure to Humidified Air. *Journal of the American Chemical Society* **2015,** *137* (4), 1530-1538.

71. Song, Z. N.; Abate, A.; Watthage, S. C.; Liyanage, G. K.; Phillips, A. B.; Steiner, U.; Graetzel, M.; Heben, M. J., Perovskite Solar Cell Stability in Humid Air: Partially Reversible Phase Transitions in the PbI2-CH3NH3I-H2O System. *Advanced Energy Materials* **2016,** *6* (19).

72. Juarez-Perez, E. J.; Hawash, Z.; Raga, S. R.; Ono, L. K.; Qi, Y. B., Thermal degradation of CH3NH3PbI3 perovskite into NH3 and CH3I gases observed by coupled thermogravimetry-mass spectrometry analysis. *Energy & Environmental Science* **2016,** *9* (11), 3406-3410.

73. Weller, M. T.; Weber, O. J.; Frost, J. M.; Walsh, A., Cubic Perovskite Structure of Black Formamidinium Lead Iodide, alpha- HC(NH2)(2) PbI3, at 298 K. *Journal of Physical Chemistry Letters* **2015,** *6* (16), 3209-3212.

74. Jeon, N. J.; Noh, J. H.; Yang, W. S.; Kim, Y. C.; Ryu, S.; Seo, J.; Seok, S. I., Compositional engineering of perovskite materials for high-performance solar cells. *Nature* **2015,** *517* (7535), 476-+.

75. Li, Z.; Yang, M. J.; Park, J. S.; Wei, S. H.; Berry, J. J.; Zhu, K., Stabilizing Perovskite Structures by Tuning Tolerance Factor: Formation of Formamidinium and Cesium Lead Iodide Solid-State Alloys. *Chemistry of Materials* **2016,** *28* (1), 284-292.

76. Yu, Y.; Wang, C. L.; Grice, C. R.; Shrestha, N.; Chen, J.; Zhao, D. W.; Liao, W. Q.; Cimaroli, A. J.; Roland, P. J.; Ellingson, R. J.; Yan, Y. F., Improving the Performance of

Formamidinium and Cesium Lead Triiodide Perovskite Solar Cells using Lead Thiocyanate Additives. *Chemsuschem* **2016,** *9* (23), 3288-3297.

77. Yi, C. Y.; Luo, J. S.; Meloni, S.; Boziki, A.; Ashari-Astani, N.; Gratzel, C.; Zakeeruddin, S. M.; Rothlisberger, U.; Gratzel, M., Entropic stabilization of mixed A-cation ABX(3) metal halide perovskites for high performance perovskite solar cells. *Energy & Environmental Science* **2016,** *9* (2), 656-662.

78. Huang, J. H.; Xu, P.; Liu, J.; You, X. Z., Sequential Introduction of Cations Deriving Large-Grain Cs(x)FA(1-x)PbI(3) Thin Film for Planar Hybrid Solar Cells: Insight into Phase-Segregation and Thermal-Healing Behavior. *Small* **2017,** *13* (10).

79. Liu, T. H.; Zong, Y. X.; Zhou, Y. Y.; Yang, M. J.; Li, Z.; Game, O. S.; Zhu, K.; Zhu, R.; Gong, Q. H.; Padture, N. P., High-Performance Formamidinium-Based Perovskite Solar Cells via Microstructure-Mediated delta-to-alpha Phase Transformation. *Chemistry of Materials* **2017,** *29* (7), 3246-3250.

80. Troughton, J.; Gasparini, N.; Baran, D., Cs(0.15)FA(0.85)PbI(3) perovskite solar cells for concentrator photovoltaic applications. *Journal of Materials Chemistry A* **2018,** *6* (44), 21913-21917.

81. Lee, J. W.; Kim, D. H.; Kim, H. S.; Seo, S. W.; Cho, S. M.; Park, N. G., Formamidinium and Cesium Hybridization for Photo- and Moisture-Stable Perovskite Solar Cell. *Advanced Energy Materials* **2015,** *5* (20).

82. Park, Y. H.; Jeong, I.; Bae, S.; Son, H. J.; Lee, P.; Lee, J.; Lee, C. H.; Ko, M. J., Inorganic Rubidium Cation as an Enhancer for Photovoltaic Performance and Moisture Stability of HC(NH2)(2)PbI3 Perovskite Solar Cells. *Advanced Functional Materials* **2017,** *27* (16).

83. Zhang, M.; Yun, J. S.; Ma, Q. S.; Zheng, J. H.; Lau, C. F. J.; Deng, X. F.; Kim, J.; Kim, D.; Seidel, J.; Green, M. A.; Huang, S. J.; Ho-Baillie, A. W. Y., High-Efficiency Rubidium-Incorporated Perovskite Solar Cells by Gas Quenching. *Acs Energy Letters* **2017,** *2* (2), 438-444.

84. Turren-Cruz, S. H.; Hagfeldt, A.; Saliba, M., Methylammonium-free, high-performance, and stable perovskite solar cells on a planar architecture. *Science* **2018,** *362* (6413), 449-+.

85. Ball, J. M.; Petrozza, A., Defects in perovskite-halides and their effects in solar cells. *Nature Energy* **2016,** *1*, 1-13.

86. Meng, L.; You, J. B.; Guo, T. F.; Yang, Y., Recent Advances in the Inverted Planar Structure of Perovskite Solar Cells. *Accounts of Chemical Research* **2016,** *49* (1), 155-165.

87. Nezakati, T.; Seifalian, A.; Tan, A.; Seifalian, A. M., Conductive Polymers: Opportunities and Challenges in Biomedical Applications. *Chemical Reviews* **2018,** *118* (14), 6766-6843.

88. Tosado, G. A.; Lin, Y. Y.; Zheng, E. J.; Yu, Q. M., Impact of cesium on the phase and device stability of triple cation Pb-Sn double halide perovskite films and solar cells. *Journal of Materials Chemistry A* **2018,** *6* (36), 17426-17436.

89. Alemu, D.; Wei, H. Y.; Ho, K. C.; Chu, C. W., Highly conductive PEDOT:PSS electrode by simple film treatment with methanol for ITO-free polymer solar cells. *Energy & Environmental Science* **2012,** *5* (11), 9662-9671.

90. Kroon, R.; Mengistie, D. A.; Kiefer, D.; Hynynen, J.; Ryan, J. D.; Yu, L. Y.; Muller, C., Thermoelectric plastics: from design to synthesis, processing and structure-property relationships. *Chemical Society Reviews* **2016,** *45* (22), 6147-6164.

91. Abdelhamid, M. E.; O'Mullane, A. P.; Snook, G. A., Storing energy in plastics: a review on conducting polymers & their role in electrochemical energy storage. *Rsc Advances* **2015,** *5* (15), 11611-11626.

92. Kinder, L.; Kanicki, J.; Petroff, P., Structural ordering and enhanced carrier mobility in organic polymer thin film transistors. *Synthetic Metals* **2004,** *146* (2), 181-185.

93. Hamasaki, T.; Morimune, T.; Kajii, H.; Minakata, S.; Tsuruoka, R.; Nagamachi, T.; Ohmori, Y., Fabrication and characteristics of polyfluorene based organic photodetectors using fullerene derivatives. *Thin Solid Films* **2009,** *518* (2), 548-550.

94. Takano, T.; Masunaga, H.; Fujiwara, A.; Okuzaki, H.; Sasaki, T., PEDOT Nanocrystal in Highly Conductive PEDOT:PSS Polymer Films. *Macromolecules* **2012,** *45* (9), 3859-3865.

95. Jonas, F.; Schrader, L., CONDUCTIVE MODIFICATIONS OF POLYMERS WITH POLYPYRROLES AND POLYTHIOPHENES. *Synthetic Metals* **1991,** *41* (3), 831-836.

96. Jonas, F.; Krafft, W.; Muys, B., POLY(3,4-ETHYLENEDIOXYTHIOPHENE) - CONDUCTIVE COATINGS, TECHNICAL APPLICATIONS AND PROPERTIES. *Macromolecular Symposia* **1995,** *100*, 169-173.

97. Aydin, E.; De Bastiani, M.; De Wolf, S., Defect and Contact Passivation for Perovskite Solar Cells. *Advanced Materials* **2019,** *31* (25), 20.

98. Wang, Q.; Chueh, C. C.; Eslamian, M.; Jen, A. K. Y., Modulation of PEDOT:PSS pH for Efficient Inverted Perovskite Solar Cells with Reduced Potential Loss and Enhanced Stability. *ACS Applied Materials & Interfaces* **2016,** *8* (46), 32068-32076.

99. Zuo, C. T.; Ding, L. M., Modified PEDOT Layer Makes a 1.52 V V-oc for Perovskite/PCBM Solar Cells. *Advanced Energy Materials* **2017,** *7* (2).

100. Huang, X.; Wang, K.; Yi, C.; Meng, T. Y.; Gong, X., Efficient Perovskite Hybrid Solar Cells by Highly Electrical Conductive PEDOT:PSS Hole Transport Layer. *Advanced Energy Materials* **2016,** *6* (3).

101. Xue, Q. F.; Liu, M. Y.; Li, Z. C.; Yan, L.; Hu, Z. C.; Zhou, J. W.; Li, W. Q.; Jiang, X. F.; Xu, B. M.; Huang, F.; Li, Y.; Yip, H. L.; Cao, Y., Efficient and Stable Perovskite Solar Cells via Dual Functionalization of Dopamine Semiquinone Radical with Improved Trap Passivation Capabilities. *Advanced Functional Materials* **2018,** *28* (18).

102. Huang, J.; Wang, K. X.; Chang, J. J.; Jiang, Y. Y.; Xiao, Q. S.; Li, Y., Improving the efficiency and stability of inverted perovskite solar cells with dopamine-copolymerized PEDOT: PSS as a hole extraction layer. *Journal of Materials Chemistry A* **2017,** *5* (26), 13817-13822.

103. Tan, Z. K.; Moghaddam, R. S.; Lai, M. L.; Docampo, P.; Higler, R.; Deschler, F.; Price, M.; Sadhanala, A.; Pazos, L. M.; Credgington, D.; Hanusch, F.; Bein, T.; Snaith, H. J.; Friend, R. H., Bright light-emitting diodes based on organometal halide perovskite. *Nature Nanotechnology* **2014,** *9* (9), 687-692.

104. Li, G. R.; Tan, Z. K.; Di, D. W.; Lai, M. L.; Jiang, L.; Lim, J. H. W.; Friend, R. H.; Greenham, N. C., Efficient Light-Emitting Diodes Based on Nanocrystalline Perovskite in a Dielectric Polymer Matrix. *Nano Letters* **2015,** *15* (4), 2640-2644.

105. Xiao, Z. G.; Bi, C.; Shao, Y. C.; Dong, Q. F.; Wang, Q.; Yuan, Y. B.; Wang, C. G.; Gao, Y. L.; Huang, J. S., Efficient, high yield perovskite photovoltaic devices grown by interdiffusion of solution-processed precursor stacking layers. *Energy & Environmental Science* **2014,** *7* (8), 2619-2623.

106. Hao, F.; Stoumpos, C. C.; Chang, R. P. H.; Kanatzidis, M. G., Anomalous Band Gap Behavior in Mixed Sn and Pb Perovskites Enables Broadening of Absorption Spectrum in Solar Cells. *Journal of the American Chemical Society* **2014,** *136* (22), 8094-8099.

107. Li, C.; Wei, J.; Sato, M.; Koike, H.; Xie, Z. Z.; Li, Y. Q.; Kanai, K.; Kera, S.; Ueno, N.; Tang, J. X., Halide-Substituted Electronic Properties of Organometal Halide Perovskite Films:

Direct and Inverse Photoemission Studies. *Acs Applied Materials & Interfaces* **2016,** *8* (18), 11526-11531.

108. Comin, R.; Walters, G.; Thibau, E. S.; Voznyy, O.; Lu, Z. H.; Sargent, E. H., Structural, optical, and electronic studies of wide-bandgap lead halide perovskites. *Journal of Materials Chemistry C* **2015,** *3* (34), 8839-8843.

109. Yuan, Y.; Xu, R.; Xu, H. T.; Hong, F.; Xu, F.; Wang, L. J., Nature of the band gap of halide perovskites ABX(3) (A = CH3NH3, Cs; B = Sn, Pb; X = Cl, Br, I): First-principles calculations. *Chinese Physics B* **2015,** *24* (11), 5.

110. Butler, K. T.; Frost, J. M.; Walsh, A., Band alignment of the hybrid halide perovskites CH3NH3PbCl3, CH3NH3PbBr3 and CH3NH3PbI3. *Materials Horizons* **2015,** *2* (2), 228-231.

111. Dong, R.; Fang, Y. J.; Chae, J.; Dai, J.; Xiao, Z. G.; Dong, Q. F.; Yuan, Y. B.; Centrone, A.; Zeng, X. C.; Huang, J. S., High-Gain and Low-Driving-Voltage Photodetectors Based on Organolead Triiodide Perovskites. *Advanced Materials* **2015,** *27* (11), 1912-+.

112. Lin, Q. Q.; Armin, A.; Lyons, D. M.; Burn, P. L.; Meredith, P., Low Noise, IR-Blind Organohalide Perovskite Photodiodes for Visible Light Detection and Imaging. *Advanced Materials* **2015,** *27* (12), 2060-2064.

113. Fang, Y. J.; Huang, J. S., Resolving Weak Light of Sub-picowatt per Square Centimeter by Hybrid Perovskite Photodetectors Enabled by Noise Reduction. *Advanced Materials* **2015,** *27* (17), 2804-+.

114. Liu, C.; Wang, K.; Yi, C.; Shi, X. J.; Du, P. C.; Smith, A. W.; Karim, A.; Gong, X., Ultrasensitive solution-processed perovskite hybrid photodetectors. *Journal of Materials Chemistry C* **2015,** *3* (26), 6600-6606.

115. Li, D.; Dong, G. F.; Li, W. Z.; Wang, L. D., High performance organic-inorganic perovskite-optocoupler based on low-voltage and fast response perovskite compound photodetector. *Scientific Reports* **2015,** *5*, 6.

116. Sutherland, B. R.; Johnston, A. K.; Ip, A. H.; Xu, J. X.; Adinolfi, V.; Kanjanaboos, P.; Sargent, E. H., Sensitive, Fast, and Stable Perovskite Photodetectors Exploiting Interface Engineering. *Acs Photonics* **2015,** *2* (8), 1117-1123.

117. Guo, Y. L.; Liu, C.; Tanaka, H.; Nakamura, E., Air-Stable and Solution-Processable Perovskite Photodetectors for Solar-Blind UV and Visible Light. *Journal of Physical Chemistry Letters* **2015,** *6* (3), 535-539.

118. Deng, H.; Dong, D. D.; Qiao, K. K.; Bu, L. L.; Li, B.; Yang, D.; Wang, H. E.; Cheng, Y. B.; Zhao, Z. X.; Tanga, J.; Song, H. S., Growth, patterning and alignment of organolead iodide perovskite nanowires for optoelectronic devices. *Nanoscale* **2015,** *7* (9), 4163-4170.

119. Hu, X.; Zhang, X. D.; Liang, L.; Bao, J.; Li, S.; Yang, W. L.; Xie, Y., High-Performance Flexible Broadband Photodetector Based on Organolead Halide Perovskite. *Advanced Functional Materials* **2014,** *24* (46), 7373-7380.

120. Domanski, K.; Tress, W.; Moehl, T.; Saliba, M.; Nazeeruddin, M. K.; Gratzel, M., Working Principles of Perovskite Photodetectors: Analyzing the Interplay Between Photoconductivity and Voltage-Driven Energy-Level Alignment. *Advanced Functional Materials* **2015,** *25* (44), 6936-6947.

121. Zhang, Y.; Du, J.; Wu, X. H.; Zhang, G. Q.; Chu, Y. L.; Liu, D. P.; Zhao, Y. X.; Liang, Z. Q.; Huang, J., Ultrasensitive Photodetectors Based on Island-Structured CH3NH3PbI3 Thin Films. *Acs Applied Materials & Interfaces* **2015,** *7* (39), 21634-21638.

122. Zhuo, S. F.; Zhang, J. F.; Shi, Y. M.; Huang, Y.; Zhang, B., Self-Template-Directed Synthesis of Porous Perovskite Nanowires at Room Temperature for High-Performance Visible-Light Photodetectors. *Angewandte Chemie-International Edition* **2015,** *54* (19), 5693-5696.

123. Xia, H. R.; Li, J.; Sun, W. T.; Peng, L. M., Organohalide lead perovskite based photodetectors with much enhanced performance. *Chemical Communications* **2014,** *50* (89), 13695-13697.

124. Horvath, E.; Spina, M.; Szekrenyes, Z.; Kamaras, K.; Gaal, R.; Gachet, D.; Forro, L., Nanowires of Methylammonium Lead Iodide (CH(3)NH(3)Pbl(3)) Prepared by Low Temperature Solution-Mediated Crystallization. *Nano Letters* **2014,** *14* (12), 6761-6766.

125. Sang, L. W.; Liao, M. Y.; Sumiya, M., A Comprehensive Review of Semiconductor Ultraviolet Photodetectors: From Thin Film to One-Dimensional Nanostructures. *Sensors* **2013,** *13* (8), 10482-10518.

126. Maculan, G.; Sheikh, A. D.; Abdelhady, A. L.; Saidaminov, M. I.; Hague, M. A.; Murali, B.; Alarousu, E.; Mohammed, O. F.; Wu, T.; Bakr, O. M., CH3NH3PbCl3 Single Crystals: Inverse Temperature Crystallization and Visible-Blind UV-Photodetector. *Journal of Physical Chemistry Letters* **2015,** *6* (19), 3781-3786.

127. Wang, W. Z.; Xu, H. T.; Cai, J.; Zhu, J. B.; Ni, C. W.; Hong, F.; Fang, Z. B.; Xu, F. Z.; Cui, S. W.; Xu, R.; Wang, L. J.; Xu, F.; Huang, J., Visible blind ultraviolet photodetector based on CH3NH3PbCl3 thin film. *Optics Express* **2016,** *24* (8), 8411-8419.

128. Adinolfi, V.; Ouellette, O.; Saidaminov, M. I.; Walters, G.; Abdelhady, A. L.; Bakr, O. M.; Sargent, E. H., Fast and Sensitive Solution-Processed Visible-Blind Perovskite UV Photodetectors. *Advanced Materials* **2016,** *28* (33), 7264-+.

129. Docampo, P.; Ball, J. M.; Darwich, M.; Eperon, G. E.; Snaith, H. J., Efficient organometal trihalide perovskite planar-heterojunction solar cells on flexible polymer substrates. *Nature Communications* **2013,** *4*, 6.

130. Eperon, G. E.; Burlakov, V. M.; Docampo, P.; Goriely, A.; Snaith, H. J., Morphological Control for High Performance, Solution-Processed Planar Heterojunction Perovskite Solar Cells. *Advanced Functional Materials* **2014,** *24* (1), 151-157.

131. Wang, Q.; Shao, Y. C.; Dong, Q. F.; Xiao, Z. G.; Yuan, Y. B.; Huang, J. S., Large fill-factor bilayer iodine perovskite solar cells fabricated by a low-temperature solution-process. *Energy & Environmental Science* **2014,** *7* (7), 2359-2365.

132. Cho, H. C.; Jeong, S. H.; Park, M. H.; Kim, Y. H.; Wolf, C.; Lee, C. L.; Heo, J. H.; Sadhanala, A.; Myoung, N.; Yoo, S.; Im, S. H.; Friend, R. H.; Lee, T. W., Overcoming the electroluminescence efficiency limitations of perovskite light-emitting diodes. *Science* **2015,** *350* (6265), 1222-1225.

133. Xiao, Z. G.; Dong, Q. F.; Bi, C.; Shao, Y. C.; Yuan, Y. B.; Huang, J. S., Solvent Annealing of Perovskite-Induced Crystal Growth for Photovoltaic-Device Efficiency Enhancement. *Advanced Materials* **2014,** *26* (37), 6503-6509.

134. Zhu, L. Z.; Yuh, B.; Schoen, S.; Li, X. P.; Aldighaithir, M.; Richardson, B. J.; Alamer, A.; Yu, Q. M., Solvent-molecule-mediated manipulation of crystalline grains for efficient planar binary lead and tin triiodide perovskite solar cells. *Nanoscale* **2016,** *8* (14), 7621-7630.

135. Warren, G. W.; Henein, H., Solubility of PbCl2 in DMSO and DMSO-water solutions. *Hydrometallurgy* **1997,** *46* (1-2), 243-247.

136. Unger, E. L.; Bowring, A. R.; Tassone, C. J.; Pool, V. L.; Gold-Parker, A.; Cheacharoen, R.; Stone, K. H.; Hoke, E. T.; Toney, M. F.; McGehee, M. D., Chloride in Lead Chloride-Derived

Organo-Metal Halides for Perovskite-Absorber Solar Cells. *Chemistry of Materials* **2014,** *26* (24), 7158-7165.

137. Saidaminov, M. I.; Abdelhady, A. L.; Murali, B.; Alarousu, E.; Burlakov, V. M.; Peng, W.; Dursun, I.; Wang, L. F.; He, Y.; Maculan, G.; Goriely, A.; Wu, T.; Mohammed, O. F.; Bakr, O. M., High-quality bulk hybrid perovskite single crystals within minutes by inverse temperature crystallization. *Nature Communications* **2015,** *6*, 6.

138. Wang, Q.; Shao, Y. C.; Xie, H. P.; Lyu, L.; Liu, X. L.; Gao, Y. L.; Huang, J. S., Qualifying composition dependent p and n self-doping in CH3NH3PbI3. *Applied Physics Letters* **2014,** *105* (16), 5.

139. Dong, Q. F.; Fang, Y. J.; Shao, Y. C.; Mulligan, P.; Qiu, J.; Cao, L.; Huang, J. S., Electron-hole diffusion lengths > 175 mu m in solution-grown CH3NH3PbI3 single crystals. *Science* **2015,** *347* (6225), 967-970.

140. Saidaminov, M. I.; Abdelhady, A. L.; Maculan, G.; Bakr, O. M., Retrograde solubility of formamidinium and methylammonium lead halide perovskites enabling rapid single crystal growth. *Chemical Communications* **2015,** *51* (100), 17658-17661.

141. Kim, J.; Lee, S. H.; Lee, J. H.; Hong, K. H., The Role of Intrinsic Defects in Methylammonium Lead Iodide Perovskite. *Journal of Physical Chemistry Letters* **2014,** *5* (8), 1312-1317.

142. Yin, W. J.; Shi, T. T.; Yan, Y. F., Unusual defect physics in CH3NH3PbI3 perovskite solar cell absorber. *Applied Physics Letters* **2014,** *104* (6), 4.

143. Yin, W. J.; Shi, T. T.; Yan, Y. F., Unique Properties of Halide Perovskites as Possible Origins of the Superior Solar Cell Performance. *Advanced Materials* **2014,** *26* (27), 4653-+.

144. Yin, W. J.; Shi, T. T.; Yan, Y. F., Superior Photovoltaic Properties of Lead Halide Perovskites: Insights from First-Principles Theory. *Journal of Physical Chemistry C* **2015,** *119* (10), 5253-5264.

145. Wu, X. X.; Trinh, M. T.; Niesner, D.; Zhu, H. M.; Norman, Z.; Owen, J. S.; Yaffe, O.; Kudisch, B. J.; Zhu, X. Y., Trap States in Lead Iodide Perovskites. *Journal of the American Chemical Society* **2015,** *137* (5), 2089-2096.

146. Shkrob, I. A.; Marin, T. W., Charge Trapping in Photovoltaically Active Perovskites and Related Halogenoplumbate Compounds. *Journal of Physical Chemistry Letters* **2014,** *5* (7), 1066-1071.

147. Armin, A.; Zhang, Y. L.; Burn, P. L.; Meredith, P.; Pivrikas, A., Measuring internal quantum efficiency to demonstrate hot exciton dissociation. *Nature Materials* **2013,** *12* (7), 593-593.

148. Wang, Q.; Bi, C.; Huang, J. S., Doped hole transport layer for efficiency enhancement in planar heterojunction organolead trihalide perovskite solar cells. *Nano Energy* **2015,** *15*, 275-280.

149. Wang, D.; Wright, M.; Elumalai, N. K.; Uddin, A., Stability of perovskite solar cells. *Solar Energy Materials and Solar Cells* **2016,** *147*, 255-275.

150. Gruner, S. M.; Eikenberry, E. F.; Tate, M. W., Comparison of X-ray detectors. In *International Tables for Crystallography Volume F: Crystallography of biological macromolecules*, Springer: Netherlands, 2006; pp 143-147.

151. Sekiya, H.; Ida, C.; Kubo, H.; Kurosawa, S.; Miuchi, K.; Tanimori, T.; Taniue, K.; Yoshikawa, A.; Yanagida, T.; Yokota, Y.; Fukuda, K.; Ishizu, S.; Kawaguchi, N.; Suyama, T., A new imaging device based on UV scintillators and a large area gas photomultiplier. *Nuclear*

Instruments & Methods in Physics Research Section a-Accelerators Spectrometers Detectors and Associated Equipment **2011,** *633*, S36-S39.

152. Jansen-van Vuuren, R. D.; Armin, A.; Pandey, A. K.; Burn, P. L.; Meredith, P., Organic Photodiodes: The Future of Full Color Detection and Image Sensing. *Advanced Materials* **2016,** *28* (24), 4766-4802.

153. Wang, W. B.; Zhang, F. J.; Du, M. D.; Li, L. L.; Zhang, M.; Wang, K.; Wang, Y. S.; Hu, B.; Fang, Y.; Huang, J. S., Highly Narrowband Photomultiplication Type Organic Photodetectors. *Nano Letters* **2017,** *17* (3), 1995-2002.

154. Shen, L.; Fang, Y. J.; Wei, H. T.; Yuan, Y. B.; Huang, J. S., A Highly Sensitive Narrowband Nanocomposite Photodetector with Gain. *Advanced Materials* **2016,** *28* (10), 2043-+.

155. Shen, L.; Zhang, Y.; Bai, Y.; Zheng, X. P.; Wang, Q.; Huang, J. S., A filterless, visible-blind, narrow-band, and near-infrared photodetector with a gain. *Nanoscale* **2016,** *8* (26), 12990-12997.

156. Dong, R.; Bi, C.; Dong, Q. F.; Guo, F. W.; Yuan, Y. B.; Fang, Y. J.; Xiao, Z. G.; Huang, J. S., An Ultraviolet-to-NIR Broad Spectral Nanocomposite Photodetector with Gain. *Advanced Optical Materials* **2014,** *2* (6), 549-554.

157. Benavides, C. M.; Murto, P.; Chochos, C. L.; Gregoriou, V. G.; Avgeropoulos, A.; Xu, X. F.; Bini, K.; Sharma, A.; Andersson, M. R.; Schmidt, O.; Brabec, C. J.; Wang, E. G.; Tedde, S. F., High-Performance Organic Photodetectors from a High-Bandgap Indacenodithiophene-Based pi-Conjugated Donor-Acceptor Polymer. *Acs Applied Materials & Interfaces* **2018,** *10* (15), 12937-12946.

158. Pacholski, C.; Kornowski, A.; Weller, H., Self-assembly of ZnO: From nanodots, to nanorods. *Angewandte Chemie-International Edition* **2002,** *41* (7), 1188-+.

159. Burkhard, G. F.; Hoke, E. T.; McGehee, M. D., Accounting for Interference, Scattering, and Electrode Absorption to Make Accurate Internal Quantum Efficiency Measurements in Organic and Other Thin Solar Cells. *Advanced Materials* **2010,** *22* (30), 3293-+.

160. Skompska, M., Hybrid conjugated polymer/semiconductor photovoltaic cells. *Synthetic Metals* **2010,** *160* (1-2), 1-15.

161. Djurisic, A. B.; Ng, A. M. C.; Chen, X. Y., ZnO nanostructures for optoelectronics: Material properties and device applications. *Progress in Quantum Electronics* **2010,** *34* (4), 191-259.

162. Huang, D. M.; Mauger, S. A.; Friedrich, S.; George, S. J.; Dumitriu-LaGrange, D.; Yoon, S.; Moule, A. J., The Consequences of Interface Mixing on Organic Photovoltaic Device Characteristics. *Advanced Functional Materials* **2011,** *21* (9), 1657-1665.

163. Mauger, S. A.; Chang, L. L.; Rochester, C. W.; Moule, A. J., Directional dependence of electron blocking in PEDOT:PSS. *Organic Electronics* **2012,** *13* (11), 2747-2756.

164. Kim, D. H.; Lee, B. L.; Moon, H.; Kang, H. M.; Jeong, E. J.; Park, J. I.; Han, K. M.; Lee, S.; Yoo, B. W.; Koo, B. W.; Kim, J. Y.; Lee, W. H.; Cho, K.; Becerril, H. A.; Bao, Z., Liquid-Crystalline Semiconducting Copolymers with Intramolecular Donor-Acceptor Building Blocks for High-Stability Polymer Transistors. *Journal of the American Chemical Society* **2009,** *131* (17), 6124-6132.

165. Lide, D. R., *CRC handbook of chemistry and physics*. 86th ed., 2005-2006. ed.; Boca Raton : CRC Press: Boca Raton, 2005.

166. Jin, Y. Z.; Wang, J. P.; Sun, B. Q.; Blakesley, J. C.; Greenham, N. C., Solution-processed ultraviolet photodetedtors based on colloidal ZnO nanoparticles. *Nano Letters* **2008,** *8* (6), 1649-1653.

167. Manor, A.; Katz, E. A.; Tromholt, T.; Krebs, F. C., Electrical and Photo-Induced Degradation of ZnO Layers in Organic Photovoltaics. *Advanced Energy Materials* **2011,** *1* (5), 836-843.

168. Verbakel, F.; Meskers, S. C. J.; Janssen, R. A. J., Electronic memory effects in diodes from a zinc oxide nanoparticle-polystyrene hybrid material. *Applied Physics Letters* **2006,** *89* (10), 3.

169. Kind, H.; Yan, H. Q.; Messer, B.; Law, M.; Yang, P. D., Nanowire ultraviolet photodetectors and optical switches. *Advanced Materials* **2002,** *14* (2), 158-+.

170. Liu, J.-M., *Photonic Devices*. Cambridge University Press: UK, 2005.

171. Chen, J. H.; Zuo, L. J.; Zhang, Y. Z.; Lian, X. M.; Fu, W. F.; Yan, J. L.; Li, J.; Wu, G.; Li, C. Z.; Chen, H. Z., High-Performance Thickness Insensitive Perovskite Solar Cells with Enhanced Moisture Stability. *Advanced Energy Materials* **2018,** *8* (23).

172. Zhao, J. J.; Zheng, X. P.; Deng, Y. H.; Li, T.; Shao, Y. C.; Gruverman, A.; Shield, J.; Huang, J. S., Is Cu a stable electrode material in hybrid perovskite solar cells for a 30-year lifetime? *Energy & Environmental Science* **2016,** *9* (12), 3650-3656.

173. Conings, B.; Drijkoningen, J.; Gauquelin, N.; Babayigit, A.; D'Haen, J.; D'Olieslaeger, L.; Ethirajan, A.; Verbeeck, J.; Manca, J.; Mosconi, E.; De Angelis, F.; Boyen, H. G., Intrinsic Thermal Instability of Methylammonium Lead Trihalide Perovskite. *Advanced Energy Materials* **2015,** *5* (15).

174. Stoumpos, C. C.; Malliakas, C. D.; Kanatzidis, M. G., Semiconducting Tin and Lead Iodide Perovskites with Organic Cations: Phase Transitions, High Mobilities, and Near-Infrared Photoluminescent Properties. *Inorganic Chemistry* **2013,** *52* (15), 9019-9038.

175. Knight, A. J.; Wright, A. D.; Patel, J. B.; McMeekin, D. P.; Snaith, H. J.; Johnston, M. B.; Herz, L. M., Electronic Traps and Phase Segregation in Lead Mixed-Halide Perovskite. *Acs Energy Letters* **2019,** *4* (1), 75-84.

176. Brivio, F.; Caetano, C.; Walsh, A., Thermodynamic Origin of Photoinstability in the CH3NH3Pb(I1-xBrx)(3) Hybrid Halide Perovskite Alloy. *Journal of Physical Chemistry Letters* **2016,** *7* (6), 1083-1087.

177. Bischak, C. G.; Hetherington, C. L.; Wu, H.; Aloni, S.; Ogletree, D. F.; Limmer, D. T.; Ginsberg, N. S., Origin of Reversible Photoinduced Phase Separation in Hybrid Perovskites. *Nano Letters* **2017,** *17* (2), 1028-1033.

178. Kubicki, D. J.; Prochowicz, D.; Hofstetter, A.; Zakeeruddin, S. M.; Gratzel, M.; Emsley, L., Phase Segregation in Cs-, Rb- and K-Doped Mixed-Cation (MA)(x)(FA)(1-x)Pbl(3) Hybrid Perovskites from Solid-State NMR. *Journal of the American Chemical Society* **2017,** *139* (40), 14173-14180.

179. Lin, Y. Z.; Chen, B.; Fang, Y. J.; Zhao, J. J.; Bao, C. X.; Yu, Z. H.; Deng, Y. H.; Rudd, P. N.; Yan, Y. F.; Yuan, Y. B.; Huang, J. S., Excess charge-carrier induced instability of hybrid perovskites. *Nature Communications* **2018,** *9*, 9.

180. Ran, C. X.; Xu, J. T.; Gao, W. Y.; Huang, C. M.; Dou, S. X., Defects in metal triiodide perovskite materials towards high-performance solar cells: origin, impact, characterization, and engineering. *Chemical Society Reviews* **2018,** *47* (12), 4581-4610.

181. Yuan, Y. B.; Huang, J. S., Ion Migration in Organometal Trihalide Perovskite and Its Impact on Photovoltaic Efficiency and Stability. *Accounts of Chemical Research* **2016,** *49* (2), 286-293.

182. Khadka, D. B.; Shirai, Y.; Yanagida, M.; Miyano, K., Degradation of encapsulated perovskite solar cells driven by deep trap states and interfacial deterioration. *Journal of Materials Chemistry C* **2018,** *6* (1), 162-170.

183. Wei, D.; Wang, T. Y.; Ji, J.; Li, M. C.; Cui, P.; Li, Y. Y.; Li, G. Y.; Mbengue, J. M.; Song, D. D., Photo-induced degradation of lead halide perovskite solar cells caused by the hole transport layer/metal electrode interface. *Journal of Materials Chemistry A* **2016,** *4* (5), 1991-1998.

184. Guerrero, A.; You, J. B.; Aranda, C.; Kang, Y. S.; Garcia-Belrnonte, G.; Zhou, H. P.; Bisquert, J.; Yang, Y., Interfacial Degradation of Planar Lead Halide Perovskite Solar Cells. *Acs Nano* **2016,** *10* (1), 218-224.

185. Wang, R.; Mujahid, M.; Duan, Y.; Wang, Z. K.; Xue, J. J.; Yang, Y., A Review of Perovskites Solar Cell Stability. *Advanced Functional Materials* **2019,** *29* (47), 25.

186. Li, Z.; Lin, J. D. A.; Phan, H.; Sharenko, A.; Proctor, C. M.; Zalar, P.; Chen, Z. H.; Facchetti, A.; Nguyen, T. Q., Competitive Absorption and Inefficient Exciton Harvesting: Lessons Learned from Bulk Heterojunction Organic Photovoltaics Utilizing the Polymer Acceptor P(NDI2OD-T2). *Advanced Functional Materials* **2014,** *24* (44), 6989-6998.

187. Hu, Y. H.; Ayguler, M. F.; Petrus, M. L.; Bein, T.; Docampo, P., Impact of Rubidium and Cesium Cations on the Moisture Stability of Multiple-Cation Mixed-Halide Perovskites. *Acs Energy Letters* **2017,** *2* (10), 2212-2218.

188. Turren-Cruz, S. H.; Saliba, M.; Mayer, M. T.; Juarez-Santiesteban, H.; Mathew, X.; Nienhaus, L.; Tress, W.; Erodici, M. P.; Sher, M. J.; Bawendi, M. G.; Gratzel, M.; Abate, A.;

Hagfeldt, A.; Correa-Baena, J. P., Enhanced charge carrier mobility and lifetime suppress hysteresis and improve efficiency in planar perovskite solar cells. *Energy & Environmental Science* **2018,** *11* (1), 78-86.

189. Meggiolaro, D.; Motti, S. G.; Mosconi, E.; Barker, A. J.; Ball, J.; Perini, C. A. R.; Deschler, F.; Petrozza, A.; De Angelis, F., Iodine chemistry determines the defect tolerance of lead-halide perovskites. *Energy & Environmental Science* **2018,** *11* (3), 702-713.

190. Yang, W. S.; Noh, J. H.; Jeon, N. J.; Kim, Y. C.; Ryu, S.; Seo, J.; Seok, S. I., High-performance photovoltaic perovskite layers fabricated through intramolecular exchange. *Science* **2015,** *348* (6240), 1234-1237.

191. Jeon, N. J.; Noh, J. H.; Kim, Y. C.; Yang, W. S.; Ryu, S.; Seok, S. I., Solvent engineering for high-performance inorganic-organic hybrid perovskite solar cells. *Nature Materials* **2014,** *13* (9), 897-903.

192. Yang, S. D.; Liu, W. Q.; Zuo, L. J.; Zhang, X. Q.; Ye, T.; Chen, J. H.; Li, C. Z.; Wu, G.; Chen, H. Z., Thiocyanate assisted performance enhancement of formamidinium based planar perovskite solar cells through a single one-step solution process. *Journal of Materials Chemistry A* **2016,** *4* (24), 9430-9436.

193. Kato, Y.; Ono, L. K.; Lee, M. V.; Wang, S. H.; Raga, S. R.; Qi, Y. B., Silver Iodide Formation in Methyl Ammonium Lead Iodide Perovskite Solar Cells with Silver Top Electrodes. *Advanced Materials Interfaces* **2015,** *2* (13), 6.

194. Lee, H.; Lee, C., Analysis of Ion-Diffusion-Induced Interface Degradation in Inverted Perovskite Solar Cells via Restoration of the Ag Electrode. *Advanced Energy Materials* **2018,** *8* (11).

195. Li, J. W.; Dong, Q. S.; Li, N.; Wang, L. D., Direct Evidence of Ion Diffusion for the Silver-Electrode-Induced Thermal Degradation of Inverted Perovskite Solar Cells. *Advanced Energy Materials* **2017,** *7* (14), 8.

196. Albadri, A.; Yadav, P.; Alotaibi, M.; Arora, N.; Alyamani, A.; Albrithen, H.; Dar, M. I.; Zakeeruddin, S. M.; Gratzel, M., Unraveling the Impact of Rubidium Incorporation on the Transport-Recombination Mechanisms in Highly Efficient Perovskite Solar Cells by Small-Perturbation Techniques. *Journal of Physical Chemistry C* **2017,** *121* (45), 24903-24908.

197. Hu, Y. H.; Hutter, E. M.; Rieder, P.; Grill, I.; Hanisch, J.; Ayguler, M. F.; Hufnagel, A. G.; Handloser, M.; Bein, T.; Hartschuh, A.; Tvingstedt, K.; Dyakonov, V.; Baumann, A.; Savenije, T. J.; Petrus, M. L.; Docampo, P., Understanding the Role of Cesium and Rubidium Additives in Perovskite Solar Cells: Trap States, Charge Transport, and Recombination. *Advanced Energy Materials* **2018,** *8* (16), 11.

198. Correa-Baena, J. P.; Luo, Y. Q.; Brenner, T. M.; Snaider, J.; Sun, S. J.; Li, X. Y.; Jensen, M. A.; Hartono, N. T. P.; Nienhaus, L.; Wieghold, S.; Poindexter, J. R.; Wang, S.; Meng, Y. S.; Wang, T.; Lai, B.; Holt, M. V.; Cai, Z. H.; Bawendi, M. G.; Huang, L. B.; Buonassisi, T.; Fenning, D. P., Homogenized halides and alkali cation segregation in alloyed organic-inorganic perovskites. *Science* **2019,** *363* (6427), 627-+.

199. Zhao, C.; Chen, B. B.; Qiao, X. F.; Luan, L.; Lu, K.; Hu, B., Revealing Underlying Processes Involved in Light Soaking Effects and Hysteresis Phenomena in Perovskite Solar Cells. *Advanced Energy Materials* **2015,** *5* (14).

200. Chen, B.; Rudd, P. N.; Yang, S.; Yuan, Y. B.; Huang, J. S., Imperfections and their passivation in halide perovskite solar cells. *Chemical Society Reviews* **2019,** *48* (14), 3842-3867.

201. Shirakawa, H.; Louis, E. J.; Macdiarmid, A. G.; Chiang, C. K.; Heeger, A. J., SYNTHESIS OF ELECTRICALLY CONDUCTING ORGANIC POLYMERS - HALOGEN DERIVATIVES OF POLYACETYLENE, (CH)X. *Journal of the Chemical Society-Chemical Communications* **1977,** (16), 578-580.

202. Groenendaal, B. L.; Jonas, F.; Freitag, D.; Pielartzik, H.; Reynolds, J. R., Poly(3,4-ethylenedioxythiophene) and its derivatives: Past, present, and future. *Advanced Materials* **2000,** *12* (7), 481-494.

203. Sotzing, G. A.; Reynolds, J. R.; Steel, P. J., Poly(3,4-ethylenedioxythiophene) (PEDOT) prepared via electrochemical polymerization of EDOT, 2,2'-bis(3,4-ethylenedioxythiophene) (BiEDOT), and their TMS derivatives. *Advanced Materials* **1997,** *9* (10), 795-&.

204. Yan, J.; Sun, C. H.; Tan, F. R.; Hu, X. J.; Chen, P.; Qu, S. C.; Zhou, S. Y.; Xu, J. K., Electropolymerized poly(3,4-ethylenedioxythiophene):poly(styrene sulfonate) (PEDOT:PSS) film on ITO glass and its application in photovoltaic device. *Solar Energy Materials and Solar Cells* **2010,** *94* (2), 390-394.

205. Yamamoto, T.; Abla, M., Synthesis of non-doped poly(3,4-ethylenedioxythiophene) and its spectroscopic data. *Synthetic Metals* **1999,** *100* (2), 237-239.

206. Yamamoto, T.; Abla, M.; Shimizu, T.; Komarudin, D.; Lee, B. L.; Kurokawa, E., Temperature dependent electrical conductivity of p-doped poly(3,4-ethylenedioxythiophene) and poly(3-alkylthiophene)s. *Polymer Bulletin* **1999,** *42* (3), 321-327.

207. Wu, C. H.; Don, T. M.; Chiu, W. Y., Characterization and conversion determination of stable PEDOT latex nanoparticles synthesized by emulsion polymerization. *Polymer* **2011,** *52* (6), 1375-1384.

208. Harman, D. G.; Gorkin, R., III; Stevens, L.; Thompson, B.; Wagner, K.; Weng, B.; Chung, J. H. Y.; Panhuis, M. I. H.; Wallace, G. G., Poly(3,4-ethylenedioxythiophene):dextran sulfate (PEDOT:DS) - A highly processable conductive organic biopolymer. *Acta Biomaterialia* **2015,** *14*, 33-42.

209. Bayer, A. G. Polythiophenes, process for their preparation and their use. 1988.

210. Horii, T.; Li, Y. C.; Mori, Y.; Okuzaki, H., Correlation between the hierarchical structure and electrical conductivity of PEDOT/PSS. *Polymer Journal* **2015,** *47* (10), 695-699.

211. Kaltenbrunner, M.; Adam, G.; Glowacki, E. D.; Drack, M.; Schwodiauer, R.; Leonat, L.; Apaydin, D. H.; Groiss, H.; Scharber, M. C.; White, M. S.; Sariciftci, N. S.; Bauer, S., Flexible high power-per-weight perovskite solar cells with chromium oxide-metal contacts for improved stability in air. *Nature Materials* **2015,** *14* (10), 1032-+.

212. Li, S. X.; Zhan, L. L.; Sun, C. K.; Zhu, H. M.; Zhou, G. Q.; Yang, W. T.; Shi, M. M.; Li, C. Z.; Hou, J. H.; Li, Y. F.; Chen, H. Z., Highly Efficient Fullerene-Free Organic Solar Cells Operate at Near Zero Highest Occupied Molecular Orbital Offsets. *Journal of the American Chemical Society* **2019,** *141* (7), 3073-3082.

213. Gao, K.; Jo, S. B.; Shi, X. L.; Nian, L.; Zhang, M.; Kan, Y. Y.; Lin, F.; Kan, B.; Xu, B.; Rong, Q. K.; Shui, L. L.; Liu, F.; Peng, X. B.; Zhou, G. F.; Cao, Y.; Jen, A. K. Y., Over 12% Efficiency Nonfullerene All-Small-Molecule Organic Solar Cells with Sequentially Evolved Multilength Scale Morphologies. *Advanced Materials* **2019,** *31* (12), 10.

214. Gao, K.; Li, L. S.; Lai, T. Q.; Xiao, L. G.; Huang, Y.; Huang, F.; Peng, J. B.; Cao, Y.; Liu, F.; Russell, T. P.; Janssen, R. A. J.; Peng, X. B., Deep Absorbing Porphyrin Small Molecule for High-Performance Organic Solar Cells with Very Low Energy Losses. *Journal of the American Chemical Society* **2015,** *137* (23), 7282-7285.

215. Zhang, Q.; Tavakoli, M. M.; Gu, L. L.; Zhang, D. Q.; Tang, L.; Gao, Y.; Guo, J.; Lin, Y. J.; Leung, S. F.; Poddar, S.; Fu, Y.; Fan, Z. Y., Efficient metal halide perovskite light-emitting diodes with significantly improved light extraction on nanophotonic substrates. *Nature Communications* **2019,** *10*.

216. Wang, K.; Wu, H. P.; Meng, Y. N.; Zhang, Y. J.; Wei, Z. X., Integrated energy storage and electrochromic function in one flexible device: an energy storage smart window. *Energy & Environmental Science* **2012,** *5* (8), 8384-8389.

217. Khodagholy, D.; Rivnay, J.; Sessolo, M.; Gurfinkel, M.; Leleux, P.; Jimison, L. H.; Stavrinidou, E.; Herve, T.; Sanaur, S.; Owens, R. M.; Malliaras, G. G., High transconductance organic electrochemical transistors. *Nature Communications* **2013,** *4*, 6.

218. Rivnay, J.; Inal, S.; Salleo, A.; Owens, R. M.; Berggren, M.; Malliaras, G. G., Organic electrochemical transistors. *Nature Reviews Materials* **2018,** *3* (2), 14.

219. Mitraka, E.; Jafari, M. J.; Vagin, M.; Liu, X.; Fahlman, M.; Ederth, T.; Berggren, M.; Jonsson, M. P.; Crispin, X., Oxygen-induced doping on reduced PEDOT. *Journal of Materials Chemistry A* **2017,** *5* (9), 4404-4412.

220. Winther-Jensen, B.; Winther-Jensen, O.; Forsyth, M.; MacFarlane, D. R., High rates of oxygen reduction over a vapor phase-polymerized PEDOT electrode. *Science* **2008,** *321* (5889), 671-674.

221. del Agua, I.; Mantione, D.; Ismailov, U.; Sanchez-Sanchez, A.; Aramburu, N.; Malliaras, G. G.; Mecerreyes, D.; Ismailova, E., DVS-Crosslinked PEDOT:PSS Free-Standing and Textile Electrodes toward Wearable Health Monitoring. *Advanced Materials Technologies* **2018,** *3* (10).

222. Savagatrup, S.; Chan, E.; Renteria-Garcia, S. M.; Printz, A. D.; Zaretski, A. V.; O'Connor, T. F.; Rodriquez, D.; Valle, E.; Lipomi, D. J., Plasticization of PEDOT:PSS by

Common Additives for Mechanically Robust Organic Solar Cells and Wearable Sensors. *Advanced Functional Materials* **2015,** *25* (3), 427-436.

223. Zhu, B.; Luo, S. C.; Zhao, H. C.; Lin, H. A.; Sekine, J.; Nakao, A.; Chen, C.; Yamashita, Y.; Yu, H. H., Large enhancement in neurite outgrowth on a cell membrane-mimicking conducting polymer. *Nature Communications* **2014,** *5*.

224. Mantione, D.; del Agua, I.; Sanchez-Sanchez, A.; Mecerreyes, D., Poly(3,4-ethylenedioxythiophene) (PEDOT) Derivatives: Innovative Conductive Polymers for Bioelectronics. *Polymers* **2017,** *9* (8).

225. Hofmann, A. I.; Katsigiannopoulos, D.; Mumtaz, M.; Petsagkourakis, I.; Pecastaings, G.; Fleury, G.; Schatz, C.; Pavlopoulou, E.; Brochon, C.; Hadziioannou, G.; Cloutet, E., How To Choose Polyelectrolytes for Aqueous Dispersions of Conducting PEDOT Complexes. *Macromolecules* **2017,** *50* (5), 1959-1969.

226. Mantione, D.; del Agua, I.; Schaafsma, W.; Diez-Garcia, J.; Castro, B.; Sardon, H.; Mecerreyes, D., Poly(3,4-ethylenedioxythiophene):GlycosAminoGlycan Aqueous Dispersions: Toward Electrically Conductive Bioactive Materials for Neural Interfaces. *Macromolecular Bioscience* **2016,** *16* (8), 1227-1238.

227. Wu, Y.; Wang, J. Y.; Qiu, X. Q.; Yang, R. Q.; Lou, H. M.; Bao, X. C.; Li, Y., Highly Efficient Inverted Perovskite Solar Cells With Sulfonated Lignin Doped PEDOT as Hole Extract Layer. *Acs Applied Materials & Interfaces* **2016,** *8* (19), 12377-12383.

228. Bubnova, O.; Khan, Z. U.; Malti, A.; Braun, S.; Fahlman, M.; Berggren, M.; Crispin, X., Optimization of the thermoelectric figure of merit in the conducting polymer poly(3,4-ethylenedioxythiophene). *Nature Materials* **2011,** *10* (6), 429-433.

229. Karlsson, R. H.; Herland, A.; Hamedi, M.; Wigenius, J. A.; Aslund, A.; Liu, X. J.; Fahlman, M.; Inganas, O.; Konradsson, P., Iron-Catalyzed Polymerization of Alkoxysulfonate-Functionalized 3,4-Ethylenedioxythiophene Gives Water-Soluble Poly(3,4-ethylenedioxythiophene) of High Conductivity. *Chemistry of Materials* **2009,** *21* (9), 1815-1821.

230. Mawad, D.; Artzy-Schnirman, A.; Tonkin, J.; Ramos, J.; Inal, S.; Mahat, M. M.; Darwish, N.; Zwi-Dantsis, L.; Malliaras, G. G.; Gooding, J. J.; Lauto, A.; Stevens, M. M., Electroconductive Hydrogel Based on Functional Poly(Ethylenedioxy Thiophene). *Chemistry of Materials* **2016,** *28* (17), 6080-6088.

231. Hu, D.; Zhang, L.; Zhang, K.; Duan, X.; Xu, J.; Dong, L.; Sun, H.; Zhu, X.; Zhen, S., Synthesis and Characterization of PEDOT Derivative with Carboxyl Group and Its Chemo Sensing Application as Enhanced Optical Materials. *Journal of Applied Polymer Science* **2015,** *132* (9).

232. Sohn, J. S.; Patil, U. M.; Kang, S.; Jun, S. C., Impact of different nanostructures of a PEDOT decorated 3D multilayered graphene foam by chemical methods on supercapacitive performance. *Rsc Advances* **2015,** *5* (130), 107864-107871.

233. Segura, J. L.; Gomez, R.; Blanco, R.; Reinold, E.; Bauerle, P., Synthesis and electronic properties of anthraquinone-, tetracyanoanthraquinodimethane-, and perylenetetracarboxylic diimide-functionalized poly(3,4-ethylenedioxythiophenes). *Chemistry of Materials* **2006,** *18* (12), 2834-2847.

234. Lu, B.; Lu, Y.; Wen, Y.; Duan, X.; Xu, J.; Chen, S.; Zhang, L., Synthesis, Characterization, and Vitamin C Detection of a Novel L-Alanine-Modified PEDOT with Enhanced Chirality. *International Journal of Electrochemical Science* **2013,** *8* (2), 2826-2841.

235. Im, S. G.; Gleason, K. K., Systematic control of the electrical conductivity of poly(3,4-ethylenedioxythiophene) via oxidative chemical vapor deposition. *Macromolecules* **2007,** *40* (18), 6552-6556.

236. Ha, Y. H.; Nikolov, N.; Pollack, S. K.; Mastrangelo, J.; Martin, B. D.; Shashidhar, R., Towards a transparent, highly conductive poly(3,4-ethylenedioxythiophene). *Advanced Functional Materials* **2004,** *14* (6), 615-622.

237. Mueller, M.; Fabretto, M.; Evans, D.; Hojati-Talemi, P.; Gruber, C.; Murphy, P., Vacuum vapour phase polymerization of high conductivity PEDOT: Role of PEG-PPG-PEG, the origin of water, and choice of oxidant. *Polymer* **2012,** *53* (11), 2146-2151.

238. J.M.G. Cowie; Arrighi, V., *Polymers: Chemistry and Physics of Modern Materials*. Third Edition ed.; CRC Press: Boca Raton, 2007.

239. Massonnet, N.; Carella, A.; Jaudouin, O.; Rannou, P.; Laval, G.; Celle, C.; Simonato, J. P., Improvement of the Seebeck coefficient of PEDOT:PSS by chemical reduction combined with a novel method for its transfer using free-standing thin films. *Journal of Materials Chemistry C* **2014,** *2* (7), 1278-1283.

240. Bubnova, O.; Crispin, X., Towards polymer-based organic thermoelectric generators. *Energy & Environmental Science* **2012,** *5* (11), 9345-9362.

241. Pelzer, K. M.; Cheng, L.; Curtiss, L. A., Effects of Functional Groups in Redox-Active Organic Molecules: A High-Throughput Screening Approach. *Journal of Physical Chemistry C* **2017,** *121* (1), 237-245.

242. Zotti, G.; Zecchin, S.; Schiavon, G.; Louwet, F.; Groenendaal, L.; Crispin, X.; Osikowicz, W.; Salaneck, W.; Fahlman, M., Electrochemical and XPS studies toward the role of

monomeric and polymeric sulfonate counterions in the synthesis, composition, and properties of poly(3,4-ethylenedioxythiophene). *Macromolecules* **2003,** *36* (9), 3337-3344.

243. Garreau, S.; Louarn, G.; Buisson, J. P.; Froyer, G.; Lefrant, S., In situ spectroelectrochemical Raman studies of poly(3,4-ethylenedioxythiophene) (PEDT). *Macromolecules* **1999,** *32* (20), 6807-6812.

244. Chiu, W. W.; Travas-Sejdic, J.; Cooney, R. P.; Bowmaker, G. A., Studies of dopant effects in poly(3,4-ethylenedioxythiophene) using Raman spectroscopy. *Journal of Raman Spectroscopy* **2006,** *37* (12), 1354-1361.

245. Lapkowski, M.; Pron, A., Electrochemical oxidation of poly(3,4-ethylenedioxythiophene) - "in situ" conductivity and spectroscopic investigations. *Synthetic Metals* **2000,** *110* (1), 79-83.

246. Park, H.; Lee, S. H.; Kim, F. S.; Choi, H. H.; Cheong, I. W.; Kim, J. H., Enhanced thermoelectric properties of PEDOT: PSS nanofilms by a chemical dedoping process. *Journal of Materials Chemistry A* **2014,** *2* (18), 6532-6539.

247. Bouroushian, M., *Electrochemistry of Metal Chalcogenides*. Springer: Berlin, Heidelberg, 2010.

248. Deleeuw, D. M.; Kraakman, P. A.; Bongaerts, P. E. G.; Mutsaers, C. M. J.; Klaassen, D. B. M., ELECTROPLATING OF CONDUCTIVE POLYMERS FOR THE METALLIZATION OF INSULATORS. *Synthetic Metals* **1994,** *66* (3), 263-273.

249. Kim, N.; Kang, H.; Lee, J. H.; Kee, S.; Lee, S. H.; Lee, K., Highly Conductive All-Plastic Electrodes Fabricated Using a Novel Chemically Controlled Transfer-Printing Method. *Advanced Materials* **2015,** *27* (14), 2317-2323.

250. Fan, X.; Xu, B. G.; Wang, N. X.; Wang, J. Z.; Liu, S. H.; Wang, H.; Yan, F., Highly Conductive Stretchable All-Plastic Electrodes Using a Novel Dipping-Embedded Transfer Method

for High-Performance Wearable Sensors and Semitransparent Organic Solar Cells. *Advanced Electronic Materials* **2017,** *3* (5).

VITA

Erjin Zheng received his Bachelor of Engineering in Chemical Engineering at the East China University of Science and Technology in Shanghai, China in 2015, and his Master of Science in Chemical Engineering at the University of Washington in Seattle, WA in 2017. He is expected to receive his Doctor of Philosophy in Chemical Engineering at the University of Washington in Seattle, WA in 2020.

Publications

1. **Erjin Zheng**, Zhiyin Niu, Gabriella A. Tosado, Hao Dong, Yaqoub Albrikan, and Qiuming Yu "Revealing Stability of Inverted Planar MA-Free Perovskite Solar Cells and Electric Field-Induced Phase Instability." Submitted to *The Journal of Physical Chemistry C*
2. Hao Dong, **Erjin Zheng**, Zhiyin Niu, Xiaoyu Zhang, Yi-Yu Lin, Priyesh Jain, and Qiuming Yu "Hydroxymethyl-Functionalized PEDOT-MeOH:PSS for Perovskite Solar Cells." *ACS Applied Materials & Interfaces 12*.15 (2020): 17571-17582.
3. **Erjin Zheng**, Priyesh Jain, Hao Dong, Zhiyin Niu, Shinya Chen, Shukun Zhong, and Qiuming Yu "Chemical Polymerization of Hydroxymethyl and Chloromethyl Functionalized PEDOT:PSS." *ACS Applied Polymer Materials* 1.11 (2019): 3103-3114.
4. Xiaojun Luo, Lijuan Jiang, Tuli Kang, Yingfang Xing, **Erjin Zheng**, Ping Wu, Chenxin Cai, and Qiuming Yu "Label-Free Raman Observation of TET1 Protein-Mediated Epigenetic Alterations in DNA." *Analytical Chemistry* 91.11 (2019): 7304-7312.
5. Xiaojun Luo, Yingfang Xing, Daniel David Galvan, **Erjin Zheng**, Ping Wu, Chenxin Cai, and Qiuming Yu "A Plasmonic Gold Nanohole Array for Surface-Enhanced Raman Scattering

Detection of DNA Methylation." *ACS Sensors* 4.6 (2019): 1534-1542.

6. **Erjin Zheng**, Xiaoyu Zhang, Monica Esopi, Chen Cai, Beiying Zhou, Yi-Yu Lin, and Qiuming Yu "Narrowband Ultraviolet Photodetectors Based on Nanocomposite Thin Films with High Gain and Low Driving Voltage." *ACS Applied Materials & Interfaces* 10.48 (2018): 41552-41561.
7. Gabriella Tosado, Yi-Yu Lin, **Erjin Zheng**, and Qiuming Yu "Impact of Cesium in Phase and Device Stability of Triple Cation Pb-Sn Double Halide Perovskite Films and Solar Cells." *Journal of Materials Chemistry A* 6.36 (2018): 17426-17436.
8. Xiaoyu Zhang, **Erjin Zheng**, Monica Esopi, Chen Cai, and Qiuming Yu "Flexible Narrowband Ultraviolet Photodetectors with Photomultiplication Based on Wide Band Gap Conjugated Polymer and Inorganic Nanoparticles." *ACS Applied Materials & Interfaces* 10.28 (2018): 24064-24074.
9. Monica Esopi, **Erjin Zheng**, Xiaoyu Zhang, Chen Cai, and Qiuming Yu "Tuning the spectral response of ultraviolet organic-inorganic hybrid photodetectors via charge trapping and charge collection narrowing." *Physical Chemistry Chemical Physics* 20.16 (2018): 11273-11284.
10. **Erjin Zheng**, Brian Yuh, Gabriella Tosado, and Qiuming Yu "Solution-processed visible-blind UV-A photodetectors based on $CH_3NH_3PbCl_3$ perovskite thin films." *Journal of Materials Chemistry C* 5.15 (2017): 3796-3806.
11. Jin Sha, **Erjin Zheng**, WenJuan Zhou, Armin Liebens, and Marc Pera-Titus. "Selective oxidation of fatty alcohol ethoxylates with H_2O_2 over Au catalysts for the synthesis of alkyl ether carboxylic acids in alkaline solution." *Journal of Catalysis* 337 (2016): 199-207.

Presentations

1. “Electric field induced degradation in MA-free perovskite solar cells”, poster presentation on Fall MRS Meeting & Exhibit, December 2019, Boston, MA.
2. “Oxidative chemical polymerization of functionalized PEDOT:PSS”, poster presentation on Fall MRS Meeting & Exhibit, December 2019, Boston, MA.
3. “Solution-processed $CH_3NH_3PbCl_3$ perovskite thin films for UV-A photodetectors”, oral presentation on Spring MRS Meeting & Exhibit, April 2018, Phoenix, AZ.
4. “Ultra-sensitive, low driving voltages, flexible UV-specific photodetectors based on F8T2:ZnO nanocomposite”, poster presentation on Spring MRS Meeting & Exhibit, April 2018, Phoenix, AZ.